The background of the cover is a 3D molecular model of a porous material. It features a repeating pattern of orange, interconnected ring-like structures that form a porous framework. Within the pores of this framework, several white, cross-shaped molecular structures are visible, representing structural and chiral isomers. The overall appearance is that of a complex, crystalline lattice with significant porosity.

Separation of Structural and Chiral Isomers in Nanoporous Materials

Rocío Bueno Pérez

Separation of Structural and Chiral Isomers in Nanoporous Materials

by

Rocío Bueno Pérez

Licenciada en Biotecnología



Department of Physical, Chemical, and Natural Systems

UNIVERSITY PABLO DE OLAVIDE

SUPERVISORS

Prof. Sofía Calero

University Pablo de Olavide

Prof. Patrick J. Merkling


University Pablo de Olavide

Work presented to obtain the degree of Doctor with International Mention

SEVILLE, MARCH 2018

ISBN: 978-84-697-9701-3

Copyright © Rocío Bueno Pérez

 <https://orcid.org/0000-0002-1472-6852>



Printed by: LLARdigital

- **Doctoral Supervisors**

Prof. Sofía Calero

Prof. Patrick J. Merkling

- **Examination Committee**

Chair: Prof. Santiago Lago Aranda

Secretary: Dr. Neyvis Almora Barrios

Member: Dr. Peyman Z. Moghadam

- **External Committee**

Prof. Titus S. van Erp

Dr. Yamil J. Colon

The research reported in this thesis was carried out at the Department of Physical, Chemical and Natural Systems, University Pablo de Olavide (Seville, Spain), with financial support from the Spanish “Ministerio de Economía y Competitividad” (MINECO), from the European Research Council (ERC Consolidator Grant), and from the Andalucía Region “Junta de Andalucía” (Proyecto de Excelencia).



*A mi madre, Aurora,
porque si hubiera hecho una tesis
la habría hecho mejor*

Contents

CHAPTER 1: Introduction	1
1. Materials	1
1.1. Zeolites	1
1.2. Metal-organic frameworks (MOFs)	3
2. Methods	5
2.1. Monte Carlo	5
2.2. Molecular Dynamics	10
3. Force fields and models	11
3.1. Force fields	11
3.2. Models for adsorbents	13
3.3. Models for adsorbates	15
4. Context and outline of the thesis	16
Bibliography	18

CHAPTER 2: Enantioselective Adsorption of Ibuprofen and Lysine in Metal-Organic Frameworks	25
Conclusions	29
Acknowledgments.....	29
Bibliography	29

CHAPTER 3: Separation of Amyl Alcohol Isomers in ZIF-77	31
Conclusions	36
Acknowledgments.....	36
Bibliography	36

CHAPTER 4: Cadmium-BINOL Metal-Organic Framework for the Separation of Alcohol Isomers	39
Introduction.....	39
Computational Details.....	41
Results and Discussion	43
Conclusions	57
Acknowledgments.....	58
Bibliography	58

CHAPTER 5: Zeolite Force Fields and Experimental Siliceous Frameworks in a Comparative Infrared Study	61
Introduction.....	61
Computational Details	62
Experimental Details	66
Results and Discussion	66
Conclusions	74
Acknowledgments.....	74
Bibliography	74
CHAPTER 6: Influence of Flexibility on the Separation of Chiral Isomers in STW-Type Zeolite	77
Introduction.....	77
Computational Details	80
Experimental Details	83
Results and Discussion	83
Conclusions	95
Acknowledgments.....	96
Bibliography	96
CHAPTER 7: Conclusions	99
Resumen (Summary in Spanish)	103
Appendixes	109
Appendix 1	109
Appendix 2	119
Appendix 3	129
Appendix 4	143
Appendix 5	145
List of publications	159
Acknowledgments / Agradecimientos	161

Introduction

1

The research on nanoporous materials, such as metal-organic frameworks (MOFs) and zeolites among others, is an active field of research that includes industrial applications, based on adsorption and diffusion, for which these materials are potentially suitable.¹⁻³ These applications, such as gas storage and release, carbon capture, drug loading and delivery, purification of gas or liquid compounds from mixtures, or chiral separation, are relevant for processes in chemical, petrochemical, and pharmaceutical industries. The main characteristic of these materials is their porosity, i.e., the wide distribution of pore sizes and shapes, which along with their high surface area, ordered structure, and stability, explain their versatility.

From the very first zeolites found in nature, to those synthesized recently, linked to the development of MOFs, the knowledge on the relation between material features and their potential applications has increased exponentially and the possibility of tailoring structures for specific purposes is taking advantage of this. Molecular simulation techniques contribute to this by giving experimentalists a hint on the material

features requested for a particular application and predicting the behavior of real or hypothetical structures.⁴ Moreover, simulations are useful tools which provide in depth information on the molecular mechanisms that underlie adsorption and separation processes.⁵

The present work studies the ability of nanoporous materials to serve as “molecular sieves” in the separation of structural and chiral isomers. Molecular simulation techniques are used to study adsorption and diffusion in these materials and to analyze their structural and chiral selectivity, how these properties relate to the microassembly of adsorbed molecules and adsorbate-structure interactions, and how those are affected by the intrinsic lattice vibration of the crystalline nanoporous materials.

1. Materials

1.1. Zeolites

Zeolites are crystalline three-dimensional structures based on silica. They are built from TO_4 tetrahedra consisting of four oxygen atoms covalently bonded to one central atom (T) which is typically silicon.

This central atom can be also substituted by aluminum, boron, beryllium, zinc, germanium, or sulphur.⁶ These tetrahedra are the Primary Building Units (PBUs) and are connected with each other through the oxygen atoms at the vertices. The connected PBUs generate the ordered porous network that characterizes this material. The porosity

of this ordered structure can be arranged differently, showing many topologies (Figure 1). Thus, depending on the topology the porosity of a zeolite can be distributed into cavities and/or channels, and these channels can be straight, helicoidal, zigzag, or interconnected.

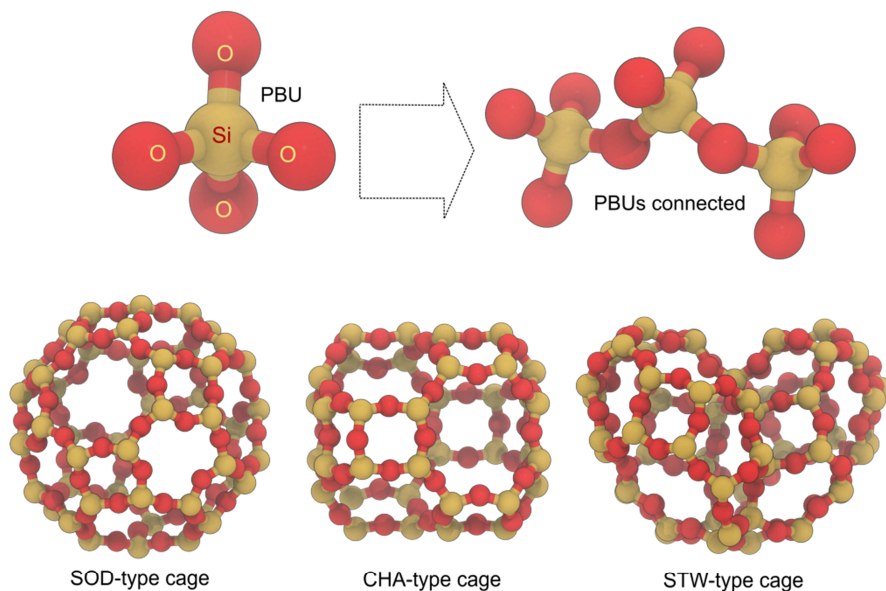


Figure 1. Graphical representation of silicon-oxygen tetrahedron (top left), three PBU connected through oxygen atoms (top right), and examples of different cage types, SOD, CHA, and STW, depending on the connection pattern of PBUs.

Zeolites were originally found in nature, in deposits of volcanic material. Their name stems from the Greek words *zeo* (to boil) and *lithos* (rock) and was introduced in the 18th century by Alex F. Cronsted after discovering their property of releasing water steam when heated. Since then, most naturally occurring zeolites have been obtained synthetically and over 230 framework types have been recognized.⁷ Their common characteristics, i.e., high surface area, and thermal and chemical stability were studied and exploited as

molecular sieves, selective adsorbents, ion exchangers, and catalysts.^{4,8-12} The research on these materials considers also the design and synthesis of zeolites with different chemical compositions, pore shapes and sizes, and particular characteristics, such as hydrophobicity and acidity of its surface, to perform a specific purpose, while maintaining the durability of the material.¹³⁻¹⁴

The robustness of the PBUs and their lack of deformability make this structural element

essentially rigid. However, some zeolites might be compressed without distorting TO_4 tetrahedra. These flexibility windows are specific for each framework.¹⁵ Although some zeolites exhibit large deformations in their three-dimensional structure under chemical or physical stimuli, the intrinsic flexibility of most zeolites are limited to atom-atom vibrations with negligible effect on most properties or crystalline regularity. However, this small-scale lattice vibration can affect the pore opening and diffusion kinetics of adsorbates.¹⁶

As a consequence of their particular characteristics and their development since they were discovered, zeolites are a group of porous materials widely used for many applications in several fields. In industry, zeolites are employed to remove atmospheric pollutants,¹⁷⁻¹⁸ to recover radioactive ions from nuclear waste,¹⁹ as catalysts in cracking and hydrocracking,²⁰ and to separate air components,²¹ among others. Commercially, they are used as additives to asphalt concrete²² and in oxygen

concentrators for medical-grade oxygen.¹ Even in daily life, zeolites can be found in cat litter, detergents, and ion exchangers for water purification.

1.2. Metal-Organic Frameworks (MOFs)

Metal-organic frameworks (MOFs) can be considered coordination polymers with an ordered crystalline structure based on metal centers or clusters linked by organic ligands with covalent or ionic bonds.²³⁻²⁶ These metal centers or clusters, identified as nodes, commonly involve transition metals,²⁷⁻³⁵ but other metals can be used, such as lanthanides.³⁶ The organic ligands, also known as connectors or spacers, are organic molecules with carboxylate,^{33,37} amine,³⁸⁻³⁹ or thiol⁴⁰⁻⁴¹ functional groups, among others, whose oxygen, nitrogen, or sulphur atoms are available to bond with the node. The coordination geometry of these building units, i.e., nodes and connectors, configures a three-dimensional network of pores, cavities, and/or channels, which is ordered and well defined with different crystalline topologies⁴² (Figure 2).

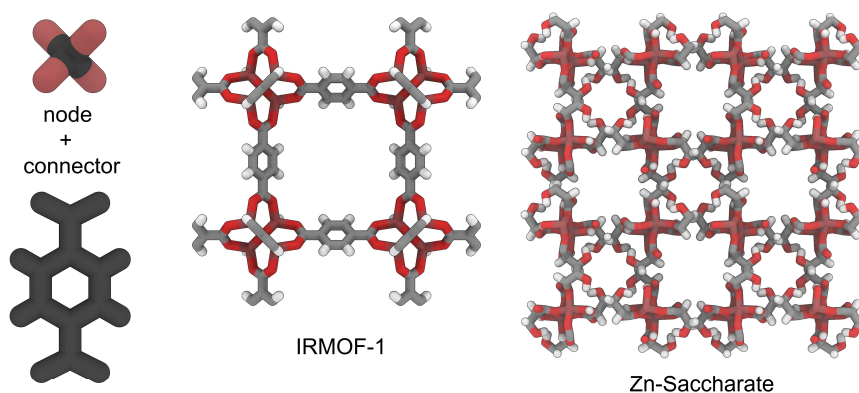


Figure 2. Graphical representation of building units (left), and atomistic view of two MOFs, IRMOF-1 (center) and Zn-Saccharate (right), which have Zn as the metal center but different organic ligand, generating different topologies.

The development of these synthetic hybrid porous materials was motivated by the fast progress of the petroleum and pharmaceutical chemistry which sought new materials with similar properties to those found in zeolites. MOFs are characterized by their high pore volume and surface area, low densities, high storage capacities, a wide range of pore sizes, and optical and magnetic properties.⁴³⁻⁵⁰ This makes these materials suitable for storage of hydrogen⁵¹⁻⁵³ and greenhouse gases,⁵⁴⁻⁵⁶ separation and purification processes,⁵⁷⁻⁶¹ drug delivery, and cosmetics.⁶²⁻⁶⁷ In addition, they have proven their potential as catalysts,⁶⁸⁻⁷² sensors,⁷³⁻⁷⁵ luminescent^{39,76-77} and magnetic materials,^{36,78} and explosives.³⁵ The tunability of these materials lies in the great diversity of organic ligands which, in combination with the metal centers, increases the number of possible designs to meet a specific purpose.⁷⁹⁻⁸² Thus, since MOFs were first synthesized in the late nineties by Yaghi *et al.*,³⁴ more than 70 000 MOFs were synthesized and reported in the Cambridge Structural Database⁸³ and more

than 130 000 hypothetical MOFs⁸⁴ were generated by combination of building units.

After synthesis MOFs can behave differently upon removal of solvent molecules, temperature variation or guest inclusion.^{42,76} In fact, many MOFs lose their crystallinity after the removal of solvent molecules or the adsorption of water. Also, an interesting feature of these materials is the structural flexibility that can be triggered by external stimuli such as guest adsorption, external force fields, temperature, or interaction with light.⁸⁵ The most commonly explored flexible phenomena of MOFs are breathing, swelling, thermal expansion, linker rotation, and subnetwork displacement. Breathing⁸⁶⁻⁹⁰ is a reversible phase transition which changes volume, distances, angles of the unit cell, and its space group. Swelling,⁹¹⁻⁹³ on the contrary, is a gradual enlargement of the unit cell volume without any change in unit cell shape or its space group. These behaviors are responsive to guest adsorption/desorption while thermal expansion⁹⁴⁻⁹⁵ is triggered by temperature

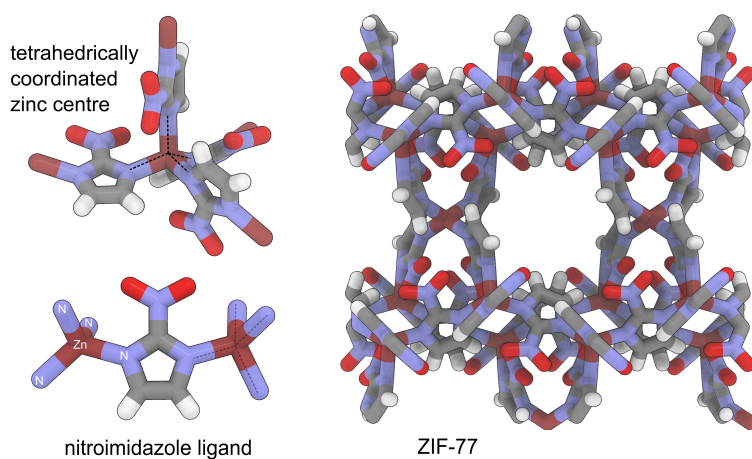


Figure 3. Graphical representation of the tetrahedrally coordinated Zn atom and the four nitroimidazole linkers building ZIF-77.

change upon which expansion or shrinkage of a framework happens without reaching a complete phase transition. Linker rotation⁹⁶⁻⁹⁷ is a continuous transition of linkers around its rotational axis causing an expansion of pore windows upon the interaction with certain guest molecules. Finally, subnetwork displacement^{42,81,98} means the relocation of subnets interacting only by weak forces in interpenetrated three-dimensional MOFs or stacked two-dimensional frameworks.

Among all MOFs reported, zeolitic imidazolate frameworks (ZIFs) are an interesting subset of materials within the group of MOFs that can be regarded as hybrids between MOFs and zeolites.⁹⁹ They can be regarded formally as zeolites because ZIFs are made of tetrahedral building units around a metal center and adopt zeolite-like topologies, while they belong to the MOFs family because of a core metal center, zinc or cobalt, tetrahedrally coordinated to an organic linker imidazolate or functionalized imidazolate as organic ligands^{38,100} (Figure 3). The properties they share with zeolites are the high chemical and thermal stability,¹⁰¹ which expands the potential applications of ZIFs.¹⁰²⁻¹⁰⁷ Further, the zeolite-like topologies open the door to synthesizing ZIFs with topologies of hypothetical zeolites due to the larger flexibility of the metal-imidazolate bond.¹⁰⁸

Taking into account the variety of chemical composition, combination of building units and functionalization possibilities, there is a vast number of possible MOFs, and that offers plenty of room for improvement and development.¹⁰⁹⁻¹¹¹

2. Methods

In the context of this thesis, molecular simulation refers to a set of techniques

based on computer simulations that have become a very useful tool in fields such as chemistry, biology, and physics. In the particular case of materials science, it complements the experimental techniques by helping to study properties that are not accessible experimentally, providing information on the microscopic level of the system under study and allowing for a better control of the variables of the system.

A different method should be selected according to the property that we want to study and the way the system under study is described. In this work, we use classical methods:

- **Monte Carlo (MC)** is a statistical method that computes macroscopic properties of a system by averaging the microscopic states of the system at equilibrium.
- **Molecular Dynamics (MD)** is a deterministic method that studies the evolution of a system by integrating Newton's laws of motion.

In general terms, simulating large systems reduces the errors in the computed properties, but it also leads to long simulation times. To avoid this, and accounting for the periodic nature of crystal lattices, the unit cell is infinitely replicated in the three directions of space, applying periodic boundary conditions.¹¹² As a consequence, the length of the simulation box used in this study is typically around 20-40 Å.

2.1. Monte Carlo

The adsorption properties of the systems are calculated through the Monte Carlo method. This is a numerical statistical method that approximates complex mathematical expressions that cannot be

evaluated accurately. It is based on the use of random numbers and probabilities to calculate the macroscopic properties of a system from its accessible microstates. When the number of microstates is too large, the technique “Markov Chain Monte Carlo” (MCMC) is used, which allows for the estimation of a macroscopic property without accounting for all the microstates. The MCMC technique generates compatible configurations of the macrostate with a probability proportional to the Boltzmann weight and assumes that only the relative probability of visiting microstates of a system is needed instead of the absolute probability with the correct frequency.¹¹²

The MCMC algorithm generates random trial moves from the current state (o) to a new state (n) that can be accepted or rejected. The probability of finding a system at either state is $P_B(o)$ and $P_B(n)$, respectively, and the conditional probability

to perform a trial move between states is denoted as $\alpha(o \rightarrow n)$ and $\alpha(n \rightarrow o)$. As is assumed in the original Metropolis scheme, a system with an arbitrary initial distribution of microstates eventually reaches the equilibrium distribution. This detailed balance condition implies that the probability of leaving a state by accepting the trial move $o \rightarrow n$, $P_{acc}(o \rightarrow n)$, is the same as that of accepting the trial move from all other states n to the state o , $P_{acc}(n \rightarrow o)$.

$$P_B(o)\alpha(o \rightarrow n)P_{acc}(o \rightarrow n) = P_B(n)\alpha(n \rightarrow o)P_{acc}(n \rightarrow o) \quad (1)$$

According to the Metropolis algorithm,¹¹³ α is assumed to be a symmetric matrix: $\alpha(o \rightarrow n) = \alpha(n \rightarrow o)$. Thus, the probability of acceptance is calculated:

$$P_{acc}(o \rightarrow n) = \min\left(1, \frac{P_B(n)}{P_B(o)}\right) \quad (2)$$

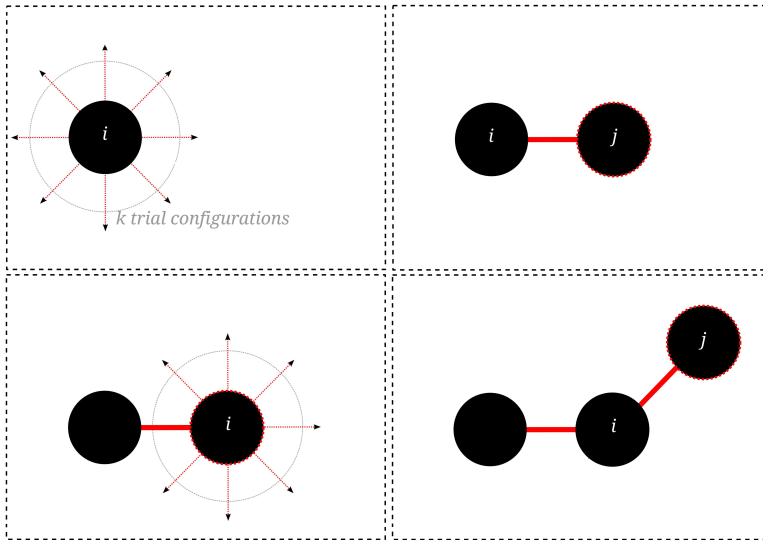


Figure 4. Schematic representation of the configurational bias Monte Carlo method.

The conventional Monte Carlo method is costly in computational terms when long and bulky molecules are involved because the efficiency of inserting these molecules in the system is normally very low. Improving the conformational sampling of these molecules increases the efficiency of insertions and avoids overlaps with the framework, and this is achieved with the configurational bias Monte Carlo (CBMC) technique.¹¹⁴ The CBMC method inserts a molecule in the simulation box bead by bead (Figure 4), generating for each bead k trial orientations according to the internal energy U^{int} . The growth of the chain is biased by selecting the most favorable orientation based on the external energy U^{ext} , which is computed for each trial position j of each bead i . Thus, one of the trial positions is selected according to the expression

$$P_i(j) = \frac{e^{-\beta U_i^{\text{ext}}(j)}}{\sum_{l=1}^k e^{-\beta U_i^{\text{ext}}(l)}} = \frac{e^{-\beta U_i^{\text{ext}}(j)}}{\omega_i}, \quad (3)$$

where $\beta = 1/(k_B T)$, k_B is the Boltzmann constant, T is the temperature and ω_i is the Rosenbluth weight.

The selected trial orientation is added to the growing chain and the same procedure is repeated until the whole molecule is grown. Then, the acceptance or rejection of the grown molecule is calculated based on the Rosenbluth factor¹¹⁵ of the new configuration:

$$W = \prod_i \omega(i) \quad (4)$$

There is also an alternative method to improve the insertion of molecules when systems are particularly dense. The continuous fractional component Monte Carlo method¹¹⁶ gradually inserts a molecule in the system or deletes it by “inflating” or “deflating” it. The CFCMC method expands the system with an additional fractional molecule and scales the intermolecular energy using a λ parameter that ranges from

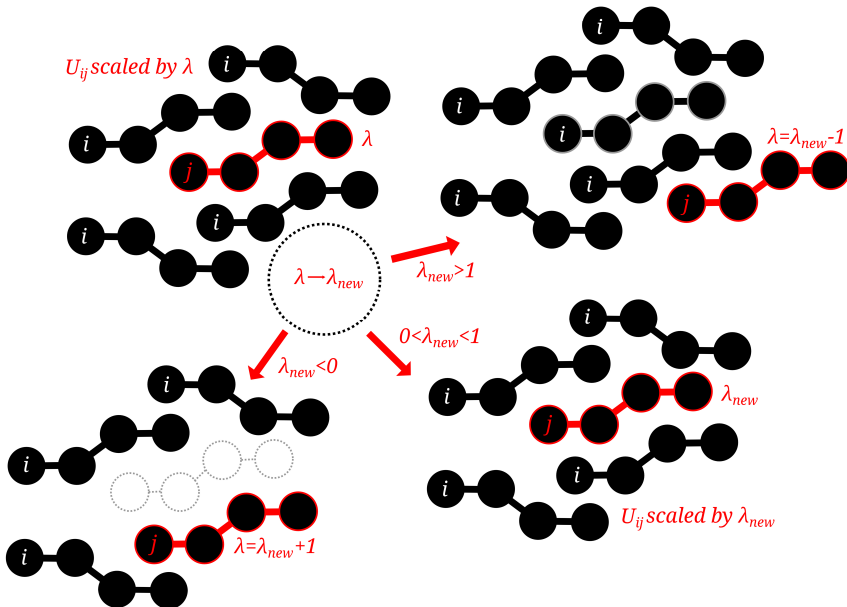


Figure 5. Schematic representation of continuous fractional component Monte Carlo.

0 to 1. Instead of inserting a new molecule, a trial change in λ is attempted using $\lambda(n) = \lambda(o) + \Delta\lambda$. To prevent the system from getting stuck at a certain λ value, an additional biasing factor η is used, associated to each state of λ , and calibrated in the system.¹¹⁷ This bias does not affect the outcome, however, as it is later compensated by the acceptance rules. After a trial change of λ , there are three possible outcomes (Figure 5):

- $\lambda(n)$ remains between 0 and 1, $0 \leq \lambda(n) \leq 1$: There is no change in the number or in the positions of molecules, but the change in intermolecular energy is calculated and compared to the old energy.
- $\lambda(n)$ exceeds the unity, $\lambda(n) = 1 + \varepsilon$: The current fractional molecule is fully inserted ($\lambda = 1$) and a new fractional molecule is generated with $\lambda = \varepsilon$.
- $\lambda(n)$ falls below 0, $\lambda(n) = -\varepsilon$: The current fractional molecule is deleted ($\lambda = 0$) and one molecule of the system is chosen to be fractional with $\lambda = 1 - \varepsilon$.

It is possible to combine CFCMC and CBMC schemes, performing insertion ($\lambda = 1$) and deletion ($\lambda = 0$) moves using configurational biasing.¹¹⁸

During MC simulations, which are divided in cycles, one of the following moves is randomly selected and applied to the system. For those that are applied to the molecules within the framework, one molecule of the system is selected on a random basis too.

- Rotation. The selected molecule is rotated around its center of mass.

- Translation. A random displacement is applied to the selected molecule.
- Regrowth. The selected molecule is partially or entirely regrown with another orientation.
- Insertion. A molecule is grown at a random position.
- Deletion. A molecule is randomly chosen and removed from the system.
- Identity Change. In a mixture of two or more components, one molecule of one component is selected and its identity is changed to a different component.
- ξ -Replica Exchange¹¹⁹ (Parallel Molar Fraction). Similar to parallel tempering scheme,¹²⁰ two neighboring systems with different molar fractions are swapped.
- Chiral Inversion¹¹⁹. It is applied to systems where chiral molecules are adsorbed in nonchiral adsorbents, and turns all *R* enantiomers into *S* enantiomers and *vice versa*. This move improves the sampling of chiral molecules.

Depending on the property that we want to compute, the system might be described differently, for which there are several ensembles in which MC simulations can be performed. In this work, two different ensembles have been used:

- Canonical Ensemble (NVT). The system is defined by the number of particles, volume, and temperature, which are fixed. It is used to calculate adsorption energies and entropies, Henry coefficients, and occupation density of molecules within the framework. It is also used in MD to compute mean squared displacements (MSDs) and infrared spectra.

- Grand Canonical Ensemble (μVT). The system is described by the volume, temperature, and chemical potential, which are kept fixed. The number of molecules can vary and insertion and deletion MC moves can be applied. It is used to compute adsorption isotherms.

Adsorption isotherms

Adsorption isotherms are usually computed with grand canonical Monte Carlo (GCMC) simulations. As explained before, in this ensemble the volume (V), temperature (T), and chemical potential (μ) are fixed. The number of molecules fluctuates during the simulation and these molecules are susceptible of being exchanged with a reservoir, which is held at the same chemical potential, until the adsorption reaches the equilibrium. The equilibrium conditions are equal temperatures and equal chemical potentials of the gas inside and outside the system. The chemical potential of the gas is related to the fugacity (f), which is the effective thermodynamic pressure, according to

$$\mu = \mu^\circ + RT \ln \left(\frac{f}{p^\circ} \right), \quad (5)$$

where p° is the standard pressure, μ° is the standard chemical potential, R is the ideal gas constant, and T is the temperature of the system. Fugacity is related to pressure with the expression $f = \phi p$, where ϕ is the fugacity coefficient. For ideal and real gases at high temperatures or low pressure, it is possible to assume that fugacity is equal to pressure ($\phi = 1$). However, when the pressure in the reservoir is too high, this assumption is no longer valid and the fugacity coefficient must be taken into account.¹¹²

Based on Margules model for activity coefficients, when a liquid mixture is

involved, it is possible to determine the partial fugacity of each component (f_i) from the saturated vapour pressures (p_i^{sat}) of the components, the liquid phase activity coefficients (γ_i), and the experimental vapor-liquid equilibrium data, following the equation:¹²¹

$$f_i = \varphi_i^{sat} p_i^{sat} \gamma_i x_i e^{\left[\frac{V_i^{mol}(p-p_i^{sat})}{RT} \right]}, \quad (6)$$

where p_i^{sat} is the saturated vapour pressure of pure component i , φ_i^{sat} is the fugacity coefficient of pure component i in the gas phase at the saturated vapor pressure, γ_i is the activity coefficient in the liquid mixture, x_i is the mole fraction of component i in the mixture, and V_i^{mol} is the molar volume of pure component i in the liquid phase at pressure p and temperature T .

The adsorption isotherms are obtained by performing a series of GCMC simulations at increasing pressures. During these simulations, millions of steps are calculated in which random translation, rotation, insertion, reinsertion and deletion, and, in mixtures, identity change moves are tried and either accepted or rejected according to an acceptance rule based on Boltzmann weights. The output of these simulations is the total amount of molecules that are adsorbed in the system, averaged over the length of the simulation. This value corresponds to the absolute adsorption (n_{abs}) but, experimentally, only the excess adsorption (n_{exc}) is measured. The excess adsorption is the amount of molecules adsorbed and interacting with the solid. Thus, in order to compare simulated and experimental data, excess adsorption is obtained from absolute adsorption as follows:

$$n_{exc} = n_{abs} - V^g \rho^g, \quad (7)$$

where V^g is the pore volume of the adsorbent and ρ^g is the density of the adsorbate in the reservoir. The pore volume of the adsorbent can be obtained by measuring the adsorption of helium in the adsorbent, which can be done experimentally or by simulation.¹²²

Henry coefficients, energies, and entropies of adsorption

Henry coefficients (K_H) and heats of adsorptions (Q_{st}) are adsorption properties that provide information about how the adsorbed molecule interacts with the adsorbent. These properties are temperature-dependent and can only be obtained accurately in the low-coverage regime. These values are calculated applying the Widom test particle insertion method¹²³ during MC simulations in the canonical ensemble (NVT) where the number of molecules (N), the volume (V), and the temperature (T) are fixed. This method inserts a “ghost” molecule in the system to compute its energy and Rosenbluth factor and deletes it afterwards. This way, the Rosenbluth factor and the energy of a molecule can be sampled in the whole system without affecting it.

Henry coefficients (K_H) and the excess free energy (F) are related and both can be obtained from the Rosenbluth factor according to the expressions:

$$K_H = \frac{1}{RT\rho} \frac{\langle W \rangle}{\langle W^{IG} \rangle}, \quad (8)$$

$$F = -RT \ln \frac{\langle W \rangle}{\langle W^{IG} \rangle}, \quad (9)$$

where R is the ideal gas constant, T is the temperature of the system, ρ is the density of the adsorbent, $\langle W \rangle$ is the average Rosenbluth factor of a single molecule in the system and $\langle W^{IG} \rangle$ is the average Rosenbluth factor of the molecule in the ideal gas.¹¹²

The isosteric heat of adsorption (Q_{st}) is calculated from the average energies sampled in the system based on the following:

$$Q_{st} = \Delta U - RT = (\langle U_{hg} \rangle - \langle U_h \rangle - \langle U_g \rangle) - (RT), \quad (10)$$

where $\langle U_{hg} \rangle$ is the average potential energy of the host-guest system, $\langle U_h \rangle$ is the average potential energy of the host, and $\langle U_g \rangle$ is the potential energy of an isolated single molecule. Finally, it is possible to calculate the entropy (ΔS) with the following equation:

$$\Delta F = \Delta U - T\Delta S \quad (11)$$

In order to obtain all average adsorption energies and properties detailed previously, two independent MC simulations in the canonical ensemble using the Widom test particle insertion method are required. Firstly, a fast simulation is performed to obtain the average energy for an isolated molecule in the reservoir. Afterwards, a long simulation is run to obtain the average energies of a single molecule interacting with the adsorbent.

2.2. Molecular Dynamics

Molecular dynamics is a deterministic method that allows studying the evolution over time of the properties of the system by predicting the evolution of the system itself. For this, MD simulations generate successive configurations that vary over time. The position, velocity, and acceleration of atoms are described through the trajectories, which are obtained by integration of Newton’s laws of motion. The velocity-Verlet algorithm¹²⁴⁻¹²⁵ is the most common method to integrate the equations of motion:

$$r(t + \Delta t) = r(t) + v(t)\Delta t + \frac{f(t)}{2m}\Delta t^2, \quad (12)$$

$$v(t + \Delta t) = v(t) + \frac{f(t)+f(t+\Delta t)}{2m}\Delta t, \quad (13)$$

where $r(t)$, $v(t)$, and $f(t)$ are the position, velocity, and force vectors at time t , respectively; Δt is the time step and m is the mass of the particle.

The MD simulations start from an initial configuration with positions and velocities known for all particles, for which forces are calculated. For the next configuration, new velocities are calculated from the obtained forces and, for these velocities fixed during one time step, new positions are calculated. This cycle is repeated to generate successive configurations and thus, we obtain the trajectories for the particles in the system.

We use MD simulations to calculate self-diffusion coefficients (D_s). Thus, diffusive motion of a single particle is measured from the computed mean squared displacement at long times:

$$D_s^\alpha = \frac{1}{2N} \lim_{t \rightarrow \infty} \frac{d}{dt} \langle \sum_{i=1}^N (r_{i\alpha}(t) - r_{i\alpha}(t_0))^2 \rangle, \quad (14)$$

$$D_s = \frac{D_s^x + D_s^y + D_s^z}{3}, \quad (15)$$

where N is the number of molecules, t is the time and $r_{i\alpha}$ is the α -component of the position of particle i , α being x , y , or z . The diffusion coefficients in the x -, y -, and z -directions (D_s^x , D_s^y , D_s^z) are averaged to obtain the self-diffusion coefficient (D_s).

MD technique can also be used to compute infrared spectra.¹²⁶ For this, the dipole moment of the system is calculated as a function of time ($\mu(t)$) from the computed trajectories of the atoms. Eventually, the infrared spectra are calculated by the Fast

Fourier Transform (FFT) of the total dipole correlation function.

It is also possible to combine MC and MD methods. First of all, to achieve a sensible initial configuration of MD simulations we perform a short NVT MC simulation after which we start collecting data. To study the structural flexibility of a framework upon the guest-adsorption process we use a hybrid grand canonical Monte Carlo algorithm (hybrid MCMD),¹²⁷⁻¹²⁹ which is a MC-move that inserts a short MD simulation in the microcanonical ensemble (NVE), defining the system through the number of molecules (N), volume (V), and energy (E) of the system during this short MD simulation. Thus, during GCMC simulations the hybrid MCMD move can be chosen with a defined probability and performs a given number of independent NVE MD simulations with a defined number of steps, one of which is eventually accepted based on the minimum difference of energy within a margin of tolerance.

3. Force fields and models

Molecular simulations use models to describe molecules and structures, and force fields to define the interactions that take place in the system.

3.1. Force fields

The interactions inside a system are reproduced by a set of functions and parameters that we call force field. There are many generic force fields such as Universal Force Field¹³⁰ (UFF) or Dreiding,¹³¹ which provide parameters for a broad range of atoms in the periodic table. There are many other force fields that are transferable and their parameters are fitted to reproduce a specific property of a certain group of atoms, a certain functional group, a specific

molecule, or molecules of a given nature. Thus, force fields like AMBER,¹³² CHARMM,¹³³⁻¹³⁴ GROMOS,¹³⁵ and CVFF¹³⁶ are parametrized for proteins and functional groups of all amino acids, and their parameters can be used to model similar molecules. OPLS¹³⁷⁻¹³⁸ is parametrized for proteins and organic molecules, COMPASS¹³⁹⁻¹⁴¹ for certain functional groups, and TraPPE¹⁴²⁻¹⁴⁴ to reproduce vapor-liquid coexistence curves of small organic molecules. Similarly, there are also force fields that are fitted specifically to reproduce the dynamics of zeolite frameworks, such as those of Nicholas,¹⁴⁵ Demontis,¹⁴⁶ or Hill-Sauer.¹⁴⁷ The decision of how to model a system and which force field must be used is made based on the nature of the molecule or group of atoms that we want to simulate and the property we are interested in. The specific values of the parameters used in this work are described in the following chapters. In this section, the most common functional forms that define the interactions in the system are explained.

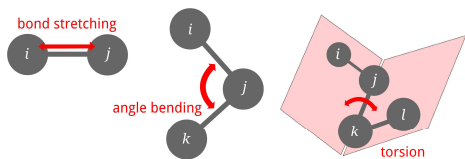


Figure 6. Schematic representation of the interatomic bonded interactions: bond stretching, angle bending, and torsion.

The total energy of the system (U^{total}) is obtained from the interaction of bonded atoms (U^{bonded}) and nonbonded atoms ($U^{\text{nonbonded}}$).

$$U^{\text{total}} = U^{\text{bonded}} + U^{\text{nonbonded}} \quad (16)$$

The energy part due to the interaction of bonded atoms (U^{bonded}) covers, as shown in

Figure 6, the energy of two bonding atoms (U^{bond}), the angle bending of three linked atoms (U^{bend}), and the torsion of four consecutive atoms (U^{torsion}).

$$U^{\text{bonded}} = U^{\text{bond}} + U^{\text{bend}} + U^{\text{torsion}} \quad (17)$$

The bond energy (U^{bond}) is associated to the interaction of two bonded atoms. It may be defined by different functional forms but the most commonly used is the harmonic potential, which considers the interatomic distance.

$$U^{\text{bond}}(r_{ij}) = \frac{1}{2}k(r_{ij} - r_{eq})^2, \quad (18)$$

where k is the force constant, r_{ij} is the interatomic distance ($r_{ij} = r_j - r_i$) and r_{eq} is the equilibrium bond length.

To define the bend energy (U^{bend}), which is related to the angle bending of three neighboring atoms, many functional forms can be used as well. Similar to the bond energy, the harmonic potential is widely used and is one of the simplest forms, since it takes into account the angle that the three linked atoms form at equilibrium:

$$U^{\text{bend}}(\theta_{ijk}) = \frac{1}{2}k(\theta_{ijk} - \theta_{eq})^2, \quad (19)$$

where k is the force constant, θ_{ijk} is the angle defined by the linked atoms ijk , and θ_{eq} is the angle at equilibrium.

The torsion term (U^{torsion}) is related to the interaction energy of four consecutively bonded atoms and the functional form is commonly expressed as a function of the dihedral angle (φ_{ijkl}):

$$U^{\text{torsion}}(\varphi_{ijkl}) = K_0 + K_1[1 + \cos(\varphi_{ijkl})] + K_2[1 - \cos(2\varphi_{ijkl})] + K_3[1 + \cos(3\varphi_{ijkl})], \quad (20)$$

where K_0 , K_1 , K_2 , and K_3 are fitted parameters.

The nonbonded energy ($U^{\text{nonbonded}}$) of Equation (21) accounts for the interaction between atoms of different molecules, between atoms of sorbate molecules and adsorbents, and between connected atoms that are separated by, at least, three bonds. It is defined by a combination of van der Waals interactions (U^{vdW}) and electrostatic interactions ($U^{\text{electrostatics}}$).

$$U^{\text{nonbonded}} = U^{\text{vdW}} + U^{\text{electrostatics}} \quad (21)$$

The van der Waals interactions (U^{vdW}) describe short-range interactions through the Lennard-Jones (LJ) potential, which depends on the distance of the two atoms involved.

$$U^{\text{vdW}}(r_{ij}) = U^{\text{LJ}}(r_{ij}) = 4\varepsilon \left[\left(\frac{\sigma}{r_{ij}} \right)^{12} - \left(\frac{\sigma}{r_{ij}} \right)^6 \right], \quad (22)$$

where r_{ij} is the distance between particles i and j , σ is the interatomic distance at which the attractive and dispersive forces are balanced so that $U^{\text{vdW}} = 0$, and ε corresponds to the energy minimum at distance r_{min} , which is $2^{1/6}\sigma$. These LJ parameters are normally defined for the interaction of two atoms of the same type. The cross terms to define the LJ potential for unlike atom types α and β are calculated with combining rules, such as Lorentz-Berthelot,¹⁴⁸ which are used in this work. Other combining rules may be used according to the specifications of the particular force field.

$$\sigma_{\alpha\beta} = \frac{\sigma_{\alpha\alpha} + \sigma_{\beta\beta}}{2}; \quad \varepsilon_{\alpha\beta} = \sqrt{\varepsilon_{\alpha\alpha} \cdot \varepsilon_{\beta\beta}} \quad (23)$$

Finally, the electrostatic interactions ($U^{\text{electrostatics}}$), which describe the long-

range interactions, are calculated according to Coulomb's law:

$$U^{\text{electrostatic}}(r_{ij}) = U^{\text{Coulomb}}(r_{ij}) = \frac{q_i q_j}{4\pi\varepsilon_0\varepsilon_r r_{ij}}, \quad (24)$$

where q_i and q_j are the atomic charges of atoms i and j , ε_0 is the electric constant of the vacuum, ε_r is the relative dielectric constant of the medium, and r_{ij} is the distance between atoms.

In computational terms, calculating the total energy of the system through the direct sum of the pair energies would be unfeasible because there are an infinite number of terms, and the long range nature of nonbonded interactions could lead to convergence problems. To avoid these issues a cutoff is set at 12 Å, after which LJ potentials are shifted to zero so that longer interactions than the cutoff are omitted from calculations. Regarding the electrostatic energy, it is calculated through the Ewald summation method¹⁴⁹ in the infinitely replicated system.

3.2. Models for adsorbents

The first part of this work is focused on MOFs. The weak nature of the metal-linker bond generally confers a certain degree of flexibility to these materials, which can cause large structural changes in the framework.⁸⁵ However, accounting computationally for this flexibility relies on the availability of accurate information on the specific flexible behavior of a given framework and the consequent development of a force field to reproduce this behavior. In addition, the complexity of these force fields increases dramatically the computational costs. Specifically, all but one MOF structure used in this work are considered rigid in the literature, and for the only one whose flexibility is recognized, no

specific force field was available. For this latter case, the most representative framework was chosen and modeled as undeformable. In this way, computational times could be held manageable. Moreover, given the large variability of chemical composition of these materials, there is a lack of specific force fields to model the host-guest interaction. Then, the studied MOF structures are modeled through generic force fields: UFF¹³⁰ and DREIDING,¹³¹ as is explained in the relevant chapter. In the simulations performed to develop this work, atomic positions were obtained from experimental data and fixed in the simulation box. LJ parameters and partial charges are assigned to each atom. Since the models for these frameworks are rigid, bonded and nonbonded host-host energies are zero, and only host-guest nonbonded interactions are considered by the use of Lorentz-Berthelot combining rules for van der Waals interactions and Ewald summations for electrostatic interactions.

In the second part of this work, we use zeolites. Pure silica zeolites are built of TO₄ tetrahedra, where T stands for silicon atoms, but can be substituted in some zeolites by germanium or aluminum atoms. In this work, only all-silica and germanosilicate frameworks are studied. The homogeneity in their composition and the structure of their primary building units facilitate the development of transferable force fields for these materials. Zeolites are typically acknowledged as rigid, given that the flexibility is generally reduced to atom vibration and does not affect their crystalline regularity. Thus, limited flexible behavior is well reported in zeolites and transferable force fields accounting for zeolite lattice vibrations were developed. As opposing to the case of MOFs, there are several force fields available to model

zeolites as flexible. These force fields provide interatomic potentials to calculate the bonded and nonbonded energies for the host. Although the interatomic potentials are derived from those shown in the previous section, they normally involve more constraints and/or terms. As an example, the Urey-Bradley harmonic potential expresses the energy as a function of the T-T distance, in order to couple bond stretching and bending. The bond-bond cross potential incorporates the distances of adjacent connected atoms to the bond energy of a single pair, and torsion potentials are smoothed to avoid discontinuities in the potential. In the present work, zeolites are modeled as flexible with the force fields of Nicholas,¹⁴⁵ Demontis,¹⁵⁰ and Hill-Sauer,¹⁴⁷ which develop different functional forms and parameters that are transferable among all-silica zeolites. Then, the starting configuration of the zeolite framework is taken from reported crystallographic information, but the atomic positions are not fixed in the simulation box. Each atom has a charge and LJ parameters assigned and the van der Waals interactions are calculated through combining rules defined for each force field. The host-guest nonbonded interactions are usually defined for zeolites and accurately fitted to experimental data, but these interactions are not established for the sorbate molecules under study. To overcome this issue TraPPE-zeo force field¹⁵¹ is used. This is a transferable force field recently parametrized for zeolites. This force field provides LJ parameters and charges for oxygen and silicon atoms that allow for the calculation of nonbonded host-guest energies as it is calculated for the rigid model of MOFs. Zeolites are also modeled as rigid in Chapter 6 by using the same approach than for MOFs.

3.3. Models for adsorbates

Adsorbates are defined through classical models. When it comes to the modeling of adsorbates there are different approaches regarding how bonded interactions are defined.

- Rigid/flexible. It is possible to define a molecule as rigid by fixing the position of the atoms relative to each other. This way, the model lacks of internal energy ($U_g = 0$) and the molecule is inserted or deleted at once in the simulation box. Another option is modeling the molecule as flexible by defining bond lengths, angles, torsions, and their functional forms. This model has internal energy and the molecule can be inserted bead by bead in the simulation box. Either definition might be used depending on the molecule under study and the requirements of the property we want to compute.
- Full-atom/united-atom. It is possible to define a molecule using full-atom, also known as all-atom models, by considering the interaction parameters for all the atoms involved. Another option is modeling the molecule by grouping the atoms in a single interaction center. These are pseudoatom models. This way, the interactions are easier to compute and, in most cases, this model leads to the same results. However, as in the previous case, choosing one definition or another depends on the molecule under study and the property we want to simulate.

In this thesis, we focus on structural and chiral isomers with known chemical and/or pharmaceutical relevance. The molecules studied and the model chosen are detailed below.

Ibuprofen. This compound belongs to the group of nonsteroidal anti-inflammatory drugs (NSAID) and is usually administered as a racemate, though several studies indicate that the therapeutic effect of the *S* enantiomer sets in faster than that of its counterpart and could be administered in a reduced dose. To perform a study on the enantioselective adsorption of this compound in MOFs, we need to establish a clear difference between each enantiomer based on their asymmetric carbon. Therefore, each enantiomer is defined as a flexible full-atom model to account for its chirality. Parameters for bonded and nonbonded interactions are taken from CVFF force field.¹³⁶

Lysine. Apart from the structural functions that this amino acid develops in the body, ibuprofen and lysine are often formulated together. This compound is also studied together with ibuprofen as a chiral probe to test the enantioselective capacity of MOFs. As in the case of ibuprofen, the model needs to lead to a three-dimensional difference between L- and D-enantiomers of lysine. Thus, a flexible full-atom model was chosen, taking parameters for bonded and nonbonded interactions from CVFF force field.¹³⁶

Water. In this work, water was necessary as a solvent for ibuprofen and lysine. Many models are reported in the literature,¹⁵²⁻¹⁵⁹ each one parametrized to reproduce a particular property of water. The model chosen is TIP5Pew,¹⁶⁰ since it reproduces properties of water in the bulk and is parametrized to use the Ewald summation method.

Amyl alcohols (C₅H₁₂O). This group of molecules is composed by eight alcoholic structural isomers of pentanol: 1-pentanol (1P), 2-pentanol (2P), 3-pentanol (3P), 2-

methylbutanol (2MB), 3-methylbutanol (3MB), 2-methyl-2-butanol (2M2B), 3-methyl-2-butanol (3M2B), and 2,2-dimethylpropanol (22DMP). They are commonly used as organic solvents but they are also used as intermediates for the production of herbicides and pharmaceuticals. These molecules are described by flexible united-atom models, where each CH_x group is defined as one pseudoatom, and for the hydroxyl group oxygen and hydrogen are considered separately. LJ parameters and charges are assigned to each interaction center based on TraPPE force field,^{144,161} as well as their bonded interactions. Molecules 2P, 2MB, and 3M2B are also chiral isomers. To describe properly their asymmetric carbon a full-atom approach must be used. For this purpose, these particular compounds are modeled based on OPLS force field¹³⁷ when the chirality of these molecules is taken into account.

Hydrocarbons of six carbon atoms (C_6H_{14}). Five structural isomers of n-hexane have been studied to compare to their alcohol analogues, the amyl alcohols, given their similar shape and molecular volume, and to tease out the effect of shape from those of polarity and hydrogen bonding. The hydrocarbons considered are n-hexane (nC6), 2-methylpentane (2MP), 3-methylpentane (3MP), 2,3-dimethylbutane (23DMB), and 2,2-dimethylbutane (22DMB). Similar to alcohols, these hydrocarbons are defined as flexible united-atom models, with each CH_x group defined as a pseudoatom. LJ parameters and bonded interactions are taken from TraPPE force field.¹⁶²

4. Context and outline of the thesis

The suitability of nanoporous materials for molecular sieving is known and well

reported. Besides this, molecular simulation techniques are useful to predict the sieving capacity of real or hypothetical materials and provide a microscopic view of the separation process, among other properties. This helps to understand the underlying molecular mechanisms of such processes and connect them with particular features of the materials. In a broader context, this would be helpful in the selection of a given structure for a specific purpose.

This thesis focuses on the separation of structural and chiral isomers through adsorption processes in nanoporous materials. Structural isomers, also known as constitutional isomers, are compounds that share the same molecular formula but have different connectivity. Amyl alcohols are treated in this work due to their relevance in the chemical and pharmaceutical industries. These isomers show very similar physicochemical properties which make difficult and costly their separation. In the case of chiral isomers, or enantiomers, this difficulty goes further. They are compounds with identical formula and similar connectivity, being each enantiomer the mirror image of the other. Unlike structural isomers, they share identical physicochemical properties. The particular applications that a pair of enantiomers performs in pharmaceutical, agrochemical, and food industries, is different according to its chirality. Still, the synthesis of enantiopure compounds is costly and, therefore, they are commonly synthesized as racemates, i.e., as a mixture of both enantiomers.

We used molecular simulations to perform adsorption and diffusion processes in MOFs and zeolites. We were interested in studying the adsorption selectivity of these materials when sieving mixtures of structural and chiral isomers. Our aim was not only to

evaluate the suitability of the materials to perform this task but also to understand their specific behaviors. Then, we tried to get a deep insight into the process by explaining the microassembly of molecules inside the structure, which is governed by intermolecular interactions, and describing the adsorbate-adsorbent interactions. Since many materials are known to show some kind of flexibility, we were also curious about how important the effect of lattice vibration is on the adsorbate-adsorbent interactions and its influence on selectivity. This computational study has been accomplished by using the methods described in this chapter and the specific techniques and force fields explained and defined in the chapter in which each issue is tackled.

Separation of chiral isomers in metal-organic frameworks (Chapter 2 and 4)

In Chapter 2 we study the enantioselective adsorption of the bioactive compounds ibuprofen and lysine in the homochiral metal-organic framework HMOF-1, also known as Cd-BINOL, and the nonchiral MOFs (MIL-47 and MIL-53). Molecular simulations were performed to obtain the adsorption of the enantiomers of ibuprofen and those of lysine from mixtures at different molar fractions. The microassembly of molecules promoted by hydrogen bonding were analyzed and connected with the specific enantioselectivity of each MOF. Likewise, the confinement of each enantiomer in the structure is understood as a key condition for this enantioselectivity in such a way that it is present even in nonchiral frameworks and might change the expected selectivity in chiral frameworks.

In Chapter 4, three chiral alcohols of the group of amyl alcohols (2P, 2MB, and

3M2B) were used as chiral probes in order to test the enantioselective adsorption of HMOF-1. In this case, the study was limited to the description of the enantiomeric excess of each compound adsorbed from a racemic mixture. These results were analyzed and explained in relation with the different areas in the channel system of HMOF-1, its surface chemistry, and the different degree of confinement.

Separation of structural isomers in metal-organic frameworks (Chapter 3 and 4)

In Chapter 3 we study the selective adsorption of the amyl alcohols, which are structural isomers of pentanol, in ZIF-77. We wanted to establish a relation between the structural features of each isomer and the particular topology of the two-dimensional channel system of this framework, built by two interconnected channels of different sizes. To this aim, we performed molecular simulations to obtain the adsorption isotherms of each compound and in mixtures of several isomers. We also studied the diffusive behavior of each compound in the structure, and compared them to the diffusive behavior of their alkane analogues. This helped us to relate the size of the molecule with the pore size of the framework and the relevance of the surface chemistry in the separation process when a particular functional group, such as hydroxyl, is involved. Finally, we established different groups of molecules according to their structural features and explained the structural selectivity of ZIF-77 towards them.

Once the structural selectivity was understood in ZIF-77 we extended the study to a more complex framework: Cd-BINOL, aforementioned as HMOF-1. This MOF shows a three-dimensional channel system, with a very intricate geometry composed by

a wide helicoidal channel and narrow zigzag pores connecting the former. In addition, the chemistry of its surface was also different. Although an analogous computational work was carried out, we also performed a deep analysis on the positive or negative contribution of adsorbate-adsorbate and adsorbate-structure interactions to the structural selectivity and hydrogen-bonding patterns. This also constituted an opportunity to test and explain the performance of ideal adsorbed solution theory¹⁶³ (IAST) and the ratio of Henry coefficients as alternative prediction methods.

Evaluation of different force fields to model flexibility in zeolites (Chapter 5)

As mentioned in previous sections, the inherent but limited flexibility of zeolites has been extensively reported so that many transferable force fields have been developed. In this chapter we wanted to evaluate three popular flexible force fields (Nicholas, Demontis, and Hill-Sauer) through their ability to reproduce the experimental infrared (IR) spectra of several all-silica zeolites. These zeolites, some of which are hypothetical siliceous frameworks, were selected as representative members of different topologies: SOD, RHO, LTA, and FAU; and FER, TON, MOR, and MFI. We also wanted to examine the sensitivity of the IR spectra to the details of the structure under study. Then, this work is based on the comparison of experimental IR spectra and those obtained computationally with each of the aforementioned force fields. To improve the objectivity of this comparison, an equation for a similarity index was developed and used, and it was then possible to evaluate the performance of each force field in a quantitative way.

Separation of structural and chiral isomers in zeolites (Chapter 6)

In this chapter, we analyze the influence of flexibility on the separation of chiral and structural isomers in the STW-type zeolite. The chosen probes were 2P, 2MB and 3M2B, which are chiral compounds and structural isomers between them. The adsorbents, the all-silica and germanosilicate frameworks of STW zeolite, were chosen due to their particular helicoidal channel. Different issues were addressed. Firstly, the structural and chiral selectivity of both STW frameworks were computationally studied and explained by modeling these frameworks as rigid. Secondly, analogous simulations were performed while modeling the adsorbents as flexible, i.e., allowing frameworks to vibrate during the adsorption process. Results obtained from the different approaches were compared and their differences were described and understood. Finally, concepts which were previously studied, such as confinement and preferential adsorption, and their connection with structural and chiral selectivity were explained in detail.

Bibliography

- (1) Mintova, S.; Jaber, M.; Valtchev, V., *Chem. Soc. Rev.* **2015**, *40*, 7207-7233.
- (2) Furukawa, H.; Cordova, K. E.; O'Keeffe, M.; Yaghi, O. M., *Science* **2013**, *341* (6149), 974-+.
- (3) DeCoste, J. B.; Peterson, G. W., *Chem. Rev.* **2014**, *114* (11), 5695-5727.
- (4) Davis, M. E., *Nature* **2002**, *417* (6891), 813-821.
- (5) Jiang, J.; Babarao, R.; Hu, Z., *Chem. Soc. Rev.* **2011**, *40* (7), 3599-3612.
- (6) Lin, Z. E.; Zhang, J.; Yang, G. Y., *Inorg. Chem.* **2003**, *42* (6), 1797-1799.
- (7) Baerlocher, C.; McCusker, L. B., Database of Zeolites Structures: <http://www.iza-structure.org/databases>.

- (8) Reut, S.; Prakash, A., *Fuel Process. Technol.* **2006**, *87*(3), 217-222.
- (9) Hedström, A., *J. Environ. Eng.* **2001**, *127*(8), 673-681.
- (10) Corma, A., *J. Catal.* **2003**, *216* (1-2), 298-312.
- (11) Martínez, C.; Corma, A., *Coord. Chem. Rev.* **2011**, *255*(13-14), 1558-1580.
- (12) Yeung, K. L.; Han, W., *Catal. Today* **2014**, *236*(PART B), 182-205.
- (13) Davis, M. E.; Lobo, R. F., *Chem. Mater.* **1992**, *4*(4), 756-768.
- (14) Li, J.; Corma, A.; Yu, J., *Chem. Soc. Rev.* **2015**, *44*, 7112-7127.
- (15) Sartbaeva, A.; Wells, S. A.; Treacy, M. M. J.; Thorpe, M. F., *Nat. Mater.* **2006**, *5*(12), 962-965.
- (16) Zimmermann, N. E. R.; Jakobtorweihen, S.; Beerdsen, E.; Smit, B.; Keil, F. J., *J. Phys. Chem. C* **2007**, *111*(46), 17370-17381.
- (17) Iwamoto, M.; Yahiro, H.; Tanda, K.; Mizuno, N.; Mine, Y.; Kagawa, S., *J. Phys. Chem.* **1991**, *95*(9), 3727-3730.
- (18) Kesraoui-Ouki, S.; Cheeseman, C. R.; Perry, R., *J. Chem. Technol. Biotechnol.* **1994**, *59*(2), 121-126.
- (19) Borai, E. H.; Harjula, R.; Malinen, L.; Paajanen, A., *J. Hazard. Mater.* **2009**, *172*(1), 416-422.
- (20) Chambellan, A.; Chevreau, T.; Khabtou, S.; Marzin, M.; Lavalley, J. C., *Zeolites* **1992**, *12*(3), 306-314.
- (21) Aguado, S.; Polo, A. C.; Bernal, M. P.; Coronas, J.; Santamaria, J., *J. Membr. Sci.* **2004**, *240*(1-2), 159-166.
- (22) Rubio, M. C.; Martinez, G.; Baena, L.; Moreno, F., *J. Cleaner Prod.* **2012**, *24*, 76-84.
- (23) Long, J. R.; Yaghi, O. M., *Chem. Soc. Rev.* **2009**, *38*, 1213-1214.
- (24) Férey, G., *Chem. Soc. Rev.* **2008**, *37*(1), 191-214.
- (25) James, S. L., *Chem. Soc. Rev.* **2003**, *32*, 276-288.
- (26) Meek, S. T.; Greathouse, J. A.; Allendorf, M. D., *Adv. Mater.* **2011**, *23*(2), 249-267.
- (27) Dybtsev, D. N.; Chun, H.; Yoon, S. H.; Kim, D.; Kim, K., *J. Am. Chem. Soc.* **2004**, *126*(1), 32-33.
- (28) Fletcher, A. J.; Cussen, E. J.; Bradshaw, D.; Rosseinsky, M. J.; Thomas, K. M., *J. Am. Chem. Soc.* **2004**, *126*(31), 9750-9759.
- (29) Bourrelly, S.; Llewellyn, P. L.; Serre, C.; Millange, F.; Loiseau, T.; Férey, G., *J. Am. Chem. Soc.* **2005**, *127*(39), 13519-13521.
- (30) Millward, A. R.; Yaghi, O. M., *J. Am. Chem. Soc.* **2005**, *127*(51), 17998-17999.
- (31) Ma, L.; Abney, C.; Lin, W., *Chem. Soc. Rev.* **2009**, *38*(5), 1248-1256.
- (32) Kondo, M.; Shimamura, M.; Noro, S. I.; Minakoshi, S.; Asami, A.; Seki, K.; Kitagawa, S., *Chem. Mater.* **2000**, *12*(5), 1288-1299.
- (33) Eddaoudi, M.; Kim, J.; Rosi, N.; Vodak, D. T.; Wachter, J.; O'Keeffe, M.; Yaghi, O. M., *Science* **2002**, *295*, 469-472.
- (34) Li, H.; Eddaoudi, M.; O'Keeffe, M.; Yaghi, O. M., *Nature* **1999**, *402*(November), 276-279.
- (35) Zhang, Q.; Shreeve, J. N. M., *Angew. Chem., Int. Ed.* **2014**, *53*(10), 2540-2542.
- (36) Pan, L.; Adams, K. M.; Hernandez, H. E.; Wang, X.; Zheng, C.; Hattori, Y.; Kaneko, K., *J. Am. Chem. Soc.* **2003**, *125*(10), 3062-3067.
- (37) Vishnyakov, A.; Ravikovitch, P. I.; Neimark, A. V.; Bulow, M.; Wang, Q. M., *Nano Lett.* **2003**, *3*(6), 713-718.
- (38) Banerjee, R.; Phan, A.; Wang, B.; Knobler, C.; Furukawa, H.; O'Keeffe, M.; Yaghi, O. M., *Science* **2008**, *319*, 939-943.
- (39) Zheng, L.-L.; Li, H.-X.; Leng, J.-D.; Wang, J.; Tong, M.-L., *Eur. J. Inorg. Chem.* **2008**, *3*(2), 213-217.
- (40) Wang, Y. L.; Zhang, N.; Liu, Q. Y.; Shan, Z. M.; Cao, R.; Wang, M. S.; Luo, J. J.; Yang, E. L., *Cryst. Growth Des.* **2011**, *11*(1), 130-138.
- (41) Matlock, M. M.; Howerton, B. S.; Henke, K. R.; Atwood, D. A., *J. Hazard. Mater.* **2001**, *82*(1), 55-63.
- (42) Kitagawa, S.; Kitaura, R.; Noro, S.-i., *Angew. Chem., Int. Ed.* **2004**, *43*(18), 2334-2375.
- (43) Yaghi, O. M.; O'Keeffe, M.; Ockwig, N. W.; Chae, H. K.; Eddaoudi, M.; Kim, J., *Nature* **2003**, *423*(6941), 705-714.
- (44) Rowsell, J. L. C.; Yaghi, O. M., *Microporous Mesoporous Mater.* **2004**, *73*(1-2), 3-14.
- (45) Rowsell, J. L. C.; Yaghi, O. M., *Angew. Chem., Int. Ed.* **2005**, *44*(30), 4670-4679.

- (46) Panella, B.; Hirscher, M., *Adv. Mater.* **2005**, *17*(5), 538-541.
- (47) Maspoch, D.; Ruiz-Molina, D.; Wurst, K.; Domingo, N.; Cavallini, M.; Biscarini, F.; Tejada, J.; Rovira, C.; Veciana, J., *Nat. Mater.* **2003**, *2*(3), 190-195.
- (48) Guillou, N.; Livage, C.; Drillon, M.; Férey, G., *Angew. Chem., Int. Ed.* **2003**, *42*(43), 5314-5317.
- (49) Holman, K. T.; Pivovar, A. M.; Swift, J. A.; Ward, M. D., *Acc. Chem. Res.* **2001**, *34*(2), 107-118.
- (50) Evans, O. R.; Lin, W., *Acc. Chem. Res.* **2002**, *35*(7), 511-522.
- (51) Zhao, X. B.; Xiao, B.; Fletcher, A. J.; Thomas, K. M.; Bradshaw, D.; Rosseinsky, M. J., *Science* **2004**, *306*(5698), 1012-1015.
- (52) Kesanli, B.; Cui, Y.; Smith, M. R.; Bittner, E. W.; Bockrath, B. C.; Lin, W., *Angew. Chem., Int. Ed.* **2005**, *44*(1), 72-75.
- (53) Thomas, K. M., *Dalton Trans.* **2009**, *0*, 1487-1505.
- (54) Sumida, K.; Rogow, D. L.; Mason, J. A.; McDonald, T. M.; Bloch, E. D.; Herm, Z. R.; Bae, T. H.; Long, J. R., *Chem. Rev.* **2012**, *112*(2), 724-781.
- (55) Chaemchuen, S.; Kabir, N. A.; Zhou, K.; Verpoort, F., *Chem. Soc. Rev.* **2013**, *42*(24), 9304-9332.
- (56) Li, Y.; Yang, R. T., *AIChE J.* **2008**, *54*(1), 269-279.
- (57) Snurr, R. Q.; Hupp, J. T.; Nguyen, S. B. T., *AIChE J.* **2004**, *50*(6), 1090-1095.
- (58) Lee, J. Y.; Olson, D. H.; Pan, L.; Emge, T. J.; Li, J., *Adv. Funct. Mater.* **2007**, *17*(8), 1255-1262.
- (59) Keskin, S.; Sholl, D. S., *J. Phys. Chem. C* **2007**, *111*(38), 14055-14059.
- (60) Van de Voorde, B.; Bueken, B.; Denayer, J.; De Vos, D., *Chem. Soc. Rev.* **2014**, *43*(16), 5766-5788.
- (61) Qiu, S.; Xue, M.; Zhu, G., *Chem. Soc. Rev.* **2014**, *43*(16), 6116-6140.
- (62) Horcajada, P.; Serre, C.; Vallet-Regi, M.; Sebban, M.; Taulelle, F.; Férey, G., *Angew. Chem., Int. Ed.* **2006**, *45*(36), 5974-5978.
- (63) Horcajada, P.; Serre, C.; Maurin, G.; Ramsahye, N. A.; Balas, F.; Vallet-Regi, M.; Sebban, M.; Taulelle, F.; Férey, G., *J. Am. Chem. Soc.* **2008**, *130*(21), 6774-6780.
- (64) McKinlay, A. C.; Morris, R. E.; Horcajada, P.; Férey, G.; Gref, R.; Couvreur, P.; Serre, C., *Angew. Chem., Int. Ed.* **2010**, *49*(36), 6260-6266.
- (65) Horcajada, P.; Chalati, T.; Serre, C.; Gillet, B.; Sebrie, C.; Baati, T.; Eubank, J. F.; Heurtaux, D.; Clayette, P.; Kreuz, C.; Chang, J.-S.; Hwang, Y. K.; Marsaud, V.; Bories, P.-N.; Cynober, L.; Gil, S.; Férey, G.; Couvreur, P.; Gref, R., *Nat. Mater.* **2010**, *9*(2), 172-178.
- (66) Keskin, S.; Kizilel, S., *Ind. Eng. Chem. Res.* **2011**, *50*(4), 1799-1812.
- (67) Bernini, M. C.; Fairen-Jimenez, D.; Pasinetti, M.; Ramirez-Pastor, A. J.; Snurr, R. Q., *J. Mater. Chem. B* **2014**, *2*(7), 766-774.
- (68) Seo, J. S.; Whang, D.; Lee, H.; Jun, S. I.; Oh, J.; Jeon, Y. J.; Kim, K., *Nature* **2000**, *404*, 982-986.
- (69) Wang, C.-C.; Li, J.-R.; Lv, X.-L.; Zhang, Y.-Q.; Guo, G., *Energy Environ. Sci.* **2014**, *7*(9), 2831-2867.
- (70) Zhang, T.; Lin, W., *Chem. Soc. Rev.* **2014**, *43*(16), 5982-5993.
- (71) Zhao, M.; Ou, S.; Wu, C. D., *Acc. Chem. Res.* **2014**, *47*(4), 1199-1207.
- (72) Leus, K.; Liu, Y. Y.; Van Der Voort, P., *Catal. Rev.: Sci. Eng.* **2014**, *56*(1), 1-56.
- (73) Harbuzaru, B. V.; Corma, A.; Rey, F.; Atienzar, P.; Jordá, J. L.; García, H.; Ananias, D.; Carlos, L. D.; Rocha, J., *Angew. Chem., Int. Ed.* **2008**, *47*(6), 1080-1083.
- (74) Allendorf, M. D.; Stavila, V., *CrystEngComm* **2015**, *17*, 229-246.
- (75) Hu, Z.; Deibert, B. J.; Li, J., *Chem. Soc. Rev.* **2014**, *43*(16), 5815-5840.
- (76) Fletcher, A. J.; Thomas, K. M.; Rosseinsky, M. J., *J. Solid State Chem.* **2005**, *178*, 2491-2510.
- (77) Liang, L.-L.; Ren, S.-B.; Zhang, J.; Li, Y.-Z.; Du, H.-B.; You, X.-Z., *Cryst. Growth Des.* **2010**, *10*(3), 1307-1311.
- (78) Kurmoo, M., *Chem. Soc. Rev.* **2009**, *38*(5), 1353-1379.
- (79) Sun, D.; Ke, Y.; Collins, D. J.; Lorigan, G. A.; Zhou, H. C., *Inorg. Chem.* **2007**, *46*(7), 2725-2734.

- (80) Qiu, S.; Zhu, G., *Coord. Chem. Rev.* **2009**, *253*, 2891-2911.
- (81) Bureekaew, S.; Sato, H.; Matsuda, R.; Kubota, Y.; Hirose, R.; Kim, J.; Kato, K.; Takata, M.; Kitagawa, S., *Angew. Chem., Int. Ed.* **2010**, *49*(42), 7660-7664.
- (82) Khan, N. A.; Hasan, Z.; Jhung, S. H., *J. Hazard. Mater.* **2013**, *244-245*, 444-456.
- (83) Groom, C. R.; Bruno, I. J.; Lightfoot, M. P.; Ward, S. C., *Acta Crystallogr., Sect. B: Struct. Sci., Cryst. Eng. Mater.* **2016**, *72*, 171-179.
- (84) Wilmer, C. E.; Leaf, M.; Lee, C. Y.; Farha, O. K.; Hauser, B. G.; Hupp, J. T.; Snurr, R. Q., *Nat. Chem.* **2012**, *4*, 83-89.
- (85) Schneemann, A.; Bon, V.; Schwedler, I.; Senkovska, I.; Kaskel, S.; Fischer, R. A., *Chem. Soc. Rev.* **2014**, *43*(16), 6062-6096.
- (86) Serre, C.; Millange, F.; Thouvenot, C.; Noguès, M.; Marsolier, G.; Louër, D.; Férey, G., *J. Am. Chem. Soc.* **2002**, *124*(45), 13519-13526.
- (87) Barthelet, K.; Marrot, J.; Riou, D.; Férey, G., *Angew. Chem., Int. Ed.* **2002**, *41*(2), 281-284.
- (88) Loiseau, T.; Serre, C.; Huguenard, C.; Fink, G.; Taulelle, F.; Henry, M.; Bataille, T.; Férey, G., *Chem. - Eur. J.* **2004**, *10*(6), 1373-1382.
- (89) Millange, F.; Guillou, N.; Walton, R. I.; Grenèche, J.-M.; Margiolaki, I.; Férey, G., *Chem. Comm.* **2008**, (39), 4732-4734.
- (90) Grosch, J. S.; Paesani, F., *J. Am. Chem. Soc.* **2012**, *134*, 4207-4215.
- (91) Mellot-Draznieks, C.; Serre, C.; Surblé, S.; Audebrand, N.; Férey, G., *J. Am. Chem. Soc.* **2005**, *127*(46), 16273-16278.
- (92) Surblé, S.; Serre, C.; Mellot-Draznieks, C.; Millange, F.; Férey, G., *Chem. Comm.* **2006**, *0*, 284-286.
- (93) Serre, C.; Mellot-Draznieks, C.; Surblé, S.; Audebrand, N.; Filinchuk, Y.; Férey, G., *Science* **2007**, *315*(5820), 1828-1831.
- (94) Dubbeldam, D.; Walton, K. S.; Ellis, D. E.; Snurr, R. Q., *Angew. Chem., Int. Ed.* **2007**, *46*(24), 4496-4499.
- (95) Balestra, S. R. G.; Bueno-Perez, R.; Hamad, S.; Dubbeldam, D.; Ruiz-Salvador, A. R.; Calero, S., *Chem. Mater.* **2016**, *28*(22), 8296-8304.
- (96) Fairen-Jimenez, D.; Moggach, S. A.; Wharmby, M. T.; Wright, P. A.; Parsons, S.; Düren, T., *J. Am. Chem. Soc.* **2011**, *133*(23), 8900-8902.
- (97) Fairen-Jimenez, D.; Galvelis, R.; Torrisi, A.; Gellan, A. D.; Wharmby, M. T.; Wright, P. A.; Mellot-Draznieks, C.; Düren, T., *Dalton Trans.* **2012**, *41*(35), 10752-10762.
- (98) Maji, T. K.; Matsuda, R.; Kitagawa, S., *Nat. Mater.* **2007**, *6*(2), 142-148.
- (99) Tian, Y. Q.; Cai, C. X.; Ji, Y.; You, X. Z.; Peng, S. M.; Lee, G. H., *Angew. Chem., Int. Ed.* **2002**, *41*(8), 1384-1386.
- (100) Phan, A.; Doonan, C. J.; Uribe-Romo, F. J.; Knobler, C. B.; O'Keeffe, M.; Yaghi, O. M., *Acc. Chem. Res.* **2010**, *43*(1), 58-67.
- (101) Park, K. S.; Ni, Z.; Côté, A. P.; Choi, J. Y.; Huang, R.; Uribe-Romo, F. J.; Chae, H. K.; O'Keeffe, M.; Yaghi, O. M., *PNAS* **2006**, *103*(27), 10186-10191.
- (102) Tian, Y. Q.; Cai, C. X.; Ren, X. M.; Duan, C. Y.; Xu, Y.; Gao, S.; You, X. Z., *Chem. - Eur. J.* **2003**, *9*(22), 5673-5685.
- (103) Saint-Remi, J. C.; Remy, T.; Vanhunskerken, V.; Vandeperre, S.; Duerinck, T.; Maes, M.; Devos, D.; Gobechiya, E.; Kirschhock, C. E. A.; Baron, G. V.; Denayer, J. F. M., *ChemSusChem* **2011**, *4*(8), 1074-1077.
- (104) Seoane, B.; Zamaro, J. M.; Téllez, C.; Coronas, J., *RSC Adv.* **2011**, *1*(5), 917-917.
- (105) Bohme, U.; Barth, B.; Paula, C.; Kuhnt, A.; Schwieger, W.; Mundstock, A.; Caro, J.; Hartmann, M., *Langmuir* **2013**, *29*, 8592-8600.
- (106) Zhang, K.; Lively, R. P.; Dose, M. E.; Brown, A. J.; Zhang, C.; Chung, J.; Nair, S.; Koros, W. J.; Chance, R. R., *Chem. Comm.* **2013**, *49*(31), 3245-7.
- (107) Van Der Perre, S.; Van Assche, T.; Bozbiyik, B.; Lannoeye, J.; De Vos, D. E.; Baron, G. V.; Denayer, J. F. M., *Langmuir* **2014**, *30*(28), 8416-8424.
- (108) Baburin, I. A.; Leoni, S.; Seifert, G., *J. Phys. Chem. B* **2008**, *112*(31), 9437-9443.
- (109) Oar-Arteta, L.; Wezendonk, T.; Sun, X.; Kapteijn, F.; Gascon, J., *Mater. Chem. Front.* **2017**, *1*(9), 1709-1745.
- (110) Solomon, M. B.; Church, T. L.; D'Alessandro, D. M., *CrystEngComm* **2017**, *19*(29), 4049-4065.

- (111) Lismont, M.; Dreesen, L.; Wuttke, S., *Adv. Funct. Mater.* **2017**, *27*(14), 1606314.
- (112) Frenkel, D.; Smit, B., *Understanding Molecular Simulation. From Algorithms to Applications*. Second Edition ed.; Academic Press, Inc.: Orlando, FL, USA, 2002.
- (113) Metropolitan, N.; Rosenbluth, A. W.; Rosenbluth, M. N.; Teller, A. H.; Teller, E., *J. Chem. Phys.* **1953**, *21*(6), 1087-1092.
- (114) Smit, B.; Siepmann, J. I., *J. Phys. Chem.* **1994**, *98*(34), 8442-8452.
- (115) Rosenbluth, M. N.; Rosenbluth, A. W., *J. Chem. Phys.* **1955**, *23*(2), 356-359.
- (116) Shi, W.; Maginn, E. J., *J. Chem. Theory Comput.* **2007**, *3*(4), 1451-1463.
- (117) Torres-Knoop, A.; Balaji, S. P.; Vlugt, T. J. H.; Dubbeldam, D., *J. Chem. Theory Comput.* **2014**, *10*(3), 942-952.
- (118) Dubbeldam, D.; Calero, S.; Ellis, D. E.; Snurr, R. Q., *Mol. Simul.* **2016**, *42*(2), 81-101.
- (119) Van Erp, T. S.; Dubbeldam, D.; Caremans, T. P.; Calero, S.; Martens, J. A., *J. Phys. Chem. Lett.* **2010**, *1*(14), 2154-2158.
- (120) Marinari, E.; Parisi, G., *Europhysics Letters* **1992**, *19*(6), 451-258.
- (121) Smith, J. M.; Ness, H. C. V.; Abbott, M. M., *Introduction to Chemical Engineering Thermodynamics*. 7th ed.; McGraw-Hill Education: New York, U.S., 2004.
- (122) Talu, O.; Myers, A. L., *AIChE J.* **2001**, *47*(5), 1160-1168.
- (123) Widom, B., *J. Chem. Phys.* **1963**, *39*(11), 2808-2812.
- (124) Verlet, L., *Phys. Rev.* **1967**, *159*(1), 98-103.
- (125) Verlet, L., *Phys. Rev.* **1968**, *165*(1), 201-214.
- (126) Berens, P. H.; Wilson, K. R., *J. Chem. Phys.* **1981**, *74*(9), 4872-4882.
- (127) Faller, R.; de Pablo, J. J., *J. Chem. Phys.* **2002**, *116*(1), 55-59.
- (128) Ghoufi, A.; Subercaze, A.; Ma, Q.; Yot, P. G.; Ke, Y.; Puente-Orench, I.; Devic, T.; Guillermin, V.; Zhong, C.; Serre, C.; Ferey, G.; Maurin, G., *J. Phys. Chem. C* **2012**, *116*(24), 13289-13295.
- (129) Balestra, S. R. G.; Hamad, S.; Ruiz-Salvador, A. R.; Domínguez-García, V.; Merkling, P. J.; Dubbeldam, D.; Calero, S., *Chem. Mater.* **2015**, *27*(16), 5657-5667.
- (130) Rappe, A. K.; Casewit, C. J.; Colwell, K. S.; Goddard, W. A.; Skiff, W. M., *J. Am. Chem. Soc.* **1992**, *114*(25), 10024-10035.
- (131) Mayo, S. L.; Olafson, B. D.; Goddard, W. A., *J. Phys. Chem.* **1990**, *101*, 8897-8909.
- (132) Cornell, W. D.; Cieplak, P.; Bayly, C. I.; Gould, I. R.; Merz, K. M.; Ferguson, D. M.; Spellmeyer, D. C.; Fox, T.; Caldwell, J. W.; Kollman, P. A., *J. Am. Chem. Soc.* **1995**, *117*(19), 5179-5197.
- (133) Mackerell, A. D.; Bashford, D.; Bellott, M.; Dunbrack, R. L.; Evanseck, J. D.; Field, M. J.; Fischer, S.; Gao, J.; Guo, H.; Ha, S.; Joseph-McCarthy, D.; Kuchnir, L.; Kuczera, K.; Lau, F. T. K.; Mattos, C.; Michnick, S.; Ngo, T.; Nguyen, D. T.; Prodhom, B.; Reiher, W. E.; Roux, B.; Schlenkrich, M.; Smith, J. C.; Stote, R.; Straub, J.; Watanabe, M.; Wiorkiewicz-Kuczera, J.; Yin, D.; Karplus, M., *J. Phys. Chem. B* **1998**, *102*(97), 3586-3616.
- (134) Brooks, B. R.; Brooks, C. L.; Mackerell, A. D.; Nilsson, L.; Petrella, R. J.; Roux, B.; Won, Y.; Archontis, G.; Bartels, C.; Boresch, S.; Cafflish, A.; Caves, L.; Cui, Q.; Dinner, A. R.; Feig, M.; Fischer, S.; Gao, J.; Hodscek, M.; Im, W.; Kuczera, K.; Lazaridis, T.; Ma, J.; Ovchinnikov, V.; Paci, E.; Pastor, R. W.; Post, C. B.; Pu, J. Z.; Schaefer, M.; Tidor, B.; Venable, R. M.; Woodcock, H. L.; Wu, X.; Yang, W.; York, D. M.; Karplus, M., *J. Comput. Chem.* **2009**, *30*(10), 1545-1608.
- (135) Scott, W. R. P.; Hünenberg, P. H.; Tironi, I. G.; Mark, A. E.; Billeter, S. R.; Fennen, J.; Torda, A. E.; Huber, T.; Krüger, P.; Gunsteren, W. F. v., *J. Phys. Chem. A* **1999**, *103*(19), 3596-3607.
- (136) Dauber-Osguthorpe, P.; Roberts, V. A.; Osguthorpe, D. J.; Wolff, J.; Genest, M.; Hagler, A. T., *Proteins: Struct., Funct., Gen.* **1988**, *4*(1), 31-47.
- (137) Jorgensen, W. L.; Maxwell, D. S.; Tirado-Rives, J., *J. Am. Chem. Soc.* **1996**, *118*(45), 11225-11236.
- (138) Kaminski, G. A.; Friesner, R. A.; Tirado-Rives, J.; Jorgensen, W. L., *J. Phys. Chem. B* **2001**, *105*(28), 6474-6487.

- (139) Rigby, D.; Sun, H.; Eichinger, B. E., *Polym. Int.* **1997**, *44* (3), 311-330.
- (140) Yang, J.; Ren, Y.; Tian, A.-m.; Sun, H., *J. Phys. Chem. B* **2000**, *104* (20), 4951-4957.
- (141) Bunte, S. W.; Sun, H., *J. Phys. Chem. B* **2000**, *104* (11), 2477-2489.
- (142) Martin, M. G.; Siepmann, J. I., *J. Phys. Chem. B* **1998**, *102* (97), 2569-2577.
- (143) Wick, C. D.; Martin, M. G.; Siepmann, J. I., *J. Phys. Chem. B* **2000**, *104* (33), 8008-8016.
- (144) Chen, B.; Potoff, J. J.; Siepmann, J. I., *J. Phys. Chem. B* **2001**, *105*, 3093-3104.
- (145) Nicholas, J. B.; Hopfinger, A. J.; Trouw, F. R.; Iton, L. E., *J. Am. Chem. Soc.* **1991**, *113* (13), 4792-4800.
- (146) Demontis, P.; Suffritti, G. B.; Quartieri, S.; Fois, E. S.; Gamba, A., *J. Phys. Chem.* **1988**, *92* (4), 867-871.
- (147) Hill, J. R.; Sauer, J., *J. Phys. Chem.* **1994**, *98* (4), 1238-1244.
- (148) Allen, M. P.; Tildesley, D. J., *Computer Simulation of Liquids*. 1989; p 408-408.
- (149) Ewald, P. P., *Ann. Phys.* **1921**, *369* (3), 253-287.
- (150) Demontis, P.; Suffritti, G. B.; Quartieri, S.; Fois, E. S.; Gamba, A., *Zeolites* **1987**, *7* (6), 522-527.
- (151) Bai, P.; Tsapatsis, M.; Siepmann, J. I., *J. Phys. Chem. C* **2013**, *117* (46), 24375-24387.
- (152) Stillinger, F. H., *J. Chem. Phys.* **1974**, *60* (4), 1545-1557.
- (153) Jorgensen, W. L.; Chandrasekhar, J.; Madura, J. D.; Impey, R. W.; Klein, M. L., *J. Chem. Phys.* **1983**, *79* (2), 926-935.
- (154) Jorgensen, W. L.; Madura, J. D., *Mol. Phys.* **1985**, *56* (6), 1381-1392.
- (155) Levitt, M.; Hirshberg, M.; Sharon, R.; LAidig, K. E.; Daggett, V., *J. Phys. Chem.* **1997**, *101* (25), 5051-5061.
- (156) Mahoney, M. W., *J. Chem. Phys.* **2000**, *112* (20), 8910-8922.
- (157) Horn, H. W.; Swope, W. C.; Pitner, J. W., *J. Chem. Phys.* **2004**, *120* (20), 9665-9678.
- (158) Abascal, J. L. F.; Vega, C., *J. Chem. Phys.* **2005**, *123*, 234505.
- (159) Wu, Y., *J. Chem. Phys.* **2006**, *124*, 024503.
- (160) Rick, S. W., *J. Chem. Phys.* **2004**, *120* (13), 6085-6092.
- (161) Maerzke, K. A.; Schultz, N. E.; Ross, R. B.; Siepmann, J. I., *J. Phys. Chem. B* **2009**, *113* (18), 6415-6425.
- (162) Martin, M. G.; Siepmann, J. I., *J. Phys. Chem. B* **1999**, *103* (21), 4508-4517.
- (163) Myers, A. L.; Prausnitz, J. M., *AIChE J.* **1965**, *11* (1), 121-127.

Enantioselective Adsorption of Ibuprofen and Lysine in Metal-Organic Frameworks

Rocío Bueno-Pérez, Ana Martín-Calvo, Paula Gómez-Álvarez, Juan J. Gutiérrez-Sevillano, Patrick J. Merkling, Thijs J. H. Vlugt, Titus S. van Erp, David Dubbeldam, and Sofía Calero

2

This study reveals efficient enantiomeric separation of bioactive molecules in the liquid phase. Chiral structure HMOF-1 separates racemic mixtures whereas heteroselectivity is observed for scalemic mixtures of ibuprofen using nonchiral MIL-47 and MIL-53. Lysine enantiomers are only separated by HMOF-1. These separations are controlled by the tight confinement of the molecules.

A chiral compound is a molecule that is nonsuperimposable with its mirror image; such a molecule and its mirror image are called enantiomers. Although the difference between enantiomers is subtle, metabolic biomolecules such as amino acids are produced in a specific chirality. This is a consequence of reactions taking place involving highly selective, chiral reaction sites in enzymes and other proteins. In contrast to the synthesis of biomolecules by organisms, laboratory techniques for the synthesis of chiral molecules generally lead to a 50/50 mixture of the enantiomers.

A large amount of pharmaceutical drugs currently in use are chiral compounds.¹ Ideally they should consist of the pure active chiral form that produces the desired biological effect (eutomer). If the other chiral form (distomer) is also administered, it may interact with different biological receptors and cause side effects often unrelated to the function of the active isomer, an effect known as chiral toxicology. These findings have motivated the

pharmaceutical industry to increasingly seek either chiral switches with the ability to provide single enantiomers, or efficient methods to separate the isomers from the racemic mixtures, such as chiral chromatography,² in which the use of chiral metal-organic frameworks (MOFs) has been introduced as stationary phases recently.³⁻⁸ These structures can exhibit high enantioselectivity and high surface area and it is in this field that molecular simulations are acquiring high relevance.⁹⁻¹¹

This work evaluates the enantioselective adsorption of three metal-organic frameworks (MOFs) looking into the conditions that enable the separation of enantiomeric mixtures. Ibuprofen and lysine are used in this study due to their commercial importance.

Ibuprofen has been used as an analgesic and anti-inflammatory agent over the last forty years. The racemate is in clinical use, though between the two enantiomers, *S*-ibuprofen is the active form both *in vivo*

and *in vitro*. It was widely believed that the sole use of the active isomer does not possess any advantages since the inactive isomer is converted to the active form after absorption in the gastrointestinal tract. However, some studies have indicated that *S*-ibuprofen provides relief three times faster than its racemic mixture with fewer side effects. This implies that a reduction of dose and of metabolic load is possible if pure *S* enantiomer is administered.¹² L-lysine is an essential amino acid. The human body therefore relies on this amino acid from food or supplements. L-Lysine is important for proper growth, and it plays an essential role in the production of carnitine, a nutrient responsible for converting fatty acids into energy and helping to lower cholesterol. This amino acid also appears to help the body absorb calcium, and plays an important role in the formation of collagen, a substance important for bones and connective tissues including skin, tendon, and cartilage. Additionally, ibuprofen and lysine are often formulated together.

The high porosity and the wide range of chemical compositions and porous structures of metal-organic frameworks (MOFs) suggest possible applications for drug delivery¹³⁻¹⁴ and in “chiral switching” to remove enantiomers. MIL-47¹⁵ and MIL-53¹⁶ are metal-organic frameworks that belong to the MIL series (Material Institut Lavoisier). The combination of 1,4-benzenedicarboxylate and metal center generates orthorhombic unit cells with straight channels in one direction. As shown in Figure 1, the unit cells in the open structure of MIL-53 ($6.82 \times 6.82 \times 13.94 \text{ \AA}^3$) are slightly smaller than in MIL-47 ($6.82 \times 16.73 \times 13.04 \text{ \AA}^3$). The metal centers in MIL-53 and MIL-47 are chromium and vanadium, respectively. HMOF-1,¹⁷ unlike the aforementioned structures, is a chiral MOF. It is formed by cadmium atoms as

metal centers and an axially chiral ligand *R*-6,6'-dichloro-2,2'-dihydroxy-1,1'-binaphthyl-4,4'-bipyridine, which connects the metal centers generating unit cells with dimensions $20.305 \times 20.305 \times 49.641 \text{ \AA}^3$ and helicoidal pores (Figure 1). The models for the structures are rigid and based on UFF¹⁸ and Dreiding¹⁹ force fields (Tables A1-A3 of the Appendix 1).

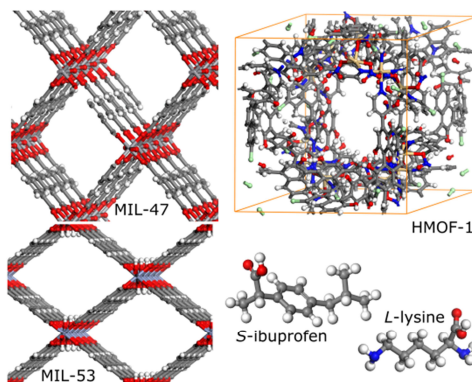


Figure 1. Front view of the unidirectional channels in MIL-47, MIL-53, and HMOF-1. Molecular representation of *S*-ibuprofen and L-lysine.

The mechanisms of enantioselective adsorption in MOFs and other porous materials such as zeolites have been recently elucidated at the atomic level for chiral hydrocarbons and other molecules, showing that enantiomeric excess (*ee*) over 50% can be achieved.^{9-11,20-25} However, to the best of our knowledge, enantioselective separation of more complex molecules in liquid phase has not yet been studied.

The molecule of ibuprofen contains a chiral center on the α -carbon of the propionate moiety. Lysine also contains a chiral center on the α -carbon and its properties will be determined by two amino and one carboxyl groups (Figure 1). Both enantiomers of these molecules have been modeled using flexible full-atom models based on CVFF

force fields²⁶⁻²⁷ (Tables A4 and A5 of the Appendix 1).

The selective adsorption of the isomers of ibuprofen and lysine was computed in the liquid phase. A liquid phase in the context of this work refers to aqueous ibuprofen or lysine solutions. The adsorption isotherms of a liquid feed with a solute/solvent mole fraction comprised between 0.2 and 1% were computed using grand canonical Monte Carlo simulations. Liquid phase fugacities are computed from the saturated vapor pressures of the components and the liquid phase activity coefficients. The latter are calculated from the experimental vapor-liquid equilibrium data. The adsorption isotherm obtained for the solutions of *S*-ibuprofen and *L*-lysine in any of the three MOFs show that at saturation pressure water does not enter the structure (Figures A4 and A5 in the Appendix 1). Similar results were obtained for *R*-ibuprofen and *D*-lysine in calculations that were similarly conducted at 300 K.

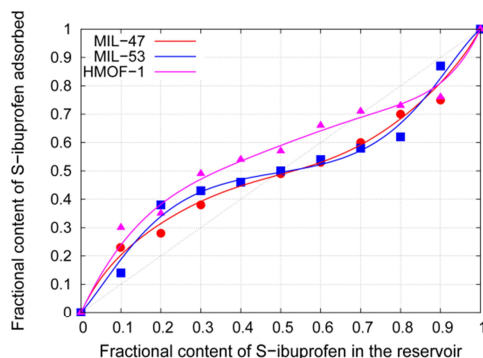


Figure 2. Adsorbed fractional content of *S*-ibuprofen as a function of the *S*-fraction in an *R/S* mixture in the reservoir for MIL-47 (red), MIL-53 (blue), and HMOF-1 (pink). The straight line would indicate that the adsorbed composition is identical to that in the reservoir.

A recent work of Bernini *et al.* reported the adsorption mechanism of ibuprofen in

MIL-53. In this structure, adsorbate-adsorbent interactions are stronger than adsorbate-adsorbate interactions. Therefore, the adsorption pattern consists of a small loading at low fugacity followed by a sudden increase to reach saturation.²⁸ This pattern is in agreement with our simulations of aqueous ibuprofen solution. The presence of water enhances the ibuprofen uptake slightly at the lowest values of fugacity, but does not affect saturation (Figure A4 in the Appendix 1). Above 10^{-10} and 10^{-3} Pa ibuprofen and lysine systems, respectively, were in the saturation regime, with 16 ibuprofen or 30 lysine molecules per simulation cell. The simulation cells are $27.28 \times 27.28 \times 27.88 \text{ \AA}^3$ (MIL-47), $27.28 \times 33.46 \times 26.08 \text{ \AA}^3$ (MIL-53), and $20.305 \times 20.305 \times 49.641 \text{ \AA}^3$ (HMOF-1). Then it is possible to study chiral mixtures in which the *S* (ibuprofen) or the *L* (lysine) fraction is varied between 0.1 and 0.9 in the external reservoir in such a way that the enantiomers can vary while the total number of molecules remains constant (Figures 2 and 3). To perform these simulations efficiently we use Monte Carlo moves that have been previously developed for dense systems²³ and that are needed to obtain highly converged values.

Figure 2 shows the fraction of adsorbed *S*-ibuprofen as a function of the enantiomeric ratio in the external reservoir in HMOF-1, MIL-53, and MIL-47. For the three structures we found a significant deviation of the curve from a straight line, which is the behavior one would expect if no preferential adsorption of one isomer over another takes place. As expected, the graph obtained for the last two MOFs were checked to be symmetric and passing through the (0.5, 0.5) point. In other words, these structures which are nonchiral are unable to induce an enantiomeric excess when starting from a racemic mixture.

However, they deplete scalemic mixtures and the form of the curve indicates heteroselective adsorption. The main enantiomeric form in the reservoir is less readily adsorbed, i.e., the adsorbent levels the enantiomeric ratio towards that of racemic mixtures and enriches the reservoir. Except at low fractions of *S*-ibuprofen, deviations from the straight line are larger for MIL-53 than for MIL-47, probably due to the narrower pores of the former structure. HMOF-1 is also heteroselective and, more importantly, this structure is able to separate the racemic mixture. At low and medium fractions of *S*-ibuprofen this enantiomer is enhanced by the heteroselective packing effect in the MOF structure that provides an R-type chiral environment. At high fractions of *S*-ibuprofen there is a competition between the heteroselective behavior in the system and the chiral effect induced by the chirality of the MOF, and thus the selectivity is reduced.

Figure 3 shows the fraction of adsorbed L-lysine as a function of the enantiomeric fraction in the reservoir for the three MOFs. No separation is observed at any mole fraction in the nonchiral structures MIL-47 and MIL-53. It appears that this molecule is less commensurable with the pores of these structures than ibuprofen. In HMOF-1, however, a heteroselective effect is present, although the intrinsic chirality of this MOF only favors a slight preference. Unlike the ibuprofen case, this structure is unable to separate racemic mixtures.

The ee obtained for ibuprofen and lysine in HMOF-1 is 18% and 4%, respectively. For the nonchiral MOFs we use an adapted enantiomeric excess (ee^*)²⁹ which graphically corresponds to the maximum vertical displacement from the diagonal of the S-curves plotted in Figures 2 and 3. The

ee^* values obtained for ibuprofen in MIL-47 and MIL-53 are 12% and 19%, and for lysine 3% (MIL-47) and 2% (MIL-53). These data highlight the importance of guest-guest interactions in these systems, occurring at saturation values, when molecules pack and create an additional chiral environment in the case of nonchiral MOFs, or enhancing this environment in homochiral MOFs.²⁵ The packing effect found for these systems is not specific to MOFs. It can also be found in other systems, since the effect is not directly related to enantioselectivity but to many other factors such as channel shape, pore size, steric fit, and interaction with the framework.^{5,7-9,25,29}

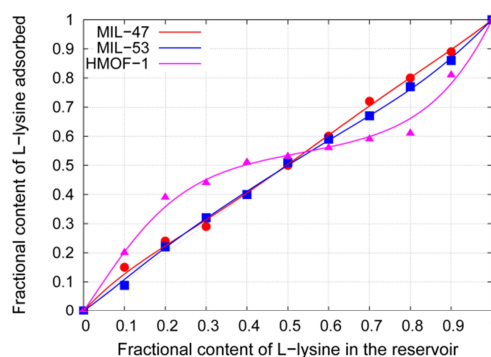


Figure 3. Adsorbed fractional content of L-lysine as a function of the L-fraction in a D/L mixture in the reservoir for MIL-47 (red), MIL-53 (blue), and HMOF-1 (pink). The straight line would indicate that the adsorbed composition is identical to that in the reservoir.

To get a deep understanding of this behavior we provide insights into the microscopic assembly in the systems. We evaluated the hydrogen bonding (HB) between guest molecules using a specific criterion for HB definition.³⁰ Results and details of calculations are given in Table A6 of Appendix 1. Overall, the molecular association between guest molecules is an important factor. Despite data dispersion, there is clear evidence of preferential

hydrogen-bond formation between *R* and *S* molecules of ibuprofen in MIL-47, which leads to heteroselectivity. In MIL-53, however, heteroselectivity is promoted by preferential hydrogen-bond formation of the minority enantiomers of the same type. In HMOF-1, it would appear that the reason for the selectivity behavior in Figure 2 is a combination of *R-S* hydrogen bonds being favored at high concentrations of *S*-ibuprofen and a preferential same-type minor enantiomer association. Regarding lysine in HMOF-1, both factors at work in ibuprofen also apply to promote heteroselectivity, although in lysine the number of guest-guest bonds formed is generally lower than in ibuprofen. Likewise, we computed the average minimum intermolecular distances between oxygen atoms of the carboxyl group and the distances of these atoms to the metal centers of the host structures (Table A7 and A8 in the Appendix 1). These values provide information on the strength of the interaction of the molecules, and host-guest forces, and show that the double-bonded oxygen in the carboxylic group (C=O) of both ibuprofen and lysine is more likely to form hydrogen bonds than the single-bonded oxygen in the carboxylic group (C-O-H). This is in agreement with the radial distribution functions obtained by Bernini *et al.* for ibuprofen in MIL-53.²⁸

Conclusions

This work shows that molecular simulation allows predicting molecular adsorption and enantioselectivity in porous materials, providing important information about the interactions established, the confinement of molecules, and the chiral environment inside the porous structures. The MOF structures studied are able to separate mixtures of lysine enantiomers and mixtures of ibuprofen enantiomers. HMOF-

1, which has a chiral structure, separates racemic mixtures of ibuprofen and surprisingly, the nonchiral structures of MIL-47 and MIL-53 are able to separate scalemic mixtures of ibuprofen. We have correlated this with the microscopical behavior. Confinement of the bulky ibuprofen in the narrow pores of MIL-47 and MIL-53 favors the formation of hydrogen bonds between *R* and *S* enantiomers. This finding opens new prospects for the development of porous materials and new interpretations regarding the molecular mechanisms involved in chiral separations. It shows that it is difficult to make predictions *a priori* without a very detailed molecular knowledge of the system, and that neither a chiral MOF necessarily implies the ability to separate small isomers nor is a nonchiral MOF necessarily unselective towards some mixtures of enantiomers.

Acknowledgments

This work was supported by the Spanish “Ministerio de Economía y Competitividad (MINECO)” (CTQ2010-16077) and the European Research Council through an ERC Starting Grant (ERC2011-StG-279520-RASPA). R. B. thanks the MINECO for her predoctoral fellowship (CTQ2010-16077). A.M. thanks the Spanish “Ministerio de Educación (MEC)” for her predoctoral fellowship.

Bibliography

- (1) Smith, S. W., *Toxicol. Sci.* **2009**, *110*(1), 4-30.
- (2) Schurig, V., *J. Chromatogr. A* **2001**, *906* (1-2), 275-299.
- (3) Nuzhdin, A. L.; Dybtsev, D. N.; Bryliakov, K. P.; Talsi, E. P.; Fedin, V. P., *J. Am. Chem. Soc.* **2007**, *129*(43), 12958-12959.

- (4) Xie, S.-M.; Zhang, Z.-J.; Wang, Z.-Y.; Yuan, L.-M., *J. Am. Chem. Soc.* **2011**, *133* (31), 11892-11895.
- (5) Zhang, M.; Pu, Z.-J.; Chen, X.-L.; Gong, X.-L.; Zhu, A.-X.; Yuan, L.-M., *Chem. Comm.* **2013**, *49* (45), 5201-5203.
- (6) Xuan, W.; Ye, C.; Zhang, M.; Chen, Z.; Cui, Y., *Chem. Sci.* **2013**, *4* (8), 3154-3159.
- (7) Kuang, X.; Ma, Y.; Su, H.; Zhang, J.; Dong, Y.-B.; Tang, B., *Anal. Chem.* **2014**, *86* (2), 1277-1281.
- (8) Zhang, M.; Zhang, J.-H.; Zhang, Y.; Wang, B.-J.; Xie, S.-M.; Yuan, L.-M., *J. Chromatogr. A* **2014**, *1325*, 163-170.
- (9) Martin-Calvo, A.; Calero, S.; Martens, J. A.; van Erp, T. S., *J. Phys. Chem. C* **2013**, *117* (3), 1524-1530.
- (10) Bao, X.; Broadbelt, L. J.; Snurr, R. Q., *Microporous Mesoporous Mater.* **2012**, *157*, 118-123.
- (11) van Erp, T. S.; Caremans, T. P.; Dubbeldam, D.; Martin-Calvo, A.; Calero, S.; Martens, J. A., *Angew. Chem., Int. Ed.* **2010**, *49* (17), 3010-3013.
- (12) Moore, R. A.; Derry, S.; McQuay, H. J., *Cochrane Database of Systematic Reviews* **2009**, (3).
- (13) Horcajada, P.; Serre, C.; Maurin, G.; Ramsahye, N. A.; Balas, F.; Vallet-Regi, M.; Sebban, M.; Taulelle, F.; Ferey, G., *J. Am. Chem. Soc.* **2008**, *130* (21), 6774-6780.
- (14) Horcajada, P.; Serre, C.; Vallet-Regi, M.; Sebban, M.; Taulelle, F.; Ferey, G., *Angew. Chem., Int. Ed.* **2006**, *45* (36), 5974-5978.
- (15) Barthelet, K.; Marrot, J.; Riou, D.; Ferey, G., *Angew. Chem., Int. Ed.* **2002**, *41* (2), 281-284.
- (16) Serre, C.; Millange, F.; Thouvenot, C.; Nogués, M.; Marsolier, G.; Louer, D.; Ferey, G., *J. Am. Chem. Soc.* **2002**, *124* (45), 13519-13526.
- (17) Wu, C.-D.; Lin, W., *Angew. Chem., Int. Ed.* **2007**, *46* (7), 1075-1078.
- (18) Rappe, A. K.; Casewit, C. J.; Colwell, K. S.; Goddard, W. A.; Skiff, W. M., *J. Am. Chem. Soc.* **1992**, *114* (25), 10024-10035.
- (19) Mayo, S. L.; Olafson, B. D.; Goddard, W. A., *J. Phys. Chem.* **1990**, *94* (26), 8897-8909.
- (20) Bao, X.; Snurr, R. Q.; Broadbelt, L. J., *Microporous Mesoporous Mater.* **2013**, *172*, 44-50.
- (21) Bao, X.; Broadbelt, L. J.; Snurr, R. Q., *Phys. Chem. Chem. Phys.* **2010**, *12* (24), 6466-6473.
- (22) Bao, X.; Snurr, R. Q.; Broadbelt, L. J., *Langmuir* **2009**, *25* (18), 10730-10736.
- (23) Van Erp, T. S.; Dubbeldam, D.; Caremans, T. P.; Calero, S.; Martens, J. A., *J. Phys. Chem. Lett.* **2010**, *1* (14), 2154-2158.
- (24) van Erp, T. S.; Dubbeldam, D.; Calero, S.; Martens, J. A., *Chem. Eng. Sci.* **2010**, *65* (24), 6478-6485.
- (25) Castillo, J. M.; Vlugt, T. J. H.; Dubbeldam, D.; Hamad, S.; Calero, S., *J. Phys. Chem. C* **2010**, *114* (50), 22207-22213.
- (26) Gaedt, K.; Holtje, H. D., *J. Comput. Chem.* **1998**, *19* (8), 935-946.
- (27) Dauberosguthorpe, P.; Roberts, V. A.; Osguthorpe, D. J.; Wolff, J.; Genest, M.; Hagler, A. T., *Proteins: Struct., Funct., Gen.* **1988**, *4* (1), 31-47.
- (28) Bernini, M. C.; Fairen-Jimenez, D.; Pasinetti, M.; Ramirez-Pastor, A. J.; Snurr, R. Q., *J. Mater. Chem. B* **2014**, *2* (7), 766-774.
- (29) Caremans, T. P.; Van Erp, T. S.; Dubbeldam, D.; Castillo, J. M.; Martens, J. A.; Calero, S., *Chem. Mater.* **2010**, *22* (16), 4591-4601.
- (30) Luzar, A.; Chandler, D., *J. Chem. Phys.* **1993**, *98*, 14.

Separation of Amyl Alcohol Isomers in ZIF-77

Rocío Bueno-Pérez, Juan J. Gutiérrez-Sevillano, Patrick J. Merkling, David Dubbeldam, and Sofía Calero

3

The separation of pentanol isomer mixtures is shown to be very efficient using the nanoporous adsorbent zeolitic imidazolate framework ZIF-77. Through molecular simulations, we demonstrate that this material achieves complete separation of linear from monobranched –and these from dibranched– isomers. Remarkably, adsorption and diffusion behaviors follow the same decreasing trend, produced by channel size of ZIF-77 and guest shape. This separation based on molecular branching applies to alkanes and alcohols, and promises to encompass numerous other functional groups.

The industrial production of alcohols yields complex mixtures that depend on the process used. In the case of amyl alcohols (pentanols) that are obtained by low-pressure rhodium-catalyzed hydroformylation (oxo process) of butenes and subsequent hydrogenation, mainly 2-methylbutanol and 1-pentanol are obtained in a catalyst-dependent ratio.¹ If amyl alcohols are produced through the hydration of pentenes, other mixtures are obtained, for example 76% 2-pentanol and 24% 3-pentanol from 2-pentene. Pentanols are also found in fuel oils and in the fermentation of starch-containing products, but their recovery is uneconomical at present.²

The fact that amyl alcohols possess an odd number of carbon atoms endow them with peculiar physical and solubility properties and make them attractive solvents, surfactants, extraction agents, and gasoline

additives.¹ Separation and purification of a wide range of alcohol isomers is therefore an important task. The main separation technique employed is distillation, an energetically costly step due to the high vaporization enthalpy of alcohols. Additionally, obtaining pure compounds is difficult because of the very similar boiling points of some of them, that is, 2-pentanol, 3-pentanol, 3-methyl-2-butanol, and 2,2-dimethylpropanol,²⁻³ and the fact that they form azeotropes.² A different strategy consists in separating these isomers over appropriate adsorbents. In this sense, the separation of a few alcohols, mostly biobutanol and bioethanol has been studied over some ZIFs, especially ZIF-8, ZIF-71, and ZIF-90.⁴⁻⁶

A recent computational study on a number of microporous materials suggested that ZIF-77⁷ is very well suited for the separation of hydrocarbons at high temperature,⁸

favoring linear over branched molecules, and these over dibranched ones, presenting the degree of branching as the driving force, a fact that has been also described experimentally, albeit on a different type of MOF.⁹ No flexibility, breathing, nor phase changes have been reported for this structure. Also, the most similar structure to ZIF-77 that has been looked into for breathing is ZIF-78, in which the thermal expansion of the cell length is below 0.1%.¹⁰ In addition, the channel system in ZIF-77 is similar to those in zeolites, and no gate-opening effect is expected where flexibility could have a strong influence. Given that no reliable, well-tested flexible force field for the adsorbent is available, we deemed it safer to assume that the structure would be retained under loading and used a rigid framework. This would additionally provide us with a lower bound for diffusion coefficients. Several papers have reported the effect of flexibility on adsorption due to a change in structure.¹¹⁻¹² ZIF-77 exhibits very high selectivity, combined with a quite large adsorption capacity. Figure A1 of the Appendix 2 shows that this structure possesses narrow channels along the *z*-direction interconnected with even smaller zigzag channels along the *x*-direction, forming a two-dimensional system. The fact that zigzag channels are narrower than the straight ones lets bulkier molecules diffuse only along the *z*-axis. Due to the zeolitic nature of the framework, metal centers are not accessible from the channels, in the same way that Si or Al atoms are not in a zeolite. The partial charge of the atoms exposed to the channels, including the nitro group, are small, therefore the channels present low polarity. In this study, we investigate the ability of ZIF-77 to separate the eight structural isomers of pentanol: 1-pentanol (1P), 2-pentanol (2P), 3-pentanol (3P), 3-methylbutanol (3MB), 2-methylbutanol (2MB), 3-methyl-2-butanol

(3M2B), 2-methyl-2-butanol (2M2B), and 2,2-dimethylpropanol (22DMP). For the sake of the discussion, these structural isomers can be divided in four categories based on their heavy-atom skeleton, that is, ignoring hydrogen atoms: 1P would therefore be a linear molecule; 2P, 3P, 3MB, and 2MB monobranched molecules; while 3M2B, 2M2B, and 22DMP would be dibranched molecules. We find it useful to separate the latter three into molecules dibranched on different carbon atoms (3M2B) or on the same carbon atom (2M2B and 22DMP).

Table 1. Diffusion coefficients for alcohol molecules in ZIF-77 at 298 K.

Molecule	$D / 10^{-10} \text{ m}^2 \text{ s}^{-1}$	Molecule	$D / 10^{-10} \text{ m}^2 \text{ s}^{-1}$
1P	1.15 ± 0.25	3MB	0.074 ± 0.02
2P	0.12 ± 0.03	3M2B	0.067 ± 0.02
3P	0.17 ± 0.04	2M2B*	-*
2MB	0.20 ± 0.5	22DMP*	-*

* Self-diffusivities were too low to be computed by MD.

For a material to be an efficient adsorbent it should not suffer from diffusional limitations. The propensity of guest molecules to move through the porous environment can be expressed by the self-diffusion coefficients (D) and were obtained in this work by molecular dynamics simulations. The sets of force field parameters used are known to produce results in agreement with available experimental data and have high predictive capability.¹³ The model for the adsorbent is rigid and based on UFF¹⁴ force fields (Figures A1 and A2, and Table A1 of the Appendix 2). The point charges used were derived specially for zeolitic imidazolate

frameworks to improve the reliability of adsorption results based on UFF force field parameters.¹⁵ The adsorbates have been modeled using flexible united-atom models based on TraPPE force field¹⁶⁻¹⁷ (Figure A3 and Table A2 of the Appendix 2).

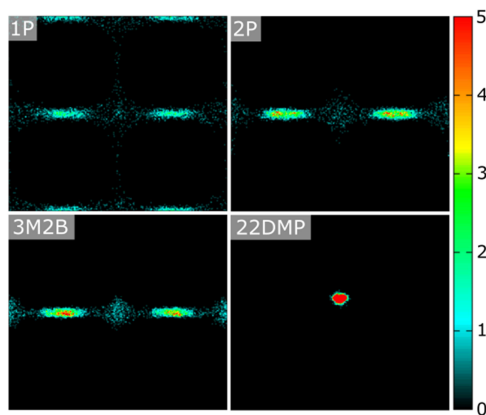


Figure 1. Molecular dynamics trajectories of adsorbates within the framework in a zx -view for four adsorbates: 1P (top left), 2P (top right), 3M2B (bottom left), and 22DMP (bottom right).

The results for the structural isomers of pentanol at low coverage at 298 K are shown in Table 1. These are directionally-averaged self-diffusion coefficients. Diffusion takes place only along the z -direction, with the exception of 1P (Table A3 of the Appendix 2) and its magnitude is similar to the one in the bulk.¹⁸ Independently from the temperature, 1P is the alcohol that diffuses most. The linear 1P alcohol is able to wind efficiently through the channels. 2P, 3P, and 2MB, molecules with one branching point as defined previously, have a self-diffusion coefficient an order of magnitude lower. Next, 3MB and 3M2B diffuse another factor 2 slower than the previous group of compounds. Whereas 3M2B possesses topologically two branching points, 3MB is ranked amongst the monobranched molecules but performs unexpectedly badly. Two structures, 2M2B and 22DMP, are seen

to have negligible diffusion: due to their bulkiness around the central carbon, they cannot enter the pores. We will therefore exclude them from further consideration. To illustrate the accessible part of the structure for each alcohol, the diffusion trail and the density profile of a randomly inserted molecule is recorded. Diffusion trails are represented in Figure 1 for 1P, 2P, 3M2B, and 22DMP. These and other views and molecules, as well as density profiles are shown in Figures A4, A5, A8, and A9 of the Appendix 2. As appears in Figure 1, the molecule in 1P is able to access the two-dimensional void space spanned by interconnected x - and z -channels. 2P and 3M2B molecules are restricted to moving through the z -channel in which they initially entered. Finally, 22DMP can only be generated in the central region of a pore cavity due to its bulkiness in all directions. Therefore, this molecule would be limited to the pore cavity.

Table 2. Diffusion coefficients for alkane molecules in ZIF-77 at 298 K.

Molecule	$D / 10^{-10} \text{ m}^2 \text{ s}^{-1}$	Molecule	$D / 10^{-10} \text{ m}^2 \text{ s}^{-1}$
nC6	0.8 ± 0.2	23DMB	0.13 ± 0.02
2MP	0.13 ± 0.03	22DMB	-*
3MP	0.13 ± 0.04		

* Self-diffusivities were too low to be computed by MD.

To place these results in a broader context, diffusion data for alkanes were obtained at 298 K (Table 2, Tables A3 and A4 of the Appendix 2). Alkanes engage in simpler intermolecular interactions than alcohols given that they lack the ability to form hydrogen bonds. They should therefore reflect the effect on diffusion of flexibility

and shape of the molecule, and of van der Waals interactions. If we substitute the hydroxyl (OH) group for a slightly larger methyl (CH₃) group to form a related alkane, based on the principle that the molecule retains a similar size and shape, we obtain a set of alkanes and can establish a correspondence between alcohols and alkanes that is helpful in the comparison of both classes of molecules. In this way, the analogue of 1-pentanol is n-hexane (nC6), the one of 2P is 2-methylpentane (2MP), and so forth. Similarly to the case of alcohols, the single linear molecule diffuses faster than the monobranched alkanes, and these faster in turn than the alkane dibranched on different carbon atoms. As already observed in alcohols, molecules dibranched on the same carbon atom are not able to diffuse as they do not cross pore windows. In the case of alkanes, no exception to this ordering principle is observed. The alcohols and their related alkane diffuse at similar rates, the slight increase in size of the alkane makes up for the polarity of the alcohol in this rather hydrophobic environment. Nevertheless, in spite of the related topologies of alkanes and alcohols, the small differences in the dynamics of the pore are influenced by the position of the hydroxyl group, given the difference in size and nature between hydroxyl and methyl groups.

The latter can be evaluated through isosteric heats and Henry constants (Table A5 of the Appendix 2) and relate to adsorption at low loading. However, both the linear alkane and alcohol fit neatly both in the large (z -) and small (x -) channels. Therefore, these molecules interact more strongly with the framework and adsorb better than mono- or dibranched molecules at low loading. The next best adsorbates are the monobranched 2P and 3P, and finally other alcohols. This is related to the behavior in alkanes, in which

both monobranched isomers adsorb better than the dibranched ones.⁸ Obviously, the picture in alcohols is a more mixed one, given that 2MB and 3MB are also monobranched molecules, but are not able to interact that effectively with the framework as 2P and 3P do.

Adsorption isotherms of liquid feeds of equimolar composition at 298 K were computed using configurational bias grand canonical Monte Carlo simulations.¹⁹ Liquid phase fugacities were computed from the saturated vapor pressures of the components, the liquid phase activity coefficients, and the external pressure of the system. The latter were calculated from the experimental vapor-liquid equilibrium data.²⁰

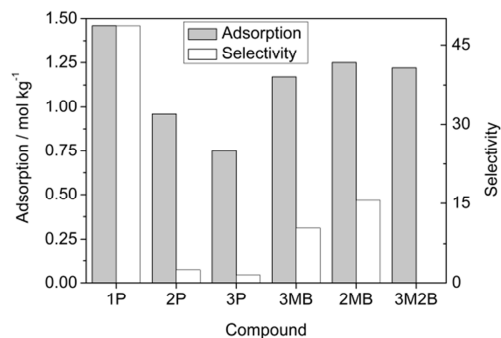


Figure 2. Histogram of adsorption properties for the separation of equimolar mixtures: adsorption of the most adsorbed species and selectivity with respect to second most adsorbed species. Moving one position from left to right in the figure means dropping the most adsorbed species from the equimolar mixture. The mixture on the left has six isomers (1P, 2P, 3P, 3MB, 2MB, 3M2B).

Figure 2 shows the adsorption values of the most adsorbed component and its selectivity *versus* the second most adsorbed one for equimolar mixtures containing up to six isomers. Thus, in ZIF-77, an equimolar mixture of all isomers (excluding 2M2B and 22DMP) adsorbs selectively 1P. The mixture

containing the remaining isomers adsorbs mainly 2P, and its selectivity over 3MB is shown in Figure 2 as explained. By removing successively the most adsorbed species, we obtain the preferential order of adsorption in ZIF-77, which can be seen from left to right in this figure: $1P \gg 2P > 3P > 3MB > 2MB \gg 3M2B$. Data are obtained at fugacity conditions that led to saturation adsorption values and high selectivities with respect to the second most adsorbed species. Therefore, 1P can be separated efficiently from all other isomers. On the contrary, 2P cannot be separated efficiently from 3P, 3MB, and 2MB, or any mixture containing significant amounts of these. These four compounds may thus be grouped together based on their topology, and these results show that similarity in shape makes separation more difficult while it is less important where the hydroxyl group is actually located. Finally, any of these four can be easily separated from 3M2B. In comparison, alkanes exhibit a similar adsorption pattern: the linear alkane is strongly favored over the monobranched ones and these over the dibranched one. Once again, the shape determines the behavior.

As seen from this study, ZIF-77 is unusual in that the molecules that diffuse best also achieve highest adsorption in a multicomponent mixture. This combination would be especially helpful in a membrane-based separation process. In this context, the overall separation ability for a mixture of two components i and j is estimated through permselectivity. The permselectivity can be approximated by the formula²¹ $S_{perm(ij)} = D_i x_i y_j / D_j x_j y_i$, where x and y represent the fraction of the components in the adsorbent and the feed, respectively.

For each of the multicomponent equimolar mixtures considered previously, one value of permselectivity has been selected and is shown in Table 3. It corresponds to the pair of the most adsorbed species of the mixture (molecule i), whereas molecule j is its closest competitor. The separation between linear and monobranched molecules turns out to be far better than could be anticipated from adsorption results, and the one between monobranched molecules and the dibranched one is also significantly improved. This is remarkable, because generally the higher the affinity for a molecule (and therefore the selectivity), the lower its diffusion. Within the group of monobranched molecules, separation is confirmed to be difficult. Results for alkanes show a similar pattern, permselectivity between linear and monobranched molecules is higher than adsorption selectivity.

Table 3. Permselectivity for alcohol molecules in ZIF-77 at 298 K.

Molecule i	Molecule j	S_{perm}
1P	2P	500
2P	3MB	4.0
3P	2MB	2.5
3MB	2MB	4.6
2MB	3M2B	39

Selectivities in this ZIF have been found to be governed essentially by the branching of the molecules, as can be seen both in alcohols and their corresponding alkanes. The hydroxyl groups affect guest-guest interactions and framework-guest interactions when exposed in the molecule but the hydrocarbon chains moderate this effect. The logarithm of octanol-water

partition coefficient ($\log K_{OW}$) can give a measure of how polar a molecule is and how it behaves in different solvents or molecular environments. This value for the alcohols studied spans from 0.89 to 1.51, for 2M2B and 1P, respectively;²² while for alkanes the values are around 3.70. Many chemical compounds possess $\log K_{OW}$ values within this range. Given a proper length of the hydrocarbon chain, linear molecules of ketones, acids, aldehydes, cis/trans alkenes, thiols and ethers should also be separated from their branched isomers by ZIF-77. Thus, an efficient adsorption relies just as much on enough interactions between hydrocarbon chains and the adsorbent as it could possibly on strong dipolar or hydrogen-bond interactions. So we expect that in the low-polarity environment inside ZIF-77 linear molecules of a wide range of chemical classes are better suited for diffusing and adsorbing than branched ones.

Conclusions

This work shows that ZIF-77 is a promising material for the separation of pentanol isomers. The order of preferential adsorption and diffusion is linear over monobranched over dibranched molecules on different C-atoms. Molecules dibranched on the same C-atom are not able to enter the framework. The same is true for alkanes, indicating that the hydroxyl group does not significantly affect the separation behavior, but that it is instead sterically driven. It is thus able to achieve the separation of polar, hydrogen-bond-forming molecules with a hydrocarbon tail on one side and of nonpolar molecules altogether on the other. This makes ZIF-77 a prime candidate for separation of linear from branched molecules of intermediate size (five to six carbon atoms), independently of the chemical functional group involved, at least

as long as it retains the hydrophobic character in part of the molecule.

Acknowledgments

This work was supported by the European Research Council through an ERC Starting Grant (S.C., ERC2011-StG-279520-RASPA) and through a VIDI grant by NWO (D.D., 700.10.428). R. B. thanks the MINECO for her predoctoral fellowship (CTQ2010-16077).

Bibliography

- (1) Kroschwitz, J. I.; Seidel, A., In *Kirk-Othmer Encyclopedia of Chemical Technology. 5th Edition*, Wiley Interscience: 2006.
- (2) Ullmann, F.; Gerhartz, W.; Yamamoto, Y. S.; Campbell, F. T.; Pfefferkorn, R.; Rounsaville, J. F., In *Ullmann's Encyclopedia of Industrial Chemistry. 7th Edition*, Wiley-VCH Verlag GmbH: 2011.
- (3) Linstrom, P. J.; Mallard, W. G., *NIST Chemistry WebBook, NIST Standard Reference Database Number 69*. National Institute of Standards and Technology: Gaithersburg MD, 20899, 2014.
- (4) Demessence, A.; Boissière, C.; Grosso, D.; Horcajada, P.; Serre, C.; Ferey, G.; Soler-Illia, G. J. A. A.; Sanchez, C., *J. Mater. Chem.* **2010**, *20* (36), 7676-7681.
- (5) Dong, X.; Ling, Y. S., *Chem. Comm.* **2013**, *49*, 1196-1198.
- (6) Zhang, K.; Zhang, L.; Jiang, J., *J. Phys. Chem. C* **2013**, *117*, 25628-25635.
- (7) Banerjee, R.; Phan, A.; Wang, B.; Knobler, C.; Furukawa, H.; O'Keeffe, M.; Yaghi, O. M., *Science* **2008**, *319*(5865), 939-943.
- (8) Dubbeldam, D.; Krishna, R.; Calero, S.; Yazaydin, A. O., *Angew. Chem., Int. Ed.* **2012**, *51* (47), 11867-11871.
- (9) Herm, Z. R.; Wiers, B. M.; Mason, J. A.; Baten, J. M. v.; Hudson, M. R.; Zajdel, P.; Brown, C. M.; Masciocchi, N.; Krishna, R.; Long, J. R., *Science* **2013**, *340*, 960-964.

- (10) Dong, X.; Huang, K.; Liu, S.; Ren, R.; Jin, W.; Lin, Y. S., *J. Mater. Chem.* **2012**, *22*, 19222-19227.
- (11) Clark, L. A.; Snurr, R. Q., *Chem. Phys. Lett.* **1999**, *308*, 155-159.
- (12) Vlugt, T. J. H.; Schenk, M., *J. Phys. Chem. B* **2002**, *206*, 12757-12763.
- (13) Lange, M. F. D.; Gutierrez-Sevillano, J. J.; Hamad, S.; Vlugt, T. J. H.; Calero, S.; Gascon, J.; Kapteijn, F., *J. Phys. Chem. C* **2013**, *117*, 7613-7622.
- (14) Rappe, A. K.; Casewit, C. J.; Colwell, K. S.; Goddard, W. A.; Skiff, W. M., *J. Am. Chem. Soc.* **1992**, *114* (25), 10024-10035.
- (15) Gutierrez Sevillano, J. J.; Calero, S.; Ania, C. O.; Parra, J. B.; Kapteijn, F.; Gascon, J.; Hamad, S., *J. Phys. Chem. C* **2013**, *117* (1), 466-471.
- (16) Chen, B.; Potoff, J. J.; Siepmann, J. I., *J. Phys. Chem. B* **2001**, *105* (15), 3093-3104.
- (17) Kelkar, M. S.; Rafferty, J. L.; Maginn, E. J.; Siepmann, J. I., *Fluid Phase Equilib.* **2007**, *260* (2), 218-231.
- (18) Karger, N.; Wappmann, S.; Shakergaafar, N.; Ludemann, H. D., *J. Mol. Liq.* **1995**, *64* (3), 211-219.
- (19) Frenkel, D.; Smit, B., *Understanding Molecular Simulations. From Algorithms to Applications*. Elsevier: San Diego. California, 2002.
- (20) Gutierrez-Sevillano, J. J.; Dubbeldam, D.; Bellarosa, L.; Lopez, N.; Liu, X.; Vlugt, T. J. H.; Calero, S., *J. Phys. Chem. C* **2013**, *117* (40), 20706-20714.
- (21) Nalaparaju, A.; Zhao, X. S.; Jiang, J. W., *Energy Environ. Sci.* **2011**, *4* (6), 2107-2116.
- (22) Sangster, J., *J. Phys. Chem. Ref. Data* **1989**, *18* (3), 1111-1227.

Cadmium-BINOL Metal-Organic Framework for the Separation of Alcohol Isomers

Rocío Bueno-Pérez, Patrick J. Merkling, Paula Gómez-Álvarez,
and Sofía Calero

4

The large-scale isolation of specific isomers of amyl alcohols for applications in the chemical, pharmaceutical, and biochemical industries represents a challenging task due to the physicochemical similarities of these structural isomers. The homochiral metal-organic framework cadmium-BINOL (BINOL=1,1'-bi-2-naphthol) is suitable for the separation of pentanol isomers, combining adsorption selectivities above 5 with adsorption capacities of around 4.5 mol kg⁻¹. Additionally, a slight ability for separation of racemic mixtures of 2-pentanol is also detected. This behavior is explained based on matching shapes, strength of the host-guest interactions, and on the network of hydrogen bonds. The last of these explains both the relative success and shortfalls of prediction methods at high loadings (ideal adsorbed solution theory) or at low coverage (separation factors), which are therefore useful here at a qualitative level, but not accurate in quantitative terms. Finally, the high selectivity of cadmium-BINOL for 1-pentanol over its isomers offers prospects for practical applications and some room for optimizing conditions.

Introduction

The group of compounds commonly known as amyl alcohols or pentyl alcohols is composed of 1-pentanol (1P) and seven alcohol structural isomers. Three of these exist in two chiral forms. The commercialized product “amyl alcohol” is a mixture of several of these isomers.¹ These compounds play an important role in industry as organic solvents,² but their applications go further. Pentyl alcohols act as intermediates in the production of herbicides and pharmaceuticals, and are also used as additives, flavoring, extraction, and flotation agents.³⁻⁴ They are frequent byproducts of the chemical, pharmaceutical, and biochemical industries,⁵ and the large-

scale production process is mostly based on halogenation of pentane^{2-4,6-7} or a rhodium-catalyzed hydroformylation and hydrogenation.² Given this wide range of production methods, a flexible separation method to obtain higher specific isomers is especially important. The physicochemical similarities of the isomers of pentyl alcohols make the current purification of these compounds by distillation of the alcohol mixtures difficult, and requires numerous unit operations,^{2-4,6-7} a solution that is costly both energetically and economically, and polluting. From this perspective, an alternative method of purification of these isomers might reduce expenses in the production process, reduce the polluting effect on the environment, and generate

puer products in less time. In this regard, adsorption-based separation in nanoporous materials represents a relevant option.

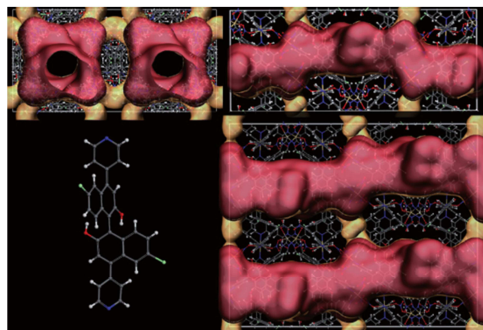


Figure 1. The xy -view of the channel network inside Cd-BINOL (top left) and the zy -view of the network inside the structure (top right). Chiral bridging ligand *R*-6,6'-dichloro-2,2'-dihydroxy-1,1'-binaphthyl-4,4'-bipyridine (bottom left); the zx -view of the network inside the structure (bottom right). In these framework views, the semitransparent red region highlights the main channels, whereas the ochre region signals the side channels. For maximum clarity, a $2 \times 1 \times 1$ simulation cell is shown.

Metal-organic frameworks (MOFs) consist of small metal-containing clusters connected three-dimensionally by a variety of polydentate ligands,⁸⁻¹³ which create open porous structures with high pore volumes and surface areas.¹⁴ The rich design possibilities of MOFs offer a large diversity of chemical compositions and pore dimensions¹⁵⁻¹⁷ and allow the molecular-sieving properties of MOFs to be extended to larger molecules with a different chemical nature. Recent studies on the adsorption of alcohols in MOFs were focused on the design of stable MOFs to extract alcohols from water¹⁸⁻²² and for alcohol storage.²¹⁻²³ Adsorption mechanisms^{18,24} and flexibility induced by alcohols have also been studied,^{19,21,24-25} but most of these works involve only short-chain alcohols such as methanol, ethanol, and propanol.

Homochiral MOFs (HMOFs) are a subset of structures from the MOF family. They were first synthesized to perform enantioselective heterogeneous catalysis and study the underlying molecular mechanisms.²⁶⁻²⁸ Similarly to other MOFs, these HMOFs are made up of organic and inorganic building units, although in this case at least one of these building units has to be chiral. Recently, 1,1'-bi-2-naphthol (BINOL)-based ligands have been used to generate the first isorecticular series of HMOFs.²⁸⁻²⁹ Increasing emphasis on chiral drugs and chemicals is fueling the development of new adsorbents for enantioselective separation, and BINOL-based materials have proven to be useful for this type of application.³⁰⁻³²

This study focuses on Cd-BINOL,²⁷ a HMOF also known as HMOF-1, due to its distinctive geometry. This MOF is a colorless crystal with the chemical formula $\text{Cd}_3\text{L}_4(\text{NO}_3)_6$, in which L is *R*-6,6'-dichloro-2,2'-dihydroxy-1,1'-binaphthyl-4,4'-bipyridine (Figure 1). The space group ($P4_122$) and chiral ligand of this structure define helical pores running in the z -direction connected by zigzag channels running perpendicular to the z -direction and parallel to the x - or y -axes. The analysis and visualization of the accessible void space of the structure reveals the unusual twisted pore shape of the main channel through which a probe of up to 9.25 Å in diameter can diffuse. Likewise, a probe of up to 5.5 Å in diameter can diffuse through the zigzag channels that connect horizontally or vertically with the main channels. As described in Figure A2 in the Appendix 3, the main channels are connected horizontally by their bottom surface with zigzag channels of a total length of 13.5 Å. This pattern is repeated four times along the z -axis with a rotation of 90°. The aforementioned zigzag channels are referred to as “side channels” hereafter. The areas

that can be occupied by molecules that cannot cross these side channels are considered as “windows” with a diameter of 6.5 Å. Thus, Cd-BINOL is characterized by the presence of big pores and unusual pore shapes. This not only ensures a high adsorption capacity, but also suggests a possible selective behavior. This study is aimed at investigating the selective adsorption of Cd-BINOL for mixtures of pairs of enantiomers of the chiral molecules 2-pentanol (2P), 2-methylbutanol (2MB), and 3-methyl-2-butanol (3M2B). It also encompasses mixtures involving structural isomers 1P, 2P, 3-pentanol (3P), 2MB, 3-methylbutanol (3MB), 2-methyl-2-butanol (2M2B), 3M2B, and 2,2-dimethylpropanol (22DMP). These molecules are displayed for reference in Figure A1 in the Appendix 3. They are aliphatic alcohol isomers with five carbon atoms that differ in the position of the hydroxyl group, chain structure, or both. We conducted Monte Carlo (MC) simulations at room temperature to compute both single and multicomponent adsorptions that were related to behavior at the molecular level. In particular, apart from thermodynamic analysis, we characterized the host-guest and guest-guest interactions through calculations of populations inside the MOF, radial distribution functions (RDFs), and hydrogen-bonding properties. In addition, we discuss the suitability of the ideal adsorbed solution theory (IAST)³³ to predict selectivities and compare them to those obtained at saturation and low-coverage regimes.

Computational Details

Models and force fields

The Cd-BINOL structure was taken from crystallographic information in the literature²⁷ and is compiled in Table A1 in the Appendix 3. In the discussion

throughout this work, the atom numbering followed the crystallographic CIF file: thus, there were four crystallographically distinct oxygen atoms on the naphthols (O₁-O₂ and O₃-O₄ on ligands 1 and 2, respectively), nine oxygen atoms in three nitrate ions (O₅-O₇, O₈-O₁₀, and O₁₁-O₁₃), and chlorine on the naphthols (Cl₁-Cl₂ and Cl₃-Cl₄ on ligands 1 and 2, respectively). The pyridine N atoms were coordinated to Cd, and thus, not accessible. To gain a better insight into the accessible space inside the structure and the shape and size of its channels, probes of different diameter sizes were moved along the channels by using Pore Blazer software.³⁴ This software considered the van der Waals radii of framework atoms and checked the connectivity of channels by using probes of a given diameter. Thus, a detailed view of the accessible space was available and analyzed.

Given that no validated flexible force field has yet been developed, it was a safer approach to keep the framework rigid throughout the simulations. Most of the accessible area available to the guests stemmed from a ligand containing fused aromatic rings that were very rigid, and merely binding of the ligand to the framework metal cations could allow for structural low-frequency deformations. The computer resources saved in this way were available for improving the statistics of the runs. The host-guest and guest-guest interactions were defined through both Lennard-Jones (LJ) and Coulombic potentials. Cd-BINOL was modeled using the LJ parameters from UFF³⁵ and the charges described previously³⁰ (Table A2 in Appendix 3). The alcohol adsorbates were flexible and based on LJ parameters; charges (Table A3 in Appendix 3) and geometries were defined by the TraPPE force field,³⁶⁻³⁷ with flexible bonds (Table A4 in Appendix 3). The LJ cross interactions were calculated

according to Lorentz-Berthelot combining rules.

Simulation details

Adsorption isotherms of the target alcohols for both single components and mixtures were computed at 298 K with RASPA software³⁸ by using grand canonical MC (GCMC) simulations. In this ensemble, the chemical potential, volume, and temperature were kept fixed (μ VT). The chemical potential (μ) is related to the imposed fugacity. A $1 \times 1 \times 1$ unit cell was chosen and, given that the LJ cutoff radius was set to 10 Å, all dimensions of the simulation box were larger than twice the cutoff radius. Periodic boundary conditions³⁹ were applied. Long-range electrostatic interactions were evaluated using the Ewald summation technique. Simulations were arranged in cycles of trial moves, including configurational-biased insertions, deletions, and total and partial reinsertions, as well as random translations and rotations of the molecules. In the case of mixtures, simulations could be speeded up by introducing an additional energy-biased identity change move with the same probability as other intended moves. Each point of the isotherm was obtained after 4×10^6 cycles.

Six independent MC μ VT simulations at 10^5 Pa were carried out in systems of a single adsorbate species, whereas 12 simulations were launched per binary mixture and 18 for each ternary mixture. In the case of chiral compounds, a racemic bulk composition was chosen. All errors given in the tables and figures herein were standard deviations of the mean. After 10^5 cycles of initialization, simulations comprised 4×10^6 cycles of production. The number of adsorbate molecules in the system was monitored throughout the simulations and

so was their average over the independent simulations, and analyzed as a function of production time. An increase of typically around one adsorbate molecule was observed in the systems of both pure adsorbates and mixtures thereof throughout the first 500 000 cycles. This sequence of the simulation had therefore to be reassigned to initialization time and production was only considered from that point on. Following this procedure, calculations of the excess number of adsorbates in mixtures maintained the errors within reasonable boundaries for a statistically meaningful analysis.

Configurations from simulations at saturation taken every 1000 cycles were used to determine valuable microscopic information, such as chirality of the adsorbates, side-channel occupancy, and average hydrogen-bonding properties of the systems.

Hydrogen-bond (HB) analysis relied on a well-established set of geometric criteria for hydrogen bonds:⁴⁰ O-O distance less than 3.5 Å, intermolecular O-H distance below 2.6 Å, and $\text{H-O}_{\text{intra}}\text{-O}_{\text{inter}}$ angle below 30°. No distinction was made between hydrogen-bond donors and acceptors. Alcohols were considered to be within one of the four side channels (or zigzag pores) of Cd-BINOL if their center of mass was within 4 Å of the geometrical center of the $\text{O}_{11}\text{-O}_{11}\text{-Cl}_4\text{-Cl}_4$ moiety (atom indices were according to the CIF-file).²⁷ Chirality was determined by the sign of the chiral volume (obtained by calculating the scalar triple product). TraPPE models carbon centers as united atoms, and therefore, the sign of the chiral volume revealed the handedness of the center.

Complementary simulations in the canonical ensemble (NVT) were also

conducted at 298 K for a single molecule, together with simulations in the grand canonical ensemble at 1 and 10 Pa, and at saturation (10^5 Pa) to compute density profiles (single-molecule simulations), RDFs (at saturation), and hydrogen bonding with framework atoms (single-molecule simulations and at saturation). Henry coefficients, enthalpies, and entropies were obtained by using the Widom test particle insertion method.³⁹ In the canonical ensemble (NVT), random moves involve molecular translation, rotation, and reinsertion.

The adsorption isotherms of the considered mixtures were also predicted by using IAST³³ from results of the pure components. In the IAST methodology, the adsorption isotherm of each compound can be integrated from either experimental or calculated data of the pure adsorbates and fitted to an isotherm model. Herein, the adsorption isotherm for each compound was obtained by MC simulations. The following isotherm models were probed: Toth,⁴¹ Jensen,⁴² Langmuir-Freundlich dual site,⁴³ Janovic,⁴⁴ and Langmuir.⁴⁵ None of them outperformed the others in reproducing the data, so pure isotherms were fitted using the Langmuir model (Figure A3 in the Appendix 3), which was the simplest, best-established model available able to reproduce the computed adsorption isotherms reasonably well. An added benefit of this model is that the fitting procedure was very robust.

All mixtures discussed herein maintained equimolar amounts in the reservoir and, depending on the affinity of the components for the adsorbent, this translated into different numbers of molecules or mole fractions within the adsorbent structure. Both bi- and ternary mixtures of isomers were examined, but this

was not set up as a systematic study aimed at exhausting all possible combinations. Rather, mixtures comprised isomers related by some common structural feature or modification thereof. We also explored the relative adsorption of two components in ternary mixtures *versus* their adsorption in binary mixtures by using IAST methodology and MC simulations. In this way, the 2MB-3MB mixture was compared directly and in combination with 1P, and all three pairwise combinations of 2P-2M2B-3M2B were compared with the ternary mixture. In all cases and methodologies, not only was the qualitative behavior the same, but the ratio of adsorbed molecules was also similar within the error bars of the technique.

Results and Discussion

Separation of optical isomers in Cd-BINOL

Given that Cd-BINOL is a chiral structure, it may well be able to separate chiral mixtures. Therefore, binary mixtures of *R/S* enantiomers have been investigated. Three of the pentyl alcohol isomers possess an asymmetric carbon, namely, 2P, 2MB, and 3M2B, whereas the other structural isomers have no asymmetric carbon. Simulations were performed with a racemic mixture as the reservoir. This is expected to be the most challenging separation. It is also the most important and relevant type of separation, on the grounds that most nonenzymatic synthetic routes lead to racemic mixtures. Figure 2 reflects the evolution of the handedness throughout the simulations, averaged over six independent simulations for improved statistics. These simulations were run under conditions of saturation, as specified in the Computational Details section, and general results, such as the average number of molecules, can be found

in Table 1. The results for the overall handedness are expressed as ee values, which, for our purposes, are obtained by using the Equation (1):

$$\%ee = 100(x_R - x_S), \quad (1)$$

in which x_R and x_S are the mole fractions of R and S isomers adsorbed, so that the ee is a signed value. We expect the system to start in the most favored chiral form and increment that imbalance the longer the simulation goes on, provided the framework is selective towards a chiral form. Changes in chirality do indeed occur spontaneously at this temperature for this force field by inverting like an umbrella. Based on an exponential fit to the autocorrelation function of the handedness (Figure A4 in the Appendix 3), a characteristic correlation length is calculated: its value is four million steps (MSteps) for 2P, and 3 MSteps for 2MB and 3M2B. Given that these lengths are comparable to the lengths of the simulation runs, equilibrium is not reached, but it is still enough for tendencies to emerge. In the R/S -2MB and R/S -3M2B mixtures, no separation is found within this level of accuracy. For 2MB, the overall ee is $-4 \pm 4\%$, whereas for 3M2B it is $-5 \pm 4\%$. On the other hand, 2P slightly favors the R enantiomer: the ee in this case is $10 \pm 4\%$. With respect to evolution of the curve in the last case, a slight increase in ee is observed over the duration of the simulation, as evidenced by the slope of the regression line. On the whole, of all pentyl alcohol isomers, only one pair of stereoisomers presents some degree of separation. For the others, our results show Cd-BINOL to be essentially unfit for the separation of enantiomeric mixtures of either 2MB or 3M2B. This is not to say that Cd-BINOL could not be an interesting material for the separation of some combinations of pentyl alcohols, and

thus, the ability of the material to separate structural isomers will be explored next.

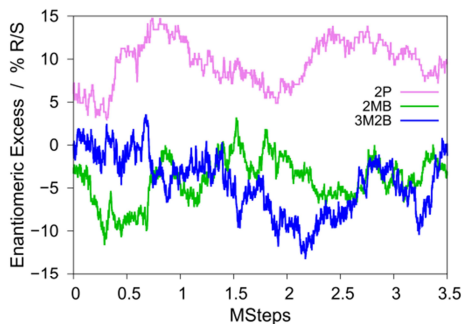


Figure 2. Instantaneous enantiomeric excess (ee) of 2P (pink), 2MB (green), and 3M2B (blue) throughout the simulation. The x -axis indicates the number of MC steps in millions.

Separation of structural isomers in Cd-BINOL

The behavior of eight structural isomers of the general formula $C_5H_{12}O$ is investigated; first, as pure compounds in the Cd-BINOL framework. Figure 3 shows the computed single-component adsorption isotherms for each of these amyl alcohols. Overall, the curves exhibit similar shapes, revealing related adsorption behavior. The onset pressure of adsorption ranges from 0.1 to 10 Pa, approximately, depending on the guest alcohol; it is lowest in 1P and highest in 2M2B. The steep slope of the isotherms provides evidence of rapid pore filling for all the adsorbates. A fit of the isotherms by using the Langmuir model increases more slowly, as can be seen in Figure A3 in the Appendix 3. This is because the shape of the isotherms is known as an S-curve that the Langmuir model is not able to mimic, and it usually involves some cooperativity to drive the filling.

Loadings at saturation are between 4 and 5 mol kg^{-1} of adsorbent (about 50 molecules

per unit cell). The increasing trend in adsorption capacity correlates loosely with the order of onset of adsorption identified previously. It can also be related to structural features of the alcohol isomers that govern packing ability, that is, increasing level of ramification and position of the hydroxyl group. The interplay between features will be key in the case of competitive adsorption of alcohols in mixtures and shall be examined later in this study.

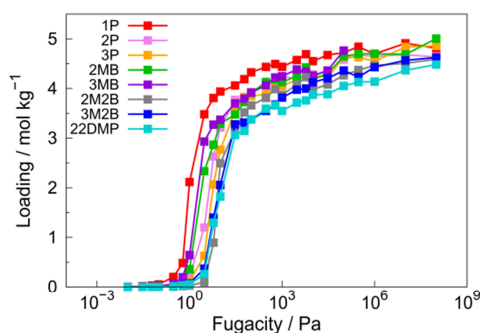


Figure 3. Unary adsorption isotherms of pentanol isomers at 298 K.

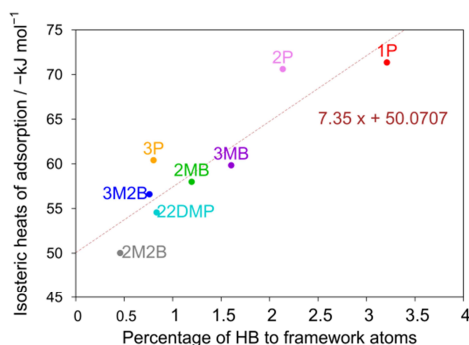


Figure 4. Adsorption enthalpy *versus* percentage of hydrogen bonds to framework.

Low-loading conditions offer an especially interesting perspective for analysis because Henry coefficients used to characterize adsorption behavior relate directly to

thermodynamic properties. In contrast to this macroscopic interpretation, from the point of view of intermolecular forces, one might think that adsorption ought to be mediated by the establishment of hydrogen bonds. Figure 4 represents adsorption enthalpy *versus* the percentage of hydrogen bonds formed between the adsorbate and framework at infinite dilution. Indeed, the more hydrogen bonds formed with the structure, the lower the adsorption enthalpy, and therefore, the stronger the interactions. A linear fit of the data for the different isomers yields an r^2 value of 0.82; a typical value in quantitative structure-activity relationship (QSAR) analysis. Surprisingly, the figures of the percentages of hydrogen bonds formed are very low and cannot account, by themselves, for the lowering of the enthalpy. The slope of the linear fit indicates that 735 kJ mol^{-1} would be achieved per hydrogen bond, which is roughly 30 times the enthalpy lowering contribution of the hydrogen bond itself. The overwhelming majority is due to dispersion forces that arise from confinement. In other words, there is correlation with hydrogen bonding, but not causation. Also, extrapolation of the linear fit to zero hydrogen bonds yields a residual enthalpy of -50 kJ mol^{-1} , also due mainly to dispersion interactions. Full thermodynamic data are available in Table A5 in the Appendix 3.

To characterize the favored adsorption sites, the average occupational density profiles at infinite dilution (substance-volume-temperature (NVT) calculations for a single molecule) for all isomers are displayed in Figure 5. They show that molecules tend to occupy three different areas: the main channel, the side channels, and/or the windows to these channels. All isomers occupy the region of the main channel, but only some of them are also located around

the windows (3P, 2MB, and 3MB) or within the side channels (1P and 2P). This is not to say that at higher densities side channels cannot be occupied given that this analysis only reveals the behavior at infinite dilution. Figure 5 also highlights that atoms O₅ and O₈ of the framework are located at the windows, whereas atoms Cl₄ and O₁₁ are within the channels (atom numbering according to CIF file).

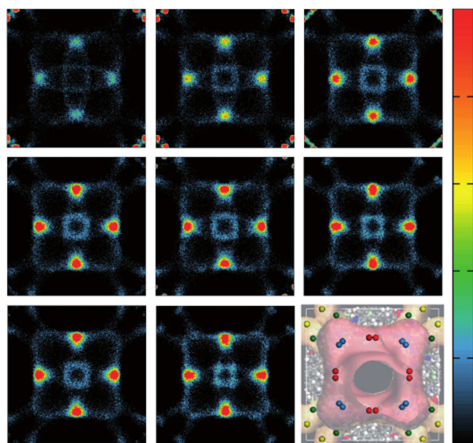


Figure 5. Average occupational density profiles of adsorbate center of mass in an xy -view. From left to right: 1P, 2P, 3P (top); 2MB, 3MB, 2M2B (middle); 3M2B, 22DMP (bottom); and a representation along the same view that highlights several crucial items of the framework: the location of oxygen atoms O₅, O₈, and O₁₁ according to CIF-file notation, belonging to three different nitrate groups, in red, blue, and green, respectively. The yellow spheres mark the center of the side channels.

As the fugacity of the alcohols increases, the framework gradually fills up. To determine the pattern of filling, side-channel occupancy was compared with overall occupancy. This is represented in Figure 6; the x -axis reports the fraction of molecules adsorbed in the whole structure, taking as a reference a fugacity of 100 kPa, whereas the y -axis represents the number of molecules

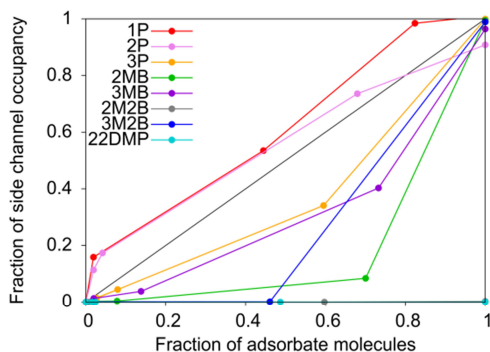


Figure 6. Fraction of side channels occupied *versus* fraction of total occupancy (referenced to saturation occupancy). The black line graphs the identity function representative of equal affinity for side and main channels.

adsorbed per side channel. Analyzing the occupancies reveals that a maximum of one amyl alcohol molecule is adsorbed per side channel. The number of molecules per side channel can thus also be interpreted as the fraction of side channels occupied. In this sense, for those amyl alcohols, the curve of which lies above the identity function, side channels fill before the rest of the framework does. This is the case for 1P and 2P. These two isomers had been found previously (in Figure 4) to exhibit the highest (in absolute value) heats of adsorption and fraction of hydrogen bonds to the framework, although the calculation included all interactions of the guest molecule with the framework, not just the ones within the side channels. Conversely, isomers 3P, 2MB, 3MB, and 3M2B fill side channels after the rest of the framework does. Finally, the remaining two isomers, 2M2B and 22DMP, do not enter side channels at all. These two isomers share the characteristic of possessing an exceptionally bulky and rigid environment around one of their carbon atoms: based on their heavy-atom skeleton, they are the only isomers in the study that are dibranched on the same carbon atom. As a consequence, they cannot

enter narrow channels or pores; this was previously observed in zeolitic imidazolate framework ZIF-77.⁴⁶

In the case of isomers that present chirality, namely 2P, 2MB, and 3M2B, we explored whether handedness was favored in the special confinement conditions of the side channels. The $\epsilon\epsilon$ in the side channels was found to be: $26 \pm 12\%$ (2P), $4 \pm 18\%$ (2MB), and $-23 \pm 9\%$ (3M2B). Isomer 2MB showed no selective adsorption towards any of the enantiomers, whereas only slightly increased adsorptions are detected in 2P and in 3M2B. Based on these results it does not appear promising to design a separation strategy based on exploiting solely the low-coverage regime in 2P.

After studying the low-coverage regime and the filling behavior with increasing loading, we now turn our attention to the high-loading regime. For pure systems at a fugacity of 100 kPa (close to saturation conditions), Table 1 compiles the results. The hydrogen-bond information in Tables 1-3 is also available as bar charts in the Appendix 3 for visual inspection (Figures A5-A7 in the Appendix 3). In Table 1, the percentage of hydrogen bonds between guest molecules is labeled as f_{1-1} . This notation can be straightforwardly extended to pair interactions in binary and ternary mixtures of guest molecules (Tables 2 and 3, respectively, below) and is therefore consistent herein. All isomers maintain, on average, close to four molecules in the four side channels, except 2M2B and 22DMP, as previously noted. The total number of molecules that fit in the framework lies at around 50, except in 2M2B (44.8) and 22DMP (41.2). The difference in the case of 2M2B is satisfactorily explained as a consequence of the empty side channels, whereas in the case of 22DMP packing is also less efficient at this fugacity. As the

adsorption isotherm in Figure 3 showed, however, the latter difference gradually vanishes at higher fugacities.

The hydrogen-bonding probabilities of the alcohols are similar. Those to other guest molecules f_{1-1} have values above 100%, typically around 110%. This means that a number of alcohol molecules are involved in more than one hydrogen bond, generally one as a hydrogen-bond donor and one as an acceptor. By taking into account the probability of hydrogen bonding to the framework, the total probability lies at around 125%. A tendency emerges, in which the probabilities are higher in those molecules with more accessible hydroxyl groups, such as in 1P, 2P, or 22DMP, than in less accessible ones such as 3P, 2M2B, or 3M2B. This effect is small, but significant. Hydrogen bonds form preferably to other guest molecules rather than to the framework. This is a bit surprising, given that the majority of oxygen atoms of the 24 nitrate ions in the framework are accessible (40 out of the 72 atoms) and competing with the alcohol molecules as hydrogen-bond acceptors. Considering only the accessible oxygen atoms of the nitrates, and assuming that a hydrogen-bond donor has the same probability of forming a hydrogen bond to a nitrate oxygen atom as that of an alcohol molecule, we would expect f_{1-frwk} to take values from 25 to 33%. This can also be expressed in a different way. We can define hydrogen-bond selectivity according to Equation (2) in much the same way as adsorption selectivity is defined:

$$S_{HB,ij} = \frac{\frac{n_{HB,i}}{N_i}}{\frac{n_{HB,j}}{N_j}}, \quad (2)$$

in which $n_{HB,i}$ is the number of hydrogen bonds to molecule i and N_i the number of sites of i (in the case of the framework, it is taken to be the accessible sites). The

Table 1. Hydrogen-bond statistics for pure compounds in Cd-BINOL at 100 kPa fugacity.*

	Pure compounds			
	1P	2P	3P	22DMP
no. simulations	6	6	6	6
N	52.7 ± 0.2	52 ± 0.4	51.2 ± 0.2	41.23 ± 0.11
$N^{\text{side channel}}$	4.04 ± 0.05	3.63 ± 0.17	3.997 ± 0.002	0.000 ± 0.001
f_{1-1}	114 ± 2	117 ± 3	102.1 ± 1.5	113.5 ± 1.8
f_{1-frwk}	14.8 ± 1	13.6 ± 1.4	13.5 ± 0.5	18.5 ± 0.8
$f_{1-1}^{\text{side channel}}$	53 ± 9	37 ± 7	7.4 ± 3.5	-
$f_{1-frwk}^{\text{side channel}}$	13.5 ± 4.5	24 ± 6	1.2 ± 0.5	-
	2MB	3MB	2M2B	3M2B
no. simulations	6	6	6	6
N	51.7 ± 0.2	50.7 ± 0.6	44.8 ± 0.4	49.2 ± 0.5
$N^{\text{side channel}}$	3.98 ± 0.02	3.86 ± 0.14	0.01 ± 0.004	3.957 ± 0.015
f_{1-1}	110 ± 2	108.4 ± 1.1	108.7 ± 1.6	112 ± 2
f_{1-frwk}	17.6 ± 1.5	20.6 ± 1.2	15.4 ± 0.4	13.9 ± 0.5
$f_{1-1}^{\text{side channel}}$	37 ± 12	26 ± 5	-	15 ± 4
$f_{1-frwk}^{\text{side channel}}$	30 ± 8	14 ± 3	-	11 ± 3

* N is the total number of guest molecules in the unit cell (and simulation box) and $N^{\text{side channel}}$ the number of guest molecules in the four side channels. All probabilities are given as percentages. The probability for a guest molecule to be hydrogen-bonded to other guest molecules is labeled f_{1-1} . The probability for a guest molecule to be hydrogen-bonded to atoms of the framework is labeled f_{1-frwk} .

hydrogen-bond selectivity, $S_{HB,ij}$, varies between values of 2.3-2.6 (3MB and 2MB, respectively) and values of 3.5-3.65 (2P and 3M2B, respectively). Because these values are all well above one, a guest molecule has a stronger affinity to other molecules than to framework sites in terms of hydrogen bonding.

This hydrogen-bond bias towards other guest molecules explains the S-curve behavior of the pure isotherms in Figure 3

noticed previously: once guest molecules bind to the framework, other alcohol molecules are easily added due to the preferred formation of alcohol-alcohol hydrogen bonds. The cooperativity occurs in those molecules settled in the framework draw in further molecules.

In line with the observations made around the results in Figure 6, the inner surface of the side channels is a more hydrophobic environment. All isomers within the side

channels form, on average, considerably fewer hydrogen bonds to guest molecules due to confinement, while maintaining comparable probabilities of hydrogen-bond formation to the framework, and as a consequence they form fewer hydrogen bonds per molecule overall. Marked differences can be observed between isomers: especially for 3P, the hydroxyl group of which is buried deep within the channel, which is almost unable to form hydrogen bonds either to the framework or to other guest molecules. The hydroxyl group in 3M2B lies also quite close to the center of mass of the molecule and, as a result, forms fewer hydrogen bonds than the rest of the isomers. This behavior of 3P and 3M2B is also observed at low coverage (Table A6 in the Appendix 3).

The pure adsorption isotherms discussed earlier revealed that 1P was the most easily adsorbed alcohol of those considered herein. Therefore, equimolar binary mixtures of 1P with any other isomer should lead to adsorption isotherms that contain mostly 1P. To check this, to check the ability of Cd-BINOL to separate effectively 1P from mixtures with other pentanol isomers, and to test the ability of IAST to predict adsorption behavior, MC simulations of binary mixtures 1P-2M2B, 1P-3M2B, and 1P-22DMP were conducted. The remaining isomers were also tested against 1P, albeit as part of ternary mixtures. Given that alcohol molecules form many hydrogen bonds with each other, we would expect failure of the IAST model. Nonetheless, these hydrogen bonds already form in the pure compounds that are used as inputs to the model. It is therefore interesting to determine if IAST works and, regardless of the finding, if it can be related to hydrogen-bond networks in the mixtures.

Are they a straightforward extension of the hydrogen bonds of pure substances and calculated by applying preset probabilities? Or, on the contrary, is there a special affinity between different isomers that arises from matching shapes in this confined environment?

The adsorption isotherms of 1P-2M2B, 1P-3M2B, and 1P-22DMP indeed favor strongly 1P at all fugacities (Figure 7). This can be inferred from the MC simulation data, which also show that selectivities are good. However, selectivities are discussed in more detail later. The bulkiest isomers (2M2B and 22DMP) are comparatively the least adsorbed. With respect to IAST predictions, they are qualitatively correct, although serious discrepancies are observed. IAST overestimates the separation capacity for these mixtures. In fact, IAST predicts very similar isotherms for 1P-2M2B and 1P-3M2B, suggesting that 2M2B and 3M2B are adsorbed to the same degree.

The IAST prediction for the binary 2M2B-3M2B mixture even predicts a slight edge for 2M2B, which is contrary to MC simulation results (Figure A9 in the Appendix 3). Also, in the 1P-22DMP mixture, at the higher end of the fugacity range 22DMP would appear to be almost completely excluded according to IAST.

Three ternary mixtures were also studied: 1P-2P-3P, in which the influence of the hydroxyl position was assessed; 1P-3MB-2MB, in which “methylated 1-butanol” was studied with a methyl grafted at carbons 4 (yielding 1P), 3 (3MB), or 2 (2MB); and 2P-3M2B-2M2B, in which methylated 2-butanol was studied with methyl grafted at carbons 4 (2P), 3 (3M2B), or 2 (2M2B). In the equimolar ternary mixture of the linear

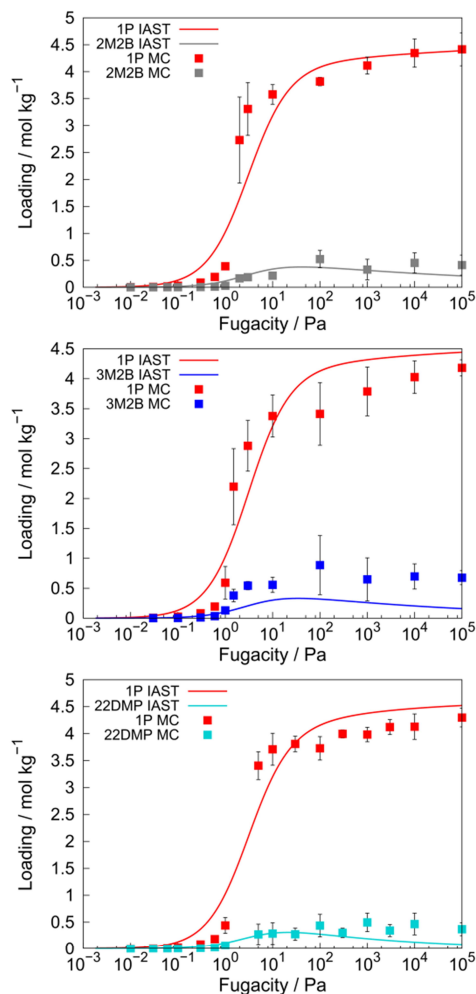


Figure 7. From top to bottom, adsorption isotherms at 298 K of mixtures of 1P-2M2B (red and gray, respectively), 1P-3M2B (red and blue, respectively), and 1P-22DMP (red and turquoise, respectively) obtained by MC simulations (symbols) and predicted by IAST (lines).

(in the chemical sense) alcohols, the most adsorbed species is again 1P (the only molecule with a linear heavy-atom backbone in a topological sense), followed by 2P and then 3P (Figure 8). This holds

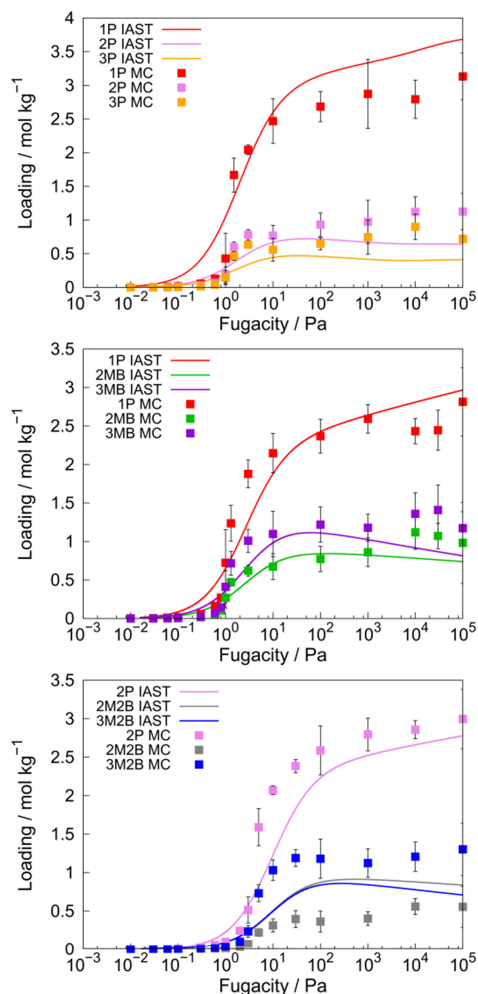


Figure 8. From top to bottom, adsorption isotherms at 298 K of mixtures of 1P-2P-3P (red, magenta, and orange, respectively), 1P-2MB-3MB (red, green, and blue, respectively) obtained by MC simulations (symbols) and predicted by IAST (lines)

true at all fugacities, and the relationship between these three isomers is also roughly maintained throughout the whole fugacity range.

These same observations also hold true in IAST predictions, although IAST overestimates the difference between 1P adsorption and any of the other components. The 1P-2MB-2MB mixture leads to very similar conclusions. These compounds are adsorbed in the 1P, 3MB, 2MB order. Two observations can be made: first, the biggest difference is found between linear and branched isomers; and, second, the further away the methyl group, the better for adsorption. These facts are also reflected by IAST predictions in a qualitative way: again, selectivities are overestimated in favor of 1P, whereas the 3MB/2MB selectivity is reproduced fairly well. We now turn to the mixture of 2P-2M2B-3M2B, which, as noted previously, can be formally seen as instances of 2-butanol molecules on which a methyl group has been grafted at positions 4, 2, and 3, respectively, and that is adsorbed in the 2P, 3M2B, 2M2B order. Again, the further away the methyl group, the better for the loading; 3M2B and 2M2B were expected to be rather similar, even with a slight bias towards 2M2B, which was the least favored guest in the mixture, according to the authoritative MC simulations. The reason for this failure of IAST is not due to selective interactions with 2P: in the binary mixture of 3M2B-2M2B, the same mismatch between IAST and MC simulations is observed (Figure A9 in the Appendix 3). To sum up the observations of the adsorption isotherms, the freer the hydroxyl group, the more molecules are adsorbed.

The tendencies observed in isotherms beg the question whether they can be related to hydrogen-bonding patterns. We therefore had a close look at the statistics of the mixtures, including hydrogen bonding, with an eye to comparing them with the pure compounds. In Table 2, the number of molecules per unit cell is recorded. This

number reflects the information given in Figure 8, in which the affinity of the structure for 1P was seen. Table 2 shows that the total number of molecules is higher than that predicted from the number of molecules in the pure systems. This can be quantified as a percentage of excess molecules in the framework, as expressed by Equation (3):

$$\%ads_{\text{excess}} = \frac{N_{\text{tot}} - \sum x_i N_{i,\text{pure}}}{\sum x_i N_{i,\text{pure}}} \times 100, \quad (3)$$

in which x_i is the mole fraction of component i in the adsorbent. This percentage is positive in all cases, and similar among the mixtures studied. Roughly 4% more molecules (in absolute numbers, 2 molecules per unit cell) fit in the porous structure. This fact can be explained because combining molecules of different shapes enables more efficient packing. Although all guest molecules are deformable, their conformational flexibility is not big enough to offset the opportunities for better packing offered by using more than one isomer. Additionally, in those mixtures that contain one of the bulky molecules, 2M2B or 22DMP, that are not able to enter the side channels, excess adsorption will take place because in the mixture the side channels are occupied by the nonbulky isomer, such that there is one molecule in each of the four side channels. This effect is systematic, but small, as it accounts for only 0.6% excess molecules (0.3 excess molecules) in the mixtures of 1P-2M2B and 1P-22DMP.

For the mixture 1P-3M2B, the composition of the side channel is interesting. In this case, each of the adsorbates in the pure state is able to populate the side channels, but in the mixture, the side channels only contain 1P. As we established in Figure 6, isomer 1P favors side channels, whereas 3M2B does not and therein lies the explanation.

Table 2 also reveals the percentages of hydrogen bonds formed. For instance, for the first component in the mixture, f_{1-1} is the percentage of self-association, whereas f_{1-2} is the percentage of cross-association to the second component. Variable $f_{1-1} + f_{1-2} + f_{1-frwk}$ is the total percentage of hydrogen bonds formed per molecule of the first type, and it is significantly greater than that in single-component adsorptions. Typically, in the mixture, the total percentage is close to 155% and most molecules engage in one hydrogen bond as a donor and one as an acceptor. In fact, f_{1-1} alone is (in 1P-2M2B and 1P-22DMP) bigger than in the single-component case. How should we then best think of the

arrangement of molecules in the pore? Given that the structure favors markedly 1P and the numbers of molecules of this type in the pure system and the mixtures, we can almost think of the structure as being filled with almost as many 1P molecules as in the single-component case plus a few molecules of different shape. However, the last of these do not merely take advantage of voids in the structure that are unfit for 1P molecules, they completely distort the arrangement within the pores and enhance the average number of hydrogen bonds created. Hydroxyl groups are present in more than one local environment and can adapt better to enable the formation of more hydrogen bonds.

Table 2. Hydrogen-bond statistics for binary mixtures.*

	Binary mixtures (1)-(2)		
	1P-2M2B	1P-3M2B	1P-22DMP
no. simulations	12	12	11
N_1	50.0 ± 0.5	44.4 ± 0.5	50.2 ± 0.4
N_2	4.1 ± 0.5	9.7 ± 0.5	3.8 ± 0.3
N_{tot}	54.13 ± 0.15	54.13 ± 0.17	53.9 ± 0.2
%ads _{excess}	4.2 ± 0.5	3.9 ± 0.6	3.9 ± 0.6
$N_1^{\text{side channel}}$	3.997 ± 0.003	3.91 ± 0.07	3.985 ± 0.015
$N_2^{\text{side channel}}$	0.000 ± 0.000	0.0005 ± 0.0003	0 ± 0
f_{1-1}	127 ± 2	109 ± 3	126.8 ± 1.4
f_{2-2}	13 ± 3	25 ± 5	9 ± 3
f_{1-2}	11.5 ± 1.5	28.6 ± 1.6	10.5 ± 0.9
f_{2-1}	130 ± 5	129 ± 5	134 ± 4
f_{1-frwk}	16.8 ± 0.7	16.8 ± 0.9	17.1 ± 0.7
f_{2-frwk}	14 ± 3	17 ± 2	14.5 ± 2

*Percentages of average self- and cross-association, f_{i-i} and f_{i-j} respectively, refer to compound i in the binary mixture. N_i denotes the number of adsorbed molecules of compound i in the mixture. Conditions are at 100 kPa fugacity.

Table 3. Hydrogen-bond statistics for ternary mixtures.*

	Ternary mixtures (1)-(2)-(3)		
	1P-2P-3P	1P-2MB-3MB	2P-2M2B-3M2B
no. simulations	16	18	18
N_1	33.4 ± 0.5	31.1 ± 0.4	33.9 ± 0.4
N_2	11.9 ± 0.4	10.4 ± 0.3	5.4 ± 0.2
N_3	9.2 ± 0.2	13.1 ± 0.2	14.4 ± 0.3
N_{tot}	54.50 ± 0.16	54.62 ± 0.08	53.72 ± 0.13
%ads _{excess}	4.2 ± 0.5	5.0 ± 0.6	6.3 ± 0.8
$N_1^{side\ channel}$	3.63 ± 0.07	3.90 ± 0.04	3.92 ± 0.05
$N_2^{side\ channel}$	0.32 ± 0.09	0.020 ± 0.009	0.0 ± 0.0
$N_3^{side\ channel}$	0.031 ± 0.008	0.033 ± 0.007	0.002 ± 0.001
f_{1-1}	86 ± 3	78 ± 2	78 ± 2
f_{2-2}	35.2 ± 1.5	31.4 ± 1.5	19.5 ± 1.0
f_{3-3}	28 ± 2	39.0 ± 1.2	48 ± 2
f_{1-2}	31.2 ± 1.5	26.8 ± 0.8	13.8 ± 0.5
f_{2-1}	86 ± 2	79 ± 2	84.9 ± 1.3
f_{1-3}	24.2 ± 1.2	32.7 ± 0.6	38.6 ± 1.0
f_{3-1}	85 ± 2	77.6 ± 1.6	91.7 ± 1.8
f_{2-3}	29.7 ± 1.3	38.3 ± 1.1	45.9 ± 1.6
f_{3-2}	37.8 ± 1.3	30.9 ± 1.3	17.8 ± 0.9
f_{1-frwk}	16.0 ± 0.9	16.4 ± 0.7	16.3 ± 0.5
f_{2-frwk}	14.5 ± 1.1	16.8 ± 0.9	8.8 ± 0.9
f_{3-frwk}	17.5 ± 1.4	16.9 ± 0.7	12.5 ± 0.7

*Percentages of average self- and cross-association, f_{i-i} and f_{i-j} ($i \neq j$), respectively, refer to compound i in the ternary mixture. N_i denotes the number of adsorbed molecules of compound i in the mixture.

The percentage of hydrogen bonds formed to the framework, on the other hand, remains similar to that of the single-component case. Neither the major nor minor components engage in a significantly

greater number of hydrogen bonds to the framework on a per molecule basis, instead they both stay similar. This is slightly counterintuitive because one might think that, given that 1P molecules are already

adsorbed at lower fugacities and in greater numbers, they would attach preferably to the framework and pull the other ones in, but this is not what happens under these near-saturation conditions. We already alluded to the reason for this behavior in the comments on Figure 4: the hydrogen bonds to the framework are not the driving force for adsorption; they represent only a small portion of the interaction enthalpy.

The three ternary mixtures, 1P-2P-3P, 1P-2MB-3MB, and 2P-2M2B-3M2B, previously introduced were analyzed with respect to hydrogen bonding and results are shown in Table 3. Again, excess adsorption similar to or larger than that of the binary mixtures is observed. Isomer 1P is the major component, but its share is even larger in the side channels. The only significant minor component in the side channel is 2P, in keeping with observations made around Figure 6. Components of the ternary mixtures are involved in many hydrogen bonds on a per molecule basis, comparable to those of the binary mixtures. Hydrogen bonding to the framework is also similar to binary (and pure) systems and similar among components, regardless of them being major or minor components of the mixture. One noticeable exception is the unusually low hydrogen-bonding probability of 2M2B to the framework in the last mixture. A possible explanation for this is that 2M2B is less prone to form hydrogen bonds to the framework at low coverage (Figure 4), and, although at saturation it ultimately does, it is probably less competitive than the rest of the isomers in the mixture. All in all, the findings for the ternary mixtures are similar to those in the binary mixtures.

To refine the analysis and answer the question whether there is a special affinity for hydrogen bonds of a given type, for

instance, self- or cross-association, we must take into account the number of molecules of each type within the adsorbent. This can be done by comparing the percentages to those from a probabilistic model fitted to reproduce the total association of every component. Details are described and discussed in the Appendix 3 and results are presented in Tables A7 and A8. The most important conclusions are that all components of the mixture engage in more hydrogen bonds than their pure counterpart system, especially the minor components. Although the distribution is roughly random, significant deviations occur. Self-association is favored over cross-association. In ternary mixtures, the cross-association between the two minor components of the mixture appears also to be comparatively favored.

The analysis of pure isotherms or the IAST method generally work well to single out the minor components of a mixture, but the numbers for these minor components in the MC simulations are boosted by the fact that they are able to occupy suitable local environments in the structure in which they can establish more hydrogen bonds on average. This is because the higher adsorbate loading in the mixtures makes hydrogen bonds less prone to break.

Hydrogen bonds have thus an influence on the capacity of IAST results to predict satisfactorily the results of the much more time consuming (but more reliable) MC simulations. In Table A9 in the Appendix 3, qualitative IAST performance is matched against a qualitative assessment of hydrogen-bonding abnormalities based on quantitative criteria. Overall, the qualitative agreement is satisfactory: there are eight coincidences, three tests are inconclusive, and there is one failure.

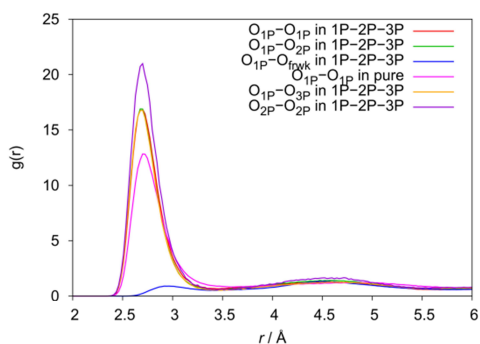


Figure 9. Oxygen-oxygen RDFs at saturation, in a ternary mixture of 1P-2P-3P: $O_{1P}-O_{1P}$, $O_{1P}-O_{2P}$, $O_{1P}-O_{3P}$, $O_{1P}-O_{frwk}$, $O_{2P}-O_{2P}$, and pure $O_{1P}-O_{1P}$.

The previous conclusions reached by introducing the probabilistic model could have also been derived, or at least suspected, from the analysis of RDFs (also known as $g(r)$ functions), such as those shown in Figure 9. Nevertheless, this is a less reliable procedure because the RDFs graph oxygen-oxygen distributions, but not hydrogen bonds directly. Of those oxygen pairs within a suitable distance for hydrogen bonding, roughly 10% are not actually engaged in hydrogen bonding. Figure 9 shows as a representative case the 1P-1P RDF of the pure system and compares it with several oxygen-oxygen RDFs taken from the 1P-2P-3P mixture. The RDF for the oxygen atoms in the single 1P adsorbate system has a peak value of 12.8, whereas 1P oxygen involved in ternary mixtures of 1P-2P-3P has a considerably higher peak value if measured against 1P, 2P, or 3P, as a consequence of 1P engaging generally in more hydrogen bonds in the mixture. The $O_{2P}-O_{2P}$ peak in this mixture is also displayed; it is in fact the highest peak in the graph and highlights the increased self-association over cross-association. The distance distribution of O_{1P} to the oxygen atoms of the framework has a local first maximum of 0.9, which highlights weak interactions with the framework, but RDFs also provide new information. In the

mixture, peaks are slightly shifted towards smaller distances.

The effect is small, but is a consequence of the higher number of molecules found in the mixtures relative to pure adsorbates. That is also the reason why RDFs of the mixture are slightly less broad. The second maximum in the RDFs has a value in the range 1.3-1.6 and is located at around 4.60 Å (*versus* values of 0.85-1.2 in the pure compounds and shifted 0.05-0.30 Å), and the third is generally barely noticeable. In the pure substances, this second maximum is lower. This shows that the order within the pores increases in the mixtures.

Adsorption isotherms in pure systems and mixtures thereof have been considered so far and rationalized. Likewise, we examine these data more specifically from the important point of view of adsorption selectivity. Although we are mainly interested in selectivity at high loadings, which would be the ones of most practical interest, we are also keen on assessing the suitability of the calculations of this magnitude at low coverage from the ratio of Henry coefficients to predict the values at finite pressure. These values can be calculated quite quickly, and we therefore compare them with IAST selectivity stemming from our previous calculations.

The ratio of Henry coefficients of pure components has been demonstrated to be a very useful approximation to the selectivity at low loading.⁴⁷⁻⁴⁸ Pore type and size of the adsorbent, and molecular weight and shape of the adsorbate have a profound effect on enthalpy and entropy, which determine the Henry coefficients.⁴⁹⁻⁵⁰ Thus, Henry coefficients reflect the adsorption equilibrium at low coverage and the interaction of the molecules with the strongest adsorption sites.⁵¹ The selective

potential of an adsorbent can be determined through the separation factor (α_{ij}), which expresses the over- or under-representation of component i over j in the adsorbent and is calculated as the ratio of the Henry coefficients for these compounds: K_{Hi} and K_{Hj} in Equation (4).

$$\alpha_{ij} = \frac{K_{Hi}}{K_{Hj}} \quad (4)$$

The separation factor corresponds to the adsorption selectivity calculated for the low-coverage regime. To evaluate the accuracy and reliability of this separation factor, adsorption selectivity (S_{ij}) is also calculated through the ratio of adsorption loadings, N_i and N_j , of components i and j in the mixture at a fugacity of 100 kPa, as expressed in Equation (5).

$$S_{ij} = \frac{N_i}{N_j} \quad (5)$$

Figure 10 provides a comparison of the values of separation factor and selectivity. The pairs of compounds are those involved in the equimolar mixtures studied through the analysis of adsorption, as shown in Figures 7 and 8 and Figures A8-A10 in the Appendix 3. In general terms, separation factors overestimate selectivity by up to a factor of two. Underestimation, on the contrary, is not frequent and, when it happens, it is only small. As mentioned previously, Henry coefficients reveal the adsorption equilibrium at low coverage and the separation factor that explains selectivity considers only host-guest interactions. The selectivity calculated from adsorption loadings at finite fugacity (100 kPa), on the contrary, is influenced by host-guest and guest-guest interactions. Thus, especially in systems with low guest-guest interactions, the match between separation factor and adsorption selectivity is expected to be good. Clearly, this is not the case for the pentanol

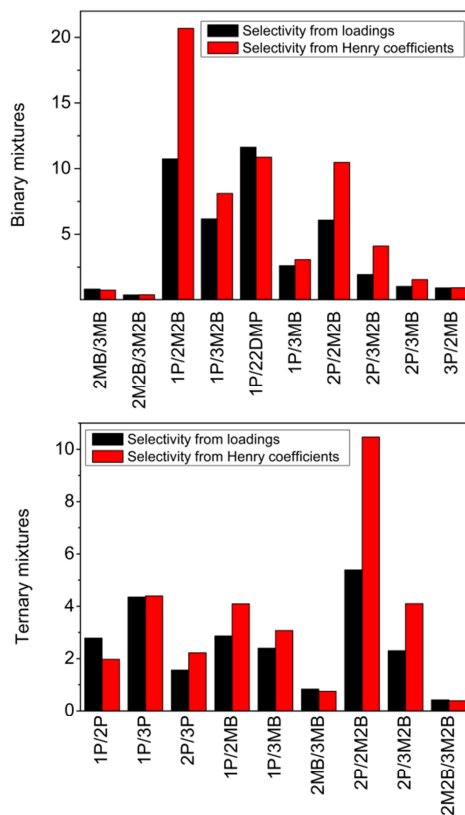


Figure 10. Adsorption selectivity calculated through adsorption loadings (black) and Henry coefficients (red) for several components of bi- (top) and ternary (bottom) mixtures.

isomers in this study, but selectivity is a competition and, if guest-guest interactions affect the components similarly, these selectivities can still be rather similar due to error compensation. Taking into account the crudeness of the approach for these models, it is indeed surprising that extrapolation of the adsorption selectivity from infinite dilution is quite good. In fact, a linear regression yields a better correlation factor than that of IAST to the MC adsorption selectivity. In short, adsorption selectivity can be predicted both by the separation factor and by IAST; it is crudely similar to those obtained from MC

simulations, although generally too optimistic for altogether different reasons.

On the other hand, looking exclusively at adsorption selectivity, there are some pairs that show values over five at high loading, which means adsorption in the structure of the first compound, whereas the second compound is largely excluded. The fact that this is achieved in an adsorbent with big pores, at high loading, is important because it enables fast separation of great amounts of matter without clogging up the structure. Generally speaking, some combinations of adsorbent and mixtures of adsorbates are known to achieve impressive values of selectivity at low loading,⁵² but at higher loading these selectivities decrease considerably, which makes the adsorbent of less practical value. Cd-BINOL strongly favors 1P over 2M2B, 3M2B, and 22DMP. As explained before, 1P is an unbranched isomer and 2M2B, 3M2B, and 22DMP are the bulkiest isomers, the structural features of which shield the functional group. The three-dimensional shape of the rest of the compounds in the group of alcohol isomers, 2P, 3P, 2MB, and 3MB, are intermediate between 1P and the 2M2B/3M2B/22DMP group, and their separation from each other is more difficult.

Conclusions

The adsorption of pentanol isomers and mixtures thereof has been studied in Cd-BINOL. This chiral structure adsorbs slightly more *R*-2P than the *S* isomer from a racemic mixture.

Results at low coverage indicate that only the linear (1P) or closest to linear (2P) isomers are found in the side channels of the structure preferably to the main channels. Two of the isomers, 2M2B and

22DMP, do not enter the side channels at all up to the fugacity probed (100 kPa).

At higher values of fugacity, adsorption of the linear 1P is favored over branched molecules. As a general rule, adsorption is most favored the further away the bulkiest part of the molecule is from the hydroxyl group. Therefore, 1P is clearly favored over 3MB and this, in turn, slightly favored over 2MB. This also indicates that isomers that share similar structural features are difficult to separate by using this framework. This is the case for 3MB, 3P, and 2MB.

Adsorption selectivities at low coverage, that is, separation factors, recorded values up to 20 and did not drop too strongly, at most by a factor of two and only for the highest values, when fugacity increased to 100 kPa. It follows that separation factors could have been used to predict selectivities at higher fugacities: they prove reliable in their tendencies, although not accurate. The selective behavior is generally overestimated. Alternative predictions through the IAST method reproduce mixture isotherms qualitatively. Despite accounting implicitly for some guest-guest interactions, overall selectivity predictions do not improve. As a quantitative predictive tool, IAST is therefore not fit for purpose in these systems.

To find out the reasons for the behavior of IAST, hydrogen bonds were analyzed. For the pure substances, all isomers engage in similar numbers of hydrogen bonds, around 1.25 per molecule, of which an unexpectedly low 0.15 correspond to bonds to the framework. In mixtures containing 1P, the total number of hydrogen bonds rises to around 1.55 for the major component 1P, and the total number of molecules in the framework increases by 4%. As a consequence, the order increases, as

manifested by oxygen-oxygen $g(r)$ functions. The number of hydrogen bonds to the framework remains similar to the pure case, both for major and minor components. Side channels are occupied almost exclusively by 1P (or in its absence by 2P). All components of the mixture engage in more hydrogen bonds than their pure counterpart system, especially the minor components. Furthermore, self-association is found to be slightly favored over cross-association. Qualitative IAST performance is matched against a qualitative assessment of hydrogen-bonding abnormalities based on quantitative criteria to yield satisfactory agreement.

The picture that emerges for these mixtures is a departure from the major component network. Minor components are instrumental in increasing the packing due to shape complementarity and increased hydrogen bonding. Hydroxyl groups in a multicomponent system are present in more than one local environment and can adapt better to enable the formation of more hydrogen bonds.

Finally, and keeping in mind possible applications for purification, we have found that Cd-BINOL behaves selectively towards 1P at saturation, notwithstanding the large size of the main channel. This is promising because this structure achieves a high loading under these conditions that should enable fast separation. Overall, this MOF thus appears as a promising candidate for adsorption-based separations of mixtures of alcohol isomers, providing a low-energy separation alternative to current technologies.

Acknowledgments

This work was supported by the European Research Council through an ERC Starting

Grant (ERC2011-StG-279520-RASPA), by MINECO (CTQ2013-48396-P), and the Andalucía Region (FQM-1851).

Bibliography

- (1) Gosselin, R. E.; Smith, R. P.; Hodge, H. C.; Braddock, J. E., *Clinical Toxicology of Commercial Products. 5th*. Williams & Wilkins: Baltimore, 1994.
- (2) Ullmann, F.; Gerhartz, W.; Yamamoto, Y. S.; Campbell, F. T.; Pfefferkorn, R.; Rounsaville, J. F., In *Ullmann's Encyclopedia of Industrial Chemistry. 7th Edition*, Wiley-VCH Verlag GmbH: 2011.
- (3) Browning, E.; Buhler, D. R.; Reed, D. J., *Toxicity & Mechanisms of Industrial Solvents. 2nd Edition*. Elsevier Science: 1989.
- (4) O'Neil, M. J., In *The Merck Index: An Encyclopedia of Chemical, Drugs and Biologicals. 14th Edition*, Royal Society of Chemistry: 2006.
- (5) Ivanova, E. P.; Kostova, M. A.; Koumanova, B. K., *Asia-Pac. J. Chem. Eng.* **2010**, 5 (6), 869-881.
- (6) Jr., R. J. L., *Hawley's Condensed Chemical Dictionary*. John Wiley & Sons: 2002.
- (7) Kroschwitz, J. I.; Seidel, A., In *Kirk-Othmer Encyclopedia of Chemical Technology. 5th Edition*, Wiley Interscience: 2006.
- (8) Chen, B. L.; Eddaoudi, M.; Hyde, S. T.; O'Keeffe, M.; Yaghi, O. M., *Science* **2001**, 291 (5506), 1021-1023.
- (9) Cheetham, A. K.; Rao, C. N. R., *Science* **2007**, 318(5847), 58-59.
- (10) Rowsell, J. L. C.; Spencer, E. C.; Eckert, J.; Howard, J. A. K.; Yaghi, O. M., *Science* **2005**, 309 (5739), 1350-1354.
- (11) Zhao, X. B.; Xiao, B.; Fletcher, A. J.; Thomas, K. M.; Bradshaw, D.; Rosseinsky, M. J., *Science* **2004**, 306(5698), 1012-1015.
- (12) Eddaoudi, M.; Kim, J.; Rosi, N.; Vodak, D.; Wachter, J.; O'Keeffe, M.; Yaghi, O. M., *Science* **2002**, 295(5554), 469-472.
- (13) Li, H.; Eddaoudi, M.; O'Keeffe, M.; Yaghi, O. M., *Nature* **1999**, 402(6759), 276-279.

- (14) Jiang, D.; Urakawa, A.; Yulikov, M.; Mallat, T.; Jeschke, G.; Baiker, A., *Chem.- Eur. J.* **2009**, *15*(45), 12255-12262.
- (15) Kitagawa, S.; Kitaura, R.; Noro, S., *Angew. Chem., Int. Ed.* **2004**, *43*(18), 2334-2375.
- (16) Ferey, G., *Chem. Soc. Rev.* **2008**, *37*(1), 191-214.
- (17) Kitagawa, S.; Matsuda, R., *Coord. Chem. Rev.* **2007**, *251*(21-24), 2490-2509.
- (18) Nalaparaju, A.; Zhao, X. S.; Jiang, J. W., *J. Phys. Chem. C* **2010**, *114*(26), 11542-11550.
- (19) Liu, X.-L.; Li, Y.-S.; Zhu, G.-Q.; Ban, Y.-J.; Xu, L.-Y.; Yang, W.-S., *Angew. Chem., Int. Ed.* **2011**, *50*(45), 10636-10639.
- (20) Borjigin, T.; Sun, F.; Zhang, J.; Cai, K.; Ren, H.; Zhu, G., *Chem. Comm.* **2012**, *48*(61), 7613-7615.
- (21) Inumaru, K.; Kikudome, T.; Fukuoka, H.; Yamanaka, S., *J. Am. Chem. Soc.* **2008**, *130*(31), 10038-10039.
- (22) Chen, Y. F.; Lee, J. Y.; Babarao, R.; Li, J.; Jiang, J. W., *J. Phys. Chem. C* **2010**, *114*(14), 6602-6609.
- (23) Li, H.; Shi, W.; Zhao, K.; Niu, Z.; Chen, X.; Cheng, P., *Chem. - Eur. J.* **2012**, *18*(18), 5715-5723.
- (24) Uemura, K.; Yamasaki, Y.; Onishi, F.; Kita, H.; Ebihara, M., *Inorg. Chem.* **2010**, *49*(21), 10133-10143.
- (25) Walton, R. I.; Munn, A. S.; Guillou, N.; Millange, F., *Chem.- Eur. J.* **2011**, *17*(25), 7069-7079.
- (26) Wu, C. D.; Hu, A.; Zhang, L.; Lin, W. B., *J. Am. Chem. Soc.* **2005**, *127*(25), 8940-8941.
- (27) Wu, C.-D.; Lin, W., *Angew. Chem., Int. Ed.* **2007**, *46*(7), 1075-1078.
- (28) Gedrich, K.; Heitbaum, M.; Notzon, A.; Senkovska, I.; Froehlich, R.; Getzschmann, J.; Mueller, U.; Glorius, F.; Kaskel, S., *Chem. - Eur. J.* **2011**, *17*(7), 2099-2106.
- (29) Ma, L.; Falkowski, J. M.; Abney, C.; Lin, W., *Nat. Chem.* **2010**, *2*(10), 838-846.
- (30) Bao, X.; Broadbelt, L. J.; Snurr, R. Q., *Mol. Simul.* **2009**, *35*(1-2), 50-59.
- (31) Suh, K.; Yutkin, M. P.; Dybtsev, D. N.; Fedin, V. P.; Kim, K., *Chem. Comm.* **2012**, *48*(4), 513-515.
- (32) Moghadam, P. Z.; Dueren, T., *J. Phys. Chem. C* **2012**, *116*(39), 20874-20881.
- (33) Myers, A. L.; Prausnitz, J. M., *AIChE J.* **1965**, *11*(1), 121-127.
- (34) Sarkisov, L.; Harrison, A., *Mol. Simul.* **2011**, *37*(15), 1248-1257.
- (35) Rappe, A. K.; Casewit, C. J.; Colwell, K. S.; Goddard, W. A.; Skiff, W. M., *J. Am. Chem. Soc.* **1992**, *114*(25), 10024-10035.
- (36) Chen, B.; Potoff, J. J.; Siepmann, J. I., *J. Phys. Chem. B* **2001**, *105*(15), 3093-3104.
- (37) Kelkar, M. S.; Rafferty, J. L.; Maginn, E. J.; Siepmann, J. I., *Fluid Phase Equilib.* **2007**, *260*(2), 218-231.
- (38) Dubbeldam, D.; Calero, S.; Ellis, D. E.; Snurr, R. Q. *RASPA Code Version 1.0*, RASPA Version 1.0; Northwestern University, Evanston, IL, 2008.
- (39) Frenkel, D.; Smit, B., *Understanding Molecular Simulations. From Algorithms to Applications*. Elsevier: San Diego. California, 2002.
- (40) Haughney, M.; Ferrario, M.; McDonald, I. R., *J. Phys. Chem.* **1987**, *91*, 4934-4940.
- (41) Toth, J., *Acta Chim. Acad. Sci. Hung.* **1962**, *15*, 415-430.
- (42) Jensen, C. R. C.; Seaton, N. A., *Langmuir* **1996**, *12*, 2866-2867.
- (43) Sips, R., *J. Phys. Chem.* **1948**, *16*, 490-495.
- (44) Jovanovic, D. S., *Kolloid Z. Z. Polym.* **1969**, *235*(1), 1203-1213.
- (45) Langmuir, I., *J. Am. Chem. Soc.* **1916**, *40*, 1361-1368.
- (46) Bueno-Perez, R.; Gutierrez-Sevillano, J. J.; Dubbeldam, D.; Merkling, P. J.; Calero, S., *ChemPhysChem* **2015**, *16*, 2.
- (47) Ruthven, D. M., *Principles of Adsorption and Adsorption Processes*. Wiley-Interscience: New York, 1984.
- (48) Duerinck, T.; Bueno-Perez, R.; Vermoortele, F.; Vos, D. E. D.; Calero, S.; Baron, G. V.; Denayer, J. F. M., *J. Phys. Chem. C* **2013**, *117*, 12.
- (49) Denayer, J. F.; Baron, G. V., *Adsorption* **1997**, *3*, 15.
- (50) Ocakoglu, R. A.; Denayer, J. F.; Marin, G. B.; Martens, J. A.; Baron, G. V., *J. Phys. Chem. B* **2003**, *107*, 9.

(51) Denayer, J. F.; Baron, G. V.; Vanbutsele, G.; Jacobs, P. A.; Martens, J. A., *Chem. Eng. Sci.* **1999**, *54*, 9.

(52) Dubbeldam, D.; Krishna, R.; Calero, S.; Yazaydin, A. Ö., *Angew. Chem.* **2012**, *124* (47), 12037-12041.

Zeolite Force Fields and Experimental Siliceous Frameworks in a Comparative Infrared Study

Rocío Bueno-Pérez, Sofía Calero, David Dubbeldam, Conchi O. Ania, José B. Parra, Ana P. Zaderenko, and Patrick J. Merkling

5

Infrared spectra (IR) of a great variety of zeolite frameworks in the limit of pure silica composition are calculated by molecular dynamics and also recorded experimentally. This enables us to study and assess the effect of three flexible force fields from the literature developed for zeolites in reproducing the IR spectra: the force fields by Demontis (*J. Phys. Chem.* **1988**, *92*, 867), Nicholas (*J. Am. Chem. Soc.* **1991**, *113*, 4792), and Hill (*J. Phys. Chem.* **1995**, *99*, 9536). On one side, a qualitative comparison is undertaken; on the other, a similarity index is introduced to perform a quantitative assessment of the similarity of spectra. It is applied to experimental spectra and enables us to arrange the frameworks in three different sets. It can also be applied to study the agreement of the spectra obtained with the three force fields with experimental spectra on a quantitative basis. The force field by Nicholas performs best, followed by the force field by Demontis. Frameworks are therefore analyzed purely theoretically with the Nicholas force field to investigate the dependency on frameworks. This yields a new classification in sets, which is found to be related to the topology of the frameworks. Surprisingly, these sets do not agree with the sets obtained with experimental spectra. As a consequence, it is found that none of the force fields is good enough to enable the identification of frameworks based on their experimental spectra. In a comparison of spectra generated by different force fields, it is found that the Nicholas and Hill force fields generate the most similar IR spectra

Introduction

Zeolites are a class of compounds of great industrial and natural importance made of frameworks of high regularity and beauty. When trying to understand and model these frameworks in order to reproduce some of their physicochemical properties, they are normally considered rigid for simplicity and for reasons of computational cost. However, these frameworks vibrate, giving rise to IR and Raman spectra,¹ where some of the bands are sensitive to details of the structure and to the Si/Al ratio. Therefore, IR and

Raman techniques are often used in the characterization of the structures under study. But flexibility is also important in the industrially important diffusion processes, since it favors intermittent opening of the windows.²⁻³ And from the computational point of view, IR spectroscopy is a good probe to validate force fields that are intended at reproducing changes in phase of the host molecules or other structural changes.

Siliceous zeolites, although consisting of only two types of atoms and a single type of

bond (the Si-O single bond), exhibit nevertheless a surprising variety of frameworks. These differ in their symmetry properties, both locally through the choice and combination of so-called Secondary Building Units (SBUs) and in their space groups, the dimensionality of channels for suitable host molecules, their overall porosity and pore size, etc. The frameworks selected in this study are representative members of a wide variety of topologies. They can be divided into two classes, based on structural features: the first class encompasses highly symmetric zeolites made up of a reduced number of SBUs, in the second class we have put together more complex frameworks including SBUs formed by an odd number of tetrahedral units forming one-, two-, or three-dimensional channels.

Within pure silica frameworks that are targeted in this study, secondary building units are responsible for noticeable changes in the IR spectra. This was used as a testfield for three popular silicate force fields of varying levels of sophistication. The present study of flexible siliceous zeolites has been undertaken both by computer simulation and experimentally.

The aim of this work is to study three force fields through their ability to reproduce IR spectra of siliceous zeolites. A further goal lies in the investigation of the sensitivity of the IR spectra to details of the structure of the framework.

Computational Details

Molecular dynamics (MD) simulations were performed in the NVT ensemble at 300 K. Integration of the equations of motion was performed using the velocity Verlet algorithm with a time step of 0.5 fs. The cutoff radius for short-range interactions

was set to 12 Å. Simulations were run for a total of at least 2 ns. The systems studied belong to two classes of flexible frameworks. The first class is formed by sodalite (SOD), a hypothetical pure silica version of zeolite rho (RHO), a pure silica version of LTA called ITQ-29 that was synthesized by Corma *et al.*,⁴ and a hypothetical pure silica version of faujasite (FAU). The second class contains ferrierite (FER), theta-1 (TON), mordenite (MOR), MEL, and silicalite (MFI). The latter was calculated in the monoclinic form for being the stable crystallographic form at room temperature.⁵

Three different popular force fields for zeolites were applied that are published in the literature: Nicholas *et al.*,⁶ Demontis *et al.*,⁷ and Hill and Sauer.⁸ A number of other alternative force fields for zeolites have been developed and tested by calculating IR spectra.⁹⁻¹¹ Demontis' harmonic force field was implemented as published. It consists for our case of harmonic silicon-oxygen stretch interactions and O-Si-O bend interactions only. Nicholas' force field contains, in addition to these, the Si-O-Si bend, which incorporates cubic and quadratic terms. It also contains a Si-Si Urey-Bradley term and a contribution from the dihedral angle. It also defines nonbonded interactions (of the 12-6 type) and partial charges. The potential by Hill and Sauer finally defines Si-O stretching and bendings as quartic functions, and torsions as dihedral functions. It also incorporates cross terms of the bond-bond, bond-angle, angle-angle, and angle-angle-torsion types. It also defines nonbonded interactions (of the 9-6 type) and partial charges. In the case of the force fields by Nicholas and Hill, the Ewald summation was used to handle electrostatic interactions. The Demontis version of the force field does not include partial charges for the dynamics in the simplest model presented, although

for the calculation of spectra more or less arbitrary charges were considered, as given by the authors in their paper. Anyway, since we are dealing with purely siliceous systems, with only two types of atoms, and due to the requirement of electroneutrality of the lattice, this choice does not affect results. According to the number of parameters involved, Demontis' force field would be the simplest and Hill's force field would be of greatest complexity. In fact, Demontis' force field relies on just two force terms (4 parameters), so its priority lies in simplicity.

Infrared spectra were computed from the molecular dynamics trajectories by the Fast Fourier Transform (FFT) of charge weighted velocity autocorrelation functions, which is equivalent to the Fourier transform of the correlation function of the total dipole moment. The components were sampled every four time steps. The spectra had a bandwidth of approximately 16 600 cm^{-1} , therefore ruling out aliasing artifacts. Multiple time origins at half-overlapping sampling lengths are used in calculating the correlation functions and the spectrum is convoluted with a triangular window function. The intensities obtained by this method are qualitative because quantum corrections needed to give completely accurate intensities are impractical for such a large system. The simulated spectra show no intensities at near-zero wavenumbers, which indicates that the translation and rotation of the systems as a whole was properly removed. For the sake of drawing the spectra given in Figures 1-9, intensities were scaled by the inverse wavenumbers for Hill's force field and by the squared inverse wavenumbers for Nicholas' force field to appreciate better the low-intensity bands obtained with these force fields at low wavenumbers.

The quantitative comparison of two spectra f and g was undertaken based on their weighted overlap according to the following:

$$S(f, g) = \frac{1}{\sqrt{N_f N_g}} \iint f(v)g(v+v')e^{-\frac{1}{2}(v/\sigma)^2} dv' dv, \quad (1)$$

where N_f and N_g are normalization factors such that $S(f, f) = 1$ and $S(g, g) = 1$, and σ is the standard deviation that characterizes how close is "acceptably close". In our case, σ is taken to be 25 cm^{-1} . v and v' are wavenumbers and the integration intervals were taken to be 0.5 cm^{-1} . With respect to the limits of integration, they were subject to the available spectral data. In the most favorable case, the lower limit was 200 cm^{-1} and the upper limit 1400 cm^{-1} . S can be termed a global similarity index and takes values between 0 (no similarity) and 1 (identical spectra).

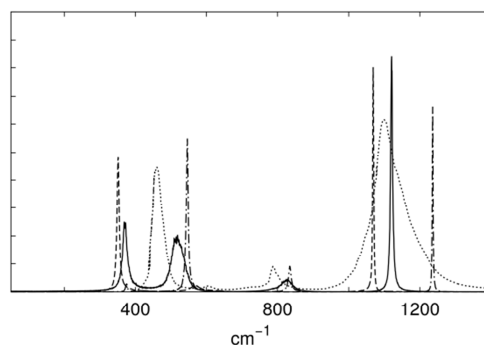


Figure 1. Comparison of the bands in the IR spectra of SOD obtained by molecular simulation for the three popular force fields by Demontis⁷ (dashed), Nicholas⁶ (solid line), and Hill⁸ (dot dashed), and the experimental spectrum¹² (dotted). Intensities are arbitrary.

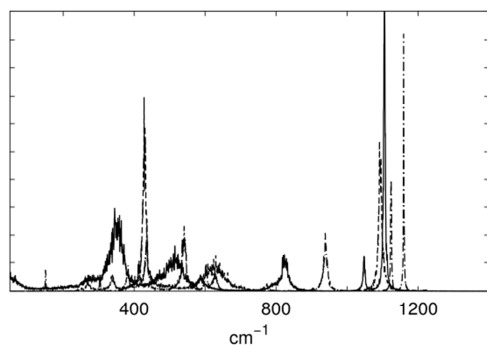


Figure 2. Comparison of the bands in the IR spectra of RHO obtained by molecular simulation for the three popular force fields by Demontis⁷ (dashed), Nicholas⁶ (solid line), and Hill⁸ (dot dashed). Intensities are arbitrary.

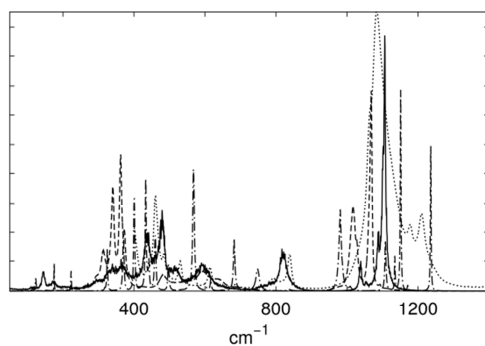


Figure 4. Comparison of the bands in the IR spectra of FAU obtained by molecular simulation for the three popular force fields by Demontis⁷ (dashed), Nicholas⁶ (solid line), and Hill⁸ (dot dashed), and the experimental spectrum (this work, dotted line). Intensities are arbitrary.

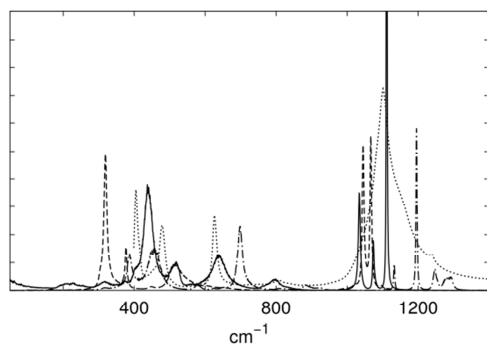


Figure 3. Comparison of the bands in the IR spectra of ITQ-29 obtained by molecular simulation for the three popular force fields by Demontis⁷ (dashed), Nicholas⁶ (solid line), and Hill⁸ (dot dashed), and the experimental spectrum (this work, dotted line). Intensities are arbitrary.

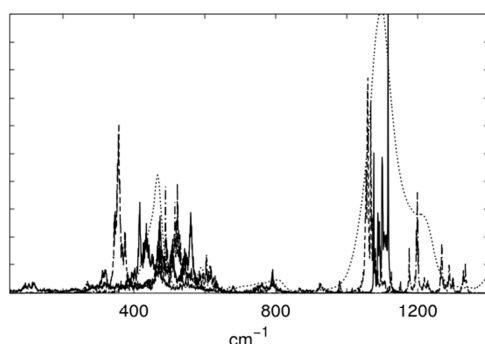


Figure 5. Comparison of the bands in the IR spectra of FER obtained by molecular simulation for the three popular force fields by Demontis⁷ (dashed), Nicholas⁶ (solid line), and Hill⁸ (dot dashed), and the experimental spectrum (this work, dotted line). Intensities are arbitrary.

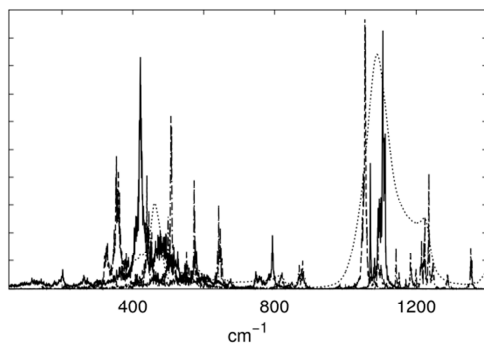


Figure 6. Comparison of the bands in the IR spectra of MOR obtained by molecular simulation for the three popular force fields by Demontis⁷ (dashed), Nicholas⁶ (solid line), and Hill⁸ (dot dashed), and the experimental spectrum (this work, dotted line). Intensities are arbitrary.

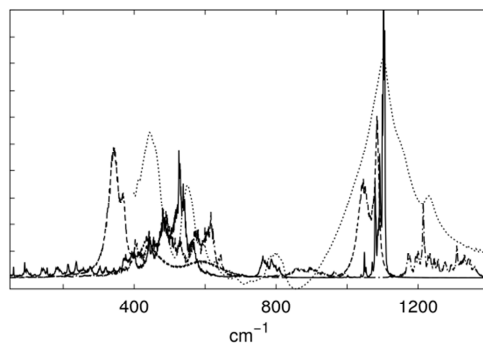


Figure 8. Comparison of the bands in the IR spectra of MFI obtained by molecular simulation for the three popular force fields by Demontis⁷ (dashed), Nicholas⁶ (solid line), and Hill⁸ (dot dashed), and the experimental spectrum (this work, dotted line). Intensities are arbitrary.

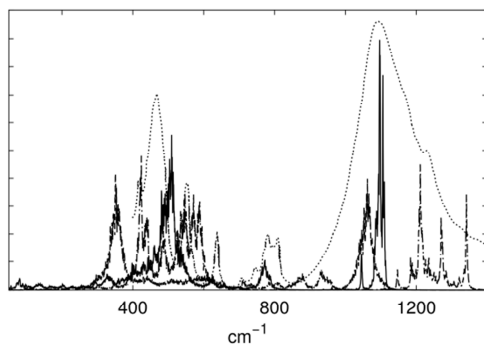


Figure 7. Comparison of the bands in the IR spectra of TON obtained by molecular simulation for the three popular force fields by Demontis⁷ (dashed), Nicholas⁶ (solid line), and Hill⁸ (dot dashed), and the experimental spectrum¹³ (dotted). Intensities are arbitrary.

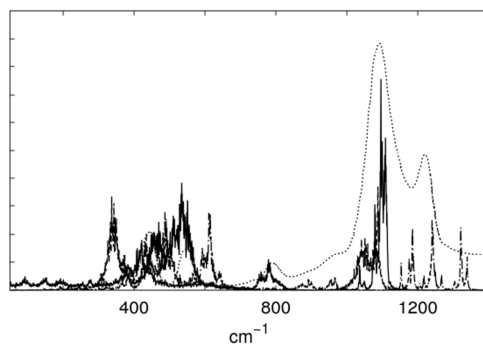


Figure 9. Comparison of the bands in the IR spectra of MEL obtained by molecular simulation for the three popular force fields by Demontis⁷ (dashed), Nicholas⁶ (solid line), and Hill⁸ (dot dashed), and the experimental spectrum¹⁴ (dotted). Intensities are arbitrary.

Experimental Details

All-silica MFI and ITQ-29 (pure silica LTA structure) were kindly supplied by ITQ (CSIC) and both correspond to a pure porous crystalline silicon dioxide ($\text{Si/Al} \approx \infty$). FAU with a Si/Al ratio of 40 ($\text{H}_x\text{Al}_x\text{Si}_{192-x}\text{O}_{384}$, $96 < x < 0$), MOR (nominal cation NH_4) with a Si/Al ratio 10, and FER (nominal cation NH_4) with a Si/Al ratio 10 were purchased from Zeolyst International SA.

For the IR spectra, as-received powders were pressed into KBr pellets (dilution 1:1000) and outgassed overnight under primary vacuum at 600 K to eliminate the absorption bands corresponding to surface water. The dried pellets were clamped into the sample holder and the spectra were registered in a Nicolet spectrometer equipped with a DTGS detector. The level of rehydration of the samples during the measurements –due to moisture present in the chamber– was found to be essentially negligible. Each spectrum resulted from the accumulation of 256 scans, recorded with a spectral resolution of 2 cm^{-1} in the mid-IR range ($4000\text{-}400 \text{ cm}^{-1}$) spectral domain. Most of the samples were baseline corrected.

The recorded spectra were crosschecked with literature data as available. However, in some cases aluminum content was unknown and in most cases aluminum contents differed from our data. The presence of aluminum leads to red shifts in many of the absorption bands due to the force constants of the Al-O bonds being lower than the ones of the Si-O bonds. Taking into account this predictable pattern, agreement was found to be satisfactory with literature data for LTA,¹⁵⁻¹⁶ FAU,¹⁷⁻¹⁹ FER,²⁰⁻²¹ MOR,^{21-22,13} and MFI.^{16,20-21} Experimental spectra for zeolites SOD^{12,23}

(pure silica), MEL,^{14,21,24} and TON^{13,22} were taken from the literature.

Results and Discussion

Comparative studies of experimental IR spectra of zeolites have been examined prominently by Flanigen.²⁵ Therein, absorption bands have been assigned to local vibrations of structural units involving mainly the SiO_4 tetrahedra (the primary building units), which should be unaffected by structure, and external linkages that reflect changes in structure. His interpretation is still in wide use, although far more detailed studies in some of the frameworks have been published by several groups.²⁶⁻²⁷ Since Flanigen's interpretation is the most widely used we will base our discussions on it, although we are aware that in some cases it can lead to oversimplifications.

Table 1. Zeolite IR assignments (in cm^{-1}).

internal tetrahedra	asym. stretch	1110-1080
	sym. stretch	690-640
	Si-O bend	490-440
external linkages	ring blocks	630-530
	ring	410-290
	sym. stretch	840-750
	asym. stretch	1240-1170 sh

Within our first class of selected zeolites, the SOD, RHO, ITQ-29 (the idealized LTA framework), FAU sequence represents a transition from simple to increasingly complex frameworks and from tiny to large pores. In effect, these frameworks possess a single crystallographic silicon position and 1, 2, 3, and 4 types of oxygen positions, respectively. The absorption bands observed in zeolites and their traditional interpretation are summed up in Table 1 for the sake of facilitating the discussion, rather than referring the reader to the original

report.²⁵ It has been, however, adapted to pure silica frameworks of this work, and therefore the ranges are a little narrower than in the more general case treated in the original publication. This affects especially the location of the maximum of the asymmetric stretch (due to “internal tetrahedra”) that is very well-defined around 1100 cm^{-1} . The traditional assignment distinguishes between bands that are structure sensitive (“external”) and those that arise mainly from vibrations of the SiO_4 tetrahedron and are rather insensitive to structure. One of these bands, the asymmetric stretch due to external linkages, is weak and corresponds to a shoulder (sh) in the spectra.

The experimental spectra have been interpreted in terms of an asymmetric stretch at $1080\text{--}1100\text{ cm}^{-1}$ with little dependence on the framework. Among other largely structure-insensitive bands is the one due to the Si-O bend at around $450\text{--}460\text{ cm}^{-1}$. In the more complex frameworks FAU and those of the second class, a shoulder or a moderate intensity band is observed at $1210\text{--}1240\text{ cm}^{-1}$. The absorption bands that are structure sensitive in the experimental spectra are located at $786\text{ (SOD)} \rightarrow 810\text{ (ITQ)} \rightarrow 839\text{ cm}^{-1}\text{ (FAU)}$ as can be observed from the comparison of spectra in Figures 1, 3, and 4, and in the second class $787\text{ (MEL)} \rightarrow 808\text{ (FER)} \rightarrow 781/808\text{ (TON)} \rightarrow 797\text{ (MFI)} \rightarrow 816\text{ cm}^{-1}\text{ (MOR)}$. Then, in those frameworks that contain double ring SBUs, a band at about 600 cm^{-1} is seen. The observed sequence is $627\text{ (ITQ)} \rightarrow 614\text{ cm}^{-1}\text{ (FAU)}$ and $629\text{ (MFI)} \rightarrow 637\text{ cm}^{-1}\text{ (TON, MOR)}$. In the second class, the evolution of absorption bands with frameworks due to some other ring block vibrations is as follows: $550\text{ (TON, MEL, MFI)} \rightarrow 565/586\text{ (MOR)} \rightarrow 590\text{ cm}^{-1}\text{ (FER)}$. In the far-infrared, which is seldom measured, larger scale ring vibrations (ring

blocks involving several rings) are detected at 289 cm^{-1} in SOD, ITQ, and FAU,²³ while another sequence is found for $405\text{ (ITQ-29)} \rightarrow 399\text{ cm}^{-1}\text{ (FAU)}$, but has no correspondence in SOD.¹⁷ The force fields will be evaluated based on the ability to reproduce these characteristic structure-dependent features and the shifts of these features from one framework to another.

Among structure-insensitive bands, the asymmetric stretch at around 1070 cm^{-1} is found to be reproduced satisfactorily by the force field created by Demontis.⁷ Given the extreme simplicity of the force field model, it is surprising to observe that in sodalite a unique band is found at around 1070 cm^{-1} , which corresponds to the stretching of the internal tetrahedron and no minor band or shoulder is found. Upon switching to ITQ-29, bands split in two, and in FAU this separation becomes more important, a result that is in line with the broadening of the experimental band at around 1100 cm^{-1} . In the second class, all frameworks have two clearly separated bands, except TON that has one broad band. This is in good qualitative agreement with experimental spectra. Since the Demontis force field does not include cross terms, the distinct bands are a consequence of the different types of atoms within the frameworks. Among other largely structure-insensitive bands is the one due to the Si-O bend at around 450 cm^{-1} . With the Demontis force field, this absorption band is reproduced qualitatively, although at about 20% lower wavenumbers, as a result of the somewhat low O-Si-O bending force constant chosen. It even leads to the split absorption features observed experimentally in faujasite and in ITQ-29, and not in sodalite. On the other side, the shoulder at around 1150 cm^{-1} , formally ascribed to an external asymmetric stretch, and the vibration ascribed formally to ring block deformations are displaced in the

Demontis force field, but still found to be structure sensitive. Ring block vibrations of the double ring type that are expected around 600 cm^{-1} are found in RHO, ITQ (albeit at 516 cm^{-1}), FAU, MOR, MFI, and MEL. On the backside, the band at about 800 cm^{-1} is missing generally in all spectra.

The force field by Nicholas⁶ reproduces sodalite reasonably well (Figure 1), all the bands are present although some of them are shifted. In RHO the bands are essentially the same, a shoulder appears in the 1100 cm^{-1} band and the ring-opening band lowers 20 cm^{-1} . In ITQ-29, the asymmetric stretch band at 1100 cm^{-1} broadens, in line with experiment. The $400/460\text{ cm}^{-1}$ splitting in ITQ-29, attributed by Dutta²⁸ to a 6R and D4R vibration, respectively, is reproduced very satisfactorily by Nicholas. Also, the new experimental band at 600 cm^{-1} (considering the SOD \rightarrow RHO \rightarrow ITQ-29 sequence) emerges with this force field. The symmetric stretch at 800 cm^{-1} is present in all frameworks. In FAU, all experimental bands are found. The new band is located at 531 cm^{-1} and is reproduced very weakly by the Nicholas force field.

In the second class, FER is reproduced very well, except for the shoulder at 1215 cm^{-1} . The bands are quite close to the experimental values of 1097 , 808 , and 590 cm^{-1} , and even the band at 460 cm^{-1} and shoulder at 440 cm^{-1} are reproduced with appropriate broadening. Moving on to other frameworks of this class, it is observed that the band or shoulder that is expected at around $1225\text{-}1230\text{ cm}^{-1}$ is missing in all of the calculated spectra. Otherwise, we observe that MOR is reproduced well. The spectrum of the TON framework reproduces well the 781 cm^{-1} external symmetric stretch, although its companion band expected at 808 cm^{-1} is missing. Noticeably, the 637 cm^{-1} band is present,

although weakly. MFI and MEL are reproduced quite well. It is to be recalled that the IR spectrum of SOD was used originally by the developers of the force field for the parametrization and MFI was used as a check.

Overall, with the Nicholas force field the position of the structure-independent asymmetric stretch stays fairly constant at around 1100 cm^{-1} for all frameworks, as should be the case, and is the most intense band in the spectra. The position of the absorption band of the Si-O bend should also be quite constant but in this case, greater shifts between frameworks are observed. As to the external linkages, the band due to the symmetric stretches at around 800 cm^{-1} have a low dependency on the framework, in agreement with experimental findings. The experimental band at and above 600 cm^{-1} is found in ITQ, FAU, FER, MOR, and TON, but is missing in MFI. The absorption band at $550\text{-}590\text{ cm}^{-1}$ found in most elements of the second class, is reproduced at least qualitatively, although the assignment to an experimental band is sometimes ambiguous.

The force field by Hill⁸ reproduces the internal asymmetric stretch at 1100 cm^{-1} very badly. It becomes clear from scrutiny of the force constants in the Hill force field why this is so. In the harmonic approximation, the force constants chosen for the symmetric stretch are clearly too high, almost double those of the Demontis force field. Therefore, in the high-wavenumber regime above 900 cm^{-1} , the Hill force field performs inadequately in all frameworks. As to the other supposedly easily reproduced vibration (for being weakly coupled to other force constants), the Si-O bend, it is strongly shifted from its true position in sodalite, while in ITQ-29 it is very convincing since the double band is

reproduced well, and in FAU several bands are present between 324 and 497 cm^{-1} , including those of the experimental spectrum. With appropriate weighting and broadening of the bands, it would easily be possible to reproduce a posteriori the experimental bands in this region of the spectrum. In the second class, a double band is obtained in FER, although shifted from its experimental value, and reproduced well in MOR, MFI, and MEL. As to the bands in the 800 cm^{-1} region, they are strongly framework-dependent with the use of the Hill force field. In SOD, this band is 50 cm^{-1} too high, in ITQ virtually absent, while in FAU it is 90 cm^{-1} too low. In FER, this mode vibrates at its expected experimental frequency, in MOR the 816 cm^{-1} band appears about 80 cm^{-1} blue-shifted, and in TON the complex bands in the spectrum (at least four bands) are reproduced, albeit over a larger frequency interval. In MFI and MEL, low-intensity bands appear blue-shifted. The double ring vibration at around 600 cm^{-1} is blue-shifted in ITQ, FAU, FER, and MEL, and probably in MFI as well, where the assignment of the bands is not clear. In TON, the correspondence is not clear either, because many bands appear in the place of the two experimental bands of 550 and 637 cm^{-1} .

Overall, the qualitative inspection of the spectra revealed that the Nicholas force field reproduced generally IR spectra better than the other force fields. It accounts for the appearance of absorption bands with new structural features in frameworks, and reproduces better than the other force fields the positions of the absorption bands. Neither of the force fields is able to reproduce convincingly the shifts in position of the bands between frameworks, although some of them do and most show the right dependence. The force field by Hill gives rise to complex spectra with many

absorption bands, and it accounts for the appearance of absorption bands with new structural features in frameworks, but the bands are generally blue-shifted with respect to experiment. The force field by Demontis reproduces well some of the absorption bands, and there is also a dependence upon frameworks, but some absorption bands are missing. This must be due to the partial neglect of some force constants between atoms.

Although the detailed, direct comparison of spectra is important to assess the quality of force fields with respect to dynamical properties, it is desirable to be able to quantify the similarities. Therefore, a similarity index was developed in the Computational Details section of this work, and results are presented in Table A1 of the Appendix 4 for the comparison of experimental spectra. The details about the matching bands and those that are not are lost, but a quantitative value is gained.

First of all, all values in Table A1 (Appendix 4) are above 0.85, so the overall high values of the similarity index should be pointed out. This is due not only to the fact that we are dealing with spectra of closely related frameworks, but also that the resolution of bands is similar (i.e., we are dealing with experimental spectra and their broad bands, a situation very different from the simulated spectra). The very intense and broad absorption of the asymmetric stretch that is weakly dependent on structure is by far the major contribution to the similarity index of these experimental spectra. But most of the characteristic features of the spectra are at low wavenumbers. It therefore is useful to break down the similarity index in two regions: a region of low wavenumbers below 900 cm^{-1} , and a region above this value that will be called from now on a region of “high” wavenumbers.

$$\begin{aligned}
S(f, g) = & \frac{1}{\sqrt{N_f N_g}} [\\
& \int_{v=v(\text{low})}^{v(\text{mid})} \int_{v'=v(\text{low})-v}^{v(\text{mid})-v} f(v)g(v+v')e^{-\frac{1}{2}(v'\sigma)^{-2}} dv' dv + \\
& \int_{v=v(\text{mid})}^{v(\text{high})} \int_{v'=v(\text{mid})-v}^{v(\text{high})-v} f(v)g(v+v')e^{-\frac{1}{2}(v'\sigma)^{-2}} dv' dv + \\
& \int_{v=v(\text{low})}^{v(\text{mid})} \int_{v'=v(\text{mid})-v}^{v(\text{high})-v} \dots + \int_{v=v(\text{mid})}^{v(\text{high})} \int_{v'=v(\text{low})-v}^{v(\text{mid})-v} \dots]
\end{aligned} \tag{2}$$

Symbols in Equation (2) are defined as for Equation (1). The integration limits $v(\text{low})$, $v(\text{mid})$, and $v(\text{high})$ have been assigned the values 200 (or the lowest available wavenumber in the case of experimental spectra), 900, and 1400 cm^{-1} , respectively. In Equation (2), S is broken down into four contributions, S'_{low} , S'_{high} and two leakage terms due to the cross correlation between spectral regions. With our choice of defining the midwavenumber to be 900 cm^{-1} and our choice of standard deviation parameter, leakage was found to be negligible (below 0.1 %).

As a result of this separation of contributions, it is found that the bands above 900 cm^{-1} are responsible for typically 85-97% of the power spectrum. The extremes are composed of MFI at 77%, and MEL, the highest at 97%. As a consequence of this slightly different balance of the MFI and MEL spectra in comparison with the other experimental spectra of this study, the global similarity index of these two frameworks with others is lower, but it does not necessarily mean that they look very different from the others: on the contrary, this fact highlights a limitation of the global similarity index. Another structure that has comparatively low similarity to other structures is TON (where the high region is responsible for 85% of the power spectrum).

Since much of the structural identity of the framework is expressed in the low-wavenumber region of the spectrum, special attention was paid to this region. We may use the S -value integrated from the minimum wavenumber available simultaneously in both experimental spectra to 900 cm^{-1} , and then normalized in this region. We will call this similarity index in the low-wavenumber region S_{low} . There is another reason for paying close attention to the low-wavenumber region: the comparison of FAU with a Si/Al ratio of 2.55 with our reference framework of FAU Si/Al of 40 yields a global similarity index of 0.70. However, the value of S_{low} is 0.89. Since we need in some cases to make use of spectra of frameworks with a non-negligible amount of aluminum as indicated in the Experimental Details section, the use of S_{low} is more reliable for the sake of ensuring valid comparisons in the limit of pure silica structures. Values of S_{low} for the pairwise comparison of all frameworks are indicated nonredundantly in Table 2.

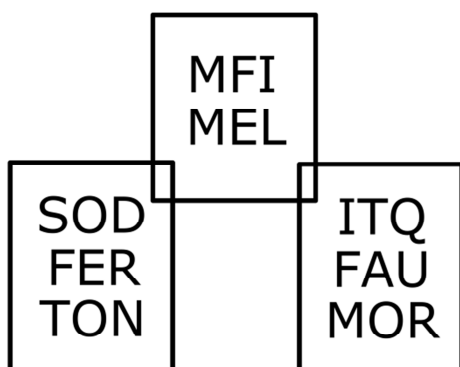
Based on the analysis of S_{low} and S , we may group frameworks together based on the similarity of their spectra: a first set encompasses SOD, FER, and TON; a second set ITQ, FAU, and MOR; and a third set, in between the former two, contains somewhat loosely MFI and MEL. This is illustrated in Scheme 1. The striking feature about this classification is that it does not follow the classification based on topologies of the frameworks. We note also that there is no correlation with the Si/Al ratio since all three sets contain pure silica frameworks.

The spectra calculated with the three force fields can now be compared on a one to one basis to the corresponding experimental ones. The results are indicated in Table 3. A

Table 2. Similarity of experimental IR spectra of different frameworks using the similarity index S_{low} .*

	ITQ	FAU	FER	MOR	TON	MFI	MEL
SOD	0.76	0.92	0.96	0.91	0.93	0.80	0.69
ITQ		0.88	0.82	0.87	0.83	0.83	0.66
FAU			0.96	0.97	0.97	0.93	0.85
FER				0.98	0.98	0.92	0.83
MOR					0.97	0.95	0.86
TON						0.95	0.87
MFI							0.93

*A value of 1 means maximum similarity.

**Scheme 1.** Similarity of experimental spectra grouped into sets.

minor correction has been undertaken with the Nicholas force field, although it does not affect significantly the results: Unlike the case of the Demontis and Hill force fields, it was found that the power spectra by the Nicholas force field in the low region are underestimated with respect to the experimental ones. The spectra were therefore rescaled by the inverse wavenumber.

The analysis of Table 3 reveals that the agreement with experiment is generally not too good. The upside is that the similarity index is able to discriminate between good and bad agreement. The force field by Nicholas is the one that performs best. In

most of the frameworks, it leads to the best agreement and it yields good agreement with frameworks of the first topological class (i.e., SOD, ITQ, and FAU) and of the second class. We have averaged the similarity indices over available frameworks, and the result is again that the Nicholas force field achieves the highest average similarity with experiment (S_{low} averages in this case to 0.81). This average is lower, however, than the average over all the values in Table 2 (0.88). In other words, on average, a spectrum of a known framework generated with the best force field is less similar to the experimental spectrum than an experimental spectrum of another pure silica framework. As to the other two force fields, the one by Demontis performs better in more frameworks and in its average value than the force field by Hill. The Demontis force field is able to reproduce the spectra of the second topological class (FER-MEL with the exception of TON) acceptably well, but the first class is not reproduced well. This does not happen with the Hill force field. However, the behavior of the Hill force field in the high-wavenumber region is clearly inadequate.

Given that the Nicholas force field was just established as the best choice for calculating IR spectra of zeolites, the analysis of spectral similarities was conducted in an analogous

way to the analysis of experimental spectra in Table 2, but this time with the calculated ones. The results of these pairwise comparisons are given in Table 4. With the spectra obtained by using the Nicholas force field, the kinship that can be established based on the similarity index distinguishes a total of four sets: a first set with SOD as the sole element; a second set containing RHO, ITQ, and FAU; a third set that contains

FER, TON, MFI, and MEL. MOR is best classified in a set of its own, in between the second and third set. It is striking to notice that, unlike the sets established from experimental spectra, the sets from the Nicholas force field agree with the classes based on topological criteria. Sodalite, as the simplest structure, is unique in its simplicity and therefore it is not surprising that it should belong to a set of its own.

Table 3. Similarity of calculated spectra with their experimental counterpart using S_{low} and S .*

	SOD	ITQ	FAU	FER	MOR	TON	MFI	MEL	Avg
D S_{low}	0.26	0.48	0.64	0.93	0.81	0.77	0.97	0.83	0.71
D S	0.55	0.51	0.62	0.70	0.70	0.66	0.75	0.69	0.65
N S_{low}	0.41	0.90	0.93	0.87	0.91	0.80	0.79	0.83	0.81
N S	0.74	0.84	0.86	0.84	0.81	0.69	0.72	0.70	0.77
H S_{low}	0.11	0.59	0.72	0.69	0.80	0.73	0.83	0.65	0.64
H S	0.13	0.39	0.53	0.40	0.43	0.55	0.61	0.44	0.43

*D, N, and H refer to spectra obtained with the force fields by Demontis, Nicholas, and Hill, respectively. The last column contains the averaged value over all frameworks.

Table 4. Similarity S_{low} of calculated IR spectra of different frameworks.*

	RHO	ITQ	FAU	FER	MOR	TON	MFI	MEL
SOD	0.85	0.48	0.71	0.73	0.61	0.84	0.89	0.86
RHO		0.52	0.82	0.67	0.61	0.67	0.71	0.71
ITQ			0.82	0.82	0.89	0.65	0.62	0.69
FAU				0.86	0.85	0.76	0.75	0.79
FER					0.92	0.85	0.90	0.95
MOR						0.75	0.74	0.80
TON							0.94	0.91
MFI								0.99

*The force field by Nicholas was used.

The average index obtained by averaging over all values in Table 4 yields a value of 0.77 for the Nicholas force field, or 0.78 if correlations with the RHO framework are omitted. The corresponding value for experimental spectra from Table 2 is, as mentioned earlier, 0.88. The lower this

value, the greater is the sensitivity of the technique or force field to the framework. This means that calculated spectra with Nicholas actually overemphasize differences between frameworks. The corresponding values for Demontis and Hill in the case where the RHO framework is not included

are 0.91 and 0.68, respectively. That is, the Hill force field is the most sensitive to framework variations while the Demontis force field is the least. To understand these values better, we should make a technical note at this point. Simulated spectra are expected to exhibit a higher sensitivity because the bands are narrower, so the overlap will intrinsically be smaller when the shift in frequencies is the same as in the experiment. We can therefore conclude that the force field by Demontis is actually noticeably less sensitive to frameworks than the experimental spectra, although the average values differ little.

Based on the dependence of the simulated spectra on the framework we have just discussed, it is interesting to ask the following question: Is the force field able to identify correctly the framework for an experimental spectrum supposedly unknown? We report the results in Table 5. It is clear from this table that it is not possible to recognize an experimental spectrum based on calculated spectra with the Nicholas force field. With Demontis and Hill, similar results are observed. Only two

matches are found with the Nicholas force field. It might be helpful to analyze the table based on the sets of similar spectra that were defined previously. If the spectrum is not recognized correctly, is it at least assigned to a related framework? Since the force field by Nicholas is more sensitive to the nature of the framework than the experimental spectra, we use the partitioning of frameworks in sets according to the Nicholas force field. As a reminder, we found 4 sets: set one contains SOD and is not closely related to any other; set 2 contains RHO, ITQ, and FAU; set 3 contains MOR and is halfway between sets 2 and 4 (and could therefore easily be assigned to either of them); and set 4 contains FER, TON, MFI, and MEL and is only related to set 3. Especially in SOD, the failure is complete since the closest calculated spectrum is FAU, which belongs to another set of spectra. As to the other frameworks, they are identified as a framework of the correct family or at least as a framework related to it. Thus, FER is identified as MOR, which belongs to a closely related set.

Table 5. Ability of the force field to recognize the framework from an experimental reference spectrum.*

Exp	SOD	ITQ	FAU	FER	MOR	TON	MFI	MEL
Nicholas	FAU	ITQ	FAU	MOR	ITQ	FER	FER	FER

*Based on similarity indices at low wavenumbers.

Table 6. Similarity indices of calculated IR spectra averaged over different frameworks.*

	N vs. H	D vs. N	D vs. H
$\langle S_{low} \rangle$	0.73	0.45	0.38
$\langle S \rangle$	0.36	0.45	0.23

*D, N, and H refer to spectra obtained with the force fields by Demontis, Nicholas, and Hill, respectively.

The comparison of the spectra from the force fields can also be performed directly between one another to analyze how they match. Thus, a similarity index for the calculated SOD spectra with two force fields was obtained, and the procedure repeated for the frameworks RHO, ITQ, FAU; FER, MOR, TON, MFI, and MEL, and the indices of these 9 comparisons averaged. The results for every combination of force fields are shown in Table 6. According to this, the two “complex” force fields, Nicholas and Hill, lead to more similar spectra. This is probably a bit surprising, since Nicholas has been found to perform far better than Hill does, and Demontis was found to perform “in between” those two but rather close to the performance of Hill.

Conclusions

Infrared spectra (IR) of a great variety of zeolite frameworks in the limit of pure silica composition were calculated by molecular dynamics and also recorded experimentally. This enabled us to study and assess the effect of three flexible force fields from the literature developed for zeolites in reproducing the IR spectra. On the basis of a qualitative comparison, it was found that the force field by Nicholas reproduced the spectra better than the other two force fields. A similarity index was introduced to perform a quantitative assessment of the similarity of spectra. It was applied to experimental spectra and enabled us to classify the frameworks in three different sets of the following compositions: SOD-FER-TON, MFI-MEL, and ITQ-FAU-MOR. It was also applied to study the agreement of the spectra obtained with the three force fields with experimental spectra on a quantitative basis. Again, the force field by Nicholas performed clearly better, followed by the force field by Demontis. Frameworks were analyzed with the Nicholas force field

to investigate the dependency on frameworks. The frameworks could be classified in four sets related to the topology of the frameworks: SOD, RHO-ITQ-FAU, MOR, and FER-TON-MFI-MEL. Surprisingly, these sets do not agree with the sets obtained with experimental spectra. As a consequence, it was found that none of the force fields was good enough to enable the identification of frameworks based on their experimental spectra. The force fields’ main purpose is to behave well in reproducing adsorption, but their design was not concerned with reproducing structural changes upon hydration or more generally loading. Even though IR spectra were tested in a few structures, the transferability has proven not to be good. In a comparison of spectra generated by different force fields, it was found that the Nicholas and Hill force fields generate the most similar IR spectra in the low wavenumber region.

Acknowledgments

This work was supported by the Spanish MICINN (CTQ2010-16077), the European Research Council through an ERC Starting Grant (S. Calero), and by the Junta de Andalucía (P10-FQM-06615). R.B. thanks MICINN (CTQ2010-16077) for her predoctoral fellowship.

Bibliography

- (1) Garcia-Perez, E.; Parra, J. B.; Ania, C. O.; Dubbeldam, D.; Vlugt, T. J. H.; Castillo, J. M.; Merkling, P. J.; Calero, S., *J. Phys. Chem. C* **2008**, *112* (27), 9976-9979.
- (2) Leroy, F.; Rousseau, B.; Fuchs, A. H., *Phys. Chem. Chem. Phys.* **2004**, *6* (4), 775-783.
- (3) Garcia-Sanchez, A.; Dubbeldam, D.; Calero, S., *J. Phys. Chem. C* **2010**, *114* (35), 15068-15074.
- (4) Corma, A.; Rey, F.; Rius, J.; Sabater, M. J.; Valencia, S., *Nature* **2004**, *431* (7006), 287-290.

- (5) Hay, D. G.; Jaeger, H., *J. Chem. Soc. Chem. Commun.* **1984**.
- (6) Nicholas, J. B.; Hopfinger, A. J.; Trouw, F. R.; Iton, L. E., *J. Am. Chem. Soc.* **1991**, *113* (13), 4792-4800.
- (7) Demontis, P.; Suffritti, G. B.; Quartieri, S.; Fois, E. S.; Gamba, A., *J. Phys. Chem.* **1988**, *92* (4), 867-871.
- (8) Hill, J. R.; Sauer, J., *J. Phys. Chem.* **1995**, *99* (23), 9536-9550.
- (9) Bougeard, D.; Smirnov, K. S.; Geidel, E., *J. Phys. Chem. B* **2000**, *104* (39), 9210-9217.
- (10) Ermoshin, V. A.; Smirnov, K. S.; Bougeard, D., *Chem. Phys.* **1996**, *202* (1), 53-61.
- (11) Schröder, K. P.; Sauer, J., *J. Phys. Chem.* **1996**, *100* (26), 11043-11049.
- (12) Deman, A. J. M.; Vansanten, R. A., *Zeolites* **1992**, *12* (3), 269-279.
- (13) Burchart, E. D.; Verheij, V. A.; Vanbekkum, H.; Vandegraaf, B., *Zeolites* **1992**, *12* (2), 183-189.
- (14) Dong, J. P.; Zou, J.; Long, Y. C., *Microporous Mesoporous Mater.* **2003**, *57* (1), 9-19.
- (15) Huang, Y. N.; Jiang, Z. M., *Microporous Mater.* **1997**, *12* (4-6), 341-345.
- (16) Bornhauser, P.; Bougeard, D., *J. Phys. Chem. B* **2001**, *105* (1), 36-41.
- (17) Anderson, M. W.; Klinowski, J., *J. Chem. Soc., Faraday Trans. 1* **1986**, *82*, 1449-1469.
- (18) Jacobs, W.; Vanwolput, J.; Vansanten, R. A., *J. Chem. Soc., Faraday Trans.* **1993**, *89* (8), 1271-1276.
- (19) Halasz, I.; Agarwal, M.; Marcus, B.; Cormier, W. E., *Microporous Mesoporous Mater.* **2005**, *84* (1-3), 318-331.
- (20) Long, Y. C.; Ma, M. H.; Sun, Y. J.; Jiang, H. W., *J. Inclusion Phenom. Macrocyclic Chem.* **2000**, *37* (1-4), 103-120.
- (21) Jansen, J. C.; Vandergaag, F. J.; Vanbekkum, H., *Zeolites* **1984**, *4* (4), 369-372.
- (22) Jacobs, P. A.; Martens, J. A., *Synthesis of High-Silica Aluminosilicate Zeolites*. Elsevier: Amsterdam, 1987; Vol. 33.
- (23) Godber, J.; Ozin, G. A., *J. Phys. Chem.* **1988**, *92* (17), 4980-4987.
- (24) Zhao, X.; Wang, X., *Catal. Lett.* **2010**, *135* (3-4), 233-240.
- (25) Flanigen, E. M.; Khatami, H.; Szymanski, H. A., *Molecular Sieve Zeolites*. American Chemical Society: Washington D.C., 1971; Vol. 101.
- (26) Creighton, J. A.; Deckman, H. W.; Newsam, J. M., *J. Phys. Chem.* **1994**, *98* (2), 448-459.
- (27) Iyer, K. A.; Singer, S. J., *J. Phys. Chem.* **1994**, *98* (48), 12670-12678.
- (28) Dutta, P. K.; Delbarco, B., *J. Phys. Chem.* **1988**, *92* (2), 354-357.

Influence of Flexibility on the Separation of Chiral Isomers in the STW-Type Zeolite

Rocio Bueno-Perez, Salvador R. G. Balestra, Miguel A. Cambor, Jung Gi Min,
Suk Bong Hong, Patrick J. Merklung, and Sofia Calero

6

Molecular simulation, through the computation of adsorption isotherms, is an useful predictive tool for the selective capacity of nanoporous materials. Generally, adsorbents are modeled as rigid frameworks, as opposed to allowing for vibrations of the lattice, and this approximation is assumed to have negligible impact on adsorption. In this work, we test this approach in an especially challenging system by computing the adsorption of the chiral molecules 2-pentanol, 2-methylbutanol, and 3-methyl-2-butanol in the all-silica and germanosilicate chiral zeolites STW, and study their lattice vibrations upon adsorption. The analysis of single and multicomponent adsorption isotherms shows the suitability of the STW-type zeolites as molecular sieves for chiral separation processes, which pose a challenging task in the chemical and pharmaceutical industries. We also provide new experimental adsorption data that validate the force field employed. Our results reveal that the lattice vibrations of the all-silica framework are sorbate-independent, while those of germanosilicate STW, on the other hand, display host-guest coupling modulated by uptake and sorbate type that disrupt the chiral recognition sites. This study points out that the effects of intrinsic flexibility on the selective capacity of nanoporous materials may range from low to high impact, some of which could not have been foreseen even after the examination of the structural dynamics of an empty framework.

Introduction

Biological systems, from the very lowest to the highest life forms, are homochiral entities that fulfill a broad variety of functions through a complex network of three-dimensional structure-activity interactions performed by enantiopure compounds.¹ As a consequence, any technology or technical advance derived from or focused on biosystems should take these complex interactions into account. Indeed, as nature is increasingly dealing with synthetic chemicals, the awareness of chiral toxicity is increasing as well. The

most representative cases are featured in the pharmaceutical industry,² where only one enantiomer of the racemic drug is therapeutically effective while the other is inactive or might even have undesired effects, which might be just different or, in the worst case, adverse. Likewise, in the food industry the chirality of a flavor enhancer results in a compound being tasty or tasteless, as happens with monosodium glutamate; and in the perfume industry chirality is also key since depending on the chiral form different organoleptic properties are achieved.³ Prominent examples of this are the distinct fragrances of limonene or

menthol. Finally, following the same trend, the agrochemical industry is improving the safety of herbicides, as many of these are chiral though still being manufactured as racemates, which can have nonintended effects on target weeds and nontarget organisms.⁴ Thus, chiral toxicology has become an area of study which is still relatively unexplored and is a relevant issue in several chemical manufacturing industries. However, the synthesis of enantiopure compounds is difficult and costly, and many approaches have been proposed from the areas of enzymatic and chemical synthesis. The enzymatic synthesis takes advantage of the specificity of enzymes and metabolic routes, yet scaling it up to increase its performance involves long-term research and, moreover, is not transferable.^{5,6} Chemical synthesis is less specific but achieves higher yields and, combined with the development of chromatographic separation techniques, enantiomeric resolution is possible. Specifically, high-performance liquid chromatography (HPLC) is currently the most widely used technique for analytical purposes and preparative separations of chiral compounds.^{7,8-9} Recently, special attention has been drawn to the role of stereoregular polymers as chiral stationary phases (CSPs) among which crystalline nanoporous materials are found.⁸ Several studies report the chiral recognition skills of metal-organic frameworks (MOFs)^{8,10-12} and zeolites.¹³⁻¹⁷ These studies analyze in depth the molecular mechanisms for chiral recognition and rationalize the features of these materials that relate to several enantioselective behaviors such as selective adsorption^{13-15,18-20} or asymmetric catalysis.^{16,21-23} As a consequence, many efforts have been made for the rationalized design of new chiral materials and the methods for their synthesis.²⁴⁻³¹

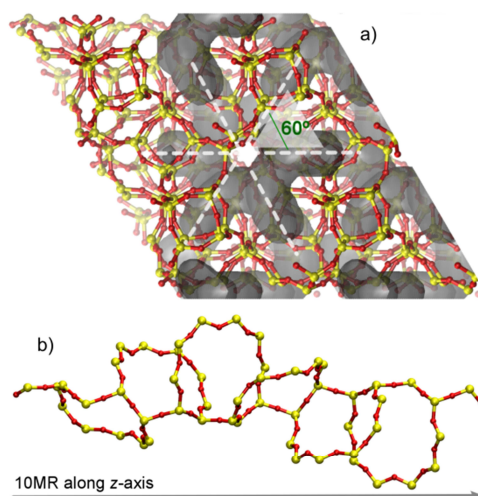


Figure 1. Atomistic *xy*-view of the chiral pore topology of one enantiomer of zeotype STW, which consists of six rectangular cages oriented in the three dimensions of space with a rotation of 60° along the *x*-axis (a). This view was generated with Pore Blazer³² by moving a probe particle with a diameter of 3.5 \AA in STW-Si (gray area). *xz*-view of 10-membered rings of a single channel along the *z*-axis (b). Both views were obtained with VMD.³³

Up to now, a small number of zeolite frameworks have been crystallized in chiral space groups. Among them, STW is a recently discovered zeolite that was first synthesized as a germanosilicate zeolite called SU-32.³⁴ This material was difficult to prepare in a pure form and suffered from thermal and hydrothermal stability problems typical of germanosilicates. Later on, a different synthetic strategy afforded a pure silica zeolite with the same STW framework type,³⁵⁻³⁶ known as HPM-1 zeolite, which exhibits the high thermal and hydrothermal stability of silica materials. The pore topology of the STW zeotype can be described as a helicoidal channel running along the *z*-axis, which consists of six rectangular cages oriented in the three dimensions of space and perpendicular to the direction of the channel (Figure 1). Each

cage is rotated 60° to the right of the previous one in space group $P6_122$, all of them connected through 10-membered rings.²¹ There is, of course, an enantiomeric crystal in space group $P6_522$, in which the cages are rotated to the left and, in principle, the actual crystalline powder is a racemic conglomerate. The helicoidal channel defined is intersected by 8-membered rings which shape the cages (Figure A1 in the Appendix 5). Given the chiral topology of this zeotype, and the fact that individual crystals are enantiopure,³⁷ it is a useful study model on enantioselectivity connected with potential applications.¹³ This idea is reinforced by the very recent report of the synthesis of enantioenriched germanosilicates with the STW structure using enantiopure organic structure-directing agents and the evidence of significant chiral selectivity over the resulting enriched material in both catalysis and adsorption processes.³⁸

One of the most widespread ideas is that chiral recognition is led by the confinement of the molecule inside the pores or channels of the materials.^{14-15,39} Along with the experimental results related to enantioselective separation which reveals the actual potential of chiral nanoporous materials as molecular sieves and CSPs,¹⁰⁻¹¹ theoretical studies based on molecular simulations unravel the underlying molecular mechanisms. In addition to the close match of the molecule to the size of the channel, other factors related to guest-guest and host-guest interactions must be considered. Some materials, such as homochiral MOFs,¹⁸ might have more than one chiral recognition site based on host-guest interactions. These sites could be selective either to the opposite enantiomer, or to the same one, which would increase chiral selectivity.^{20,40} Also, the channel surface chemistry might change the affinity

with which the molecules are adsorbed within the pore, influencing the confinement and selectivity consequently.⁴¹ Regarding guest-guest interactions, dispersive forces, dipole-dipole interactions, and hydrogen bonding may be especially effective for the same or the opposite enantiomer inside the channel thus determining the packing of enantiomers and, therefore, the selectivity.¹¹ As an example of the relevance of the overall contribution of the aforementioned factors, additional mechanisms exist that allow nonchiral materials to be enantioselective in nonracemic mixtures. In the “random cell” mechanism, the unordered packing of one enantiomer leaves asymmetric spaces that can be occupied by the opposite enantiomer.⁴² In the case of the “chiral cell” mechanism, these asymmetric spaces are generated by extra-framework cations.⁴³ To conclude, the key to the chiral selectivity is the confinement, i.e., the adequate match of size and shape between the molecule and the channel, though this factor can be considered a consequence of or modulated by the contribution of host-guest and guest-guest interactions related to the features of a given material.

In the context of the relationship between confinement and chiral selectivity, the flexibility of porous crystalline materials can have a profound effect. Some of them undergo flexible phenomena⁴⁴ such as breathing,⁴⁵ swelling,⁴⁶⁻⁴⁷ linker reorientation,⁴⁸⁻⁴⁹ negative/positive thermal expansion,⁵⁰ or subnetwork displacement,⁵¹ which are generally triggered by external stimuli, such as temperature, pressure, or guest adsorption.¹² But for most frameworks, this intrinsic flexibility⁵² involves just lattice vibrations and does not affect strongly adsorption properties or the crystalline regularity. These frameworks are commonly treated as rigid and zeolites are

typically ascribed to this category. However, the intrinsic flexibility of a zeolite might also induce changes in the pore opening able to disrupt the structural selectivity of this material.⁵³ Another aspect to bear in mind is that changes in the chemical composition can also alter the flexibility pattern of a framework since the presence of germanium in zeolites confers static and dynamic flexibility⁵⁴ to an otherwise rigid framework. Considering this, the interplay between flexibility and confinement might alter dramatically the chiral recognition capacity of a framework. Recently, several studies have focused on the development of efficient methods to approach computationally the effects of flexibility on adsorption properties, which otherwise lead to very time-consuming simulations.⁵⁵ Unfortunately, it is not clear yet how accurately these methods capture the flexibility effects without having to simulate a fully flexible framework, and reporting the behavior of the framework upon adsorption is likely to be relevant in the case of chiral selectivity.

The current work presents simulation results of an extensive research on chiral separation in chiral flexible zeolites. Both the all-silica and germanosilicate frameworks of the chiral zeotype STW are used as adsorbents. The chiral probes chosen are the chiral isomers belonging to the group of amyl alcohols: 2-pentanol (2P), 2-methylbutanol (2MB), and 3-methyl-2-butanol (3M2B). The *R* enantiomer of 2P is widely used as an intermediate in the synthesis of drugs against Alzheimer's disease.⁵⁶ Additionally, aiming to gather a deeper knowledge of the physical chemistry behind the chiral separation and to study the effect of the molecular arrangement induced by host-guest and guest-guest interactions on a chiral separation, we have studied the separation of structural isomers

of 2P and have contrasted these results with those obtained in the chiral separation. Thus, we selected 2MB and 3M2B, which are structural isomers of 2P with methyl groups in different relative positions, as it can be seen in Figure A2 of Appendix 5.

Computational Details

The structures for HPM-1 and SU-32, all-silica and germanosilicate frameworks of STW, respectively, were built through a meticulous process of energy optimization using the Vienna *ab initio* simulation package (VASP)⁵⁷⁻⁶⁰ to get the most stable structure of each configuration. The two sets of experimental atomic positions reported for the all-silica³⁶ and the germanosilicate frameworks³⁴ were geometrically optimized while keeping the cell parameters fixed. To this aim 100 germanosilicate structures with varying Si, Ge distributions were previously constructed from the experimental set of SU-32 positions constrained by the reported distributions of silicon and germanium atoms for each crystallographic site³⁴ (Figure A3). The energy of these structures were calculated with VASP by single-point calculation using the PBEsol exchange-correlation functional,⁶¹ from which the one with the lowest energy is retained. Finally, the all-silica and the selected germanosilicate structures were relaxed with VASP, optimizing both atomic positions and cell parameters. The resulting structures are used in this study.

To study the chiral recognition capacity of the adsorbent, the asymmetric carbon that confers chirality to the guest molecules must be properly defined. Therefore, a full-atom flexible force field is used to model each pair of enantiomers for each of the alcohols: *R/S*-2-pentanol (2P), *R/S*-2-methylbutanol (2MB), and *R/S*-3-methyl-2-butanol

(3M2B). Thus, the alcohol adsorbates are flexible and based on Lennard-Jones (LJ) parameters, charges, and geometries defined by OPLS-AA force field⁶² (Table A1 and A2 in the Appendix 5). To define the host-guest interactions, Lorentz-Berthelot combining rules were applied to the LJ parameters of guests and host. In order to study the adsorption process, the choice of the force field for host, guest, and host-guest interactions cannot be arbitrary. Rather, the set of charges of the models for host and guest molecules must be compatible, i.e., van der Waals and electrostatic interactions should be correctly balanced. Thus, charges and LJ parameters of silicon and oxygen atoms of the host were defined through the TraPPE force field specific for zeolites,⁶³ which uses comparable charges to the OPLS-AA force field, and both lead to similar results (see Figure A4 in Appendix 5). Given that silicon and germanium atoms have rather similar electronegativity and polarizability,⁶⁴ as well as having identical valence, the main difference is attributed to the size of germanium, affecting the Ge-O equilibrium bond distance and the structural distortions generated by these asymmetric distances. The interaction of Si and Ge atoms (at the center of the TO_4 tetrahedron) with sorbate molecules are taken into account, but are smaller than the corresponding interactions of O atoms. Thus, LJ parameters and charge of germanium atoms are assumed equal to silicon atoms, as previously validated in the literature.¹⁴ Both HPM-1 and SU-32 structures are modeled either as rigid or as flexible. When rigid, the crystallographic positions of each atom are fixed in space. In contrast, when the structure is considered flexible, Hill⁶⁵ force field is used to model the host-host interactions, bond stretching, angle bending, and torsions in the framework, since it has been efficiently used for similar computational works.^{48,55} For this

work, geometric parameters of Hill were adjusted to consider the Ge-O bond equilibrium distance ($r_{\text{Ge-O}} = 1.77 \text{ \AA}$), which is longer than the Si-O bond ($r_{\text{Si-O}} = 1.61 \text{ \AA}$). This equilibrium distance was selected from the average of Ge-O distances of the optimized structures with VASP. Specific functions for Ge-O-Ge and O-Ge-O angles are not needed given that the distortions generated by the specific Ge-O equilibrium distance in heteroatomic tetrahedra are in relatively good agreement with experimental structures. Charges, LJ parameters, and models for bond stretching, angle bending, and torsions in hosts and guests, and further information are properly detailed in the Appendix 5.

Adsorption data of each enantiomer of 2P, 2MB, and 3M2B for both single components and mixtures were computed using grand canonical Monte Carlo simulations (GCMC) at 298 K with the RASPA software.⁶⁶ A $2 \times 2 \times 1$ super cell was chosen for the simulation box for both all-silica and germanosilicate STW structures (STW-Si and STW-SiGe). Given that the LJ cutoff radius was set to 12 \AA , all the dimensions of the simulation box are larger than twice the cutoff radius. Periodic boundary conditions were applied⁶⁷ and long-range electrostatic interactions calculated through Ewald summations. Simulations were arranged in cycles of trial moves: insertions and deletions based on the continuous fractional component move,⁶⁸ total and partial reinsertions, and random translations and rotations of the molecules. Each point of the isotherms computed for single components were obtained from the average of four independent simulations after 10^5 cycles of initialization and 10^6 cycles of production. The adsorption values for binary mixtures of structural isomers were computed in the same way. For mixtures of enantiomers, S-curves at 10^6 Pa were calculated. An S-curve

displays a plot in which each point represents the molar fraction of adsorbed molecules for a given enantiomer against the molar fraction fixed in the bulk for the same enantiomer. Each point on this type of graph is obtained as the average of eight independent simulations after 10^4 cycles of initialization and 500 000 cycles of production. For these mixtures, simulations were speeded up by introducing an additional energy-biased identity change move with the same probability as other intended moves.

Every simulation was performed for both rigid and flexible frameworks. In the latter, insertion moves are handled with the configurational bias insertion move.⁶⁹ To study the structural flexibility upon adsorption and to ensure a proper host-guest interaction we use a MC-move which inserts a short molecular dynamics (MD) simulation in the microcanonical (NVE) ensemble in a hybrid grand canonical Monte Carlo algorithm (here called hybrid MCMD). This allows for the flexibility of the framework without changing its volume. Because of the ill-defined nature of simulating both the molecular adsorption and framework thermal coupling with the inserted/deleted molecule, this kind of algorithm is crucial to capture the distortions upon the guest-adsorption process.⁷⁰⁻⁷² In all of the simulations performed incorporating MD moves, pure compound isotherms, adsorption isotherms of binary mixtures, and S-curves, each point was obtained after 15 000 cycles of initialization, 300 000 cycles of production and a 2 ns overall time of framework dynamics. From these simulations, framework snapshots were taken to study the behavior of intermediate frameworks.

Diffusion data were obtained through MD simulations in the canonical ensemble

(NVT), at 298 K and infinite dilution, with one single molecule moving inside the simulation supercell. The canonical ensemble was chosen to obtain average values at the same temperature than the rest of our simulation results, and the thermostat used is the Nosé-Hoover chains algorithm.⁷³⁻⁷⁴ The time step was set to 0.5 fs and the mean squared displacement (MSD) of the molecule was recorded for 250 ns on average. These simulations were performed for each enantiomer of the three alcohols considering a rigid framework only to evaluate the capacity of each adsorbate to cross the structure. The MSD were fitted to a linear regression in the diffusive regime to obtain diffusion coefficients for each enantiomer in each structure.⁷⁵ Likewise, MD simulations were also carried out in the canonical ensemble, at 298 K with a time step of 0.5 fs, to study the flexibility pattern of empty STW-Si and STW-SiGe up to 5 ns.

To shed light on the effects exerted by the vibration of the frameworks we computed the average minimum aperture distribution of 8- and 10-membered rings, i.e., the time average of the minimum O-O separation across the aperture. This calculation was performed for each snapshot generated during the hybrid MCMD simulations that provided the single-component adsorption isotherms and the adsorbed fractional content of *R* enantiomer from racemic mixtures. The resulting values were averaged and shown by component. The reference used in the comparison is the average minimum aperture obtained from the snapshots from MD simulations carried out with the empty frameworks. Furthermore, to gain additional insight we calculated the pore size distributions with RASPA and obtained a detailed view of the accessible space inside the structures using Pore Blazer software³² to move probes of different diameter sizes along the channels.

This software considers the van der Waals radii of framework atoms and checks the connectivity of channels by using probes of a given diameter. To understand the relevance of host-guest interactions thermodynamic data were calculated through the Widom test particle insertion method⁶⁷ along with simulations in the canonical ensemble for a single molecule moving randomly (molecular translation, rotation, and reinsertion) to compute average occupational density profiles and energy histograms. Simulations in the canonical ensemble at 298 K were also run for a total number of adsorbed molecules of 4, 8, 12, 16, 20, 24, and 28 *versus* a racemic bulk to study the loading-dependent enantiomeric composition in the framework. In the latter simulations, random moves and identity change operations were permitted. Simulations were performed five times independently using the rigid STW-Si and STW-SiGe, and their intermediate frameworks taken from the hybrid MCMD simulations run for the adsorption of chiral mixtures. The simulations carried out in this study were mostly for the right-handed STW structures (space group $P6_122$). However, to test the enantioselectivity in the inverted structures, complementary simulations were also conducted to obtain the S-curve for the enantiomeric mixtures of 2P and 3M2B in the left-handed all-silica and germanosilicate rigid structures ($P6_522$).

Experimental Details

Pure silica HPM-1 (STW) was synthesized according to previously reported procedures using 2-ethyl-1,3,4-trimethylimidazolium and fluoride as structure-directing agents.³⁵⁻³⁶ Adsorption data for 1-pentanol, 2-pentanol, and 3-pentanol on HPM-1 were obtained volumetrically at 313 K and pressure ranging from 0 to 10 Torr using

3Flex Micromeritics analyzer. The system guaranteed high accuracy with a resolution of 10^{-5} Torr. The temperature within the chamber was maintained at a constant value with a precision of ± 0.3 K. The purity of all organic adsorbates studied here were higher than 99.8%, purchased from Sigma-Aldrich. Each of the three pentanol isomer vapors was generated by heating, and the adsorbent was placed into the cylindrical quartz bucket (flat bottom, 9×12 mm) and evacuated to a residual pressure of 10^{-3} Torr at 523 K for 6 h. A point isotherm was recorded at equilibrium when no further uptake change was observed. Note that data were not corrected for nonideality and kinetic limitations were not considered.

Results and Discussion

In this work, we consider two materials with different chemical compositions but the same STW zeolite topology and the same space group of symmetry ($P6_122$ or $P6_522$, #178 and #179, respectively, depending on the chiral configuration) so that the characteristic chiral channel of this topology is present in both frameworks. As explained in the Computational Details section the germanosilicate framework has been generated based on the relative population of Si/Ge atoms in each one of the five crystallographic sites³⁴ with an overall ratio Si/Ge ~ 1 . The cell parameters of the germanosilicate framework (STW-SiGe) are 4% larger than those of the all-silica structure (STW-Si), as depicted in Table A5 of the Appendix 5. The accessible pore volume is lower for STW-Si (1297.49 \AA^3) than for STW-SiGe, (1583.99 \AA^3) and account for approximately 34% and 37% of the total volume of each unit cell, respectively. Even though the two frameworks share the same topology, their correspondence is not merely obtained by scaling, as can be seen in Figure 2 (left) from

the pore size distribution (PSD). Three discernible peaks are found and the ones for STW-SiGe are displaced *circa* 0.4 Å to the right. STW-Si shows three peaks at increasing diameters: 4.15, 4.37, and 4.71 Å. STW-SiGe shows also three peaks at 4.5, 4.81, and 5.11 Å, although the intensity of the medium-sized peak is low compared to the others. Since the topology of STW consists of one-dimensional chiral channels, the PSD describes sections of different sizes inside the pore. To study the accessibility through these pore sections the void space distribution inside the frameworks has been computed using Pore Blazer and analyzed. Thus, probe particles with increasing diameter sizes, from 2 to 7 Å, were used to explore the pore. The pore space of STW-Si is visualized in Figure 2 for probe particles of 4 (blue) and 4.5 Å (red). These diameters were selected because they allow for a clear view of each pore section, which are analogous in both structures. The maximum probe particle diameters for the channel are 4.2 Å for the STW-Si, and 4.7 Å for STW-SiGe, which matches the medium-sized peaks of each PSD. The largest peak (I) represents the widest section of the pore, with a larger diameter than the largest diffusing particle. As the red area indicates

in Figure 2, this peak corresponds to curved channels that connect other sections of the pore. The medium-sized peak (II) limits the diffusion of particles along the chiral channel of STW and, as seen in the blue area of Figure 2, is a neck between the curved channels (I). The leftmost peak (III) is found in each distribution at a lower diameter than the largest diffusing particle for each case. This section of the pore, as it does not limit the diffusion of particles along the chiral channel, can be described as an elongation of the curved channels (I) with the shape of a pocket (III). For clarity, the different pore sections of the pore will be referred to as curved channels (I), necks (II), and pockets (III) throughout the manuscript. The contribution of these pore sections builds the chiral channel and cages characterizing the topology of STW. Although both structures are very similar, the chiral channel in STW-SiGe is significantly larger and the proportional contribution of necks to the accessible volume is smaller (II).

The adsorption mechanisms of three structural isomers of pentanol ($C_5H_{12}O$) in the frameworks STW-Si and STW-SiGe are investigated first. Since the force field used

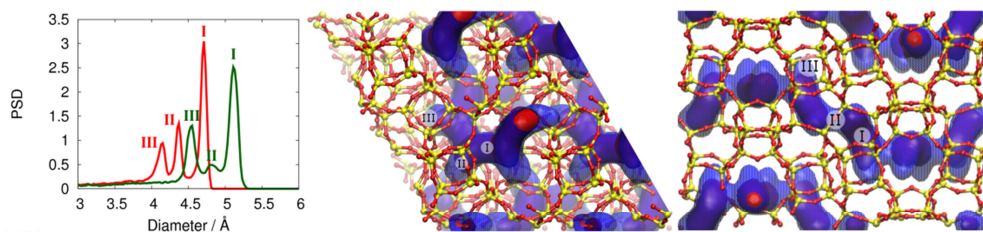


Figure 2. Pore size distribution (left) of STW-Si (red) and STW-SiGe (green). xy - (center) and zy - (right) views of STW geometry showing the internal pore space featuring wide sections (I) in red, and diffusion limiting necks (II) and pockets (III) in blue. These views were generated with Pore Blazer by moving probe particles of increasing diameter sizes in STW-Si: 4 Å (blue area) and 4.5 Å (red area). VMD was used as the visualization tool.

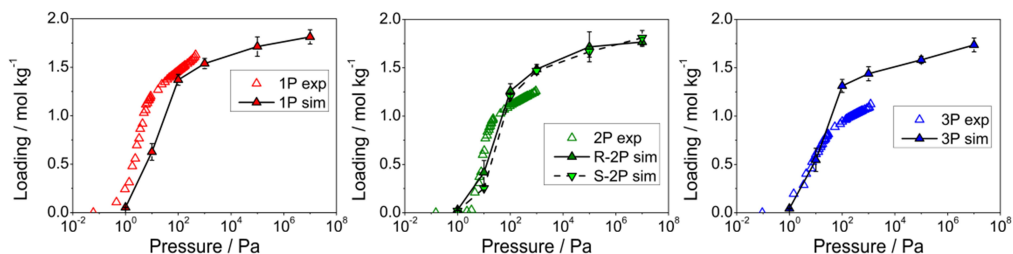


Figure 3. Adsorption isotherms of 1P, *R/S*-2P, and 3P in STW-Si at 313 K: comparison of experimental data (open symbols) and data obtained computationally (full symbols).

in this work has been derived by combining different parametrizations, the consistency of the overall force field had to be established. For this purpose, adsorption isotherms for 1-, 2-, and 3-pentanol (1P, 2P, 3P) were computed in STW-Si at 313 K by GCMC simulations. The resulting data are plotted in Figure 3 along with experimental data obtained according to the Experimental Details section. Considering that no adjustment was required, the agreement proves that the calculated host-guest interactions are reliable. Next, the adsorption isotherms of the *R* and *S* enantiomers of 2P, 2MB, and 3M2B as pure compounds are studied in both structures at 298 K (Figure 4). Given the size of the channels of STW-Si and STW-SiGe, mean squared displacements (MSD) were calculated by molecular dynamics simulations only to check if the compounds can diffuse inside the frameworks (Figure A6 of the Appendix 5). Only those compounds crossing the diffusive regime after 100 ns are considered for adsorption. Thus, the chiral channel in STW-SiGe, which is 0.4 Å wider than the channel in STW-Si, allows diffusion of all compounds, while only 2P diffuses in STW-Si. Consequently, in the all-silica structure we focus on the adsorption isotherms of *R*- and *S*-2P.

Overall, the isotherms exhibit a similar shape with a steep slope evidencing the rapid pore filling usual in adsorption of alcohols.⁷⁶⁻⁷⁷ The onset pressure of adsorption is at 1 Pa for 2P, 10 Pa for 2MB, and 100 Pa for 3M2B. At saturation, 2P reaches about 6.6 and 8.7 molecules per unit cell in STW-Si and STW-SiGe, respectively. Saturation in STW-SiGe is reached with about 7.6 (2MB) and 7 (3M2B) molecules per unit cell. In general terms, differences in the adsorption values between *R* and *S* enantiomers of each pair stay within the error bars. Nevertheless, there are clear differences in the adsorption of *R*- and *S*-3M2B. In the low-coverage regime, the value of the *S* enantiomer is twice the value of *R*, and, at saturation, *S* enantiomer packs better than *R* and it allows one additional molecule in the structure. The six cages that form the chiral channel of STW are occupied with one molecule each up to 6 molecules per unit cell. Once this value is reached the molecules pack tighter, freeing space for additional molecules (Figure A7). This packing capacity depends on the structural features of each molecule and the available space, i.e., the pore size, for the molecular arrangement. The adsorption of 2P is higher in STW-SiGe than in STW-Si as expected by the higher volume and wider pore size of the former framework. The increasing adsorption of 3M2B, 2MB, and

2P in STW-SiGe indicates that linear isomers pack more efficiently in the structure than branched isomers.

The adsorption of the molecules in the flexible and rigid structures is shown in Figure 4. Differences between values of adsorption using the rigid and flexible frameworks lie generally within the error bars and validate the host-host bonded and nonbonded interaction terms defined in the Hill force field. Therefore, the adsorption in the saturation regime reaches similar values, i.e., the adsorption capacity of the structures is not altered by the flexibility of the lattice. However, we found some differences in the low-coverage regime: The adsorption of 2P (in STW-Si) and 2MB (in STW-SiGe) at 10 Pa is slightly larger in the flexible framework for both pairs of enantiomers, while the

adsorption of *R/S*-2P (at 10 Pa) and *R/S*-3M2B (at 100 Pa) in the flexible STW-SiGe is lower than in the rigid framework. The adsorption of *R* and *S* enantiomers of 3M2B in the low-coverage regime follows the same trend than at saturation. The value of adsorption of *S*-3M2B in the flexible framework compared to the rigid one decreases to the same value than *R*-3M2B, reducing the *R/S* difference in the adsorption which apparently reflects absence of selectivity. This behavior upon switching on flexibility in the framework model suggests some coupling between the thermal lattice vibration and the adsorbates.

To analyze the changes that frameworks undergo during adsorption, we calculated the minimum aperture of 8- and 10-membered rings, i.e., the shortest distance

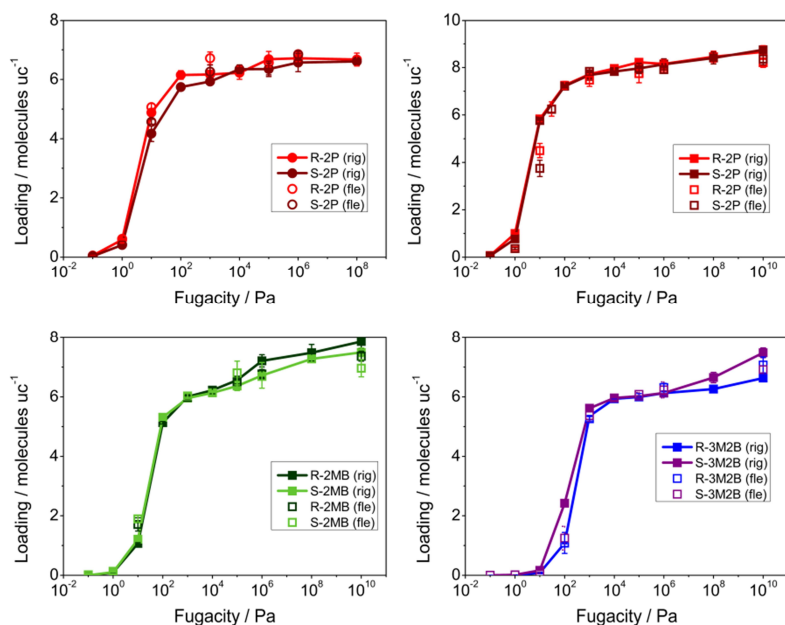


Figure 4. Single-component adsorption isotherms (298 K) of enantiomeric pairs of a) 2P in STW-Si, b) 2P in STW-SiGe, c) 2MB in STW-SiGe, and d) 3M2B in STW-SiGe, modeled as rigid (full symbols) and flexible frameworks (open symbols).

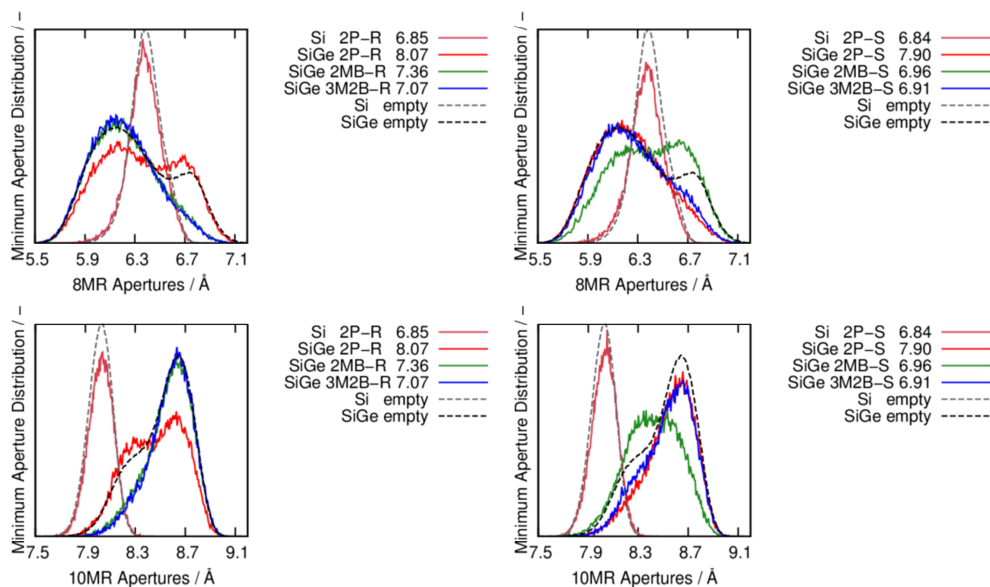


Figure 5. Distribution of minimum apertures of 8MR (top) and 10MR (bottom) in the empty STW-Si and STW-SiGe frameworks (dashed lines), and saturated with molecules (solid lines). Loading is indicated for each compound in molecules per unit cell.

between opposite oxygen atoms. These calculations were performed from snapshots generated during the hybrid MCMD simulations. The values obtained were time averaged for each compound, and compared to the values of minimum aperture calculated for the empty frameworks. The resulting histograms are plotted in Figure 5, and the corresponding atomistic views of ring distortions can be seen in Figures A8 and A9 (Appendix 5). The empty STW-SiGe framework used as a reference shows a broad peak with maxima at 6.1 and 6.75 Å in the 8-membered rings (8MR), whereas the 10-membered rings (10MR) show a maximum at 8.61 Å and a shoulder at 8.3 Å. This suggests a non-trivial geometric coupling between the 8MR and 10MR: the former shrinks even below the STW-Si level while the latter broadens. The distribution of window apertures changes

for all components when molecules saturate the structure, which points to a host-guest coupling in the flexible STW-SiGe framework. However, given that the adsorption of different compounds leads to different distributions, it can be inferred that the widening or shrinkage of window apertures must be related to the adsorption sites and the microassembly of molecules, depending on the nature of the adsorbate and the loading in the structure. In general terms, upon alcohol adsorption the aperture of 8MR tends to a smaller size and narrower distribution while that in 10MR tends to a wider size and narrower distribution, effectively constraining the aperture and evidencing the geometric coupling between 8- and 10MR. A noticeable exception is *S*-2MB that broadens the distribution and makes it less specific than in the empty framework. Contrary to this, the STW-Si

framework shows two single peak at 6.4 Å and 8 Å, for the 8MR and 10MR, respectively, whether empty or with sorbate molecules. Thus, the thermal lattice vibration of STW-Si is not coupled to the sorbate molecules, since the defined peaks remain unaffected by the different loadings and sorbate molecules.

The fact that 2P is adsorbed in STW-SiGe at lower pressure values than 2MB and 3M2B, points to a preferential adsorption of the linear isomer in this structure, which is linked to the different degree of confinement of each compound in the framework. To understand this behavior and get a deeper insight into the interplay between sorbate molecules and the thermal lattice of STW-SiGe framework, we study the selectivity of these frameworks towards structural isomers by computing adsorption isotherms of equimolar binary mixtures of racemic 2P-2MB, 2P-3M2B, and 2MB-3M2B in STW-SiGe at 298 K (Figure 6). The adsorption isotherms reveal that STW-SiGe strongly favors the adsorption of 2P over 2MB and 3M2B, as expected, and of 2MB over 3M2B. The trend in the preferential adsorption from 2P to 3M2B follows a similar pattern than that established in previous studies,⁷⁶⁻⁷⁸ where a linear molecule is preferred over mono or dibranched molecules. This selective behavior of STW-

SiGe holds true both in the rigid and flexible model of the framework. Still, as in the case of the pure systems, the adsorption in the flexible STW-SiGe shows some differences. Firstly, discrepancies in the filling behavior are consistent with those observed in the pure systems. Next, in the mixture of 2P-2MB, adsorption values of 2P are slightly lower in the flexible framework, while those for 2MB are higher, yet these differences are no greater than 1 molecule per unit cell. Finally, in the third mixture, 2MB and 3M2B, the adsorption of 3M2B reaches values below 1 molecule per unit cell, and 2MB reaches higher values, although at saturation they are equal to those of the rigid structure. It is worth considering that the coupling between lattice vibration and sorbate depends on the uptake and sorbate type. Thus, most of the differences observed are connected to the wider amplitude of vibrations of the STW-SiGe framework seen in Figure 5. This may create variable sites into which a further molecule fits, leading to subtle changes in the structural selectivity (Figure 6). Specifically, the different trends that window apertures show for 2MB and 3M2B or 2P, and the competition of each component for adsorption sites (Figures A10 and A11 in the Appendix 5) generate adsorption values that are not predicted when the framework is modeled

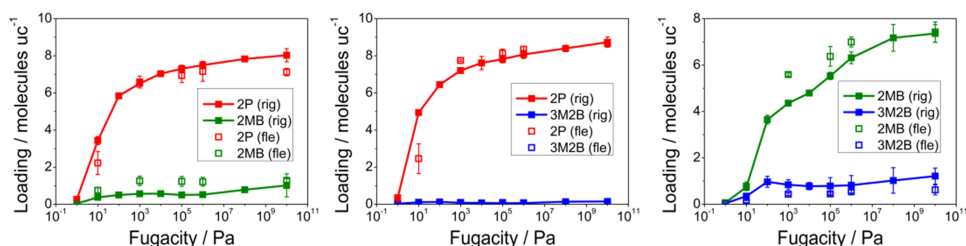


Figure 6. Adsorption isotherms of the equimolar mixtures of 2P-2MB (left), 2P-3M2B (center), and 2MB-3M2B (right) at 298 K in STW-SiGe, calculated with rigid and flexible frameworks.

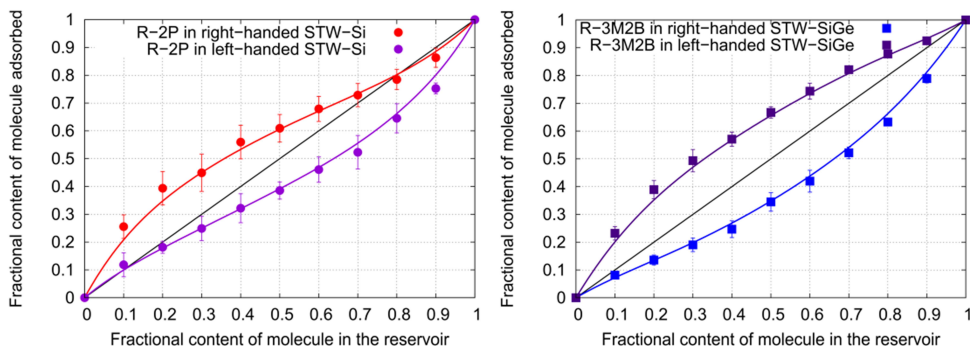


Figure 7. Adsorbed fractional content of *R* enantiomers as a function of the *R*-fraction in an *R/S* mixture in the reservoir for right- and left-handed STW-Si (left) and STW-SiGe (right) taken as rigid frameworks, at 10^6 Pa and 298 K. The black straight line represents unselective adsorption (i.e., the adsorbed composition is identical to that in the reservoir). Colored solid lines are an approximation to the data trend using the Bezier curve smoothing.

as rigid. However, the trends in preferential adsorption remain, and the selectivity for each mixture is at least 5.

The main aspect addressed in this work is the effect of flexibility on the enantioselectivity of STW-Si and STW-SiGe. For this purpose, enantioselectivity is analyzed first for the rigid frameworks. Figure 7 shows the fractional content of the *R* enantiomer in the adsorbed phase against the fractional content of the same enantiomer imposed on the bulk at conditions of 10^6 Pa and 298 K. The straight line would indicate a lack of enantioselectivity, i.e., values of fractional content in the adsorbed phase equal to those in the bulk. For 2P in STW-Si and 3M2B in STW-SiGe, a significant deviation from the straight line is seen in Figure 7, while 2P and 2MB in STW-SiGe remain close to the straight line as is shown in Figure A12 of the Appendix 5. In the case of 2P in STW-Si the fractional content of the *R* enantiomer is higher than that set in the bulk below 0.7, and falls on top of the straight line above 0.8. This indicates that right-handed STW-

Si is selective towards the *R*-2P enantiomer while the fractional content is below 0.7. On the contrary, the fractional content of *R*-3M2B in right-handed STW-SiGe is lower than that in the bulk for all compositions. This reveals that right-handed STW-SiGe is selective towards *S*-3M2B.

In addition, since enantioselectivity is affected in a predictable way by the handedness of the framework, Figure 7 shows the curves obtained with GCMC simulations using the right- and left-handed frameworks. As expected, these curves are inverted around the central point (0.5, 0.5). Then, the left-handed STW-Si enriches the mixture in *S*-2P instead of *R*-2P. The left-handed STW-SiGe adsorbs preferentially the opposite enantiomer, *R*-3M2B, throughout the composition range. This “inversion” in adsorption selectivity is not unheard of, since opposite enantioselectivity in enantiomeric frameworks has been reported previously.^{13,17} However, it has not been analyzed yet in scalemic mixtures and, to the best of our knowledge, this almost exact symmetry in the chiral adsorption has

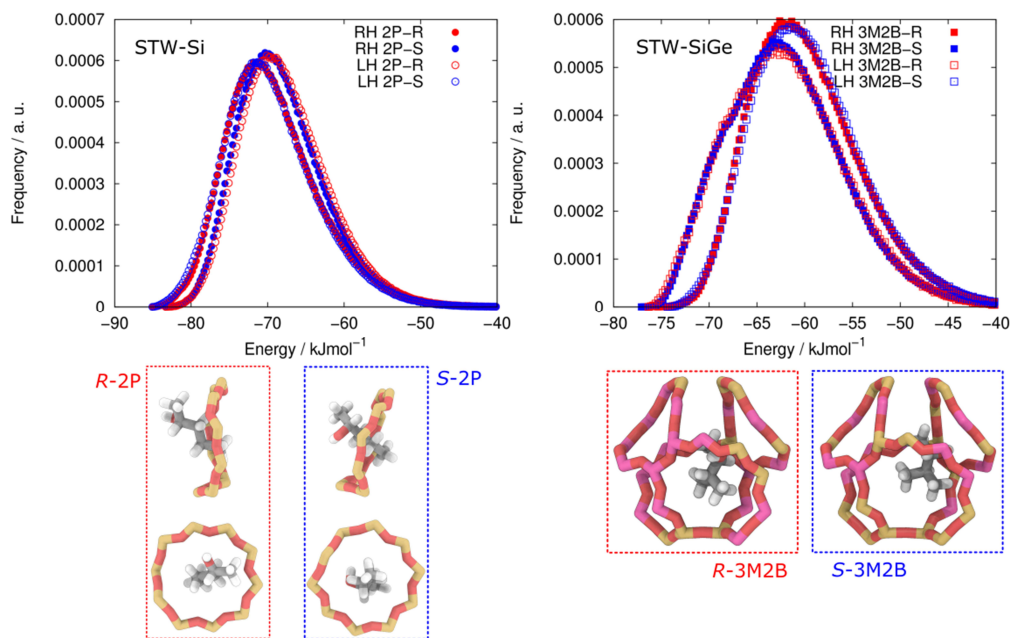


Figure 8. Energy histograms for pairs of enantiomers of 2P and 3M2B in the right- (RH) and left-handed (LH) frameworks of STW-Si and STW-SiGe (top). Binding energies and sites for *R* (red) and *S* (blue) enantiomers of 2P in STW-Si (bottom left) and 3M2B in STW-SiGe (bottom right), both right-handed frameworks. Bottom images were made with ambient occlusion using QuteMol.⁷⁹

not been shown before. It also shows in an independent analysis from our error bars that the uncertainties on the data are small given that the simulations are independent from each other.

In order to examine closely the host-guest interactions, we computed host-guest energy distributions for a single molecule of each enantiomer of either 2P or 3M2B when sampling the accessible volume of the right- and left-handed frameworks (Figure 8, top). The inversion in the adsorption selectivities when switching from right- to left-handed framework is also observed in the host-guest energy distributions. Thus, the energy

profile of *S*-2P in the left-handed STW-Si falls on top of that of *R*-2P in the right-handed counterpart. Likewise, the energy distribution of *R*-3M2B in the left-handed STW-SiGe matches the one for *S*-3M2B in the right-handed STW-SiGe. From these previous calculations we chose the configuration with the most negative host-guest potential energy for each enantiomer in the right-handed frameworks and performed minimizations to find the binding sites, which are also shown in Figure 8 (bottom). The different spatial configuration of each pair of enantiomers causes a difference in their binding energies of ~ 3 kJ mol⁻¹ for both 2P and 3M2B. The

stronger interaction of *R*-2P with the right-handed framework is due to its orientation relative to the 10MR which is tilted with respect to the plane of the ring while the orientation of *S*-2P molecule is perpendicular (Figure 8, bottom left). In the case of 3M2B, the interaction of *S*-3M2B with the right-handed framework is stronger than the interaction of *R*-3M2B due to the shorter distances, on average, between the guest atoms and atoms of the 8- and 10MR (Figure 8, bottom right). The main inertia axes of the *S*-3M2B guest molecule are essentially coplanar with the 10MR. In addition, we have also calculated thermodynamic data at 298 K for *R* and *S* enantiomers of 2P and 3M2B in the right- and left-handed frameworks of STW-Si and STW-SiGe (Table A6 in the Appendix 5). In agreement with the findings above, the isosteric heat of adsorption (Q_{st}) is more negative for *R*-2P ($-69.28 \text{ kJ mol}^{-1}$) than *S*-2P ($-67.06 \text{ kJ mol}^{-1}$) in the right-handed STW-Si, and the values are swapped in the left-handed framework. Similarly, the heat of adsorption of *S*-3M2B ($-56.86 \text{ kJ mol}^{-1}$) in the right-handed STW-SiGe is more negative than that of *R*-3M2B ($-51.3 \text{ kJ mol}^{-1}$),

whereas the values are swapped in the left-handed framework. Finally, the differences in the entropy between *R* and *S* enantiomers of each compound, $-T\Delta S$, for each case suggest that the possible configurations of the preferred enantiomer inside the structure are more constrained compared to those of its counterpart. This, along with the isosteric heat of adsorption and the analysis of binding sites, points to the confinement and the specific chiral topology of the channel as the driving forces of the preferential adsorption, at least at low coverage.

The analysis of the adsorption of mixtures of structural isomers too helps clarify the complex relationship between confinement and enantioselectivity. Even though STW-Si and STW-SiGe have the same topology, the 0.4 \AA wider pores of the latter are enough to disrupt the chiral selectivity towards *R*-2P in STW-SiGe, whereas STW-Si does display chiral resolution. Thus, 2P fits tightly enough in the chiral channel of STW-Si, but both enantiomers can move and adsorb more freely in the wider channel of STW-

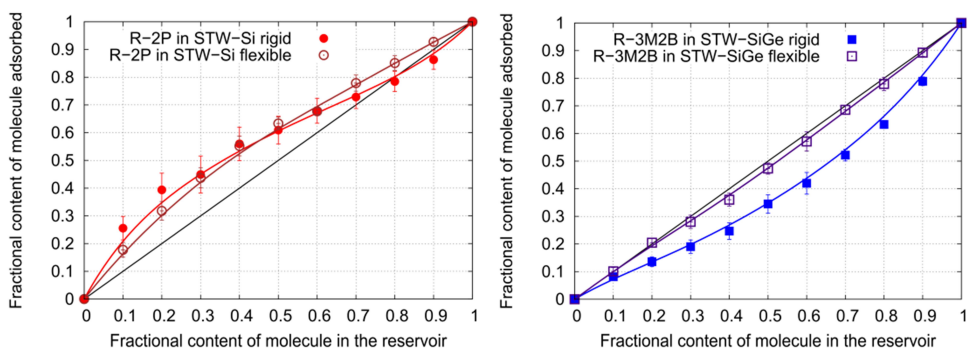


Figure 9. Adsorbed fractional content of *R* enantiomers as a function of the *R*-fraction in a *R/S* mixture in the reservoir for right-handed frameworks, STW-Si (left) and STW-SiGe (right), taken as flexible (open symbols) and rigid (full symbols) frameworks, at 10^6 Pa and 298 K. The straight line indicates that the adsorbed composition is identical to that in the reservoir. Solid lines capture the data trend by using Bezier curves smoothing.

SiGe with the corresponding loss of selectivity. Indeed, STW-SiGe is not selective for 2MB either, yet it is for 3M2B. As mentioned in the analysis of the structural adsorption, 3M2B is a dibranched molecule, which is the bulkiest among these three compounds. Consequently, the chiral recognition of the enantiomers of 3M2B happens only in STW-SiGe, in whose channels the molecules of 3M2B fit tightly.

Once the chiral selectivity of the structures under study had been understood in the rigid frameworks, we investigated how this selectivity is affected by lattice vibrations. To this end, we performed hybrid MCMD simulations in which framework atoms are allowed to move. The obtained results are compared to the values obtained for the rigid model using energetically optimized frameworks. As shown in Figure 9 the flexible STW-Si framework maintains the enantioselectivity towards *R*-2P. Minor variations with respect to the rigid structure are observed and fall within the error bars. In the case of the flexible STW-SiGe framework, the observed preference towards *S*-3M2B decreases strongly and the values of fractional content of this enantiomer in the framework reach the straight line, indicating no selectivity. In terms of enantiomeric excess (*ee*), it decreases from $31 \pm 7\%$ in the rigid model for the framework of STW-SiGe to $5 \pm 4\%$ when the framework atoms are allowed to move at 298 K. Despite this, in the case of STW-Si the vibration of the lattice retains its chiral selectivity (*ee* of $26 \pm 5\%$ in the flexible framework vs. $22 \pm 10\%$ in the rigid framework).

We performed additional GCMC simulations to ensure that differences in the enantioselective behavior are not a consequence of a lack of efficiency of the insertion method during the hybrid MCMD simulations. The fractional content of *R*

enantiomers in the adsorbed phase from a racemic feed has been calculated by averaging results from 34 individual simulations based on snapshots of STW-Si and STW-SiGe frameworks taken from the most stable framework configurations during the hybrid MCMD simulations performed to compute enantioselectivity and freezing the framework atoms. The average *R*-fraction obtained is $0.622 (\pm 0.045)$ and $0.489 (\pm 0.033)$ for the snapshots of STW-Si and STW-SiGe, respectively. This indicates that the lattice vibrations in STW-Si generate intermediate frameworks that are still enantioselective, whereas the intermediate frameworks of STW-SiGe show an average that is barely enantioselective.

In the very recent report by Brand *et al.*, the single-component adsorption of 2-butanol on enantiomerically enriched STW-SiGe suggested a moderate enantioselectivity for *R* and *S* enantiomers on the right- and left-handed enriched zeolites, respectively, i.e., the same hand preference as calculated by us for 2-pentanol. The adsorbents were significantly enriched in Si compared to Ge (Si/Ge ratio in the gels were of at least 2), so their enantioselectivity could be larger than the one we calculate for the materials with Si/Ge=1. Our findings suggest, however, that a significantly larger selectivity could be achieved by the pure silica zeolite. Considering the larger thermal and hydrothermal stability of pure silica zeolites, that material could also avoid the low adsorption values obtained by Brand *et al.* with materials with low crystallinity (a factor of 4 between the butanol uptakes in right- and left-handed materials was considered due to differences in crystallinity).³⁸

It would be an oversimplification to conclude from the analysis of the chiral

selectivity in STW-Si and STW-SiGe that the intrinsic flexibility of zeolites, that is, their natural lattice vibrations, may disrupt the enantioselectivity of the framework, and that therefore a careful analysis of the empty framework yields all the information required to explain or predict loss of enantioselectivity or absence thereof. The underlying reasons for this loss of enantioselectivity are more complex. To understand how the framework is changing in such a way that it can alter its preferential adsorption, PSDs have been calculated for the intermediate frameworks and compared to that obtained from a MD simulation without sorbates (Figure 10). The corresponding window apertures calculated from snapshots generated during the related hybrid MCMD simulations are shown in Figure A13 in the Appendix 5. The window aperture of 8MR and 10MR of STW-Si in Figure A13 remains as invariable as in Figure 5. Their counterparts in STW-SiGe saturated with 3M2B show one wide peak at 6.15 Å and another at 8.61 Å, corresponding to the narrow-sized 8MR and the large-sized 10MR, respectively. Regarding the PSDs (Figure 10), the peaks are well separated in the rigid frameworks but in the flexible

structures the distribution of pore sizes is broad. This explains the greater structural disorder and greater variety of adsorption sites found for the flexible framework. More precisely, the STW-Si framework maintains two peaks, corresponding to the curved channels (4.71 Å) and necks connecting channels (4.41 Å) while the leftmost peak corresponding to the pockets disappears. This is true even in the empty, flexible framework (Figure 10). In the STW-SiGe framework, the leftmost, large peak disappears too, and the central peak, which is of low intensity in the rigid framework, blends with the largest-pore peak, corresponding to the curved channels (5.13 Å). However, in the empty, flexible framework of STW-SiGe the largest-pore peak is slightly displaced to the left (ca. 5.05 Å) and a small shoulder arises (4.49 Å) at a position between the central and small-pore peaks of the rigid framework. This difference is comparable to that observed in the distribution of window apertures for empty and saturated germanosilicate frameworks (Figures 5 and A13), and consistent with the host-guest coupling enabled by the flexibility of the framework.

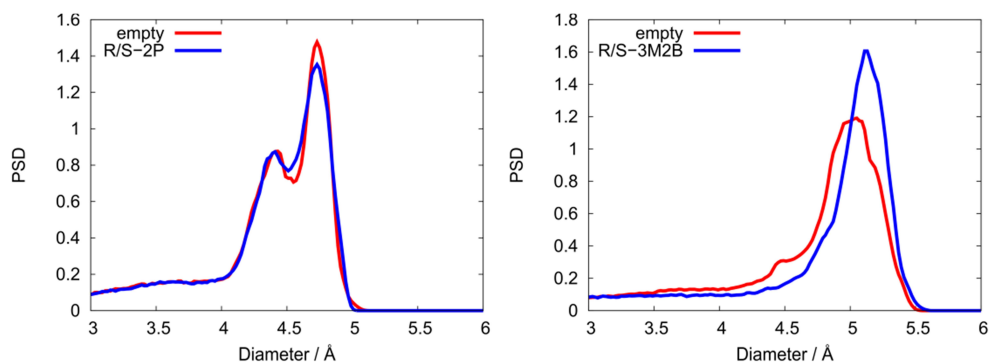


Figure 10. Pore size distribution of flexible STW-Si (left) and STW-SiGe (right) averaged from snapshots of frameworks taken during MD simulations of the empty frameworks (red) and hybrid MCMD simulations from a racemic feed (blue).

Thus, the intrinsic flexibility of the all-silica framework is rather limited and largely sorbate-independent. On the contrary, the flexibility of the germanosilicate framework is large and sorbate-dependent, and responsible for the loss of well-defined pore spaces. In addition, the shrinkage of 8MR is related to the smoothing of the cage surface which, coupled to the aperture of 10MR, leads to a loss of adsorption restrictions and, therefore, a loss of selectivity.

The last question is how the change in the pore size distribution is causally related to the selective adsorptions of enantiomers of 3M2B in STW-SiGe and 2P in STW-Si. The loss of selectivity in a model structure in which smoothing out of the internal pore space is observed strongly supports that the geometry of the chiral channel rather than guest-guest interactions is responsible for chiral separation in these systems. In fact, hydrogen bonding or polar interactions between hydroxyl groups of alcohols in these specific systems is very infrequent (Figure A14 in the Appendix 5). In STW-Si, only the smallest pore sections (necks and pockets) are slightly smoothed and chiral separation for 2P is retained, whereas in STW-SiGe the pore space smoothing is large and chiral separation for 3M2B is lost. To understand the relevance of the topology of the channel in the saturation regime, selectivity was studied depending on loading (Figure A15 in the Appendix 5). These results were obtained by averaging five independent GCMC simulations from a racemic feed in STW-Si and STW-SiGe rigid frameworks selected from the intermediate frameworks used previously. It can be observed that from 1 molecule per unit cell up to 7, the *R*-fraction remains nearly constant. Indeed, *R*-fraction values of 2P are similar and constant in the rigid minimized STW-Si and its intermediate frameworks. In the rigid STW-SiGe, the *R*-

fraction of 3M2B remains stable with increasing loading. Over the intermediate frameworks of STW-SiGe, the averaged *R*-fraction of 3M2B is also found to be loading-independent, but so close to 0.5 that STW-SiGe cannot be considered enantioselective. Given this, it might be interesting to understand how the adsorption sites in the structure relate to the PSD. The average occupational density profiles found in Figures A10 and A11 in the Appendix 5 show the preferential sites of adsorption for each of the molecules under study. Specifically, 2P is mostly present in the curved channels, whereas 3M2B density is especially high in the pockets that arise from the curved channels. Thus, since the widest peak in the PSD of STW-Si, corresponding to the curved channels, is maintained, the adsorption site where the chiral recognition of 2P happens is not altered. Indeed, this means that the binding site of 2P, which is described by the relative orientation of the molecule to the 10MR, is not disrupted by the distortion of the 10MR. In the case of STW-SiGe, the peak corresponding to the pockets, where 3M2B is preferentially adsorbed, is lost. This is caused by the smoothing of the cage, because of the shrinkage of the 8MR in STW-SiGe. Thus, the adsorption site where the chiral recognition of 3M2B occurs is disrupted. As stated before, the binding site of 3M2B is located in the pore space between 8- and 10MR and, as a consequence, a subtle distortion of one of them or both hinders the molecule from adopting the precise, favorable orientation. In fact, the consequences of this can be observed to a lesser degree in the single-component adsorption isotherm of 3M2B (Figure 4). In the rigid STW-SiGe, slight differences in the adsorption of *R*- and *S*-3M2B could be seen at low-loading regime and at saturation. In the flexible STW-SiGe, the chiral recognition site of 3M2B is

disrupted and the previously observed differences in the adsorption of different enantiomers vanish. Then, although the molecules can be adsorbed, the framework exhibits no preference for a specific enantiomer.

Conclusions

The adsorption of 2P, 2MB, and 3M2B has been studied in the all-silica and germanosilicate frameworks of STW zeolite. The theoretical methods are validated by a satisfactory match of the calculated and new experimental adsorption isotherms.

In a first approach, adsorption has been calculated assuming rigid frameworks. In terms of structural separation, STW-Si separates the linear from the branched isomers since the latter cannot enter the framework. The germanosilicate structure shows preferential adsorption in the order 2P, 2MB, and 3M2B. This preferential adsorption is attributed to molecular arrangement that increases from 3M2B to 2P and points to an increasing level of steric confinement from 2P to 3M2B. Regarding chiral selectivity, the right-handed STW-Si is selective towards *R*-2P, while right-handed STW-SiGe is selective towards *S*-3M2B. This enantioselectivity is driven by the geometry of the chiral channel and, therefore, chiral recognition is mainly due to confinement and orientation of the guest within the framework.

The introduction of NVE MD simulations into a GCMC scheme revealed a coupling between adsorbates and lattice vibration in the case of STW-SiGe which depends on the sorbate. However, the intrinsic flexibility of the STW-Si is independent of the presence of sorbate and loading thereof. The wide distribution of window apertures in the germanosilicate framework affects its

internal aperture size distribution and leads to differences in the separation performance. In general terms, the adsorption calculated using the rigid and flexible models matches, and we found this structure suitable for the separation of the structural isomers, independently of the model used.

Chiral selectivity is altered when the intrinsic flexibility of the zeolite that causes structural changes affects the chiral recognition sites. The static lattice vibration around the equilibrium position of the all-silica framework of right-handed STW smooths the surface of the structure but keeps the adsorption sites that select *R*-2P over *S*-2P. Lattice vibration is larger for STW-SiGe due to the presence of germanium atoms. This distorts the pore size distribution of the structure and results in the loss of selectivity by altering the chiral recognition site for 3M2B. These results suggest an enantioenriched pure silica STW should show a better enantioselectivity than the germanosilicates recently reported.³⁸

The increasing degree of influence that intrinsic flexibility might have on selective behaviors leads to the question of how to approach these issues computationally. Although computing flexibility for the systems under study is currently effective and could provide a more realistic view of the further separation process, it is still very expensive in terms of computational cost. Specifically, accounting for structural flexibility during GCMC simulations implies computation times that are four times longer than GCMC simulations with rigidly modeled frameworks. Thus, regardless of modeling the structure as rigid or flexible, it is interesting to consider the possible effect of lattice vibrations on selectivity by focusing on structural distortions in the lattice, the possible host-

guest coupling, and how it might affect the molecular mechanism of separation. In fact, as this work has proven, reliable predictions of the suitability of a given structure for the separation of similar compounds, such as enantiomers, are difficult to obtain if its flexibility is not considered appropriately such as for instance studying empty frameworks.

Acknowledgments

This work was supported by the Spanish Ministerio de Economía y Competitividad (CTQ2016-80206-P and MAT2015-71117-R) and the National Creative Research Initiative Program (2012RIA3A-2048833) through the National Research Foundation of Korea. S. R. G. Balestra thanks the Spanish MINECO for his predoctoral fellowship (BES-2014-067825). We thank A. R. Ruiz-Salvador for his useful discussions about the generation of realistic distributions of silicon and germanium atoms in the structures and J. M. Vicent-Luna for implementing a new tool to plot average density profiles more efficiently.

Bibliography

- (1) Zhang, J.; Chen, S.; Wu, T.; Feng, P.; Bu, X., *J. Am. Chem. Soc.* **2008**, *130*(39), 12882-12883.
- (2) Smith, S. W., *Toxicol. Sci.* **2009**, *110*(1), 4-30.
- (3) Berger, R. G., *Flavors & Fragrances: Chemistry, Bioprocessing and Sustainability*. Springer-Verlag Berlin Heidelberg: Heidelberg, Germany, 2007.
- (4) Hasaneen, M. N., *Herbicides - Mechanisms and Mode of Action*. InTech: Rijeka, Croatia, 2011.
- (5) Daiha, K. d. G.; Angeli, R.; Oliveira, S. D. d.; Almeida, R. V., *PLOS One* **2015**, *10*, e0131624.
- (6) Sharma, R.; Chisti, Y.; Banerjee, U. C., *Biotechnol. Adv.* **2001**, *19*, 627-662.
- (7) Blaser, H.-U.; Pfaltz, A.; Wennemers, H., Chiral compounds. In *Ullmann's Encyclopedia of Industrial Chemistry*, John Wiley and Sons: Online, 2012.
- (8) Shen, J.; Okamoto, Y., *Chem. Rev.* **2016**, *116*, 1094-1138.
- (9) Okamoto, Y.; Ikai, T., *Chem. Soc. Rev.* **2008**, *37*(12), 2593-2608.
- (10) Kuang, X.; Ma, Y.; Su, H.; Zhang, J.; Dong, Y.-b.; Tang, B., *Anal. Chem.* **2014**, *86*(2), 1277-1281.
- (11) Zhang, M.; Pu, Z.-J.; Chen, X.-L.; Gong, X.-L.; Zhu, A.-X.; Yuan, L.-M., *Chem. Commun.* **2013**, *49*(49), 5201-5203.
- (12) Jiang, J.; Babarao, R.; Hu, Z., *Chem. Soc. Rev.* **2011**, *40*(7), 3599-3612.
- (13) Zhang, L.; Jiang, J., *J. Membr. Sci.* **2011**, *367*(1-2), 63-70.
- (14) Castillo, J. M.; Vlugt, T. J. H.; Dubbeldam, D.; Hamad, S.; Calero, S., *J. Phys. Chem. C* **2010**, *114*(50), 22207-22213.
- (15) Clark, L. A.; Chempath, S.; Snurr, R. Q., *Langmuir* **2005**, *21*(6), 2267-2272.
- (16) Avery, K. A.; Mann, R.; Norton, M.; Willock, D. J., *Top. Catal.* **2003**, *25*(1-4), 89-102.
- (17) Dryzun, C.; Mastai, Y.; Shvalb, A.; Avnir, D., *J. Mater. Chem.* **2009**, *19*(14), 2062-2069.
- (18) Bao, X.; Broadbelt, L. J.; Snurr, R. Q., *Microporous Mesoporous Mater.* **2012**, *157*, 118-123.
- (19) Bao, X.; Broadbelt, L. J.; Snurr, R. Q., *Phys. Chem. Chem. Phys.* **2010**, *12*(24), 6466-6473.
- (20) Bao, X.; Broadbelt, L. J.; Snurr, R. Q., *Mol. Simul.* **2009**, *35*(1-2), 50-59.
- (21) Jo, D.; Hong, S. B.; Cambor, M. A., *ACS Catal.* **2015**, *5*(4), 2270-2274.
- (22) Peng, Y.; Gong, T.; Cui, Y., *Chem. Commun.* **2013**, *49*(74), 8253-8255.
- (23) Xuan, W.; Ye, C.; Zhang, M.; Chen, Z.; Cui, Y., *Chem. Sci.* **2013**, *4*(8), 3154-3159.
- (24) Bonnefoy, J.; Legrand, A.; Quadrelli, E. A.; Canivet, J.; Farrusseng, D., *J. Am. Chem. Soc.* **2015**, *137*(29), 9409-9416.
- (25) Demuynck, A. L. W.; Goesten, M. G.; Ramos-Fernandez, E. V.; Dusselier, M.; Vanderleyden, J.; Kapteijn, F.; Gascon, J.; Sels, B. F., *ChemCatChem* **2014**, *6*(4), 2211-2214
- (26) Canivet, J.; Farrusseng, D., *RSC Adv.* **2015**, *5*(15), 11254-1125.

- (27) Kumar, P.; Guliants, V. V., *Microporous Mesoporous Mater.* **2010**, *132* (1-2), 1-14.
- (28) Li, Y.; Yu, J.; Wang, Z.; Zhang, J.; Guo, M.; Xu, R., *Chem. Mater.* **2005**, *17* (17), 4399-4405.
- (29) Yu, J.; Xu, R., *J. Mater. Chem.* **2008**, *18* (34), 4021-4021.
- (30) Mazur, M.; Wheatley, P. S.; Navarro, M.; Roth, W. J.; Položij, M.; Mayoral, A.; Eliášová, P.; Nachtigall, P.; Čejka, J.; Morris, R. E., *Nat. Chem.* **2015**, *8* (1), 58-62.
- (31) Sun, J.; Bonneau, C.; Cantin, A.; Corma, A.; Díaz-Cabañas, M. J.; Moliner, M.; Zhang, D.; Li, M.; Zou, X., *Nature* **2009**, *458* (7242), 1154-1157.
- (32) Sarkisov, L.; Harrison, A., *Mol. Simul.* **2011**, *37* (15), 1248-1257.
- (33) Humphrey, W.; Dalke, A.; Schulten, K., *J. Mol. Graphics* **1996**, *14*, 33-38.
- (34) Tang, L.; Shi, L.; Bonneau, C.; Sun, J.; Yue, H.; Ojuva, A.; Lee, B.-L.; Kritikos, M.; Bell, R. G.; Bacsik, Z.; Mink, J.; Zou, X., *Nat. Mater.* **2008**, *7* (5), 381-385.
- (35) Rojas, A.; Arteaga, O.; Kahr, B.; Cambor, M. A., *J. Am. Chem. Soc.* **2013**, *135* (32), 11975-11984.
- (36) Rojas, A.; Cambor, M. A., *Angew. Chem., Int. Ed.* **2012**, *51* (16), 3854-3856.
- (37) Ma, Y.; Oleynikov, P.; Terasaki, O., *Nat. Mater.* **2017**, *16*, 755-769.
- (38) Brand, S. K.; Schmidt, J. E.; Deem, M. W.; Daeyaert, F.; Ma, Y.; Terasaki, O.; Orazov, M.; Davis, M. E., *PNAS* **2017**, *114* (20), 5101-5106.
- (39) Bao, X.; Snurr, R. Q.; Broadbelt, L. J., *Microporous Mesoporous Mater.* **2013**, *172*, 44-50.
- (40) Bao, X.; Snurr, R. Q.; Broadbelt, L. J., *Langmuir* **2009**, *25* (18), 10730-10736.
- (41) Moghadam, P. Z.; Düren, T., *J. Phys. Chem. C* **2012**, *116*, 20874-20881.
- (42) Martin-Calvo, A.; Calero, S.; Martens, J. A.; Van Erp, T. S., *J. Phys. Chem. C* **2014**, *118* (27), 14991-14997.
- (43) Caremans, T. P.; Van Erp, T. S.; Dubbeldam, D.; Castillo, J. M.; Martens, J. A.; Calero, S., *Chem. Mater.* **2010**, *22* (16), 4591-4601.
- (44) Schneemann, A.; Bon, V.; Schwedler, I.; Senkovska, I.; Kaskel, S.; Fischer, R. A., *Chem. Soc. Rev.* **2014**, *43* (16), 6062-6096.
- (45) Llewellyn, P. L.; Bourrelly, S.; Serre, C.; Filinchuk, Y.; Ferey, G., *Angew. Chem., Int. Ed.* **2006**, *118*, 7915-7918.
- (46) Zhang, J.; Wu, H.; Emge, T. J.; Li, J., *Chem. Comm.* **2010**, *46*, 9152-9154.
- (47) Mellot-Draznieks, C.; Serre, C.; Surble, S.; Audebrand, N.; Ferey, G., *J. Am. Chem. Soc.* **2005**, *127* (46), 16273-16278.
- (48) Gee, J. A.; Sholl, D. S., *J. Phys. Chem. C* **2016**, *120*, 370-376.
- (49) Fairen-Jimenez, D.; Moggach, S. A.; Wharmby, M. T.; Wright, P. A.; Parsons, S.; Düren, T., *J. Am. Chem. Soc.* **2011**, *133* (23), 8900-8902.
- (50) Balestra, S. R. G.; Bueno-Perez, R.; Hamad, S.; Dubbeldam, D.; Ruiz-Salvador, A. R.; Calero, S., *Chem. Mater.* **2016**, *28* (22), 8296-8304.
- (51) Kitaura, R.; Seki, K.; Akiyama, G.; Kitagawa, S., *Angew. Chem., Int. Ed.* **2003**, *42* (4), 428-431.
- (52) Sartbaeva, A.; Wells, S. A.; Treacy, M. M. J.; Thorpe, M. F., *Nat. Mater.* **2006**, *5* (12), 962-965.
- (53) Haldoupis, E.; Watanabe, T.; Nair, S.; Sholl, D. S., *ChemPhysChem* **2012**, *13* (15), 3449-3452.
- (54) Jose Gutierrez-Sevillano, J.; Calero, S.; Hamad, S.; Grau-Crespo, R.; Rey, F.; Valencia, S.; Palomino, M.; Balestra, S. R. G.; Rabdel Ruiz-Salvador, A., *Chem. - Eur. J.* **2016**, *22* (29), 10036-10043.
- (55) Awati, R. V.; Ravikovitch, P. I.; Sholl, D. S., *J. Phys. Chem. C* **2013**, *117*, 13462-13473.
- (56) Patel, R. N., *Adv. Appl. Microbiol.* **2000**, *47*, 33-78.
- (57) Kresse, G.; Hafner, J., *Phys. Rev. B* **1993**, *47* (1), 558-561.
- (58) Kresse, G.; Hafner, J., *Phys. Rev. B* **1994**, *49* (20), 14251-14269.
- (59) Kresse, G.; Furthmüller, J., *Comput. Mater. Sci.* **1996**, *6* (1), 15-50.
- (60) Kresse, G.; Furthmüller, J., *Phys. Rev. B* **1996**, *54* (16), 11169-11186.
- (61) Perdew, J. P.; Ruzsinszky, A.; Csonka, G. I.; Vydrov, O. A.; Scuseria, G. E.; Constantin, L. A.; Zhou, X.; Burke, K., *Phys. Rev. Lett.* **2008**, *100* (13), 136406.
- (62) Jorgensen, W. L.; Maxwell, D. S.; Tirado-Rives, J., *J. Am. Chem. Soc.* **1996**, *118* (45), 11225-11236.

- (63) Bai, P.; Tsapatsis, M.; Siepmann, J. I., *J. Phys. Chem. C* **2013**, *117*(46), 24375-24387.
- (64) Gould, T.; Bucko, T., *J. Chem. Theory Comput.* **2016**, *12*(8), 3603-3613.
- (65) Hill, J. R.; Sauer, J., *J. Phys. Chem.* **1994**, *98*(4), 1238-1244.
- (66) Dubbeldam, D.; Calero, S.; Ellis, D. E.; Snurr, R. Q., *Mol. Simul.* **2016**, *42*(2), 81-101.
- (67) Frenkel, D.; Smit, B., *Understanding Molecular Simulation. From Algorithms to Applications*. Second Edition ed.; Academic Press, Inc.: Orlando, FL, USA, 2002.
- (68) Shi, W.; Maginn, E. J., *J. Chem. Theory Comput.* **2007**, *3*(4), 1451-1463.
- (69) Dubbeldam, D.; Torres-Knoop, A.; Walton, K. S., *Mol. Simul.* **2013**, *39*(14-15), 1253-1292.
- (70) Balestra, S. R. G.; Hamad, S.; Ruiz-Salvador, A. R.; Domínguez-García, V.; Merklings, P. J.; Dubbeldam, D.; Calero, S., *Chem. Mater.* **2015**, *27*(16), 5657-5667.
- (71) Faller, R.; de Pablo, J. J., *J. Chem. Phys.* **2002**, *116*(1), 55-59.
- (72) Ghoufi, A.; Subercaze, A.; Ma, Q.; Yot, P. G.; Ke, Y.; Puente-Orench, I.; Devic, T.; Guillerm, V.; Zhong, C.; Serre, C.; Ferey, G.; Maurin, G., *J. Phys. Chem. C* **2012**, *116*(24), 13289-13295.
- (73) Martyna, G. J.; Klein, M. L., *J. Chem. Phys.* **1992**, *97*(4), 2635-2643.
- (74) Tuckerman, M. E.; Alejandre, J.; Lopez-Rendon, R.; Jochim, a. L.; Martyna, G. J., *J. Phys. A: Math. Theor.* **2006**, *39*(19), 5629-5651.
- (75) Dubbeldam, D.; Beerdsen, E.; Vlugt, T. J.; Smit, B., *J. Chem. Phys.* **2005**, *122*, 17.
- (76) Bueno-Perez, R.; Gutierrez-Sevillano, J. J.; Dubbeldam, D.; Merklings, P. J.; Calero, S., *ChemPhysChem* **2015**, *16*(13), 2735-2738.
- (77) Bueno-Perez, R.; Merklings, P. J.; Gomez-Alvarez, P.; Calero, S., *Chem. - Eur. J.* **2017**, *23*(4), 874-885.
- (78) Dubbeldam, D.; Krishna, R.; Calero, S.; Yazaydin, A. O., *Angew. Chem., Int. Ed.* **2012**, *51*(47), 11867-11871.
- (79) Tarini, M.; Cignoni, P.; Montani, C., *IEEE Trans. Vis. Comput. Graphics* **2006**, *12*(5), 1237-1244.

Conclusions

7

This thesis relied on molecular simulations and force fields available in the literature to study the loading capacity, and structural and chiral selectivity of several nanoporous materials through adsorption and diffusion processes. The use of computational techniques allowed for the unraveling of the molecular mechanisms underlying this molecular sieving by providing a detailed microscopical view of the system which was analyzed to understand the host-host, host-guest, and guest-guest interactions and explain the microassembly of molecules.

The conclusions concerning the separation of chiral isomers in metal-organic frameworks are:

1. The adsorption of enantiomeric mixtures at different molar fractions in the nonchiral MOFs, MIL-47 and MIL-53, shows heteroselectivity for ibuprofen mixtures. No separation was observed in the case of lysine due to the lesser degree of confinement in the channels of these porous materials (Chapter 2).

2. The adsorption of enantiomeric mixtures at different molar fractions in the homochiral MOF HMOF-1 (Cd-BINOL)

shows a heteroselective behavior for mixtures of *L/D*-lysine and *R/S*-ibuprofen, being able to separate the racemic mixture of the latter (Chapter 2).

3. The relevance of guest-guest interactions is observed as heteroselectivity is attributed to hydrogen bonding of *R* and *S* enantiomers at high concentration of *S*-ibuprofen in MIL-47, and self-association of the minor component in the mixture seems responsible for the heteroselectivity in MIL-53. The same pattern for guest-guest interactions is observed in HMOF-1 for ibuprofen and lysine (Chapter 2).

4. The implications of confinement for selectivity are noticeable in the adsorption of racemic mixtures of 2-pentanol (2P), and 3-methyl-2-butanol (3M2B) in HMOF-1, for which enantiomeric excess is only achieved from the adsorption within the narrow side channels, but not within the larger main channels (Chapter 4).

Regarding the separation of structural isomers in MOFs, the main conclusions are:

5. The results of adsorption and diffusion of isomers of pentanol and hexane in the two-

dimensional channel system of ZIF-77 point to the branching of molecules as the driving force in the separation of structural isomers. According to this, linear molecules are adsorbed preferentially over monobranched molecules, and these over dibranched molecules on different carbon atoms. Molecules dibranched on the same carbon atom are the last ones in this preferential order since they cannot enter the pores of ZIF-77. Along with this preferential adsorption, the low polarity and the size of channels in ZIF-77 make this structure suitable for the separation of structural isomers of intermediate-sized molecules of different chemical nature if the molecule is at least partially hydrophobic (Chapter 3).

6. The three-dimensional channel system of Cd-BINOL (HMOF-1) is composed of a helicoidal and wide main channel with a polar surface and zigzag narrow side channels with low polarity. Despite this, the results of adsorption of the structural isomers of amyl alcohols in Cd-BINOL follow the same pattern described for ZIF-77. The order in the preferential adsorption is led by the least branched isomers. In addition, due to the increasing relevance of guest-guest interactions in this specific system, adsorption is most favored the least shielded the hydroxyl group (Chapter 4).

7. At low-coverage regime, the analysis of adsorption enthalpies and the formation of hydrogen bonds of adsorbates with the oxygen atoms exposed in the main channel of Cd-BINOL reveals that the contribution of hydrogen bonding to the adsorption of the first molecule is 3% at best, which means that this stabilization is mainly governed by confinement and dispersion forces. Afterwards, hydrogen-bond formation between adsorbates leads to rapid pore filling (Chapter 4).

8. The analysis of hydrogen-bond formation at saturation in Cd-BINOL shows that, for pure compounds, each molecule forms around 1.25 hydrogen bonds on average. In mixtures, self- and cross-association increase, especially the latter. As a consequence, the total number of molecules adsorbed in the structure increases by 4% with respect to their pure counterpart systems due to shape complementarity of major and minor components generating, through hydrogen bonding, a more ordered molecular arrangement (Chapter 4).

9. The ratio of Henry coefficients, which is equal to adsorption selectivity at low coverage, is useful to estimate tendencies in adsorption selectivity of pentanol isomers in Cd-BINOL at saturation, though not accurately. The IAST method, which calculates the adsorption isotherms of mixtures from those of pure compounds, reproduces the adsorption of mixtures qualitatively. IAST calculations account implicitly for self-association, while cross-association is not considered, and therefore, the agreement between IAST-predicted adsorption isotherms of mixtures and those obtained by molecular simulation is not quantitatively accurate (Chapter 4).

10. Cd-BINOL is especially selective towards 1-pentanol which, in mixtures with the bulkier isomers of amyl alcohols, excludes the minor component from the structure. This, along with its high storage capacity, makes this structure very suitable to perform adsorption-based separations of mixtures of alcohol isomers (Chapter 4).

Related to the evaluation of available force fields to model the flexibility in zeolites, the most relevant concluding remarks are:

11. Three popular silicate force fields (Nicholas, Hill, and Demontis) with varying

levels of sophistication were tested using IR spectra as the test field. The qualitative inspection of spectra revealed that Nicholas force field reproduced the absorption bands of new structural features in the framework and its positions. Hill generates complex spectra with many absorption bands, accounting also for the appearance of new structural features, and blue-shifted positions. Demontis, considering its extreme simplicity, is in good qualitative agreement but some absorption bands are missing (Chapter 5).

12. A similarity index (S) was developed to compare quantitatively experimental and calculated IR spectra. The quantitative comparison of calculated and experimental IR spectra shows that Nicholas performs the best given its highest average similarity with experiment. After Nicholas, Demontis force field performs better than Hill force field. However, regarding the sensitivity of force fields to the particular features of each framework Nicholas overemphasizes these differences, while Hill is the most sensitive to framework variations, and Demontis is the least (Chapter 5).

13. The bands of calculated IR spectra were compared to experiment, but since the reproduction of IR spectra was not the goal of the parametrization for any of the force fields studied, the quantitative comparison scheme is unable to identify frameworks based on their experimental IR spectra (Chapter 5).

Finally, the main conclusions obtained from the study on the separation of structural and chiral isomers in zeolites are:

14. The all-silica and germanosilicate frameworks of STW-type zeolite, when modeled as rigid, show a preferential adsorption of 2P, the most linear molecule,

followed by 2MB, and 3M2B. In STW-Si, 2MB and 3M2B cannot enter the framework, while in STW-SiGe this preferential adsorption is due to molecular arrangement (Chapter 6).

15. The rigidly-modeled right-handed STW-Si is selective towards R -2P, while the right-handed STW-SiGe is selective towards S -3M2B. This enantioselectivity is mainly driven by the geometry of the chiral channel, due to the steric confinement of the molecules in the structure, and the orientation within the channel. The contribution of guest-guest interactions to the chiral selectivity is negligible for this system (Chapter 6).

16. The presence of germanium atoms and the consequent asymmetric distances of Si-O and Ge-O bonds generate structural distortions and, therefore, a wide distribution of possible configurations for STW-SiGe (Chapter 6). The study of the dynamic behavior of the frameworks upon adsorption and the analysis of the distribution of window apertures, revealed that the larger lattice vibration in STW-SiGe framework depends on the nature and loading of the adsorbate, while the intrinsic flexibility of STW-Si can be considered a thermal vibration around the equilibrium positions (Chapter 6).

17. Taking flexibility into account, the chiral selectivity of STW-SiGe is lost because the structural changes distort the chiral recognition site for 3M2B. On the contrary, the static lattice vibrations of STW-Si keep the adsorption sites that select R -2P over S -2P, and, therefore, enantioselectivity is preserved. Although structural selectivity of STW-SiGe is preserved the adsorption isotherms for rigid and flexible models show differences due to structural changes of the framework (Chapter 6).

18. The introduction of hybrid MCMD simulations increases fourfold the computational cost of performing adsorption processes. However, it provides information on the dynamic behavior of the frameworks that cannot be obtained by analyzing the dynamics of the empty framework (Chapter 6).

In the light of the conclusions enumerated previously, when a structural or chiral separation has to be performed with a

specific material, there are three questions that can be asked prior to the study. First of all, whether the topology of the structure, and the size of its pores seem suitable to sieve the mixture. Secondly, which the nature of the compounds under study is, how likely they are to interact strongly with each other, and which would the effect of this interaction on the selectivity be. And last, but not least, how accurately models and force fields reproduce the main features of the system.

Resumen (Summary in Spanish)

El potencial que los materiales nanoporosos tienen como filtros moleculares es ampliamente conocido y de gran relevancia científica. Por otra parte, las técnicas de simulación molecular son muy útiles para predecir la capacidad selectiva de dichos materiales, tanto reales como hipotéticos, y proporcionan una visión microscópica del proceso de separación. Esto permite entender los mecanismos moleculares que rigen dichos procesos y relacionarlos con las características particulares de cada material.

Este trabajo de tesis se centra en la separación de isómeros estructurales y quirales a través de procesos de adsorción en materiales nanoporosos. Los isómeros estructurales comparten la misma fórmula molecular pero presentan conectividad distinta. En este trabajo se aborda la separación de los alcoholes amílicos debido a su importancia en la industria química y farmacéutica. Estos compuestos presentan propiedades fisicoquímicas muy parecidas que complican y encarecen el proceso de separación. En el caso de los isómeros quirales, que presentan la misma conectividad, estas propiedades son idénticas salvo cuando interactúan con otra entidad quiral. El hecho de que dos enantiómeros de un compuesto quiral puedan reaccionar de forma diferente con otro compuesto quiral es de enorme relevancia en las industrias farmacéutica, agroquímica o alimentaria. Sin embargo, la síntesis de un enantiómero puro es costosa instrumental y económicamente, por lo que suelen sintetizarse como mezclas racémicas o escalémicas, es decir, como mezclas de ambos enantiómeros.

En este trabajo de tesis se han utilizado técnicas de simulación molecular para estudiar la adsorción y difusión de mezclas de isómeros estructurales y quirales en MOFs (Estructuras Metal-Orgánicas) y zeolitas. A partir de los resultados obtenidos para dichos procesos se ha analizado la capacidad selectiva de estos materiales y el comportamiento específico de cada uno de ellos. Esto permite entender los mecanismos que rigen cada proceso y cómo se organizan las moléculas dentro de la estructura como consecuencia de las interacciones entre ellas y con la estructura. Además, dado que muchos materiales muestran algún tipo de flexibilidad estructural, resulta interesante entender la relevancia que puede tener la movilidad de los átomos de la estructura en la interacción con las moléculas y, como consecuencia, en la selectividad.

Separación de isómeros quirales en MOFs (Capítulos 2 y 4)

En el Capítulo 2 se estudia la separación enantioselectiva de los compuestos bioactivos ibuprofeno y lisina en el MOF homoquiral HMOF-1, también conocido como Cd-BINOL, y en MOFs no quirales (MIL-47 y MIL-53). Utilizando la simulación molecular se obtuvieron los valores de adsorción del par de enantiómeros de ibuprofeno, y de lisina, a partir de mezclas con diferente fracción molar. Se analizó también la disposición de las moléculas debida a la formación de puentes de hidrógeno, para relacionarla con la enantioselectividad de cada MOF. El grado de confinamiento de cada enantiómero en la estructura se considera

un punto clave para que una estructura muestre enantioselectividad.

En el Capítulo 4 se usaron, como sondas quirales para examinar la adsorción enantioselectiva de HMOF-1, tres alcoholes quirales del grupo de los alcoholes amílicos, es decir, isómeros estructurales del pentanol, en concreto 2-pentanol, 2-metilbutanol y 3-metil-2-butanol. En este caso, el estudio se limitó a la descripción del exceso enantiomérico de cada compuesto. Los resultados se analizaron y explicaron en relación con el sistema de canales de la estructura, las características químicas del material y la forma en que las moléculas se confinan en los poros.

Separación de isómeros estructurales en MOFs (Capítulos 3 y 4)

En el Capítulo 3 se estudia la adsorción selectiva de los alcoholes amílicos, isómeros estructurales del pentanol, en ZIF-77 con la intención de relacionar las características estructurales de cada isómero con la topología de esta estructura, formada por dos canales interconectados de diferente tamaño. Para ello se obtuvieron, mediante simulación molecular, las isotermas de adsorción de cada compuesto y de las mezclas de varios isómeros. También se ha estudiado el comportamiento difusivo de cada uno de los compuestos en la estructura y el de los alcanos análogos. Esto hizo posible relacionar el tamaño de las moléculas con el tamaño del poro, y de las características químicas de la superficie de la estructura con la presencia de grupos hidroxilo, para entender el proceso de separación. Finalmente, se establecieron diferentes grupos de moléculas en base a sus características estructurales, lo que permite explicar la selectividad estructural de ZIF-77.

Una vez analizada la capacidad de separación de isómeros estructurales en ZIF-77, se abordó el mismo estudio en una estructura más compleja: Cd-BINOL, conocida también como HMOF-1. Este MOF se caracteriza por tener un sistema de canales tridimensional, formado por un canal helicoidal y un canal en zigzag más estrecho que conecta los anteriores. Además, la composición química de su estructura es distinta a la del ZIF-77. Se llevó a cabo un trabajo computacional similar al realizado en ZIF-77, acompañado de un análisis exhaustivo sobre el efecto que tienen sobre la selectividad las interacciones entre moléculas, y de éstas con la estructura y el patrón de formación de enlaces de hidrógeno. Esto permitió también evaluar y explicar la eficacia de IAST (Ideal Adsorption Solution Theory) y del cociente de los coeficientes de Henry como métodos de predicción alternativos.

Evaluación de diferentes campos de fuerza para modelizar flexibilidad en zeolitas (Capítulo 5)

La limitada flexibilidad inherente a las zeolitas se ha estudiado ampliamente y ha dado lugar al desarrollo de campos de fuerza transferibles para este tipo de estructuras. En este capítulo se evalúan tres campos de fuerza conocidos (desarrollados por J. B. Nicholas, P. Demontis *et al.*, y J. R. Hill y J. Sauer) basándonos en su capacidad de reproducir el espectro IR experimental de zeolitas pura sílice. Junto a estas zeolitas se seleccionaron algunas estructuras pura sílice hipotéticas para obtener un grupo representativo de diferentes topologías (SOD, RHO, LTA y FAU; y FER, TON, MOR y MFI) y poder examinar también la capacidad de cada campo de fuerza para reflejar, en el espectro IR obtenido por simulación, las particularidades estructurales de cada zeolita. Para ello se

comparan espectros IR experimentales con aquellos obtenidos con cada uno de los campos de fuerza mencionados, y estos últimos entre sí. Con la idea de ser rigurosos en dicha comparación se desarrolló un índice de similitud, que permitió evaluar de forma cuantitativa la precisión de los campos de fuerza.

Separación de isómeros estructurales y quirales en zeolitas (Capítulo 6)

En este capítulo se analiza la influencia de la flexibilidad de zeolitas STW en la separación de isómeros quirales y estructurales. Los compuestos 2-pentanol, 2-metilbutanol y 3-metil-2-butanol se escogieron como sondas quirales dado que, además de compuestos quirales, son isómeros estructurales. Las estructuras pura sílice y el germanosilicato de la zeolita STW (STW-Si y STW-SiGe, respectivamente) se seleccionaron como adsorbentes por su canal helicoidal característico. Se abordaron varias cuestiones. En primer lugar, la selectividad quiral y estructural de ambas estructuras modelizadas como rígidas. En segundo lugar, un estudio análogo modelizando los adsorbentes como flexibles permitiendo, de esta forma, el movimiento de los átomos y la variación de forma de la estructura durante el proceso de adsorción. Finalmente, se explican de forma detallada algunos conceptos tratados previamente, como el grado de confinamiento y la adsorción preferente y su conexión con la selectividad quiral y estructural.

Conclusiones

En relación con la separación de isómeros quirales en MOFs, el grado de confinamiento de la molécula dentro de la estructura ha demostrado ser un factor clave. De esta forma, los MOFs no quirales muestran un comportamiento

heteroselectivo para las mezclas enantioméricas de ibuprofeno, pero no las de lisina, debido al tamaño más pequeño de esta molécula respecto al canal donde se adsorbe. De forma similar, la estructura homoquiral HMOF-1 (Cd-BINOL) muestra un comportamiento heteroselectivo para las mezclas de lisina y las de ibuprofeno, pero sólo es capaz de separar la mezcla racémica del último. Finalmente, en las mezclas racémicas de 2-pentanol y 3-metil-2-butanol el exceso enantiomérico aumenta si se contabiliza sólo en el canal más estrecho.

Por otra parte, el comportamiento heteroselectivo observado en MIL-47 y MIL-53 está relacionado con la formación de puentes de hidrógeno entre enantiómeros *R* y *S*, y la asociación entre los componentes minoritarios de la mezcla, respectivamente. Esto pone de manifiesto que, además del confinamiento, las interacciones intermoleculares pueden influir en la enantioselectividad. De hecho, estos patrones de asociación también se observan en las mezclas enantioméricas de ibuprofeno y las de lisina en HMOF-1.

El estudio de la separación estructural de los alcoholes amílicos en ZIF-77 y Cd-BINOL (HMOF-1) apunta al grado de ramificación de cada molécula como la característica que determina la preferencia de adsorción de las mismas. En términos generales, la molécula con una estructura más lineal se adsorbe preferentemente. Le siguen las que tienen una y dos ramificaciones, respectivamente. En último lugar se adsorben las moléculas con dos ramificaciones en el mismo átomo de carbono.

En el caso del ZIF-77, el diámetro de sus canales bidimensionales y su baja polaridad permiten que esta estructura pueda separar isómeros estructurales de tamaño intermedio y diferente composición

química. En el caso del Cd-BINOL, el mayor diámetro de sus canales y su diferente polaridad añaden complejidad al análisis de la selectividad estructural. De esta forma, se adsorben preferentemente las moléculas con menos ramificaciones y cuyo grupo hidroxilo está menos apantallado por el resto de la molécula. Cd-BINOL adsorbe preferentemente 1-pentanol que, en mezclas con isómeros muy ramificados, excluye al componente minoritario de la estructura. Además, esta estructura es idónea para la separación de estos alcoholes por su alta capacidad de almacenamiento.

La formación de enlaces de hidrógeno entre los alcoholes es responsable del llenado de la estructura, una vez que las moléculas empiezan a adsorberse debido a fuerzas de dispersión, y de la organización molecular dentro del canal cuando se llega a la saturación. Debido a esto, el cociente de los coeficientes de Henry sólo permite estimar la tendencia de la adsorción selectiva. Igualmente, la teoría IAST proporciona una predicción cualitativa de las isotermas de adsorción de las diferentes mezclas y, por tanto, con baja precisión. Esto pone de manifiesto la importancia de las interacciones intermoleculares en la selectividad estructural.

Como resultado de la evaluación de la capacidad de los tres campos de fuerzas, Nicholas, Demontis y Hill, para reproducir y predecir flexibilidad estructural en zeolitas, se observó que el espectro IR calculado con el campo de fuerzas desarrollado por Nicholas reproduce el espectro experimental de forma cualitativa y cuantitativa, comparándolos mediante el índice de similitud (S). En términos cuantitativos, en esta comparación el campo de fuerzas de Nicholas es seguido por los de Demontis y Hill, en este orden. Sin embargo, si se tiene en cuenta la capacidad

de reproducir las características estructurales específicas de cada zeolita, el campo de fuerzas de Nicholas sobrestima estas diferencias, mientras que con el de Hill se obtiene un espectro IR que refleja estas características. El espectro obtenido utilizando el campo de fuerzas de Demontis no refleja bien las particularidades estructurales de cada zeolita. Debido a esto, no es posible identificar una zeolita a partir de la comparación de su espectro IR experimental con uno obtenido generado por los campos de fuerzas estudiados. Esto evidencia, además, que la capacidad de un campo de fuerzas para reproducir una propiedad depende también de aquella propiedad en base a la cual está parametrizado.

En cuanto al estudio de la separación de isómeros estructurales y quirales en zeolitas, éste se llevó a cabo teniendo en cuenta el efecto de la flexibilidad en la selectividad. Se observó que la presencia de átomos de germanio en la estructura STW-SiGe le confiere una mayor flexibilidad, conduciendo a distorsiones estructurales que dependen de la cantidad y del tipo de molécula adsorbida. En relación con la selectividad estructural, esta amplitud en la vibración de la estructura no conlleva diferencias significativas en la selectividad, manteniéndose la preferencia de STW-SiGe por el 2-pentanol, seguido de 2-metilbutanol, y 3-metil-2-butanol. En cuanto a la selectividad quiral, las estructuras con canal dextrógiro STW-Si y STW-SiGe, adsorben preferentemente *R*-2-pentanol y *S*-3-metil-2-butanol, respectivamente, frente a sus enantiómeros. Sin embargo, cuando estas estructuras se modelizan como flexibles, la reducida flexibilidad de STW-Si hace que se conserve el sitio de reconocimiento quiral, por lo que mantiene su enantioselectividad, mientras que la mayor vibración de STW-SiGe hace

que la estructura del sitio de reconocimiento se distorsione levemente provocando la pérdida de la enantioselectividad. Esto indica que, dada la importancia del confinamiento para la enantioselectividad, la posible flexibilidad de la estructura y cómo puede afectar ésta a sus sitios de adsorción, es un factor importante a tener en cuenta para decidir qué tipo de modelo es el más apropiado para estudiar la selectividad de una estructura mediante simulación molecular.

Finalmente, y teniendo en cuenta las conclusiones expuestas previamente, si se quiere estudiar la separación estructural o

quiral en una estructura específica, hay una serie de cuestiones que convendría preguntarse previamente. En primer lugar, si la topología de la estructura y el tamaño de sus poros son los adecuados para la mezcla que se quiere separar. En segundo lugar, cuál es la naturaleza de los compuestos y cómo de fuertes son las interacciones que pueden establecer entre ellos, y cuál podría ser el efecto de estas interacciones en la selectividad. Por último, aunque no por ello menos importante, habría que preguntarse con qué precisión son capaces de reproducir las principales características del sistema los modelos y los campos de fuerza.

Appendix 1

Simulation details. Grand canonical Monte Carlo simulations were performed for a minimum of 10^6 steps. The following moves were probed: translation, rotation, insertion, deletion, reinsertion, and identity change. Lennard-Jones parameters and charges are given in Table A1 (MIL-47), A2 (MIL-53), A3 (HMOF-1), A4 and A5 (ibuprofen and lysine), and the corresponding atom identification are given in Figures A1-A3. Lorentz-Berthelot combining rules are used to compute interactions between unlike species. Cutoff for van der Waals interactions are 12 \AA (10 \AA in HMOF-1) and Coulombic interactions were handled with Ewald summations. Simulation cells are $4 \times 2 \times 2$ cell in MIL-47, $2 \times 2 \times 4$ in MIL-53, and $1 \times 1 \times 1$ in HMOF-1.

Table A1. Lennard-Jones parameters and charges defined for MIL-47.

MIL-47			
Atom	$\epsilon \text{ k}_B^{-1} / \text{K}$	$\sigma / \text{\AA}$	Charge (e-)
V	8.05	2.8	1.68
Oa	48.19	3.03	-0.6
Ob	48.19	3.03	-0.52
Ca	47.86	3.47	-0.15
Cb	47.86	3.47	0.0
Cc	47.86	3.47	0.56
H	7.65	2.85	0.12

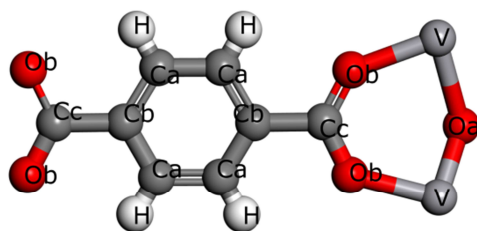


Figure A1. Atom labels in MIL-47 structure defined in the force field.

Table A2. Lennard-Jones parameters and charges defined for MIL-53.

MIL-53			
Atom	$\epsilon \text{ k}_B^{-1} / \text{K}$	$\sigma / \text{\AA}$	Charge (e-)
Cr	7.54	2.69	1.96
Oa	48.19	3.03	-0.92
Ob	48.19	3.03	-0.7
Ca	47.86	3.47	-0.08
Cb	47.86	3.47	-0.04
Cc	47.86	3.47	0.65
Ha	7.65	2.85	0.13
Hb	7.65	2.85	0.34

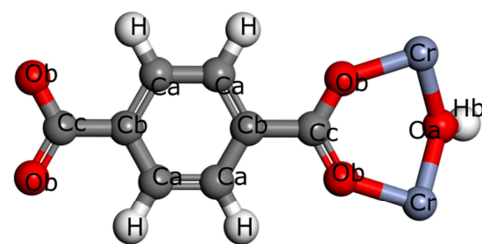


Figure A2. Atom labels in MIL-53 structure defined in the force field.

Table A3. Lennard-Jones parameters and average charges defined for HMOF-1.

HMOF-1			
Atom	$\epsilon \text{ k}_B^{-1} / \text{K}$	$\sigma / \text{\AA}$	Charge (e-) av.
Cd	114.74	2.848	0.94
Cl	114.233	3.947	-0.106
N_1	34.723	3.66	-0.434
N_2	34.723	3.66	0.9
O	30.194	3.5	-0.542
C_1	52.839	3.851	0.184
C_2	52.839	3.851	-0.214
C_3	52.839	3.851	0.0
H_1	22.142	2.886	0.157
H_2	22.142	2.886	0.404

Table A4. Lennard-Jones parameters for the pseudoatoms of ibuprofen.

Ibuprofen			
Atom	$\epsilon \text{ k}_B^{-1} / \text{K}$	$\sigma / \text{\AA}$	Charge (e-)
Cl_ring (C)	74.501	3.617	-0.222
C2_ring (CH)	74.501	3.617	-0.042
C_CH1 (chiral)	19.632	3.875	-0.342
C_CH2_ib	19.632	3.875	-0.471
C_CH3_ib	19.632	3.875	-0.673
C_COOH	90.609	3.617	0.755
O_COOH	114.772	2.859	-0.618
H_CH	19.129	2.449	0.24
H_OH	zero	zero	0.543

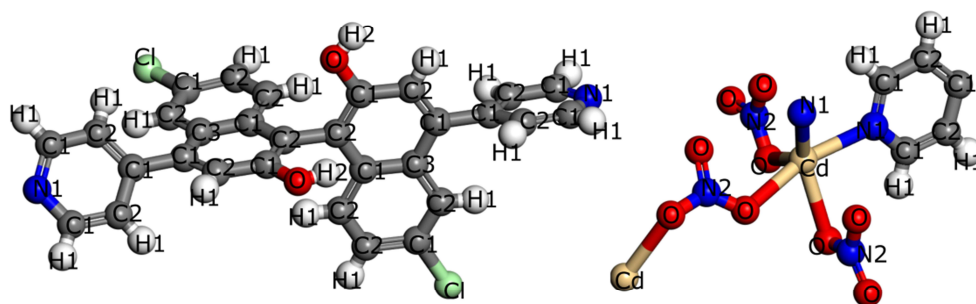
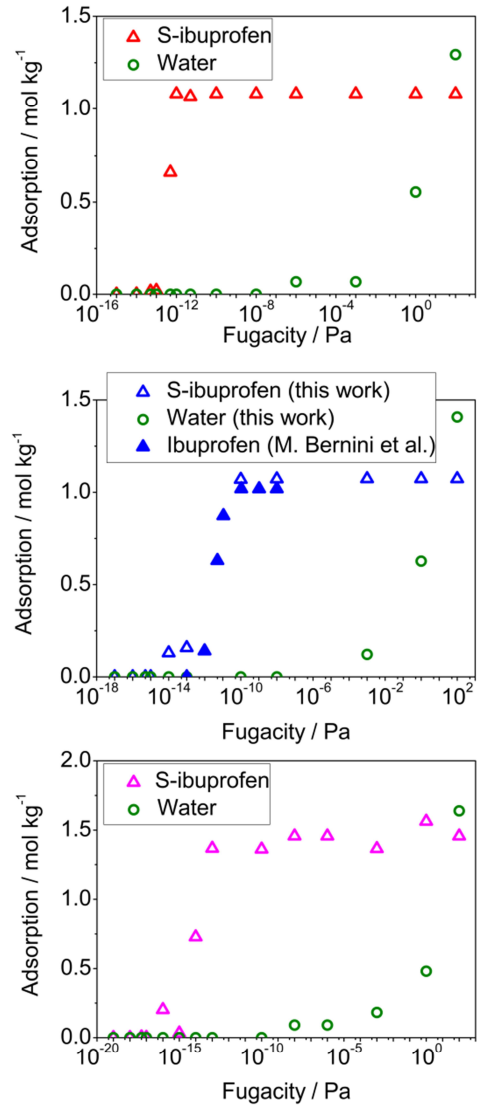
**Figure A3.** Atom labels of chiral link (left) and metal clusters (right) in HMOF-1 structure defined in the force field.

Table A5. Lennard-Jones parameters for the pseudoatoms of lysine.

Lysine			
Atom	$\epsilon \text{ k}_B^{-1} / \text{K}$	$\sigma / \text{\AA}$	Charge (e ⁻)
C_chiral	19.632	3.875	-0.1
C_CH2	19.632	3.875	-0.1
N_NH2	84.062	3.501	-0.5
C_COOH	90.609	3.617	0.41
O_COOH	114.772	2.859	-0.38
H_CH	19.129	2.449	0.1
H_OH	zero	zero	0.35
H_NH2	zero	zero	0.15

Equation A1. Expression used for the calculation of the partial fugacities of each component (f_i) in a liquid mixture.¹ In this expression p_i^{sat} is the saturated vapor pressure of pure component i , φ_i^{sat} is the fugacity coefficient of pure component i in the gas phase at the saturated vapor pressure, γ_i is the activity coefficient in the liquid mixture and calculated from the experimental vapor-liquid equilibrium data, and x_i is the mole fraction of component i in the mixture. V_i^{mol} is the molar volume of pure component i in the liquid phase, and p , R , and T are the pressure, the temperature, and the gas constant, respectively.

$$f_i = \varphi_i^{sat} p_i^{sat} \gamma_i x_i \exp \left[\frac{V_i^{mol} (p - p_i^{sat})}{RT} \right]$$

**Figure A4.** Adsorption isotherms for the mixtures ibuprofen-water in a molar fraction 0.01-0.99, at 300 K in the three structures studied: MIL-47, MIL-53, and HMOF-1 (top to bottom). The adsorption data of *S*-ibuprofen as pure compound in MIL-53 at 310 K (Bernini *et al.*)² is plotted in blue solid symbols.

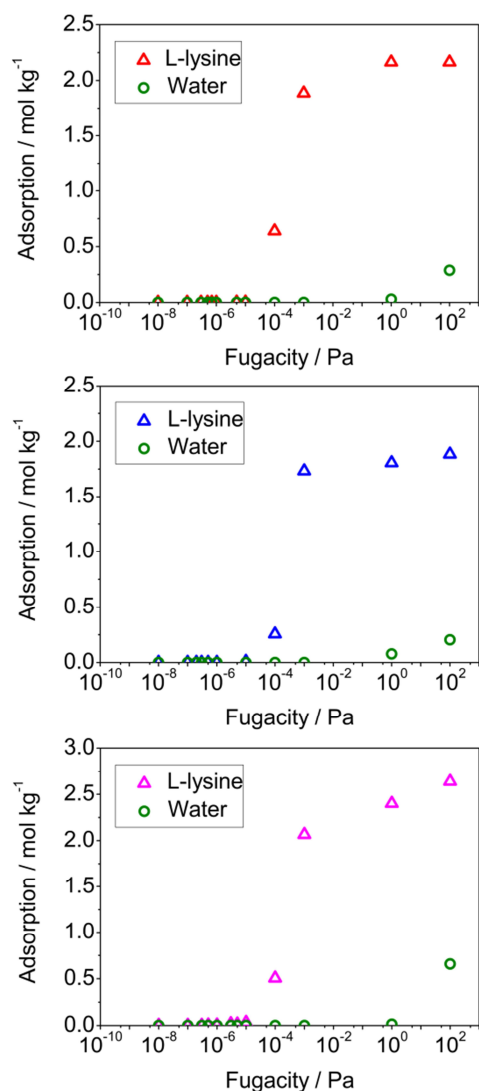


Figure A5. Adsorption isotherms for the mixtures lysine-water in a molar fraction 0.01-0.99, at 300 K in the three structures studied: MIL-47, MIL-53, and HMOF-1 (top to bottom).

Simulation details. The molecular association in the system was computed using a geometric criterion of hydrogen bonding, which was applied to every pair of molecules in a considerable number of generated configurations. Specifically, two molecules were considered hydrogen-bonded if the following conditions were fulfilled: (1) the intermolecular distance between the oxygen atoms of the carboxyl group is less than 3.6 Å, (2) the distance between the oxygen of the acceptor molecule and the hydrogen of the donor is less than 2.4 Å, and (3) the angle between the O-O direction and the molecular O-H direction of the donor, where H is the hydrogen which forms the bond, is less than 30°. Although molecules were considered flexible, a fixed O-H intramolecular distance corresponding to the equilibrium value was assumed for the calculations involved in the angular condition.

Table A6. a) Fraction of associated molecules for *R*- and *S*-ibuprofen (f_{ass}^R and f_{ass}^S , respectively), and fraction of bonds of each type (f_{RR} , f_{SS} , f_{RS}) as a function of the *S*-ibuprofen concentration in the reservoir (x_S^{res}) or adsorbed (x_S^{ads}) in the three structures. b) Fraction of associated molecules for D- and L-lysine (f_{ass}^D and f_{ass}^L , respectively), and fraction of bonds of each type (f_{DD} , f_{LL} , f_{DL}) as a function of the L-lysine concentration in the reservoir (x_L^{res}) or adsorbed (x_L^{ads}) in the three structures.

a)

HMOF-1							
x_S^{res}	0	0.2	0.4	0.5	0.6	0.8	1
x_S^{ads}	0	0.35	0.53	0.59	0.65	0.71	1
f_{ass}^R	0.21	0.46	0.26	0.34	0.65	0.34	
f_{ass}^S		0.33	0.07	0.31	0.18	0.45	0.39
f_{RR}	1.00	0.71	0.51	0.25	0.31	0.00	
f_{SS}		0.28	0.00	0.35	0.01	0.51	1.00
f_{RS}		0.00	0.49	0.40	0.69	0.49	
MIL-47							
x_S^{res}	0	0.2	0.4	0.5	0.6	0.8	1
x_S^{ads}	0	0.31	0.44	0.50	0.56	0.69	1
f_{ass}^R	0.39	0.43	0.73	0.40	0.55	0.35	
f_{ass}^S		0.64	0.66	0.40	0.55	0.49	0.73
f_{RR}	1.00	0.20	0.18	0.02	0.00	0.04	
f_{SS}		0.00	0.00	0.03	0.13	0.56	1.00
f_{RS}		0.80	0.82	0.95	0.87	0.39	
MIL-53							
x_S^{res}	0	0.2	0.4	0.5	0.6	0.8	1
x_S^{ads}	0	0.38	0.50	0.50	0.50	0.63	1
f_{ass}^R	0.48	0.79	0.16	0.43	0.48	0.61	
f_{ass}^S		0.84	0.35	0.41	0.47	0.49	0.47
f_{RR}	1.00	0.38	0.05	0.03	0.25	0.23	
f_{SS}		0.15	0.44	0.00	0.24	0.38	1.00
f_{RS}		0.47	0.52	0.97	0.50	0.40	

b)

HMOF-1							
x_L^{res}	0	0.2	0.4	0.5	0.6	0.8	1
x_L^{ads}	0	0.38	0.50	0.53	0.56	0.63	1
f_{ass}^D	0.53	0.33	0.39	0.32	0.15	0.22	
f_{ass}^L		0.33	0.22	0.21	0.22	0.35	0.35
f_{DD}	1.00	0.31	0.29	0.34	0.25	0.06	
f_{LL}		0.09	0.02	0.08	0.50	0.55	1.00
f_{DL}		0.60	0.69	0.58	0.25	0.39	
MIL-47							
x_L^{res}	0	0.2	0.4	0.5	0.6	0.8	1
x_L^{ads}	0	0.24	0.39	0.48	0.61	0.79	1
f_{ass}^D	0.28	0.33	0.25	0.26	0.17	0.24	
f_{ass}^L		0.09	0.39	0.42	0.36	0.28	0.29
f_{DD}	1.00	0.87	0.24	0.14	0.08	0.00	
f_{LL}		0.00	0.25	0.33	0.60	0.63	1.00
f_{DL}		0.13	0.51	0.53	0.32	0.37	
MIL-53							
x_L^{res}	0	0.2	0.4	0.5	0.6	0.8	1
x_L^{ads}	0	0.22	0.41	0.50	0.59	0.78	1
f_{ass}^D	0.28	0.35	0.38	0.52	0.26	0.29	
f_{ass}^L		0.38	0.16	0.35	0.25	0.34	0.36
f_{DD}	1.00	0.58	0.60	0.40	0.15	0.00	
f_{LL}		0.05	0.03	0.13	0.34	0.64	1.00
f_{DL}		0.36	0.38	0.47	0.51	0.36	

Table A7. a) Average intermolecular minimum distances d_{min} between oxygen atoms of the carboxyl group for ibuprofen as a function of the *S*-ibuprofen concentration in the reservoir (x_3^{res}) or adsorbed (x_3^{ads}) in the three structures. b) Average intermolecular minimum distances d_{min} between oxygen atoms of the carboxyl group for lysine as a function of the L-lysine concentration in the reservoir (x_L^{res}) or adsorbed (x_L^{ads}) in the three structures. The subscripts 1 and 2 denote the oxygen atom double-bonded to the carbon atom and the oxygen atom of the hydroxyl group, respectively; the type of enantiomer is indicated through a superscript.

a)

HMOF-1							
x_S^{res}	0	0.2	0.4	0.5	0.6	0.8	1
x_S^{ads}	0	0.35	0.53	0.59	0.65	0.71	1
$d_{min} / \text{\AA}$							
$O_1^R-O_2^R$	2.34	2.49	3.12	3.20	2.59	3.31	
$O_2^R-O_2^R$	2.57	3.88	3.51	3.23	4.05	5.55	
$O_1^S-O_2^S$		2.61	5.93	2.55	2.94	2.40	2.43
$O_2^S-O_2^S$		4.88	5.87	4.30	2.96	3.75	3.52
$O_1^R-O_2^S$		2.38	2.39	2.44	2.41	2.58	
$O_2^R-O_1^S$		3.32	2.37	4.74	2.53	2.51	
$O_2^R-O_2^S$		3.35	4.18	3.16	3.59	3.75	
MIL-47							
x_S^{res}	0	0.2	0.4	0.5	0.6	0.8	1
x_S^{ads}	0	0.31	0.44	0.50	0.56	0.69	1
$d_{min} / \text{\AA}$							
$O_1^R-O_2^R$	2.34	2.45	2.46	2.80	9.17	2.61	
$O_2^R-O_2^R$	2.64	4.19	4.41	3.57	9.77	4.53	
$O_1^S-O_2^S$		8.48	6.34	2.43	2.45	2.38	2.42
$O_2^S-O_2^S$		9.28	6.95	3.32	4.40	3.79	2.51
$O_1^R-O_2^S$		3.05	2.39	2.39	2.53	2.46	
$O_2^R-O_1^S$		2.39	2.44	2.33	2.41	2.78	
$O_2^R-O_2^S$		3.40	3.50	2.73	4.40	2.89	
MIL-53							
x_S^{res}	0	0.2	0.4	0.5	0.6	0.8	1
x_S^{ads}	0	0.38	0.50	0.50	0.50	0.63	1
$d_{min} / \text{\AA}$							
$O_1^R-O_2^R$	2.42	2.49	2.39	2.47	2.53	2.49	
$O_2^R-O_2^R$	3.24	3.91	3.64	4.38	3.23	4.52	
$O_1^S-O_2^S$		2.47	2.47	8.73	2.56	2.54	2.48
$O_2^S-O_2^S$		4.22	2.89	9.24	3.63	2.69	2.55
$O_1^R-O_2^S$		2.47	2.51	2.47	2.53	2.36	
$O_2^R-O_1^S$		2.45	2.75	2.47	2.52	2.49	
$O_2^R-O_2^S$		3.49	3.67	3.17	3.51	3.50	

b)

HMOF-1							
x_L^{res}	0	0.2	0.4	0.5	0.6	0.8	1
x_L^{ads}	0	0.38	0.50	0.53	0.56	0.63	1
$d_{min} / \text{\AA}$							
$O_1^D-O_2^D$	2.57	2.56	2.64	2.65	2.60	3.06	
$O_2^D-O_2^D$	2.74	2.85	3.00	3.24	3.12	3.46	
$O_1^L-O_2^L$		2.56	2.72	2.75	2.62	2.53	2.53
$O_2^L-O_2^L$		4.33	3.04	2.98	3.63	3.56	2.84
$O_1^D-O_2^L$		2.61	2.70	2.59	2.62	2.63	
$O_2^D-O_1^L$		2.57	2.58	2.56	2.99	2.87	
$O_2^D-O_2^L$		3.44	3.01	2.76	2.85	3.86	
MIL-47							
x_L^{res}	0	0.2	0.4	0.5	0.6	0.8	1
x_L^{ads}	0	0.24	0.39	0.48	0.61	0.79	1
$d_{min} / \text{\AA}$							
$O_1^D-O_2^D$	2.56	2.59	2.70	2.74	3.54	8.17	
$O_2^D-O_2^D$	3.37	3.90	2.91	3.82	4.65	7.86	
$O_1^L-O_2^L$		3.30	2.65	2.66	2.62	2.60	2.57
$O_2^L-O_2^L$		5.05	4.13	4.44	3.75	3.31	3.30
$O_1^D-O_2^L$		2.59	2.63	2.57	2.62	2.59	
$O_2^D-O_1^L$		2.77	2.94	2.62	3.12	2.89	
$O_2^D-O_2^L$		3.73	3.80	3.68	3.85	3.70	
MIL-53							
x_L^{res}	0	0.2	0.4	0.5	0.6	0.8	1
x_L^{ads}	0	0.22	0.41	0.50	0.59	0.78	1
$d_{min} / \text{\AA}$							
$O_1^D-O_2^D$	2.54	2.58	2.63	2.68	2.97	7.13	
$O_2^D-O_2^D$	3.36	4.14	2.92	2.90	3.26	7.29	
$O_1^L-O_2^L$		3.19	2.60	2.75	2.63	2.53	2.50
$O_2^L-O_2^L$		3.21	3.96	4.08	3.33	3.56	4.05
$O_1^D-O_2^L$		2.68	2.65	2.62	2.61	2.79	
$O_2^D-O_1^L$		2.69	2.85	2.57	2.59	2.58	
$O_2^D-O_2^L$		3.40	4.11	3.00	3.51	3.57	

Table A8. a) Average minimum distances d_{min} from the oxygen atoms of the carboxyl group to the host metal centers for ibuprofen as a function of the *S*-ibuprofen concentration in the reservoir (x_S^{res}) or adsorbed (x_S^{ads}) in the three structures. b) Average minimum distances d_{min} from the oxygen atoms of the carboxyl group to the host metal centers for lysine as a function of the L-lysine concentration in the reservoir (x_L^{res}) or adsorbed (x_L^{ads}) in the three structures. The subscripts 1 and 2 denote the oxygen atom double-bonded to the carbon atom and the oxygen atom of the hydroxyl group, respectively; the type of enantiomer is indicated through a superscript.

a)

HMOF-1							
x_S^{res}	0	0.2	0.4	0.5	0.6	0.8	1
x_S^{ads}	0	0.35	0.53	0.59	0.65	0.71	1
$d_{min} / \text{\AA}$							
O_1^R -Cd	5.44	5.88	6.80	5.92	7.44	6.43	
O_2^R -Cd	5.09	4.90	4.87	5.29	6.32	5.56	
O_1^S -Cd		5.37	5.72	5.57	5.62	5.91	5.11
O_2^S -Cd		6.74	5.10	5.24	5.39	5.03	5.10
MIL-47							
x_S^{res}	0	0.2	0.4	0.5	0.6	0.8	1
x_S^{ads}	0	0.31	0.44	0.50	0.56	0.69	1
$d_{min} / \text{\AA}$							
O_1^R -V	3.91	4.26	4.14	4.32	4.03	4.21	
O_2^R -V	4.14	3.78	4.48	4.29	4.53	4.86	
O_1^S -V		3.89	4.22	3.83	4.40	4.59	3.61
O_2^S -V		3.89	4.33	4.20	4.47	3.92	4.44
MIL-53							
x_S^{res}	0	0.2	0.4	0.5	0.6	0.8	1
x_S^{ads}	0	0.38	0.50	0.50	0.50	0.63	1
$d_{min} / \text{\AA}$							
O_1^R -Cr	4.42	4.39	4.50	4.64	4.66	5.04	
O_2^R -Cr	4.14	4.42	4.24	4.01	4.84	4.79	
O_1^S -Cr		4.86	4.36	4.76	4.20	4.52	4.36
O_2^S -Cr		4.60	4.76	4.59	4.40	4.21	4.19

b)

HMOF-1							
x_L^{res}	0	0.2	0.4	0.5	0.6	0.8	1
x_L^{ads}	0	0.38	0.50	0.53	0.56	0.63	1
$d_{min} / \text{\AA}$							
O_1^D -Cd	5.49	5.58	5.80	5.88	5.61	5.71	
O_2^D -Cd	4.90	5.18	4.86	4.37	5.36	5.06	
O_1^L -Cd		6.34	5.58	5.07	5.62	5.19	5.39
O_2^L -Cd		5.10	5.03	4.89	5.05	4.93	4.93
MIL-47							
x_L^{res}	0	0.2	0.4	0.5	0.6	0.8	1
x_L^{ads}	0	0.24	0.39	0.48	0.61	0.79	1
$d_{min} / \text{\AA}$							
O_1^D -V	3.71	3.90	3.81	3.85	4.09	4.31	
O_2^D -V	3.87	3.54	3.58	3.75	3.81	3.77	
O_1^L -V		3.77	4.11	3.94	3.74	3.90	3.57
O_2^L -V		3.89	4.04	3.47	3.92	3.76	3.66
MIL-53							
x_L^{res}	0	0.2	0.4	0.5	0.6	0.8	1
x_L^{ads}	0	0.22	0.41	0.50	0.59	0.78	1
$d_{min} / \text{\AA}$							
O_1^D -Cr	4.52	4.64	4.62	4.68	4.50	4.97	
O_2^D -Cr	4.12	4.19	4.44	4.30	4.31	4.53	
O_1^L -Cr		4.69	4.19	4.40	4.53	4.33	4.47
O_2^L -Cr		4.47	4.53	4.11	4.39	4.49	4.28

As seen in Table A7, O_1 - O_2 distances are consistently shorter than corresponding O_2 - O_2 distances. This proves the claim made in the main text that the double-bonded oxygen in the carboxyl group is more likely to form hydrogen bonds than the single-bonded oxygen.

Bibliography

- (1) Smith, J. M.; Ness, H. C. V.; Abbott, M. M., *Introduction to Chemical Engineering Thermodynamics*. McGraw-Hill: USA, 2004.
- (2) Bernini, M. C.; Fairen-Jimenez, D.; Pasinetti, M.; Ramirez-Pastor, A. J.; Snurr, R. Q., *J. Mater. Chem. B* **2014**, 2(7), 766-774.

Appendix 2

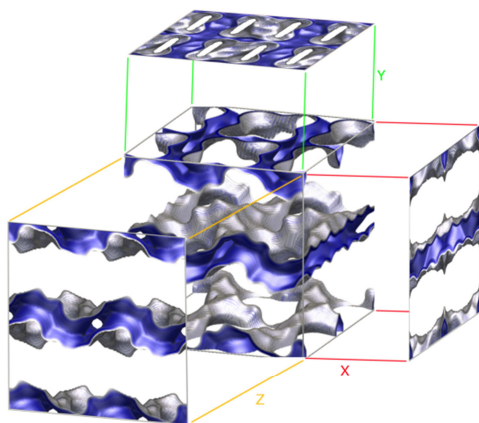


Figure A1. 3D representation of the equipotential energy surface in ZIF-77 and its projections on the three planes.

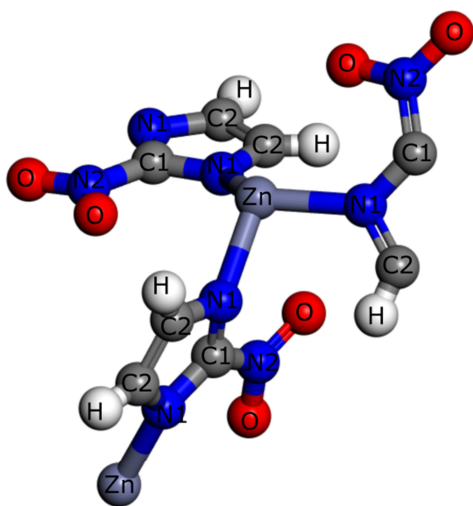


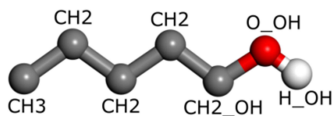
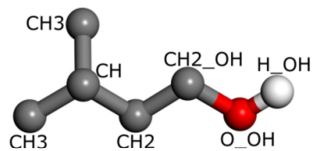
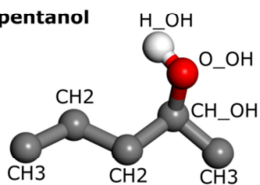
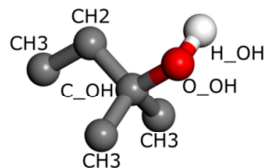
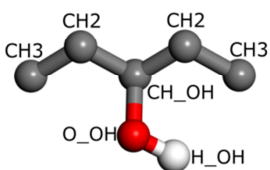
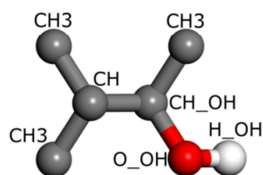
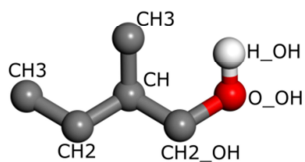
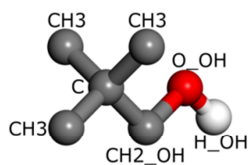
Figure A2. Asymmetric unit of ZIF-77.¹ Atoms labeled as defined in the force field.

Table A1. Lennard-Jones parameters and charges defined for ZIF-77.

ZIF-77 defined by UFF ²			
Atom	$\epsilon / k_B / K$	$\sigma / \text{Å}$	Charge (e^-) ³
Zn	62.4	2.46	-1.00
O	30.19	3.118	-0.185
C1	52.80	3.43	0.12
C2	52.80	3.43	-0.05
N1	34.72	3.26	-0.265
N2	34.72	3.26	0.23
H	22.14	2.57	0.075

Table A2. Lennard-Jones parameters and charges of pseudoatoms defined for amyl alcohols and their analogous alkanes.

Amyl Alcohols defined by TraPPE ⁴⁻⁵			
Atom	$\epsilon / k_B [K]$	$\sigma / \text{Å}$	Charge (e^-)
CH3	98.0	3.75	0
CH2	46.0	3.95	0
CH2_OH	46.0	3.95	0.265
CH	10.0	4.68	0
CH_OH	10.0	4.33	0.265
C	0.5	6.4	0
C_OH	0.5	5.8	0.265
O_OH	93.0	3.020	-0.7
H_OH	zero	zero	0.435

1-pentanol**3-methylbutanol****2-pentanol****2-methyl-2-butanol****3-pentanol****3-methyl-2-butanol****2-methylbutanol****2,2-dimethylpropanol****Figure A3.** Molecules studied in this work. Pseudoatoms labeled as defined in the force field.

Simulation details. The adsorption isotherms of the six molecules that are able to penetrate into the structure were computed with our in-house code RASPA using grand canonical Monte Carlo simulations (GCMC), in the μ VT ensemble, at 298 K and are shown in Figure A8. During each simulation, an average of 4×10^6 cycles was attempted. Configurational-biased insertions, deletions, and total and partial reinsertion, as well as random translations and rotations of the sorbate molecules, were employed to reach equilibration, each move with the same probability of attempting. The adsorption isotherms for the mixture were also calculated using GCMC simulations at 298 K, but setting equimolar mixtures in the bulk. Also, a specific move for mixtures was also performed and these energy-biased identity change moves were attempted with the same probability as other moves.

To calculate Henry coefficients Monte Carlo simulations were performed in the NVT ensemble at 298 K. Henry coefficients, enthalpies, and entropies were calculated using the Widom test particle insertion method.⁶ Density profiles were calculated applying reinsertion, translation, and rotation moves to one molecule, taking snapshots, and plotting the center of mass of each molecule in the simulation box.

Diffusion coefficients were obtained by computing the mean squared displacement (MSD) for alcohols and alkanes using molecular dynamics (MD). These simulations were performed in the NVT ensemble, at 298 K. The time step for each cycle was 0.5 fs and total simulation time was up to 1073 ns. Diffusion coefficients were extracted from the MSD over 1 ns with multiple time origins. We fitted the MSD to the equation $6 \cdot D \cdot t + b$ to calculate the diffusion coefficients. In a few cases, independent runs were performed. This yielded uncertainties of typically 25%. Given the high computational cost, this was not done in all cases. This uncertainty includes the smaller uncertainty from the fit that ranged from as low as 0.4% up to 8%. Diffusion trajectories are the trails of the molecules in the structure, showing the real accessible space inside the framework. They are generated by plotting the center of mass of the molecules present in the snapshots from MD simulations.

The dimensions of the simulation box for all the MC and MD simulations performed were $22 \times 22 \times 24 \text{ \AA}$, and consisted of two unit cells ($11 \times 22 \times 24 \text{ \AA}$) of ZIF-77. The cutoff used was 10 \AA .

Table A3. Average self-diffusion coefficients (D) and diffusion coefficients in x -, y -, and z -directions (D_x , D_y , D_z) of alcohol molecules in ZIF-77 at 298 K.

Diffusion coefficients / $10^{-10} \text{ m}^2 \text{ s}^{-1}$				
Molecule	D	D_x	D_y	D_z
1P	1.15 ± 0.25	0.012 ± 0.003	-	3.42 ± 0.75
2P	0.12 ± 0.03	-	-	0.37 ± 0.09
3P	0.17 ± 0.04	-	-	0.49 ± 0.12
3MB	0.074 ± 0.02	-	-	0.22 ± 0.06
2MB	0.20 ± 0.05	-	-	0.63 ± 0.15
3M2B	0.067 ± 0.02	-	-	0.20 ± 0.06
2M2B	-	-	-	-
22DMP	-	-	-	-

Table A4. Average self-diffusion coefficients (D) and diffusion coefficients in x -, y -, and z -directions (D_x , D_y , D_z) of alkane molecules in ZIF-77 at 298 K.

Diffusion coefficients / $10^{-10} \text{ m}^2 \text{ s}^{-1}$				
Molecule	D	D_x	D_y	D_z
nC6	0.8 ± 0.02	-	-	2.3 ± 0.6
2MP	0.13 ± 0.03	-	-	0.54 ± 0.14
3MP	0.13 ± 0.03	-	-	0.49 ± 0.13
23DMB	0.13 ± 0.03	-	-	0.58 ± 0.15
22DMB	-	-	-	-

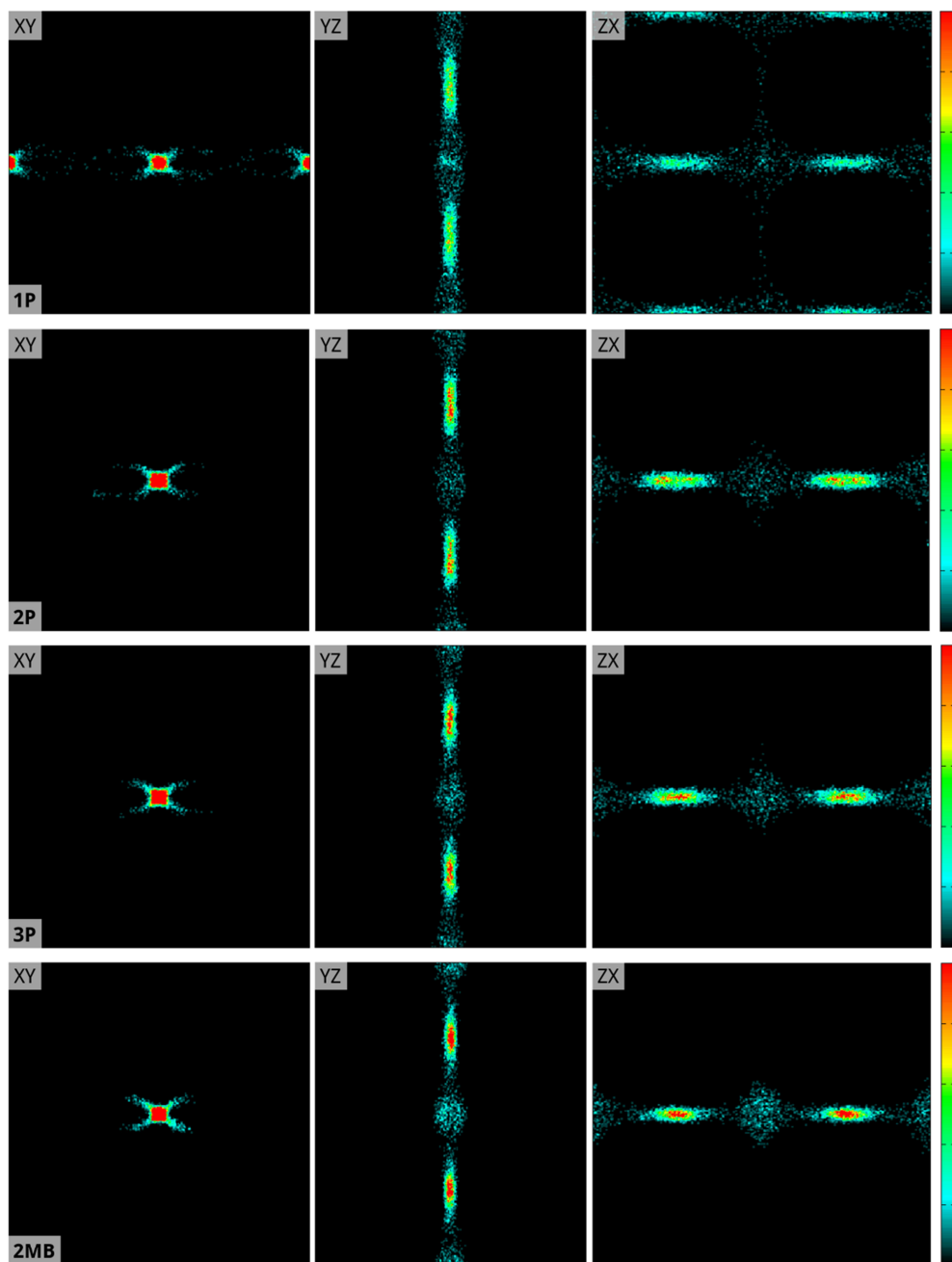


Figure A4. Molecular dynamics trajectories of adsorbates within the framework in xy -, yz -, and zx -views (left, center, and right) for the four adsorbates: 1P, 2P, 3P, and 2MB (top to bottom). The color intensity in the bar at the right indicates, from black to red, the number of molecules in each grid cell from 0 to 5.

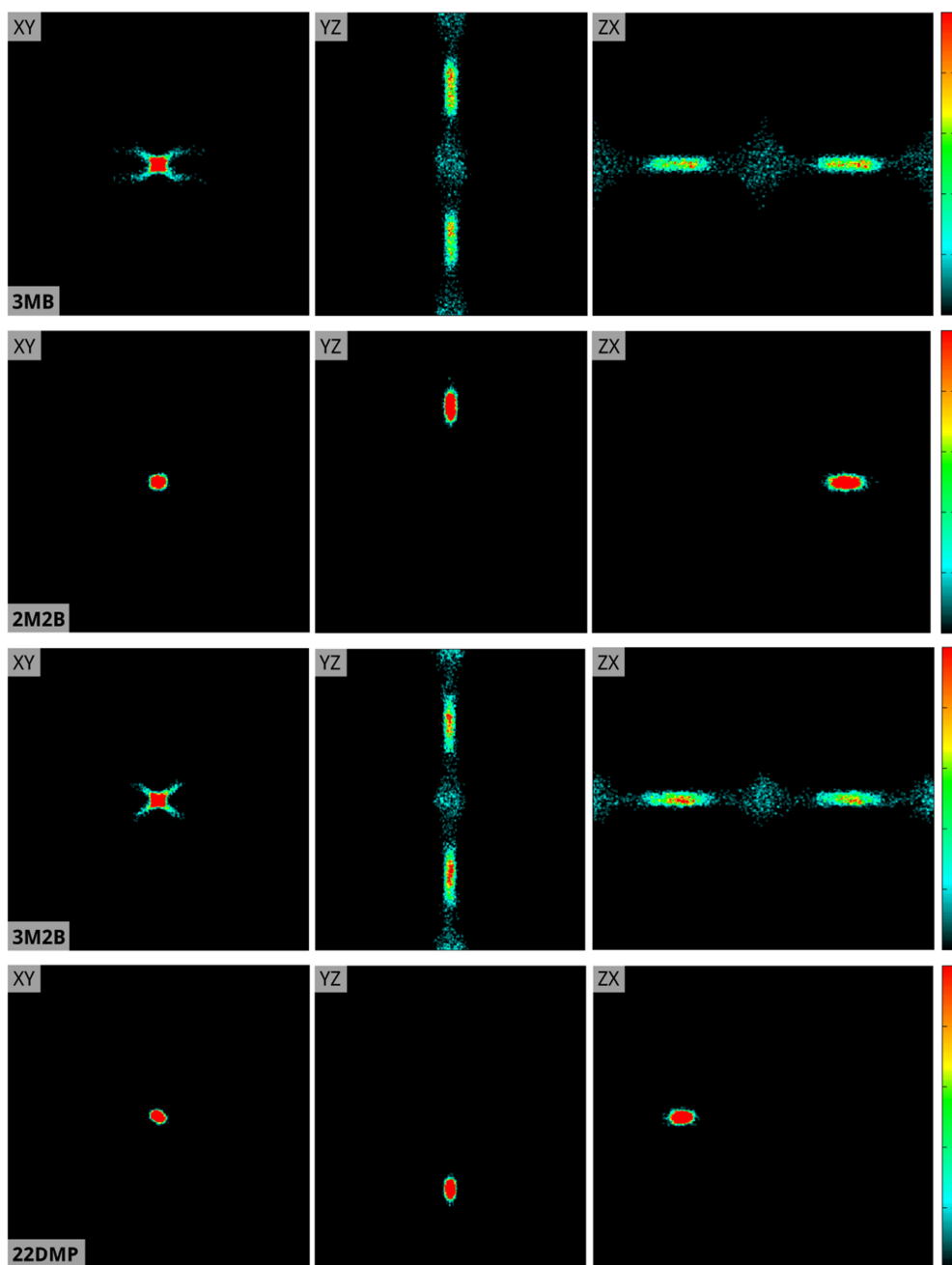


Figure A5. Molecular dynamics trajectories of adsorbates within the framework in xy -, yz -, and zx -views (left, center, and right) for the four adsorbates: 3MB, 2M2B, 3M2B, and 22DMP (top to bottom). The color intensity in the bar at the right indicates, from black to red, the number of molecules in each grid cell from 0 to 5.

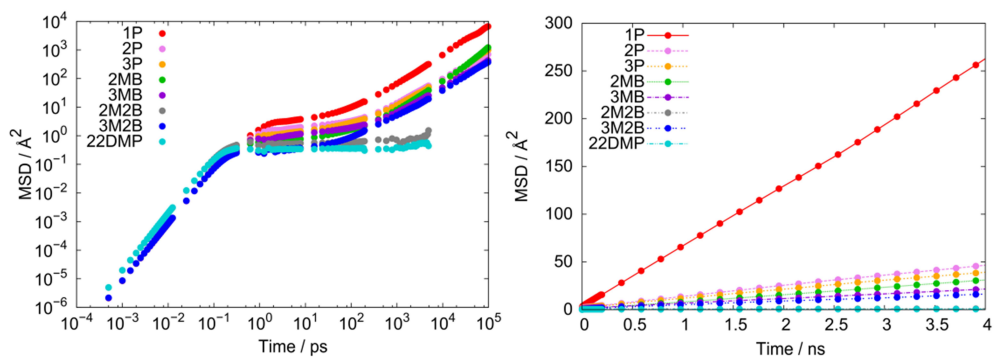


Figure A6. Graphic showing mean squared displacement (Å) against time (ps or ns) for the amylic alcohols in ZIF-77: logarithmic-scaled (left) and linearly scaled (right).

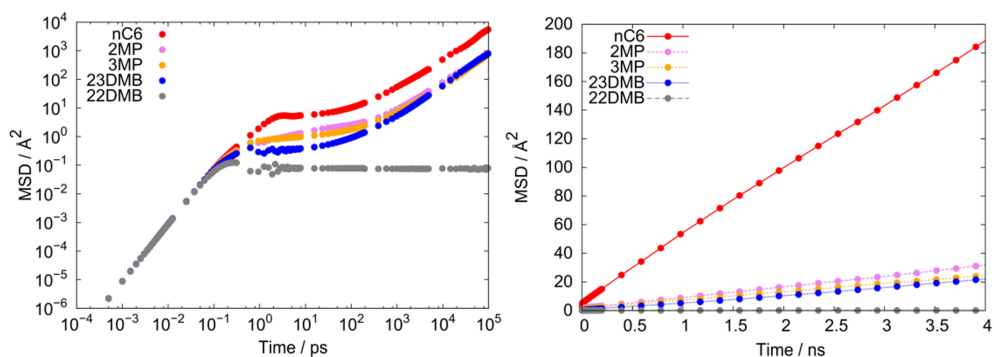


Figure A7. Graphic showing mean squared displacement (Å) against time (ps or ns) for the alkane molecules in ZIF-77: logarithmic-scaled (left) and linearly scaled (right).

Table A5. Isothermic heats of adsorption (Q_{st}) and Henry coefficients (K_H) for the amylic alcohols studied at 298K in ZIF-77.

Molecule	$K_H / \text{mol kg}^{-1}\text{Pa}^{-1}$	$Q_{st} / \text{kJ mol}^{-1}$
1P	4.853×10^{-1}	-71.795
2P	2.124×10^{-1}	-70.126
3P	2.280×10^{-1}	-71.212
2MB	1.941×10^{-2}	-68.740
3MB	3.002×10^{-2}	-67.700
2M2B	8.885×10^{-4}	-60.153
3M2B	6.582×10^{-3}	-65.537
22DMP	4.798×10^{-5}	-57.008

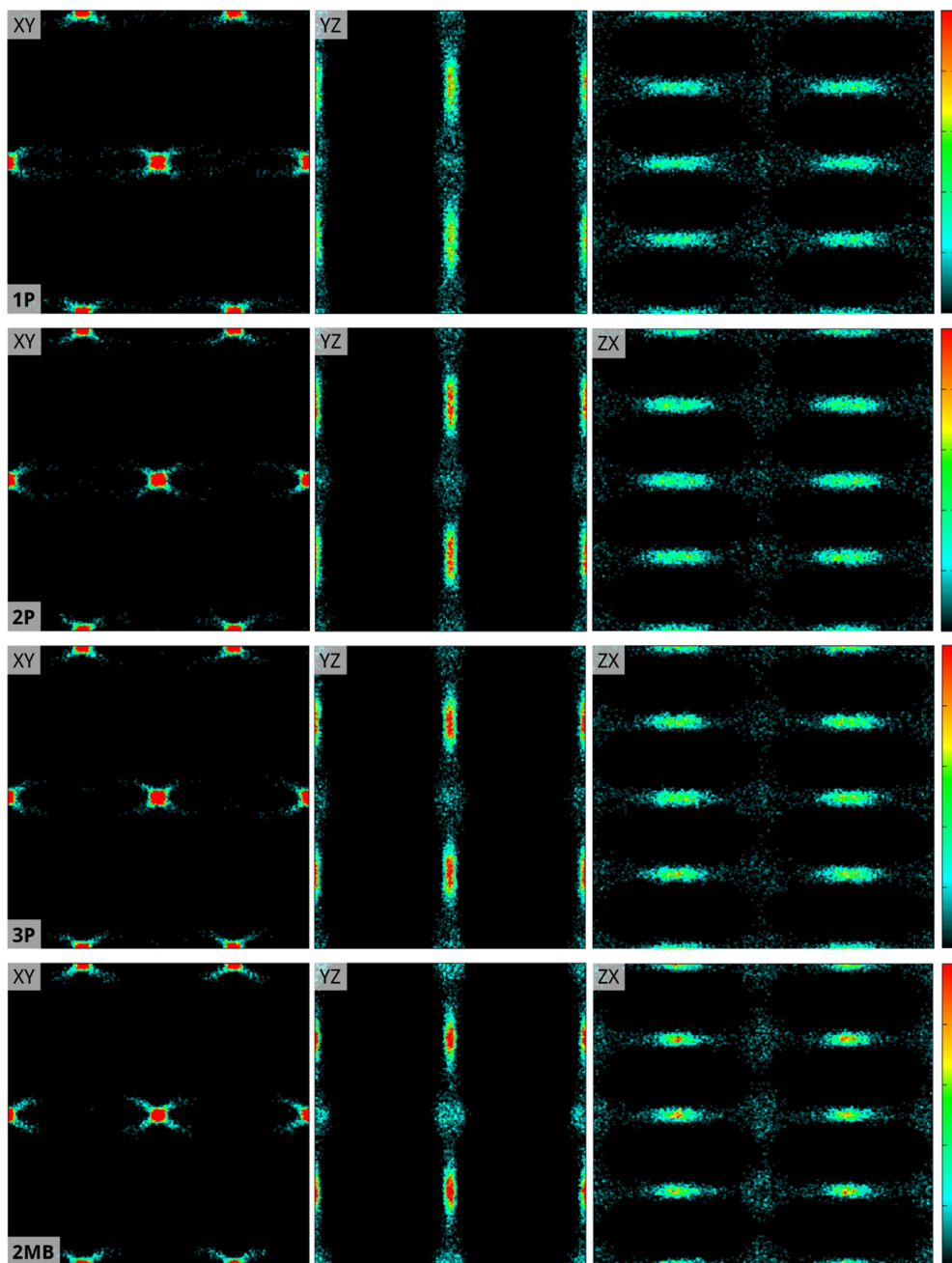


Figure A8. Density profiles of adsorbates within the framework in xy -, yz -, and zx -views (left, center, and right) for the four adsorbates: 1P, 2P, 3P, and 2MB (top to bottom). The color intensity in the bar at the right indicates, from black to red, the number of molecules in each grid cell from 0 to 5.

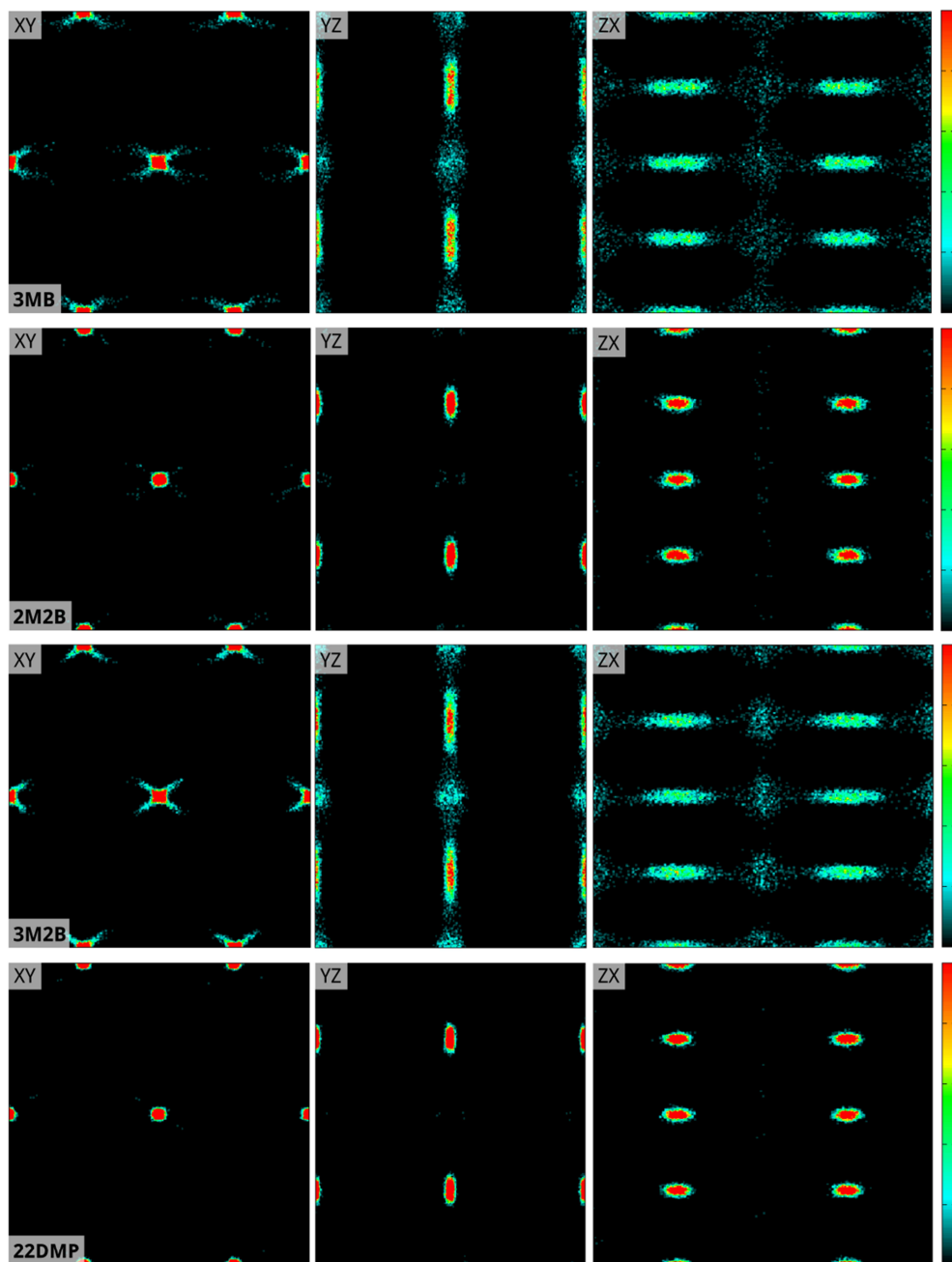


Figure A9. Density profiles of adsorbates within the framework in xy -, yz -, and zx -views (left, center, and right) for the four adsorbates: 3MB, 2M2B, 3M2B, and 22DMP (top to bottom). The color intensity in the bar at the right indicates, from black to red, the number of molecules in each grid cell from 0 to 5.

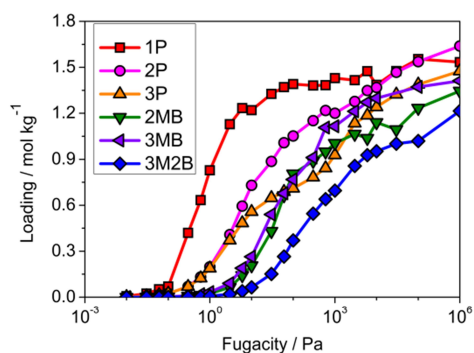


Figure A10. Adsorption isotherms of amyl alcohols as pure compounds in ZIF-77 at 298 K. 2M2B and 22DMP are excluded from this plot since they cannot diffuse in the structure and the space available for them is limited.

Bibliography

- (1) Banerjee, R.; Phan, A.; Wang, B.; Knobler, C.; Furukawa, H.; O'Keeffe, M.; Yaghi, O. M., *Science* **2008**, *319*(5865), 939-943.
- (2) Rappe, A. K.; Casewit, C. J.; Colwell, K. S.; Goddard, W. A.; Skiff, W. M., *J. Am. Chem. Soc.* **1992**, *114*(25), 10024-10035.
- (3) Gutierrez Sevillano, J. J.; Calero, S.; Ania, C. O.; Parra, J. B.; Kapteijn, F.; Gascon, J.; Hamad, S., *J. Phys. Chem. C* **2013**, *117*(1), 466-471.
- (4) Chen, B.; Potoff, J. J.; Siepmann, J. I., *J. Phys. Chem. B* **2001**, *105*(15), 3093-3104.
- (5) Kelkar, M. S.; Rafferty, J. L.; Maginn, E. J.; Siepmann, J. I., *Fluid Phase Equilib.* **2007**, *260*(2), 218-231.
- (6) Frenkel, D.; Smit, B., *Understanding Molecular Simulations. From Algorithms to Applications*. Elsevier: San Diego. California, 2002.

Appendix 3

The three-dimensional structures of the adsorbates in this study are shown in Figure A1 using a ball and sticks model. They are isomers of the structural formula $C_5H_{12}O$.

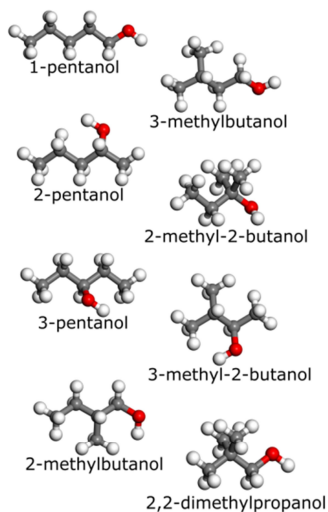


Figure A1. Structural isomers of $C_5H_{12}O$.

The adsorbent is Cd-BINOL. Crystallographic information can be found in Table A1.

Table A1. Selected crystallographic information on Cd-BINOL.¹

Formula	$C_{127}H_{110}Cd_3Cl_8N_{14}O_{38}$
Formula weight	3061.09
Crystal size / mm^3	$0.8 \times 0.5 \times 0.5$
Crystal system, space group	Tetragonal, $P4_122$
$a / \text{\AA}$	20.305
$c / \text{\AA}$	49.641
Volume / \AA^3	20 466
Z	4
Calculated density / $g\ cm^{-3}$	0.993

Table A2 reports Lennard-Jones parameters and partial charges for Cd-BINOL. Note that the partial charges are representative partial charges for a typical atom of the type given, but are subject to slight variations upon position within the framework. Full atom charges are available upon request.

Table A2. Lennard-Jones parameters and partial charges for Cd-BINOL, based on UFF.²

Atom	$\epsilon\ k_B^{-1} / K$	$\sigma / \text{\AA}$	Charge (e-) av.
Cd	114.74	2.848	0.94
Cl	114.233	3.947	-0.106
C (-Cl)	52.839	3.851	0.092
C (-OH)	52.839	3.851	0.352
C (-N)	52.839	3.851	0.170
C (-C)	52.839	3.851	0.055
C (-H)	52.839	3.851	-0.246
H (OH)	22.142	2.886	0.422
H (benz)	22.142	2.886	0.147
O (OH)	30.194	3.5	-0.539
O (NO ₃)	30.194	3.5	-0.544
N (pyr)	34.723	3.66	-0.343
N (NO ₃)	34.723	3.66	0.9

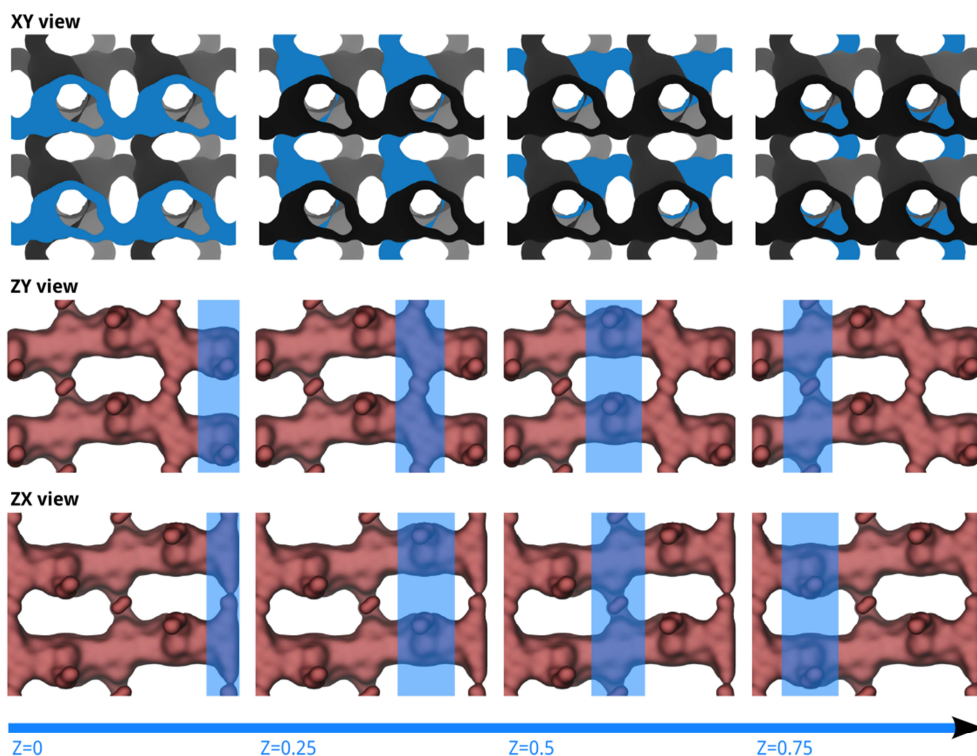


Figure A2. Schematic view of channel system in Cd-BINOL. As the accessible space computed with Pore Blazer reveals, the main channels have an unusual twisted pore shape and are connected horizontally by their bottom surface through zigzag channels. This pattern is repeated four times along the z-axis with a rotation of 90°. For maximum clarity, a $2 \times 2 \times 1$ simulation cell is shown.

Table A3. Lennard-Jones parameters defined for the pseudoatoms of the molecules studied based on TrAPPE force field.³⁻⁴

Pseudoatoms	$\epsilon \text{ k}_B^{-1} / \text{K}$	$\sigma / \text{Å}$	Charge (e ⁻)	Description
CH3	98.0	3.75	0.0	(CH ₃)-CH _x
CH2	46.0	3.95	0.0	(CH _x) ₂ -(CH ₂)
CH	10.0	4.68	0.0	(CH _x) ₃ -(CH)
C	0.5	6.4	0.0	(CH _x) ₄ -(C)
CH2_OH	46.0	3.95	0.265	CH _x -(CH ₂)-OH
CH_OH	10.0	4.33	0.265	(CH _x) ₂ -(CH)-OH
C_OH	0.5	5.8	0.265	(CH _x) ₃ -(C)-OH
O_OH	93.0	3.02	-0.7	CH _x -(O)-H
H_OH	zero	zero	0.435	O-(H)

Table A4. Geometric parameters defined for the pseudoatoms of the molecules studied based on TraPPE force field.³⁻⁴

Geometries				
Harmonic bond	k_{eq} / K	$r_{eq} / \text{\AA}$		
CH _X -CH _Y	334485.0	1.540		
CH _X -OH	386110.0	1.430		
O-H	543610.0	0.945		
Harmonic bend	k_{eq} / K	$\theta_{eq} / \text{\AA}$		
CH _X -(CH ₂)-CH _Y	62500.0	114.0		
CH _X -(CH)-CH _Y	62500.0	112.0		
CH _X -(C)-CH _Y	62500.0	109.47		
CH _X -(CH _Y)-O	50400.0	109.47		
CH _X -(O)-H	55400.0	108.50		
Torsion	K_0 / K	K_1 / K	K_2 / K	K_3 / K
CH _X -(CH ₂)-(CH ₂)-CH _Y	0.0	335.03	-68.19	791.32
CH _X -(CH)-(CH ₂)-CH _Y	-251.06	428.73	-111.85	441.27
CH _X -(CH ₂)-(CH ₂)-OH	0.0	176.62	-53.34	769.93
CH _X -(CH ₂)-(O)-H	0.0	209.82	-29.17	187.93
CH _X -(CH)-(O)-H	215.96	197.33	31.46	-173.92
CH _X -(C)-(O)-H	0.0	0.0	0.0	163.56
CH _X -(CH ₂)-(CH ₂)-O	0.0	176.62	-53.34	769.93
CH _X -(CH)-(CH ₂)-O	-251.06	428.73	-111.85	441.27
CH _X -(CH ₂)-(CH)-O	-251.06	428.73	-111.85	441.27

Harmonic bond: $U^{\text{bond}}(r_{ij}) = \frac{1}{2}k_{eq}(r_{ij} - r_{eq})^2$

Harmonic bend: $U^{\text{bend}}(\theta_{ijk}) = \frac{1}{2}k_{eq}(\theta_{ijk} - \theta_{eq})^2$

Torsion: $U^{\text{torsion}}(\varphi_{ijkl}) = K_0 + K_1[1 + \cos(\varphi_{ijkl})] + K_2[1 - \cos(2\varphi_{ijkl})] + K_3[1 + \cos(3\varphi_{ijkl})]$

Ideal Adsorbed Solution Theory (IAST)

This theory is based on the Gibbs equation of adsorption and it assumes the adsorbent to be thermodynamically inert and to have a temperature invariant area for all of the adsorbates. The thermodynamic equations are derived for the adsorbed phase using the specific area of the adsorbent (A) and the spreading pressure (π) instead of the analogous variables: volume (V) and pressure (P). The gas and adsorbed phases are considered ideal, the temperature is considered constant and an equilibrium criterion is applied. Thus, the pressure and composition are related in the gas and adsorbed phases as follows:⁵

$$Py_i = x_i P_i^0(\pi), \quad (\text{A1})$$

where y_i and x_i are the mole fractions for component i in the gas and adsorbed phases, respectively. The total pressure of the mixture in the gas phase is P and P_i^0 is the pressure in the gas phase corresponding to the spreading pressure (π) of the adsorption of pure component i . The spreading pressure is a property explained as the negative of the surface tension. It is the same for each compound and it is calculated by the integration of each single-component adsorption isotherm:

$$\frac{\pi_i^0 A}{RT} = \int_0^{P_i^0} \frac{n_i^0(P_i)}{P_i} dP_i, \quad (\text{A2})$$

where π_i^0 is the spreading pressure of the adsorption of pure component i , P_i is the pressure of the gas phase in the single-component adsorption isotherm, and n_i^0 is the adsorption value of the pure component i .

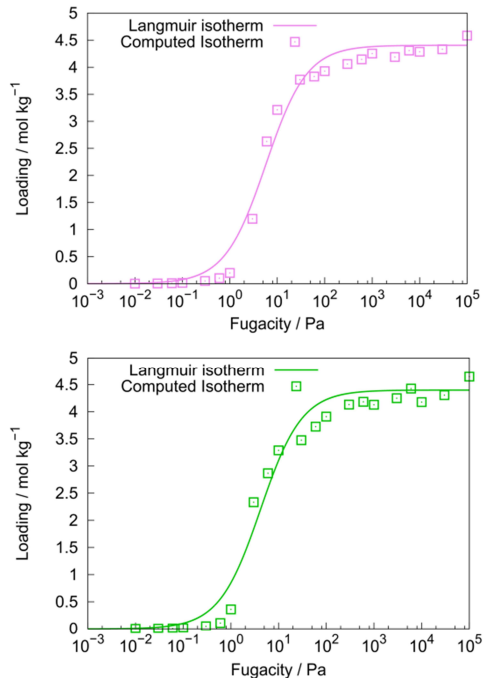


Figure A3. Adsorption isotherms of 2-pentanol (pink) and 2-methylbutanol (green) obtained by Monte Carlo simulations (squares) and fitted to the Langmuir equation (solid line).

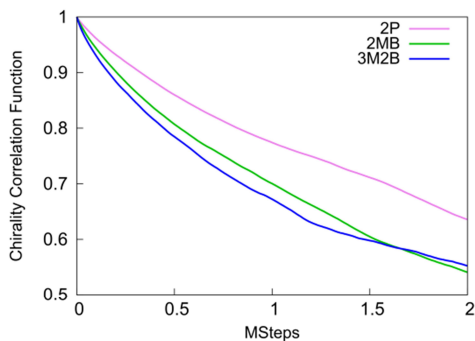


Figure A4. Chirality autocorrelation function vs. number of steps of the simulation in millions.

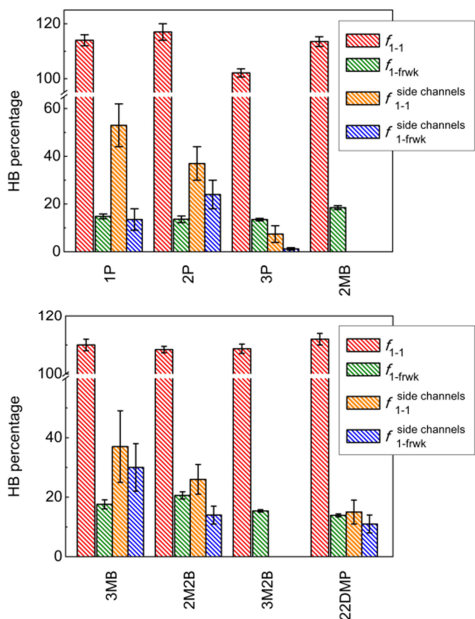


Figure A5. Diagrams for hydrogen-bonding statistics obtained from pure compounds simulations. Percentage of average for self-association (f_{1-1}) and hydrogen bonding to framework atoms (f_{1-frwk}) are shown.

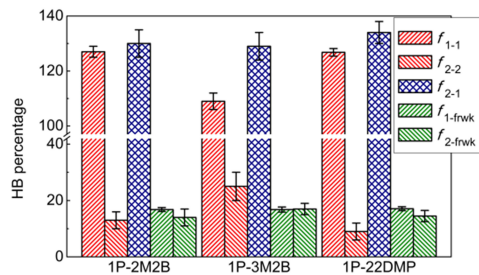


Figure A6. Diagrams for hydrogen-bonding statistics obtained from binary mixtures simulations. Percentage of average for self-association (f_{1-1} , f_{2-2}), cross-association (f_{2-1}) and hydrogen bonding to framework atoms (f_{1-frwk} , f_{2-frwk}) are shown.

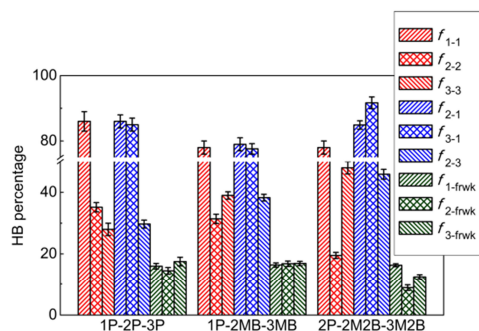


Figure A7. Diagrams for hydrogen-bonding statistics obtained from ternary mixtures simulations. Percentage of average for self-association (f_{1-1} , f_{2-2} , f_{3-3}), cross-association (f_{2-1} , f_{3-1} , f_{2-3}) and hydrogen bonding to framework atoms (f_{1-frwk} , f_{2-frwk} , f_{3-frwk}) are shown.

Table A5. Thermodynamic data of adsorption in Cd-BINOL at 298 K.

Molecules	K_H mol kg ⁻¹ Pa ⁻¹	ΔU kJ mol ⁻¹	ΔH kJ mol ⁻¹	ΔS J K ⁻¹ mol ⁻¹	ΔG kJ mol ⁻¹	ΔA kJ mol ⁻¹
1-pentanol	4.534×10^{-1}	-68.89	-71.36	-116.14	-36.73	-34.25
2-pentanol	2.294×10^{-1}	-68.14	-70.62	-119.32	-35.04	-32.56
3-pentanol	1.032×10^{-1}	-57.94	-60.42	-91.76	-33.06	-30.58
2-methylbutanol	1.107×10^{-1}	-55.52	-58.00	-83.06	-33.23	-30.76
3-methylbutanol	1.477×10^{-1}	-57.37	-59.85	-86.86	-33.95	-31.47
2-methyl-2-butanol	2.191×10^{-2}	-47.55	-50.03	-69.78	-29.22	-26.74
3-methyl-2-butanol	5.591×10^{-2}	-54.13	-56.61	-84.08	-31.54	-29.06
2,2-dimethylpropanol	4.170×10^{-2}	-52.09	-54.57	-79.67	-30.82	-28.34

Table A6. Hydrogen-bond statistics for pure compounds in Cd-BINOL at infinite dilution. N is the total number of guest molecules in the unit cell (and simulation box) and " $N^{\text{side channel}}$ " the total number of guest molecules in the four side channels. All probabilities are given as percentages. The probability for a guest molecule to be hydrogen-bonded to atoms of the framework is labeled f_{1-frwk} .

	Pure compounds			
	1P	2P	3P	22DMP
no. simulations	5	5	5	5
N	1	1	1	1
$N_1^{\text{side channel}}$	0.634 ± 0.002	0.454 ± 0.005	0.178 ± 0.001	-
f_{1-frwk}	3.21 ± 0.10	2.14 ± 0.12	0.80 ± 0.04	0.83 ± 0.03
$f_{1-frwk}^{\text{side channel}}$	4.16 ± 0.16	3.5 ± 0.3	0.43 ± 0.11	-
	2MB	3MB	2M2B	3M2B
	no. simulations	5	5	5
N	1	1	1	1
$N_1^{\text{side channel}}$	0.0106 ± 0.0004	0.0520 ± 0.0008	-	0.0046 ± 0.0004
f_{1-frwk}	1.20 ± 0.03	1.60 ± 0.10	0.46 ± 0.03	0.76 ± 0.04
$f_{1-frwk}^{\text{side channel}}$	3.6 ± 1.8	4.1 ± 0.6	-	0.4 ± 0.4

In order to interpret the hydrogen-bond statistics in the mixtures with some degree of confidence, we decided to compare the results with those of a probabilistic model. This model uses one parameter (f_{pi}^{model}) per component in the mixture to fit the total fraction of associated molecules to the simulation results. In order to keep the model as simple as possible and not to introduce any additional parameter, we did not take into account the fraction of molecules hydrogen-bonded to the framework. This should not distort the results, as this fraction remains small and quite similar throughout single and multi-component systems. For this reason, in the mixture $\sum f_{i-k} = \sum f_{i-k}^{\text{model}}$, where the index k runs over all components of the mixture. We do this because we want the model to engage in exactly as many hydrogen bonds as are observed in the mixture and to be able to study how their distribution differs. Additionally, the errors on these sums are low.

The self-associated fraction is obtained through the following equation:

$$f_{i-i}^{\text{model}} = \frac{(N_{i-1})f_{pi}^{\text{model}}}{(N_{i-1}) + N_j + N_k}, \quad (\text{A3})$$

whereas the cross-associated fraction is obtained through the following equation:

$$f_{i-j}^{\text{model}} = \frac{N_j \sqrt{f_{pi}^{\text{model}} f_{pj}^{\text{model}}}}{(N_{i-1}) + N_j + N_k} \quad (\text{A4})$$

The assumption that underlies the model is that the intrinsic probability for cross-association is the geometric mean of the probabilities.

The interpretation of the parameter f_{pi}^{model} is that it compares to f_{1-1} in the pure adsorbent system i . Indeed, in the mixture,

f_{1-1}^{model} or more generally f_{i-i}^{model} will depend greatly on the mole fraction of component i adsorbed, whereas f_{pi}^{model} extrapolates this to a mole fraction of 1.

From the data in tables A7 and A8, five observations emerge:

1. Clearly, as the results in Table A7 show in the context of Table 1, f_{p1}^{model} is in all cases significantly greater than f_{1-1} of pure 1-pentanol (114 ± 2 , see Table 1), the most adsorbed component of the mixtures by far. This component being the major component of the mixture is analyzed more reliably due to its low error. In fact, it reflects the higher proportion of hydrogen bonds per molecule formed in the mixtures as compared to the one in the pure compound. The higher number of molecules in the structure in the case of the mixtures means that there is a slight structuring effect (see RDFs of Figure 9), but most importantly, that the hydrogen bonds last more MC steps, and when broken, reform similarly fast.

2. The second observation is that the proportion of hydrogen bonds is even higher in the minor component of the mixture for all binary mixtures. This and further observations are rationalized below.

3. A third observation deals with the distribution of hydrogen bonds. If we compare the hydrogen bonds f_{1-1} , f_{2-2} , f_{1-2} , and f_{2-1} with the ones obtained in the probabilistic model, in a first order approximation they are similar. We will comment on the subtle differences later on when we include ternary mixtures in the discussion. But for now, the interpretation is that hydrogen bonds form largely randomly between components of the mixture.

Table A7. Hydrogen-bond statistics for binary mixtures. Percentages of average self- and cross-association, f_{i-i} and f_{i-j} respectively, for each compound i in the binary mixtures at saturation. The superscript “model” refers to the value obtained using the probabilistic model. f_{pi}^{model} refers to the number of hydrogen bonds (expressed as percentages) required to fit $\sum f_{i-j}$.

	Binary mixtures (1)-(2)		
	1P-2M2B	1P-3M2B	1P-22DMP
$\sum f_{1-k} = \sum f_{1-k}^{\text{model}}$	138.6 ± 1.5	138.0 ± 1.3	137.3 ± 1.8
$\sum f_{2-k} = \sum f_{2-k}^{\text{model}}$	143.1 ± 4.3	153.3 ± 1.9	143.0 ± 5.2
f_{1-1}	127 ± 2	109 ± 3	126.8 ± 1.4
f_{2-2}	13 ± 3	25 ± 5	9 ± 3
f_{1-2}	11.5 ± 1.5	28.6 ± 1.6	10.5 ± 0.9
f_{2-1}	130 ± 5	129 ± 5	134 ± 4
f_{1-1}^{model}	127.7 ± 1.9	110.4 ± 1.5	127.1 ± 2.1
f_{2-2}^{model}	8.6 ± 0.6	27.5 ± 0.9	7.8 ± 0.6
f_{1-2}^{model}	11.0 ± 0.3	27.6 ± 0.4	10.1 ± 0.4
f_{2-1}^{model}	135 ± 4.4	125.7 ± 1.4	135.3 ± 4.8
f_{p1}^{model}	138.4 ± 2.0	135.2 ± 1.9	136.9 ± 2.3
f_{p2}^{model}	147.7 ± 10.3	167.5 ± 5.3	148.8 ± 12.7

We next include ternary mixtures, whose results are shown in Table A8, in the discussion. The previous comments on binary mixtures equally apply, i.e., all components form an increased number of hydrogen bonds to the ones of the pure substances.

4. A fourth observation emerges that was less clearly seen in the binary mixtures. The number of self-associated hydrogen bonds in the simulation is higher than in the model, and as a consequence of having constrained the total number of hydrogen bonds in the model, a lower amount of cross-association takes place in the simulation. The effect lies only slightly above the noise level, but it is nonetheless observed. In the absence of data for mixtures of similar composition in the bulk, it is impossible to say whether this is a matter of genuine lack of affinity of the alcohols for each other or if it is enforced by

the confinement. It is also striking that it happens in almost all combinations of alcohols (the binary mixtures 1P-3M2B and 1P-22DMP do not exhibit this behavior above the noise level).

5. And a fifth observation can be made that is more speculative in nature. We observe in the ternary mixtures that, in spite of the previous observation that cross-association is generally less favored, the cross-association between the two minor components of the mixture is comparatively favored. In two of these mixtures they even lie above the level in the model.

We had assessed that IAST tends to systematically overestimate the loading of the major component and underestimate the one of minor components, from which it follows that the selectivity is usually overestimated. These minor components are generally bulkier and their hydroxyl

group is less exposed. This can be linked to the previous observations 2-5. An explanation could be that on one side the minor components are predicted by IAST to be less favored. In the MC simulations on the other side, the mixture creates new environments for the minor components that make them comparatively a bit more

competitive: they can strongly self-associate or associate with other minor components, in addition to the bonds formed to the major component. As for the major component, it does not benefit that much from the introduction of a relatively small number of different molecules.

Table A8. Hydrogen-bond statistics for ternary mixtures. Percentages of average self- and cross-association, f_{i-i} and f_{i-j} respectively, for each compound i in the ternary mixtures at saturation. The superscript “model” refers to the value obtained using the probabilistic model. f_{pi}^{model} refers to the number of hydrogen bonds (expressed as percentages) required to fit $\sum f_{i-j}$.

	Ternary mixtures (1)-(2)-(3)		
	1P-2P-3P	1P-2MB-3MB	2P-2M2B-3M2B
$\sum f_{1-k} = \sum f_{1-k}^{\text{model}}$	141.2 ± 1.1	137.9 ± 1.5	130.7 ± 1.7
$\sum f_{2-k} = \sum f_{2-k}^{\text{model}}$	150.8 ± 2.0	148.7 ± 1.5	150.2 ± 1.6
$\sum f_{3-k} = \sum f_{3-k}^{\text{model}}$	151.0 ± 2.2	147.5 ± 1.2	157.6 ± 1.6
f_{1-1}	86 ± 3	78 ± 2	78 ± 2
f_{2-2}	35.2 ± 1.5	31.4 ± 1.5	19.5 ± 1.0
f_{3-3}	28 ± 2	39.0 ± 1.2	48 ± 2
f_{1-2}	31.2 ± 1.5	26.8 ± 0.8	13.8 ± 0.5
f_{2-1}	86 ± 2	79 ± 2	84.9 ± 1.3
f_{1-3}	24.2 ± 1.2	32.7 ± 0.6	38.6 ± 1.0
f_{3-1}	85 ± 2	77.6 ± 1.6	91.7 ± 1.8
f_{2-3}	29.7 ± 1.3	38.3 ± 1.1	45.9 ± 1.6
f_{3-2}	37.8 ± 1.3	30.9 ± 1.3	17.8 ± 0.9
f_{1-1}^{model}	83.2 ± 1.2	75.0 ± 1.3	76.0 ± 1.6
f_{2-2}^{model}	32.0 ± 1.0	27.4 ± 0.7	13.7 ± 0.4
f_{3-3}^{model}	24.2 ± 0.8	34.3 ± 0.8	45.2 ± 1.2
f_{1-2}^{model}	32.7 ± 0.5	28.1 ± 0.4	14.5 ± 0.2
f_{2-1}^{model}	91.7 ± 1.2	83.7 ± 1.0	90.3 ± 1.2
f_{1-3}^{model}	25.4 ± 0.4	34.8 ± 0.4	40.1 ± 0.5
f_{3-1}^{model}	91.8 ± 1.3	83.1 ± 0.9	94.8 ± 1.2
f_{2-3}^{model}	27.1 ± 0.5	37.6 ± 0.5	46.3 ± 0.7
f_{3-2}^{model}	35.0 ± 0.7	30.1 ± 0.4	17.6 ± 0.3
f_{p1}^{model}	137.4 ± 2.0	133.5 ± 2.3	121.7 ± 2.6
f_{p2}^{model}	157.1 ± 4.6	155.7 ± 4.0	161.8 ± 4.9
f_{p3}^{model}	157.6 ± 5	153.2 ± 3.2	178.3 ± 4.8

Before we get back to establishing a link between hydrogen bonding and IAST prediction, supporting information on adsorption isotherms is provided. Adsorption isotherms of the binary mixture 2MB-3MB are presented in Figure A8. Structurally, the isomers can be seen as 1-butanol with either a methyl grafted at carbon 2 (2MB) or at carbon 3 (3MB). So this mixture is probing the influence of the position of the methyl group. The adsorption of 3MB is favored over 2MB. This mixture can be interestingly compared with the behavior of the ternary 1P-2MB-3MB mixture (Figure 8), in which these isomers are facing the competition of the much more strongly adsorbed 1P. In this case as well, the adsorption of 3MB had been found to be higher than the one of 2MB. But not only is this qualitative behavior identical, the values of the 3MB/2MB selectivities at 100 kPa are similar at around 1.25 (binary) vs. 1.19 (ternary) in Monte Carlo simulations, and 1.13 (binary) vs. 1.16 (ternary) for IAST predictions.

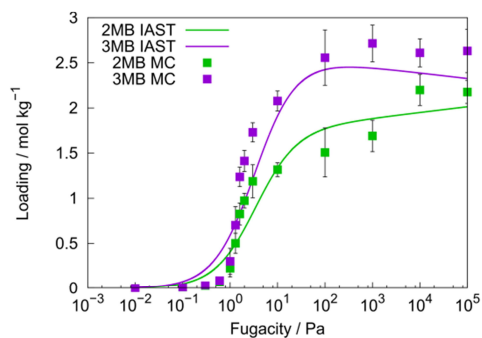


Figure A8. Adsorption isotherms at 298 K for the mixture 2MB-3MB obtained by Monte Carlo simulations (symbols) and predicted by IAST (lines).

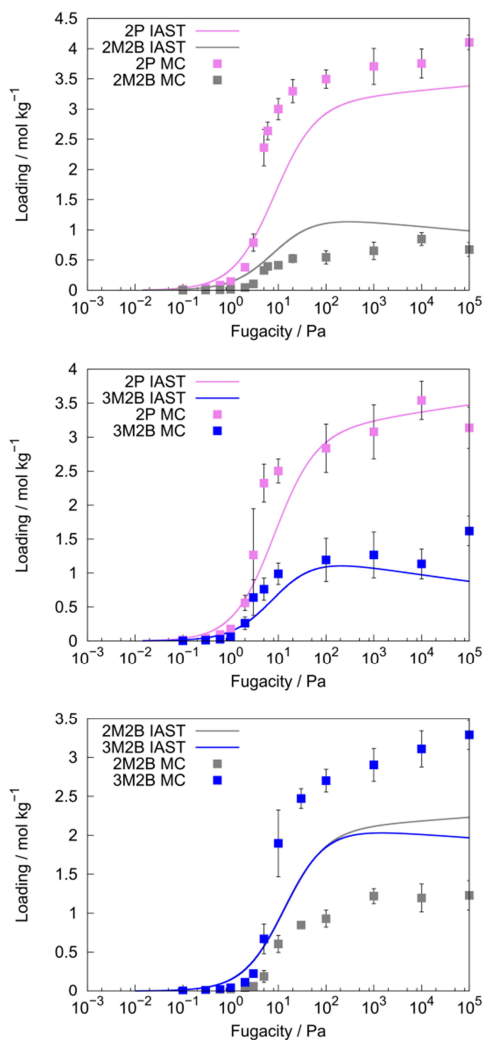


Figure A9. Adsorption isotherms at 298 K for the mixtures 2P-2M2B (top), 2P-3M2B (center), and 2M2B-3M2B (bottom), obtained by Monte Carlo simulations (symbols) and predicted by IAST (lines).

Figure A9 shows the adsorption isotherms of three binary mixtures that can be seen as modifications of 2-butanol: with a methyl at carbon 2 (yielding 2M2B), at carbon 3 (3M2B), or at carbon 4 (2P). These three binary mixtures all relate to the ternary mixture 2P-2M2B-3M2B (Figure 8). The selectivities calculated in the binary

mixtures agree remarkably with the ones in the ternary mixture, both for the independent Monte Carlo simulations and the IAST predictions.

Given that the IAST prediction favored slightly 2M2B over 3M2B, contrary to the Monte Carlo results, these isotherms were refitted using other models for the pure isotherms to make sure that this was not due to the limitations of the Langmuir adsorption model.⁶ Other models included the model by Janovic⁷ and the Langmuir-Freundlich dual site⁸ model. Although Janovic's model only has 2 parameters, the adsorption curve rises steeply and reproduces that part of the curve better. The Langmuir-Freundlich dual site model uses 6 parameters and reproduces the curve very satisfactorily over the whole fugacity range. However, all of these models, as well as those of Toth⁹ and Jensen,¹⁰ consistently reach the same conclusions as the Langmuir model.

Figure A10 shows the effect of swapping two structural elements on isotherms of the binary equimolar mixtures. The 2P-3MB mixture (Figure A10, top) can be considered either as butane with an extra hydroxyl group at carbon 3 and methyl group at carbon 1 (2P), or the other way round, hydroxyl at carbon 1 and methyl at carbon 3 (3MB). At the lower end of the fugacities, 3MB is clearly favored over 2P, and that is also predicted qualitatively by IAST, but at higher fugacities the adsorption values become very similar.

The 3P-2MB mixture (Figure A10, bottom) can be considered either as butane with an extra hydroxyl group at carbon 2 and methyl at carbon 1 (3P), or the other way round, hydroxyl at carbon 1 and methyl at carbon 2 (2MB). 2MB is consistently more strongly adsorbed than 3P over the whole

pressure range and this is also predicted by IAST. Considering both mixtures of Figure A10, this confirms a broader general trend that encompasses also the other mixtures of this article. In Cd-BINOL, adsorption is favored if the hydroxyl group is clearly separated from the hydrophobic part, for instance when located at the end of the chain.

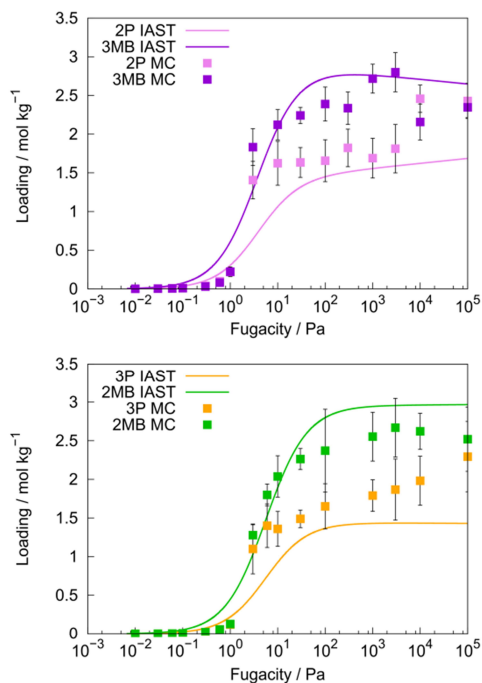


Figure A10. Adsorption isotherms at 298 K for the mixtures 2P-3MB (top) and 3P-2MB (bottom), both obtained by Monte Carlo simulations (symbols) and predicted by IAST (lines).

Table A9 finally confronts two qualitative comparisons. In the upper right triangle, IAST predictions are compared to Monte Carlo isotherms at a fugacity of 100 kPa. The comparisons are undertaken pairwise, depending upon availability either in binary or ternary mixtures. So, binary mixtures were used in the 1P-2M2B, 1P-3M2B, and 1P-22DMP comparisons, and ternary

mixtures in all other comparisons. For a given element a_{ij} of the table, the ratio of the selectivity S_{ij} (or S_{ji}) from IAST over the selectivity from Monte Carlo is calculated. Either S_{ij} or S_{ji} is picked so as to ensure that the selectivity from Monte Carlo is greater than one. The agreement is considered satisfactory provided its value is $1.00 (\pm 25\%)$ and gets a Y (Yes) label, or unless the errors are so large that when applied, the outcome would be the opposite, in which case the test is inconclusive. In this case, the result is marked with a question mark. If the test fails because the value is higher than 1.25, the label is N (No) or, if uncharacteristically it is lower than 0.75 the label is N⁻.

In the lower left triangle, the table element a_{ij} is calculated by dividing $\sum f_{i-k}$ by $\sum f_{j-k}$ or its inverse, in such a way that the numerator stands for the minor element of the mixture and j stands for the major element of the mixture. Given the very different nature of this index, a satisfactory agreement is deemed to be $1.00 \pm 4\%$, unless the errors are bigger and the test is inconclusive. These limits have been tuned in such a way as to yield roughly the same number of matches in the comparisons in both triangles. The same conventions apply in this part of the table for values below the lower limit of 0.96 (N⁻ label), 0.96-1.04 (Y label), and above 1.04 (N label). Ideally, a perfect match should be observed in the table between an element and its corresponding element, reflected over the main diagonal, i.e., a_{ij} and a_{ji} should have the same label.

The rationale for this table is as follows: if one component of a given pair is involved in significantly more hydrogen bonds than expected, then the Monte Carlo simulations should reflect this and favor this component, when compared to the IAST

predictions. Let us consider an example: the IAST-predicted adsorptions of 1P and 2P in the ternary mixtures are 3.59 and 0.60 mol kg⁻¹, respectively, yielding a selectivity of 6.02, whereas the selectivity for Monte Carlo simulations is 2.78. Therefore, the ratio of selectivities is 2.16, meaning IAST is overestimating the selectivity in favor of 1P, and given that 2.16 is outside the $1.00 (\pm 25\%)$ range, it gets marked as N in the upper right triangle. On the other side, we calculate the ratio $\sum f_{2P-k}$ over $\sum f_{1P-k}$ using data from table A8, that is 150.8/141.2. This too is significantly bigger than the range accepted for matching $1.00 \pm 4\%$, meaning more 2P is drawn into the structure by extra hydrogen bonds in the Monte Carlo simulation than IAST would let one expect.

As can be seen in the table, IAST performs best if the pairs of alcohols are adsorbed not too differently: In the 1P-2P-3P ternary mixture, the selectivities involving 1P are reproduced badly, whereas the lower selectivity of 2P-3P (1.57 according to the Monte Carlo isotherm simulations) is reproduced well, and in the other two ternary mixtures, the observation also applies.

Overall, the qualitative agreement is rather satisfactory: there are 8 coincidences, three tests are inconclusive, and there is one failure. It should be stressed that in the one case that evidenced a failure, the 2P-2M2B pair, although disagreement between IAST and Monte Carlo matched an imbalance in hydrogen bonds, uncharacteristically IAST underestimated the selectivity whereas the hydrogen-bond analysis expected 2M2B to be comparatively favored in the Monte Carlo simulations, and from this we would conclude that the 2P/2M2B selectivity should have been overestimated by IAST. We noted in the analysis of the ternary system 2P-2M2B-3M2B, from which the

IAST comparison arises, that uncharacteristically few hydrogen bonds were formed between 2M2B and the framework ($f_{2P-frwk} = 8.8 \pm 0.9$). Curves generated through the IAST approximation assumes implicitly at these fugacities a

hydrogen-bonding level of 2M2B to the framework that is comparable to the one found in the adsorption of the pure substance. And therefore we conclude that IAST predicts more 2M2B in the structure than there really are.

Table A9. Qualitative chart for pairwise comparisons of components i and j . Y: means pair compares well, N means pair does not compare well. Upper right triangle: IAST performance vs. reference Monte Carlo adsorption isotherms. Lower left triangle: Total number of hydrogen bonds are equal within tolerance, i.e., $\sum f_{i-k} = \sum f_{j-k}$.

	1P	2P	3P	2MB	3MB	2M2B	3M2B	22DMP
1P	-	N	N	N?	N	N?	N	N
2P	N	-	Y			N	N	
3P	N	Y	-					
2MB	N			-	Y			
3MB	N			Y	-			
2M2B	Y	N				-	N	
3M2B	N	N				N	-	
22DMP	N?							-

Bibliography

- (1) Wu, C.-D.; Lin, W., *Angew. Chem., Int. Ed.* **2007**, *46*(7), 1075-1078.
- (2) Rappe, A. K.; Casewit, C. J.; Colwell, K. S.; Goddard, W. A.; Skiff, W. M., *J. Am. Chem. Soc.* **1992**, *114*(25), 10024-10035.
- (3) Chen, B.; Potoff, J. J.; Siepmann, J. I., *J. Phys. Chem. B* **2001**, *105*(15), 3093-3104.
- (4) Kelkar, M. S.; Rafferty, J. L.; Maginn, E. J.; Siepmann, J. I., *Fluid Phase Equilib.* **2007**, *260*(2), 218-231.
- (5) Myers, A. L.; Prausnitz, J. M., *AIChE J.* **1965**, *11*(1), 121-127.
- (6) Langmuir, I., *J. Am. Chem. Soc.* **1916**, *40*, 1361-1368.
- (7) Jovanovic, D. S., *Kolloid Z. Z. Polym.* **1969**, *235*(1), 1203-1213.
- (8) Sips, R., *J. Phys. Chem.* **1948**, *16*, 490-495.
- (9) Toth, J., *Acta Chim. Acad. Sci. Hung.* **1962**, *15*, 415-430.
- (10) Jensen, C. R. C.; Seaton, N. A., *Langmuir* **1996**, *12*, 2866-2867.

Appendix 4

Table A1. Similarity of experimental IR spectra of different frameworks using the global similarity index S . A value of 1 means maximum similarity.

	ITQ	FAU	FER	MOR	TON	MFI	MEL
SOD	0.97	0.95	0.98	0.97	0.93	0.90	0.92
ITQ		0.97	0.98	0.98	0.92	0.89	0.95
FAU			0.99	0.99	0.90	0.87	0.95
FER				1.00	0.94	0.91	0.96
MOR					0.94	0.92	0.97
TON						0.98	0.95
MFI							0.92

Appendix 5

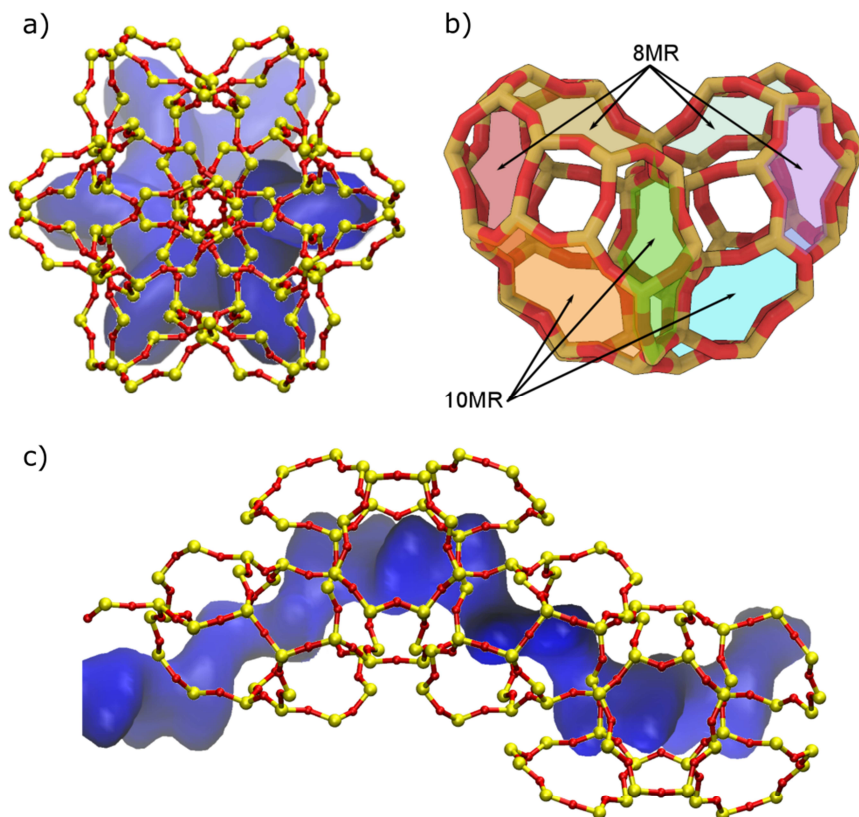


Figure A1. *xy*-view of a single chiral channel of STW zeolite showing 8- and 10-membered rings (8MR and 10MR, respectively) and the corresponding internal pore space in blue (a). *xy*-view of two of the six cages that build the chiral channel of STW zeolite and the location of 8MR and 10MR (b). *zy*-view of a single chiral channel of STW zeolite showing 8MR and 10MR and the corresponding internal pore space in blue (c). The internal pore space in figures (a) and (c) were generated with Pore Blazer¹ by moving a probe with a diameter of 3.5 Å and visualized by VMD.² Figure (b) was visualized with QuteMol.³

The three-dimensional structures of the adsorbates in this study are shown in Figure A2 using a ball and sticks model. They are structural isomers with molecular formula $C_5H_{12}O$. The asymmetric carbon that makes these compounds chiral is colored in green.

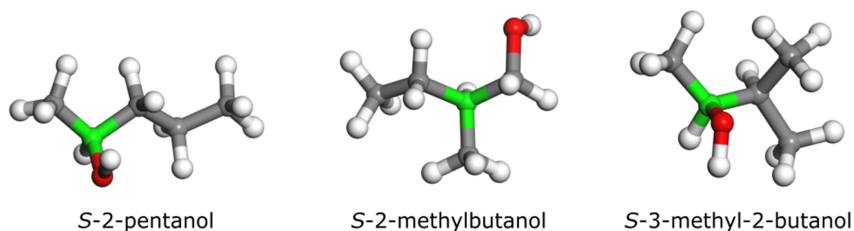


Figure A2. Chiral compounds within the group of structural isomers of $C_5H_{12}O$.

Table A1. Lennard-Jones parameters and charges defined for the atoms of the molecules studied based on the OPLS force field.⁴

Atoms	$\epsilon \text{ k}_B^{-1} / \text{K}$ [LJ 12-6]	$\sigma / \text{\AA}$ [LJ 12-6]	Charge (e^-)	Description
C_CH3	33.212	3.5	-0.18	(CH ₃)-CH _x
C_CH2	33.212	3.5	-0.12	(CH ₂)-(CH _x) ₂
C_CH	33.212	3.5	-0.06	(CH)-(CH _x) ₃
C_CH2OH	33.212	3.5	0.145	OH-(CH ₂)-CH _x
C_CHOH	33.212	3.5	0.205	OH-(CH)-(CH _x) ₂
H_C	15.09	2.5	0.06	CH _x
O_OH	85.547	3.12	-0.683	OH-CH _x
H_OH	zero	zero	0.418	OH-CH _x

Table A2. Geometric parameters defined for the atoms of the molecules studied based on OPLS force field.⁴

Geometries			
Harmonic bond	$k_{\text{eq}} \text{ k}_B^{-1} / \text{K } \text{\AA}^2$	$r_{\text{eq}} / \text{\AA}$	
CH _X -CH _Y	269725	1.529	
C-H	342188	1.09	
CH _X -OH	322060	1.41	
O-H	556560	0.945	
Harmonic bend	$k_{\text{eq}} \text{ k}_B^{-1} / \text{K rad}^2$	$\theta_{\text{eq}} / ^\circ$	
CH _X -CH _Y -CH _Z	58725	112.7	
CH _X -C-H _Y	37741	110.7	
H-C-H	33212	107.8	
CH _X -CH _Y -OH	50321	109.5	
H _X -C-OH	35225	109.5	
CH _X -O-H	55354	108.5	
Torsion	$K_1 / \text{kcal mol}^{-1}$	$K_2 / \text{kcal mol}^{-1}$	$K_3 / \text{kcal mol}^{-1}$
CH _X -CH _Y -CH _Z -CH _V	1.74	-0.157	0.279
CH _X -CH _Y -C-H _Z	0	0	0.366
H _X -C-C-H _Y	0	0	0.318
CH _X -CH _Y -CH _Z -OH	1.711	-0.5	0.663
H _X -C-CH _Y -OH	0	0	0.468
CH _X -CH _Y -O-H	-0.356	-0.174	0.492
H _X -C-O-H	0	0	0.45

$$\text{Harmonic bond: } U^{\text{bond}} = \frac{1}{2} k_{\text{eq}} (r - r_{\text{eq}})^2$$

$$\text{Harmonic bend: } U^{\text{bend}} = \frac{1}{2} k_{\text{eq}} (\theta - \theta_{\text{eq}})^2$$

$$\text{Torsion: } U^{\text{torsion}} = \frac{1}{2} K_1 (1 + \cos \varphi) + \frac{1}{2} K_2 (1 - \cos(2\varphi)) + \frac{1}{2} K_3 (1 + \cos(3\varphi))$$

Table A3. Lennard-Jones parameters and charges defined for the framework atoms based on the TraPPE-zeo (LJ 12-6)⁵ for the host-guest interactions and Hill (LJ 9-6) force field⁶ for the host-host interactions.

Host-guest interactions defined based on TraPPE-zeo force field				
Atoms	$\epsilon \text{ k}_B^{-1} / \text{K}$ [LJ 12-6]	$\sigma / \text{\AA}$ [LJ 12-6]	Charge (e^-)	Modeled for
O_zeo	53	3.3	-0.75	Combining rules to define host- guest interactions
Si_zeo	22	2.3	1.5	
Ge_zeo	22	2.3	1.5	
Host-host interactions defined based on Hill force field				
Atoms	$A_i \text{ k}_B^{-1} / \text{K \AA}^9$ [LJ 9-6]	$B_i \text{ k}_B^{-1} / \text{K \AA}^6$ [LJ 9-6]	Charge (e^-)	Modeled for
O_zeo	28891069.825	0	-0.75	Combining rules to define host- host interactions
Si_zeo	94057219.175	0	1.5	
Ge_zeo	94057219.175	0	1.5	

Table A4. Geometric parameters defined for the framework atoms based on Hill force field.⁶

Geometries					
Bond-Stretch	$K_2 \text{ k}_B^{-1} / \text{K \AA}^{-2}$	$K_3 \text{ k}_B^{-1} / \text{K \AA}^{-3}$	$K_4 \text{ k}_B^{-1} / \text{K \AA}^{-4}$	$r_{\text{eq}} / \text{\AA}$	
Si-O	231017.255	-338387.114	223109.917	1.6104	
Ge-O	231017.255	-338387.114	223109.917	1.77	
Angle-Bend	$K_2 \text{ k}_B^{-1} / \text{K rad}^{-2}$	$K_3 \text{ k}_B^{-1} / \text{K rad}^{-3}$	$K_4 \text{ k}_B^{-1} / \text{K rad}^{-4}$	$\theta_{\text{eq}} / ^\circ$	
O-Si-O	41248.441	-18408.470	58854.427	112.02	
O-Ge-O	41248.441	-18408.470	58854.427	112.02	
Si-O-Si	10417.396	13863.996	5531.891	173.7651	
Ge-O-Ge	10417.396	13863.996	5531.891	173.7651	
Si-O-Ge	10417.396	13863.996	5531.891	173.7651	
Bond-Bond	$K \text{ k}_B^{-1} / \text{K \AA}^{-2}$	$r_{\text{eq}} / \text{\AA}$	$r'_{\text{eq}} / \text{\AA}$		
Si-O-Si	76426.043	1.6104	1.6104		
Ge-O-Ge	76426.043	1.77	1.77		
Si-O-Ge	76426.043	1.6104	1.77		
Bond-Angle	$K_r \text{ k}_B^{-1} / \text{K \AA}^{-1} \text{ rad}^{-1}$	$K'_r \text{ k}_B^{-1} / \text{K \AA}^{-1} \text{ rad}^{-1}$	$\theta_{\text{eq}} / ^\circ$	$r_{\text{eq}} / \text{\AA}$	$r'_{\text{eq}} / \text{\AA}$
O-Si-O	39313.462	39313.462	112.02	1.6104	1.6104
O-Ge-O	39313.462	39313.462	112.02	1.77	1.77
Si-O-Si	4649.244	4649.244	173.7651	1.6104	1.6104
Ge-O-Ge	4649.244	4649.244	173.7651	1.77	1.77
Si-O-Ge	4649.244	4649.244	173.7651	1.6104	1.77

Angle-Angle	$K \text{ k}_B^{-1} / \text{K rad}^{-2}$	$\theta_{eq} / ^\circ$	$\theta'_{eq} / ^\circ$
O-Si-O~O	-3171.792	112.02	112.02
O-Ge-O~O	-3171.792	112.02	112.02
Torsion	$K_1 \text{ k}_B^{-1} / \text{K}$	$K_2 \text{ k}_B^{-1} / \text{K}$	$K_3 \text{ k}_B^{-1} / \text{K}$
Si-O-Si-O	15.39851	-5.2838	40.45884
Ge-O-Ge-O	15.39851	-5.2838	40.45884
Si-O-Ge-O	15.39851	-5.2838	40.45884
Angle-Angle-Torsion	$K \text{ k}_B^{-1} / \text{K rad}^{-2}$	$\theta_{eq} / ^\circ$	$\theta'_{eq} / ^\circ$
O-Si-O-Si	-2272.036	112.02	173.7651
O-Ge-O-Ge	-2272.036	112.02	173.7651
O-Si-O-Ge	-2272.036	112.02	173.7651

$$\text{Bond-Stretch: } U^{\text{bond-stretch}} = K_2(r - r_{eq})^2 + K_3(r - r_{eq})^3 + K_4(r - r_{eq})^4$$

$$\text{Angle-Bend: } U^{\text{angle-bend}} = K_2(\theta - \theta_{eq})^2 + K_3(\theta - \theta_{eq})^3 + K_4(\theta - \theta_{eq})^4$$

$$\text{Bond-Bond: } U^{\text{bond-bond}} = K(r - r_{eq})(r' - r'_{eq})$$

$$\text{Bond-Angle: } U^{\text{bond-angle}} = (\theta - \theta_{eq})[K_r(r - r_{eq}) + K'_r(r' - r'_{eq})]$$

$$\text{Angle-Angle: } U^{\text{angle-angle}} = K(\theta - \theta_{eq})(\theta' - \theta'_{eq})$$

$$\text{Torsion: } U^{\text{torsion}} = K_1(1 - \cos \varphi) + K_2(1 - \cos 2\varphi) + K_3(1 - \cos 3\varphi)$$

$$\text{Angle-Angle-Torsion: } U^{\text{angle-angle-torsion}} = K \cos \varphi (\theta - \theta_{eq})(\theta' - \theta'_{eq})$$

Table A5. Selected crystallographic information on the all-silica and germanosilicate experimental frameworks optimized frameworks HPM-1⁷⁻⁸ and SU-32⁹, and their optimized counterparts (STW-Si and STW-SiGe).

Framework	HPM-1 (experimental STW-Si)	SU-32 (experimental STW-SiGe)
Formula	SiO ₂	Si _{4.72} Ge _{5.28} O ₂₀ (Si _{11.328} Ge _{12.672} O ₄₈)
Space group	<i>P</i> 6 ₁ 22 (left-handed: <i>P</i> 6 ₅ 22)	<i>P</i> 6 ₁ 22 (left-handed: <i>P</i> 6 ₅ 22)
<i>a</i> (Å)	11.93558	12.2635
<i>c</i> (Å)	29.7500	30.2527
Volume (Å ³)	3670.33	3940.25
Framework	STW-Si (optimized HPM-1)	STW-SiGe (optimized SU-32)
Formula	SiO ₂	Si ₁₁ Ge ₁₃ O ₄₈ (Si _{4.58} Ge _{5.41} O ₂₀)
Space group	<i>P</i> 6 ₁ 22 (left-handed: <i>P</i> 6 ₅ 22)	<i>P</i> 6 ₁ 22 (left-handed: <i>P</i> 6 ₅ 22)
<i>a</i> (Å)	12.02105	12.5403
<i>c</i> (Å)	29.9889	31.2063
Volume (Å ³)	3752.75	4259.41

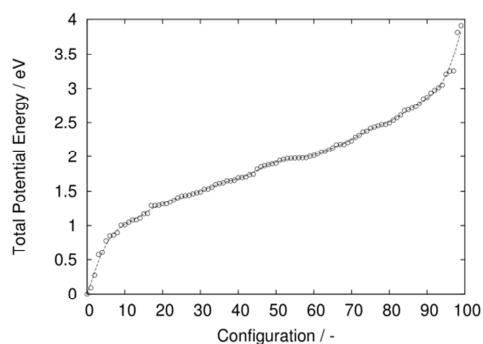


Figure A3. Configurational single-point energies of 100 different distributions of silicon and germanium atoms in STW zeolite (SU-32) according to the population of tetrahedral sites reported experimentally,⁹ ordered by increasing potential energy. Single-point energies were calculated with VASP¹⁰⁻¹³ using electronic correlations and the functional PBEsol.¹⁴

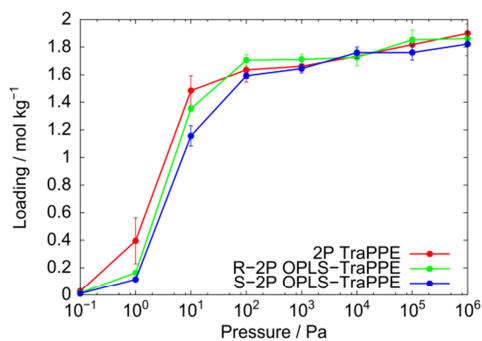


Figure A4. Adsorption isotherms for 2-pentanol in STW-Si at 298 K obtained by GCMC simulations by defining 2P with TraPPE-zeo force field (red), and *R*- and *S*-2P, with the OPLS-TraPPE combination (green and blue, respectively).

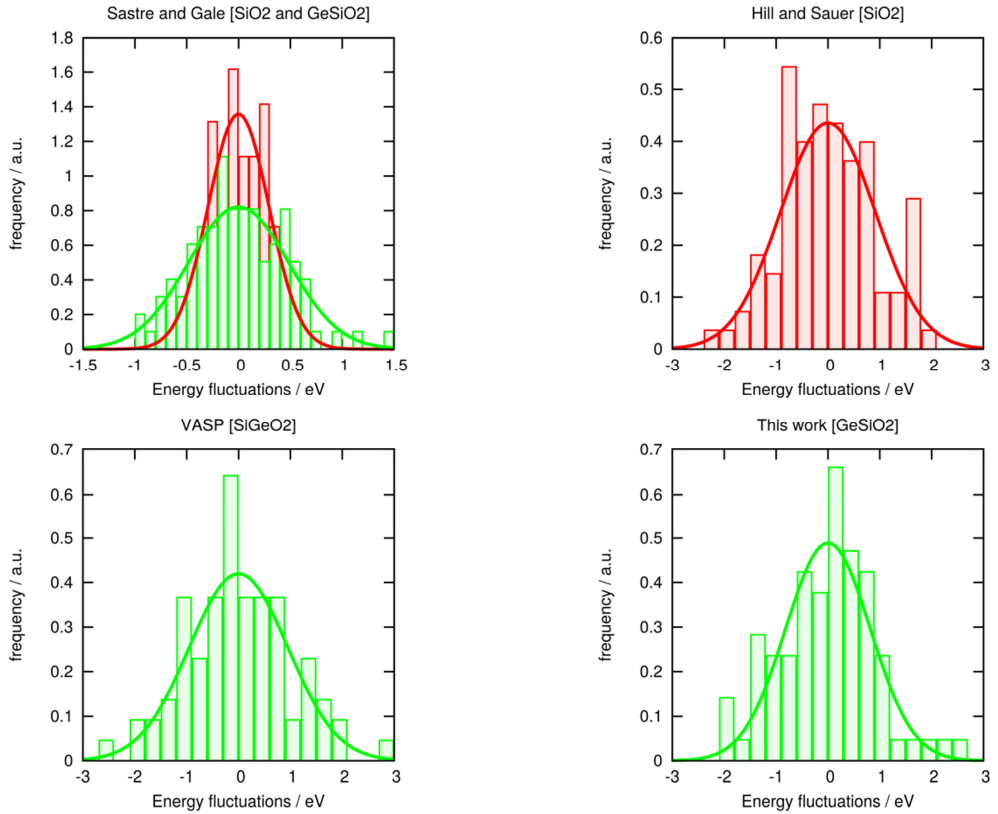


Figure A5. Energy distributions sampled over 250 ns trajectories for the all-silica and germanosilicate STW generated by MD simulations. Snapshots of the trajectories were taken at regular time intervals. Single-point energies were calculated for each snapshot using several well-known force fields and VASP.¹⁰⁻¹³ Energy fluctuations, i.e., standard deviations from the average value, of the trajectories are shown for the force field of Sastre and Gale¹⁵ (top left), the force field of Hill and Sauer⁶ (top right), the set of parameters used in the present work (bottom right), and VASP with PBESol¹⁴ functional (bottom left). Calculations for all-silica frameworks are shown with red bars and those for germanosilicate framework, with green bars. Energy fluctuations of the suggested force field and VASP are in good agreement, whereas those using Sastre and Gale's force field are roughly twice as narrow. Solid lines represent Gaussian fits to the energy fluctuations.

In order to evaluate which compounds can be adsorbed in each structure, mean squared displacements (MSDs) were computed through MD simulations in the canonical ensemble (NVT) at 298 K and infinite dilution. The time step was set to 0.5 fs and diffusion data of one single molecule was recorded for 250 ns on average. The frameworks were considered rigid since accounting for framework flexibility would increase the computational cost prohibitively and would be beyond the scope of these calculations.

Those compounds crossing the diffusive regime after 100 ns are considered as diffusing along the channel. Diffusion coefficients in the z -axis for R - and S -2P are higher for STW-SiGe ($\sim 10^{-10} \text{ m}^2 \text{ s}^{-1}$) than for STW-Si ($\sim 10^{-11} \text{ m}^2 \text{ s}^{-1}$). Diffusion coefficients (D_z) for 2MB enantiomers in STW-SiGe are around $10^{-11} \text{ m}^2 \text{ s}^{-1}$ and they do not cross the diffusive regime in STW-Si. Likewise, 3M2B only diffuses in STW-SiGe, with diffusion coefficients (D_z) around $0.6 \times 10^{-11} \text{ m}^2 \text{ s}^{-1}$ for both R and S enantiomers. While none of the enantiomers of 2MB and 3M2B are able to diffuse in the STW-Si framework, they show a lower slope in the MSD after the ballistic regime before they reach the plateau. This indicates that they can diffuse within the cage but cannot cross the cage-cage boundaries.

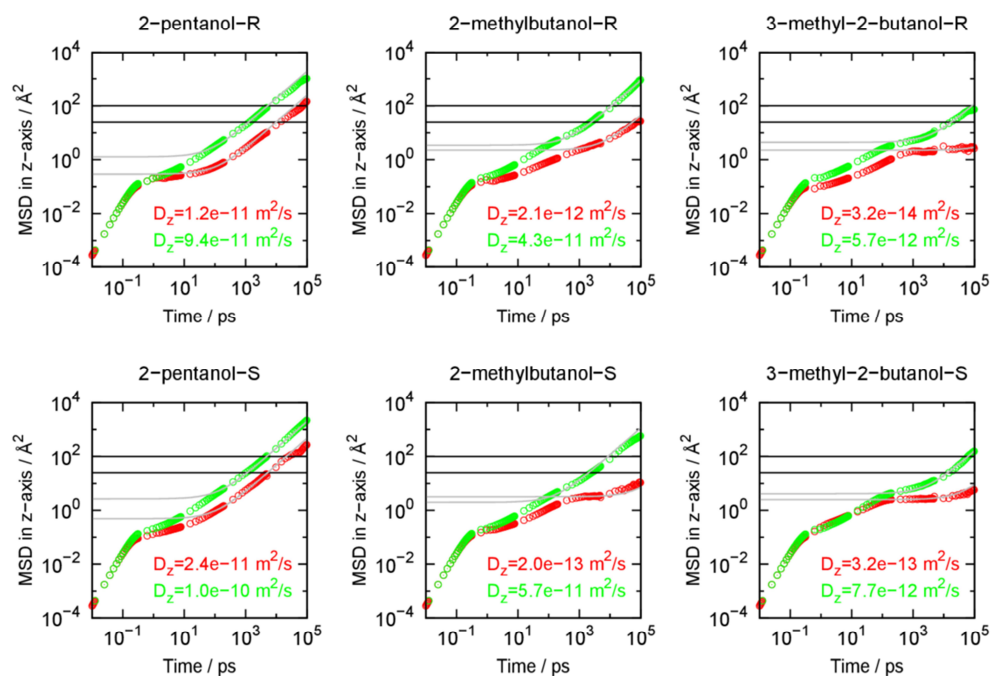


Figure A6. Mean squared displacement (MSD) along the z -axis of one single molecule of each compound in STW-Si (red) and STW-SiGe (green) at 298 K. The diffusion coefficient along the z -axis (D_z) is also given. Parallel black lines mark the diffusive regime.

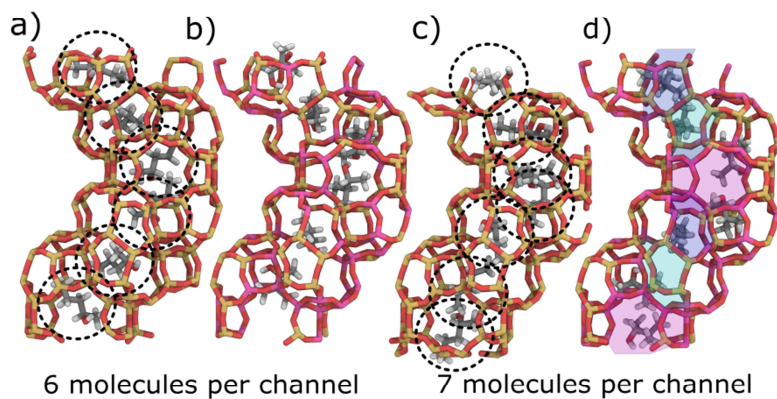


Figure A7. Chiral channel of the STW-Si (a, c) and STW-SiGe (b, d) containing 6 and 7 molecules per unit cell of 2P (a, c) and 3M2B (b, d). These views were obtained with QuteMol.

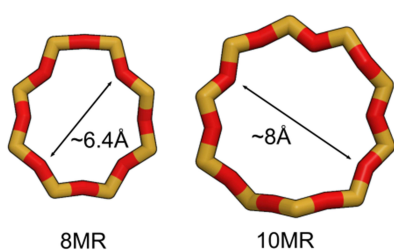


Figure A8. Atomistic view of 8MR and 10MR distortions in the STW-Si framework, related to the peaks of the histograms of minimum O-O separation across the aperture. These views were obtained with QuteMol.

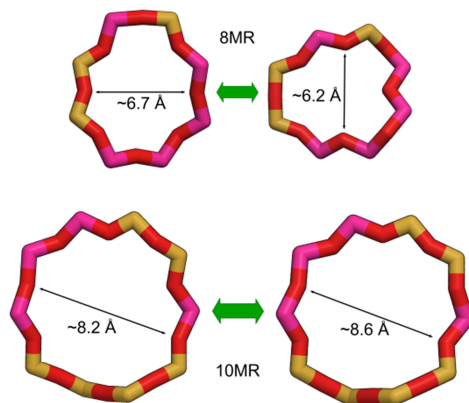


Figure A9. Atomistic view of 8MR and 10MR distortions in the STW-SiGe framework, related to the peaks of the histograms of minimum O-O separation across the aperture. These distortions are coupled: the 8MR shrinks while the 10MR broadens. These views were obtained with QuteMol.

The average occupational density profiles are calculated using MC simulations in the canonical ensemble (NVT), in which one molecule is moving randomly (molecular translation, rotation, and reinsertion) inside the framework. The center of mass is calculated and the xy - and yz -projections plotted in Figures A10 and A11. The colour scale on the right indicates, from black to red, the increasing density of molecules in the different areas of the framework. These areas are channels (I), necks (II), and pockets (III), and they are marked in each plot. Through a combination of both views, it is easy to figure out the preferential adsorption sites of each adsorbate. 2P is adsorbed mainly in the channels (I) and to a lesser degree in the necks (II) between channels. It can also be adsorbed in the pockets (III), but this site is not preferential for the linear isomer. This compound follows the same patterns in both frameworks though lines defined by the plotted molecules are thicker in STW-SiGe, the structure with wider channels. The molecules of 2MB are preferentially adsorbed in the necks (II) and pockets (III), leaving the channels (I) barely occupied. 3M2B is also adsorbed in the necks (II), but especially so in the pockets (III). The channels (I) are not preferential adsorption sites, though they can be occupied by the molecule.

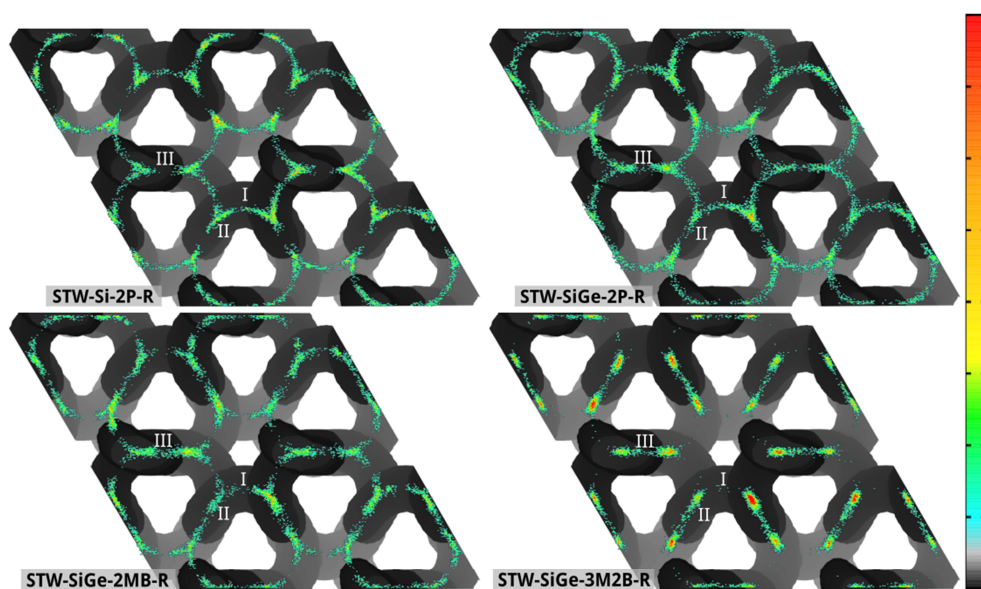


Figure A10. Average occupational density profiles of center of mass of *R* enantiomers of 2P, 2MB, and 3M2B adsorbed in STW-Si and STW-SiGe in an xy -view.

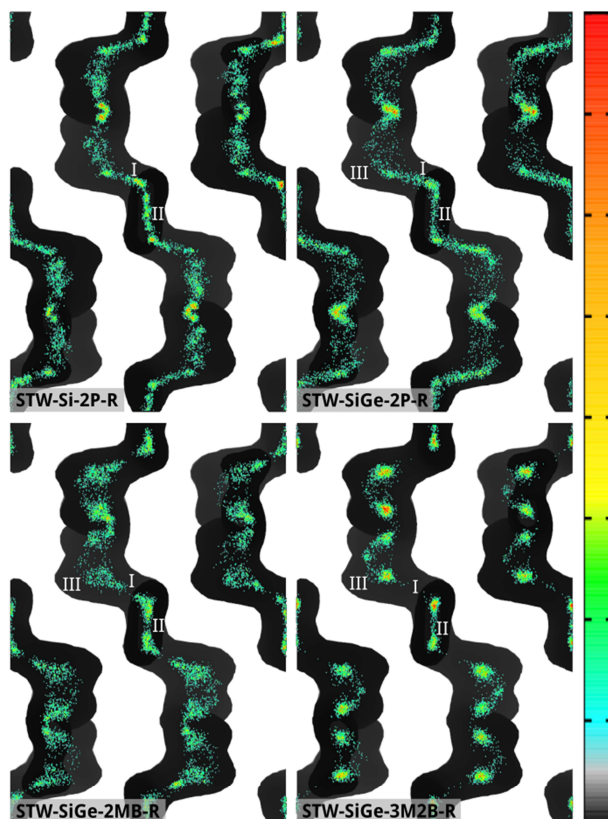


Figure A11. Average occupational density profiles of center of mass of *R* enantiomers of 2P, 2MB, and 3M2B adsorbed in STW-Si and STW-SiGe in a *yz*-view.

Table A6. Thermodynamic data for enantiomers of 2P and 3M2B in the right- and left-handed (RH and LH, respectively) STW-Si and STW-SiGe frameworks.

STW-Si	RH <i>R</i> -2P	RH <i>S</i> -2P	LH <i>R</i> -2P	LH <i>S</i> -2P
$Q_{st} / \text{kJ mol}^{-1}$	-69.28 ± 0.15	-67.06 ± 0.06	-67.04 ± 0.09	-69.43 ± 0.05
$\Delta A / \text{kJ mol}^{-1}$	-32.10 ± 0.03	-31.364 ± 0.007	-31.44 ± 0.02	-32.24 ± 0.02
$298 \text{ K} \cdot \Delta S / \text{kJ mol}^{-1}$	-34.7 ± 0.2	-33.21 ± 0.07	-33.1 ± 0.1	-34.69 ± 0.06
STW-SiGe	RH <i>R</i> -3M2B	RH <i>S</i> -3M2B	LH <i>R</i> -3M2B	LH <i>S</i> -3M2B
$Q_{st} / \text{kJ mol}^{-1}$	-51.3 ± 0.2	-56.86 ± 0.05	-56.91 ± 0.09	-51.04 ± 0.09
$\Delta A / \text{kJ mol}^{-1}$	-21.98 ± 0.02	-23.409 ± 0.008	-23.42 ± 0.03	-21.96 ± 0.01
$298 \text{ K} \cdot \Delta S / \text{kJ mol}^{-1}$	-26.8 ± 0.3	-30.96 ± 0.06	-31.0 ± 0.1	-26.6 ± 0.1

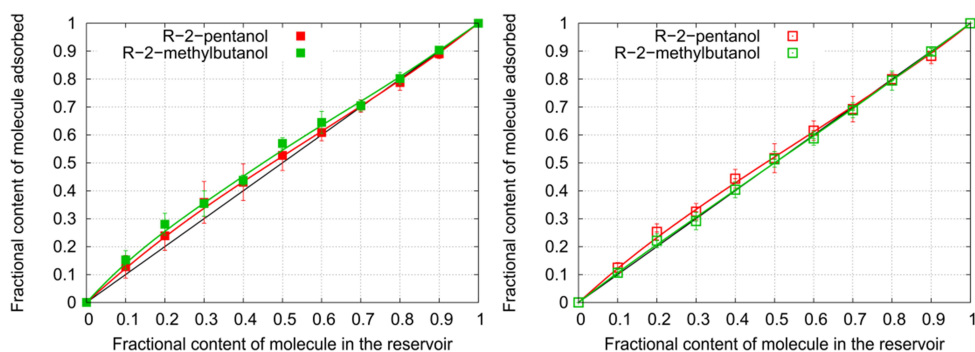


Figure A12. Adsorbed fractional content of *R* enantiomers as a function of the *R*-fraction in a *R/S* mixture in the reservoir for STW-SiGe taken as rigid frameworks (left) and considered flexible (right), at 10^6 Pa and 298 K. The straight black line indicates that the adsorbed composition is identical to that in the reservoir. Solid line shows an approximation of the data trend using the Bezier curve smoothing.

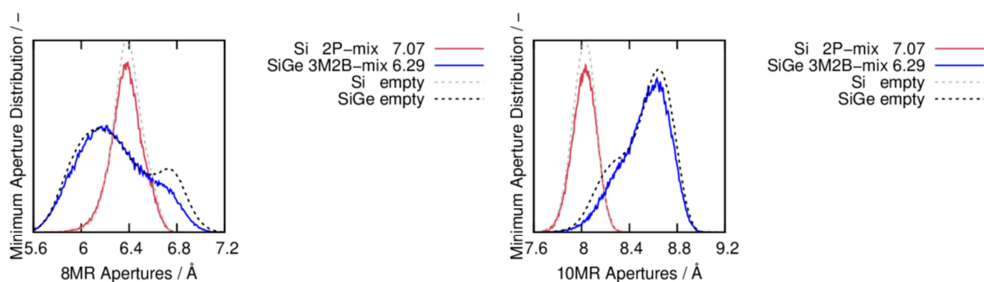


Figure A13. Distribution of minimum apertures of 8MR (left) and 10MR (right) in the empty STW-Si and STW-SiGe frameworks (dashed lines), and saturated with racemic mixtures (solid line). The loading is indicated for each compound in molecules per unit cell.

The RDF of each compound in the bulk shown in Figure A14 were calculated in an NVT simulation box of $25 \times 25 \times 25 \text{ \AA}^3$, at 298 K, with 86 molecules of *R*- and *S*-2P and 87 molecules of *R*- and *S*-3M2B, simulating their density at room temperature. In both figures there is a peak around 2.8 \AA between oxygen atoms that corresponds to hydrogen bonding. However the intensity of this peak is very low in the confined systems compared to the bulk. This means that the hydrogen bondings between hydroxyl groups of 2P or 3M2B are rather an occasional consequence of the packing of molecules at the saturation regime than the driving force for the particular molecular arrangement or the chiral selectivity.

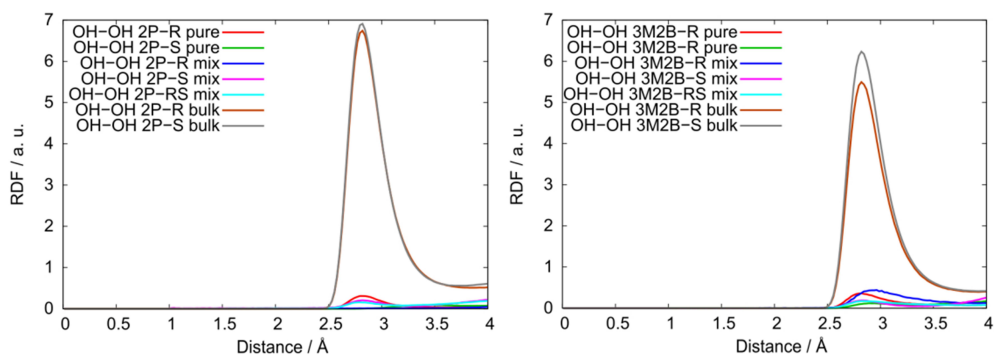


Figure A14. Oxygen-oxygen radial distribution functions (RDF) at saturation (10^6 Pa) in the rigid framework of *R* and *S* enantiomers of 2P (left) and 3M2B (right) as pure compounds, in the racemic mixture and in the bulk.

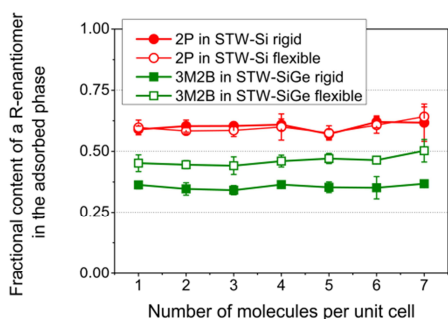


Figure A15. Loading-dependent adsorbed fractional contents of *R* enantiomers from racemic mixtures of 2P in STW-Si (red) and 3M2B in STW-SiGe (green) averaged over 5 independent GCMC simulations for the rigid frameworks, and snapshots of flexible frameworks obtained randomly from the corresponding hybrid GCMC simulation while framework atoms were allowed to move.

Bibliography

- (1) Sarkisov, L.; Harrison, A., *Mol. Simul.* **2011**, *37*(15), 1248-1257.
- (2) Humphrey, W.; Dalke, A.; Schulten, K., *J. Mol. Graphics* **1996**, *14*, 33-38.
- (3) Tarini, M.; Cignoni, P.; Montani, C., *IEEE Trans. Vis. Comput. Graphics* **2006**, *12* (5), 1237-1244.
- (4) Jorgensen, W. L.; Maxwell, D. S.; Tirado-Rives, J., *J. Am. Chem. Soc.* **1996**, *118* (45), 11225-11236.
- (5) Bai, P.; Tsapatsis, M.; Siepmann, J. I., *J. Phys. Chem. C* **2013**, *117*(46), 24375-24387.
- (6) Hill, J. R.; Sauer, J., *J. Phys. Chem.* **1994**, *98* (4), 1238-1244.
- (7) Rojas, A.; Cambor, M. A., *Angew. Chem., Int. Ed.* **2012**, *51* (16), 3854-3856.
- (8) Rojas, A.; Arteaga, O.; Kahr, B.; Cambor, M. A., *J. Am. Chem. Soc.* **2013**, *135* (32), 11975-11984.
- (9) Tang, L.; Shi, L.; Bonneau, C.; Sun, J.; Yue, H.; Ojuva, A.; Lee, B.-L.; Kritikos, M.; Bell, R. G.; Bacsik, Z.; Mink, J.; Zou, X., *Nat. Mater.* **2008**, *7* (5), 381-385.
- (10) Kresse, G.; Hafner, J., *Phys. Rev. B* **1993**, *47* (1), 558-561.

- (11) Kresse, G.; Hafner, J., *Phys. Rev. B* **1994**, *49* (20), 14251-14269.
- (12) Kresse, G.; Furthmüller, J., *Comput. Mater. Sci.* **1996**, *6*(1), 15-50.
- (13) Kresse, G.; Furthmüller, J., *Phys. Rev. B* **1996**, *54*(16), 11169-11186.
- (14) Perdew, J. P.; Ruzsinszky, A.; Csonka, G. I.; Vydrov, O. A.; Scuseria, G. E.; Constantin, L. A.; Zhou, X.; Burke, K., *Phys. Rev. Lett.* **2008**, *100* (13), 136406.
- (15) Sastre, G.; Gale, J. D., *Chem. Mater.* **2005**, *17*(4), 730-740.

List of publications

The following publications are directly related with this thesis and can be found in peer-reviewed journals.

Publications included in this thesis

• Chapter 2

R. Bueno-Pérez, A. Martín-Calvo, P. Gómez-Álvarez, J. J. Gutiérrez-Sevillano, P. J. Merklings, T. J. H. Vlugt, T. S. van Erp, D. Dubbeldam, and S. Calero. “Enantioselective Adsorption of Ibuprofen and Lysine in Metal-Organic Frameworks” *Chemical Communications*, **2014**, 50 (74), 10849-10852.

• Chapter 3

R. Bueno-Pérez, J. J. Gutiérrez-Sevillano, D. Dubbeldam, P. J. Merklings, and S. Calero. “Separation of Amyl Alcohol Isomers in ZIF-77” *ChemPhysChem*, **2015**, 16 (13), 2735-2738.

• Chapter 4

R. Bueno-Pérez, P. J. Merklings, P. Gómez-Álvarez, and S. Calero. “Cadmium-BINOL Metal-Organic Framework for the Separation of Alcohol Isomers” *Chemistry – A European Journal*, **2017**, 23 (4), 874-885.

• Chapter 5

R. Bueno-Pérez, S. Calero, D. Dubbeldam, C. O. Ania, J. B. Parra, P. Zaderenko, and P. J. Merklings. “Zeolite Force Fields and Experimental Siliceous Frameworks in a Comparative Infrared Study” *Journal of Physical Chemistry C*, **2012**, 116 (49), 25797-25805.

• Chapter 6

R. Bueno-Pérez, S. R. G. Balestra, M. A. Cambor, J. G. Min, S. B. Hong, P. J. Merklings, and S. Calero. “Influence of Flexibility on the Separation of Chiral Isomers in the STW-Type Zeolite” *Chemistry – A European Journal*, **2018**, doi: 10.1002/chem.201705627

Publications not included in this thesis

• S. R. G. Balestra, **R. Bueno-Pérez**, S. Hamad, D. Dubbeldam, A. R. Ruiz-Salvador, and S. Calero. “Controlling Thermal Expansion: A Metal-Organic Frameworks Route” *Chemistry of Materials*, **2016**, 28 (22), 8296-8304.

- S. Hamad, S. R. G. Balestra, **R. Bueno-Pérez**, S. Calero, and A. R. Ruiz-Salvador. “Atomic Charges for Modeling Metal-Organic Frameworks: Why and How” *Journal of Solid State Chemistry*, **2015**, 223 (Special Issue), 144-151.
- J. Pérez-Carbajo, P. Gómez-Álvarez, **R. Bueno-Pérez**, P. J. Merklung, and S. Calero. “Optimisation of the Fischer-Tropsch Process Using Zeolites for Tail Gas Separation” *Physical Chemistry Chemical Physics*, **2014**, 16 (12), 5678-5688.
- K. S. Deeg, J. J. Gutiérrez-Sevillano, **R. Bueno-Pérez**, J. B. Parra, C. O. Ania, M. Doblaré, and S. Calero. “Insights on the Molecular Mechanisms of Hydrogen Adsorption in Zeolites” *Journal of Physical Chemistry C*, **2013**, 117 (27), 14374-14380.
- T. Duerinck, **R. Bueno-Pérez**, F. Vermoortele, D. E. De Vos, S. Calero, G. V. Baron, and J. F. M. Denayer. “Understanding Hydrocarbon Adsorption in the UiO-66 Metal-Organic Framework Separation of (Un)saturated Linear, Branched, Cyclic Adsorbates, Including Stereoisomers” *Journal of Physical Chemistry C*, **2013**, 117 (24), 12567-12578.
- A. Martín-Calvo, E. García-Pérez, A. García-Sánchez, **R. Bueno-Pérez**, S. Hamad, and S. Calero. “Effect of Air Humidity on the Removal of Carbon Tetrachloride from Air Using Cu-BTC Metal-Organic Frameworks” *Physical Chemistry Chemical Physics*, **2011**, 13 (23), 11165-11174.
- **R. Bueno-Pérez**, E. García-Pérez, J. J. Gutiérrez-Sevillano, P. J. Merklung, and S. Calero. “A Simulation Study of Hydrogen in Metal-Organic Frameworks” *Adsorption, Science and Technology*, **2010**, 28 (8/9), 823-835.

Acknowledgments / Agradecimientos

Cada vez tengo más claro que no son sólo las personas que te acompañan las que influyen en el camino, sino también aquellas con las que simplemente te cruzas. Por eso querría empezar por dar las gracias a aquellas personas que, incluso sin saberlo, han contribuido de alguna manera a que haya llegado hasta aquí.

Pero, por supuesto, hay algunas personas sin las cuales esta tesis no habría sido posible. Hace 9 años me matriculé de una asignatura, “Modelización de Biomoléculas”, y empecé mi camino en esto de la simulación. Éramos sólo dos estudiantes por lo que Sofía y Patrick pensaron que la inmersión era el mejor método de aprendizaje. Una beca de colaboración y un máster más tarde, empecé el doctorado. Prácticamente, Sofía y Patrick me devolvieron al redil de la química, del que no tenía que haber salido. Sofía apostó por mí, literalmente, mandando a una biotecnóloga a una escuela de simulación en Amsterdam cuando ni siquiera teníamos segura la financiación. Gracias, **Sofía**, y gracias por animarme a afrontar los retos que esta tesis suponía, por enseñarme a ser práctica (o a intentarlo) y por darme la confianza que a veces me faltaba. Por su parte, Patrick supo ver mi entusiasmo analizando modos normales de vibración aunque yo intentara pintar espectros IR con *excel*. De Patrick he heredado el gusto por resolver cada detalle. Gracias, **Patrick**, por confiar en mis capacidades, por enseñarme a ajustar fino, ser exhaustiva y no dejar cabos sueltos, por ser siempre constructivo en las discusiones y dar su justo valor a cada parte del trabajo.

I reckon I have been lucky because, along these years, I was able to work with very interesting and nice people. For example, **David**, who masters and manages the in-house code mentioned in this thesis. I want also to thank him for his patience, and his willingness to help, always just one email away. And **Prof. Randall Q. Snurr**, who hosted me in his group. I would like to thank him for welcoming me and let me gain a wider perspective of what Computational Chemistry can reach. Quiero agradecer también a **Parra y Conchi**, colaboradores y aliados, por su apoyo en los congresos, sus aportaciones certeras, su ojo clínico experimental.

It was also great to work with **Thijs J. H. Vlugt, Titus S. van Erp, Miguel A. Cambor, Jung Gi Min, and Suk Bong Hong**, coauthors in the publications of this thesis, because their experience, their data, and their different points of view improved this work, and I have learnt a lot from them.

Además, día tras día he compartido espacio físico con personas que le han dado un toque diferente a esto de investigar. De aquellos que estaban antes que yo, agradezco a **Elena** por acogerme en el laboratorio y en la cola de los clúster; a **Juanma**, por acogerme en Stuttgart y enseñarme a modelizar moléculas; y a **Juanjo y Ana**, por las moléculas gordas y sus *movies*, y las magdalenas, y los carnavales. Gracias también a aquellos que vinieron después y *clusterizaron* porque siempre hay alguien con la respuesta, con un *script*, con una herramienta nueva. A **Ismael y Paco**, por las discusiones aleatorias durante el almuerzo; a

Julio, maestro del *scripting*, por su inestimable ayuda; a **Salva**, por sacarse códigos de la manga para exprimir los datos; **José**, el ruin, por no ser nada ruin; a **Vicent**, **Azahara** y **Ali**, por allanarme la recta final, tener siempre un “qué tal vas” sincero y ofrecerme papel de burbuja, respectivamente. A **Paula** por su optimismo, a **Rabdel** por sus chistes *trochos* y sus refranes, a **Said** por su sensatez y sus ganas de ayudar. A **José Luis**, nuestro espía en el 44, por descryptar para nosotros el lenguaje de las auditorías. A los que no están tan cerca, **Chema** y **Ángela**, por los ratitos de sol; y **Juan Antonio**, **Idi**, y **Paula Z.**, porque siempre nos vemos para cosas buenas. I would like also to thank **Katie** for helping me to improve my American English; and **Yamil**, **Noelia**, **Peyman**, **Diego**, and **Paola** for making me feel at home, when I actually was an ocean away.

A pesar de todo, más allá de la ciencia el mundo sigue moviéndose y girar con él ayuda a recuperar el centro. Me han hecho girar el **Club de Karate Do Herbert**, y los habitantes del **Gallo Rojo**. Giran también conmigo los **biotecnólogos** en la diáspora, con su Thesis Tour, y mis **frikis**, con su humor absurdo y nada correcto, que están deseando llamarme Doc (aunque no nos entiendan, **Javi**). Y cuando ha sido necesario parar el mundo ahí estaban las **niñas de los guantes de boxeo**, con su épica digna de una peli de *Marvel*, y la **tropa pirenaica**, enseñándome a respirar y subir montañas.

Algunas tesis son más largas que otras, pero esta ha sido un proceso largo y especialmente duro en el último año. Por eso soy muy consciente de los que me han arropado, cada uno a su manera. Por eso agradezco a **Marta**, la de los aviones, por escuchar y entenderme; a la otra **Marta**, la de la camisa retro, por ser familia; a **Jesús**, por responder siempre, raudo y veloz, para lo bueno y para lo malo, y a **Pierluigi** y **Salva**, por ofrecerme cobijo y un agua calentita. Pero, en especial, necesito agradecerle a **Mario** su apoyo incondicional, su preocupación constante, y su respeto; porque así, sí: gracias, gracias, gracias.

He dejado a mi familia para el final, pero es que son el principio de todo: condición *sine qua non*. Me han hecho sentir capaz de hacer todo lo que me propusiera, y cuando no era suficiente, me han dicho que había la luz al final del túnel. Gracias a mi madre, **Aurora**, por prestarme la fuerza, los sueños y el carácter. Muchas gracias a mi padre, **Luis**, porque sabe que soy Rocío Quirales, por comprar coquinas los fines de semana, por las conversaciones en la ría, y por hacerse fuerte para sostenerme. A mis hermanos, **Luis** y **Sylwia**, porque, primero uno y después otra, habéis estado siempre para convertir RGBs a CMYKs, opinar sobre la portada de esta tesis, subir al primo feo del Jungfrau, y hablar de lo complicado de la vida cuando supimos que la vida iba en serio.

Por último, como hemos conseguido llegar hasta aquí y lo prometido es deuda: ahora, *a juí*.

